Thermal dilepton radiation at FAIR energies as probes of the fireball *

F. Seck[†1], *T. Galatyuk*[1,2], *R. Rapp*[4], *and J. Stroth*[2,3]

[1]Technische Universität Darmstadt, Darmstadt, Germany; [2]GSI, Darmstadt, Germany; [3]Goethe-Universiät, Frankfurt, Germany; [4]Texas A&M University, College Station (TX), USA

One of the main goals of the CBM experiment is the exploration of the states of matter created in heavy-ion collisions. Under conditions of extreme temperature and baryon density, the restoration of chiral symmetry and the transition to deconfinement might (partially) take place and lead to exotic phases of strongly interacting matter. The experimental detection of the resulting modifications to the properties of matter is, however, challenging since the traces of these signals can get convoluted or washed-out by several other effects, e.g. final-state interactions.

A prime tool in this search are, therefore, electromagnetic probes. Once they are produced, dileptons decouple from the collision region and retain the valuable information about the medium at the time of their creation.

Dileptons are emitted during all stages of a heavy-ion collision. Of particular interest in this respect is the thermal excess radiation above the hadronic cocktail, i.e. after the subtraction of the decays of long-lived mesons. The yield of thermal low-mass dileptons is sensitive to the fireball lifetime, while the slope in the intermediate-mass region of the dilepton invariant-mass spectrum can serve as a thermometer which is unaffected by blue-shift effects caused by the collective expansion of the medium [1].

For a proper description of the dilepton invariant-mass spectrum realistic thermal rates have to be convoluted with a model of the fireball's space-time evolution. As a compromise between the microscopic transport and macroscopic hydrodynamics at FAIR energies a coarse-graining procedure was developed and successfully applied to the SIS energy regime [2-4]. The local matter properties extracted with this approach are fed into a parametrization of the Rapp-Wambach spectral function [5] for in-medium ρ emission and lQCD-inspired QGP rates [6] (if high enough temperatures are reached). The pertinent dilepton spectra are then obtained by integrating these rates over the whole space-time evolution. An example of an invariant-mass spectrum of thermal dileptons in Ar+KCl collisions at 1.76A GeV is shown in Fig. 1 together with the data from the HADES experiment.

The thermal rates of e^+e^- and $\mu^+\mu^-$ pairs for Au+Au collisions at top SIS-100 energies of 11A GeV are now available to the CBM collaboration. With the implementation into the fast Monte-Carlo generator Pluto, it is possible to create a large statistics sample of dileptons that can be passed into the usual simulation and reconstruction chain.

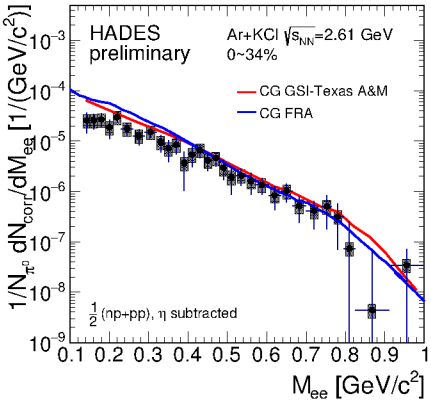

Figure 1: Comparison of dilepton excess spectra from two independent coarse-graining approaches [2-4] and the experimentally extracted yield above the hadronic cocktail in Ar+KCl collisions at 1.76A GeV from HADES [7,8].

The provided thermal spectra can serve as a basis for comprehensive experimental investigations. A significant deviation from this baseline in terms of extra yield in the low-mass range or a change in the emitting source temperature, extracted from the intermediate-mass range, could indicate a possible 1^{st} order phase transition [9]. Such scenarios and their observable consequences are currently subject to further investigations.

In the context of FAIR Phase-0 roughly 10% of the CBM time-of-flight detector modules will be installed as an endcap TOF in the STAR experiment during the upcoming RHIC beam energy scan II [10]. To fill the gap in the excitation function of dilepton production, our framework for the calculation of thermal dilepton spectra will also be applied to the proposed beam energies and be used for detector studies in the preparation of this scan in the years 2019-2020.

References

[1] R. Rapp and H. van Hees, PLB **753** (2016) 586

[2] S. Endres *et al.*, PRC **92** (2015) 014911

[3] T. Galatyuk *et al.*, EPJ A **52** (2016) 131

[4] F. Seck *et al.*, CPOD 2016 proceedings to appear in Acta Phys. Polon. Supp.

[5] R. Rapp and J. Wambach, EPJ A **6** (1999) 415

[6] R. Rapp, Adv. High Energy Phys. **2013** (2013) 148253

[7] HADES coll., G. Agakishiev *et al.*, PRC **84** (2011) 014902

[8] HADES coll., G. Agakishiev *et al.*, PLB **690** (2010) 118

[9] CBM coll., T. Alyazimov *et al.*, EPJ A **53** (2017) 60

[10] STAR coll. & CBM TOF group,arXiv:1609.05102 (2016)

* This work was supported by the U.S. National Science Foundation under grant PHY-1306359, by the Humboldt foundation (Germany), by the Helmholtz-YIG grant VH-NG-823 at GSI and TU Darmstadt (Germany), and by the Hessian Initiative for Excellence (LOEWE) through the Helmholtz International Center for FAIR (HIC for FAIR).

† f.seck@gsi.de

Design of a control and monitoring system for the mirror alignment of the CBM RICH detector*

J. Bendarouach† [1] *and C. Höhne* [1]
[1]Justus Liebig University, Giessen

The alignment of the RICH mirrors is a decisive aspect for a reliable and high quality operation of the detector. A correction cycle, consisting of three stages, has been developed to address this problem [1, 2].

First a qualitative check of the mirrors using the CLAM (Continuous Line Alignment Monitoring [3]) method has been successfully implemented in the RICH prototype and validated during a beamtime at CERN. A correlation between mirror misalignments, inducing distorted rings and broken reflected stripes has been shown [4].

An additional quantification method for detected misalignments, inspired from the HERA-B experiment [5], has been adapted and tested in the simulation framework of the CBM-RICH detector. The method uses data to extract the rotation angles of a particular tile, provided a sufficient number of accumulated events are fully hitting the considered tile [6].

The last step combines the misalignment information from the two previous techniques, to correct for track projections.

The second step of the correction cycle, namely the quantification method, has been further developed and optimized. It can now detect misalignments on different mirror tiles simultaneously misaligned.

Subsequently, the performances of the correction routine have been investigated. The accuracy of the misalignment correction was calculated for different mirror tile locations in the mirror wall. For this study misalignments have been artificially induced around the horizontal and vertical axes and reconstructed using the quantification method. Two cases have been reviewed: for mirror tiles close to the beam pipe (later called inner tiles) and for tiles located in the outer region of the mirror wall (outer tiles).

Fig. 1 shows the reconstructed rotation angle, β, depending on the applied one, α, for both an inner tile (left plot) and an outer tile (right plot). In this case the tiles were artificially rotated around their horizontal axis, with misalignments ranging with various steps from 0.1 to 5 mrad. In the case of an inner tile, the reconstructed rotation angle of the rotated axis is very close to the applied one (orange line, left plot), while the reconstructed rotation angle of the unrotated axis is not influenced (green line, left plot). In case of the outer tile, the reconstructed rotation angle of the rotated axis increasingly diverges from the applied angle (orange line, right plot) and the unrotated axis picks up misalignment angles (green line, right plot).

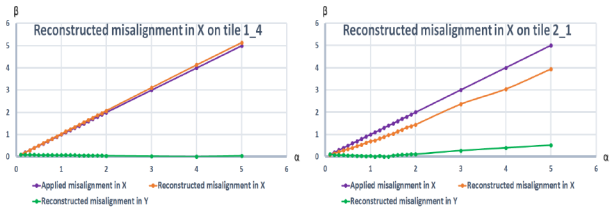

Figure 1: Reconstructed misalignment, β, depending on the applied one, α, for inner tiles (left plot) and outer tiles (right plot). The reconstructed misalignment angles, β, on the horizontal axis (orange lines) and on the vertical axis (green lines) are represented. Ideal reconstruction is shown by the purple line.

A similar behaviour, even more pronounced, has been observed in case of a rotation around the tile's vertical axis [2]. This effect is believed to be due to the detector geometry. Indeed for outer tiles, a rotation around a single axis causes a shift of the fitted ring center in both directions, which is then reconstructed as misalignment on both axes.

In the next step, the impact of misalignment and corrections on the full RICH performances will be studied. An automated correction routine, run with Urqmd events and for a fully misaligned mirror wall will be tested. The CLAM method will be further investigated in the lab.

References

[1] J. Bendarouach (CBM Collab.) J. Phys.: Conf. Ser. 742 2016 012007 http://dx.doi.org/10.1088/1742-6596/742/1/012007

[2] J. Adamczewski-Musch et al., "Design of a control and monitoring system for the mirror alignment of the CBM RICH detector", Nucl. Instr. Meth. Phys. Res. (2017), http://dx.doi.org/10.1016/j.nima.2017.02.033

[3] L. Steiger et al., Nucl. Instr. Meth. Phys. Res. A 639 (2011) 219

[4] J. Bendarouach et al., CBM Progress Report 2014, p.56

[5] M. Staric et al., Nucl. Instr. Meth. Phys. Res. A 586 (2008) 174

[6] J. Bendarouach et al., CBM Progress Report 2015, p.62

* Work supported by HIC for FAIR, HGS-HIRe, the GSI F&E-Cooperation with Giessen and BMBF grants 05P15RGFCA and 05P12RGFCG.

† jordan.bendarouach@exp2.physik.uni-giessen.de

DOI:10.15120/GR-2017-1

Procedure for charged hadrons identification in the CBM experiment

V. Klochkov[1,2] *and I. Selyuzhenkov*[1]
[1]GSI, Darmstadt, Germany; [2]Goethe-University Frankfurt, Germany

The goal of the CBM experiment at FAIR is to investigate the properties of dense baryonic matter. Important observables are the yields, spectra, collective flow, and correlations of identified particles. Particle Identification (PID) is required for a study of the mass and flavour composition of particle production in high-energy physics experiments. We present the procedure for identification of charged pions, kaons and protons tested with simulated Au+Au collisions at SIS100 energies. Particle identification via time-of-flight is based on simultaneous measurement of momentum p, time t and track lenght l of a particle using the relation to its mass m: $m^2 = p^2((t/l(p))^2 - 1)$. The CBM experiment allows identification of hadrons (pions, kaons and protons) in the angular range $2.5° < \Theta < 25°$.

To develop an automated procedure for PID a sample of 1.5M Au+Au collisions with beam energy of 10 AGeV simulated with UrQMD [2] event generator were used. CBM setup is simulated with CBMRoot version Nov16 and includes the beam pipe, magnet, MVD, STS, RICH, TRD, PSD and TOF [1]. For this analysis we used reconstructed tracks with at least 4 hits in STS and MVD, fit quality $\chi^2/NDF < 3$ and distance to primary vertex normalized to its error $\chi^2_{prim} < 3$.

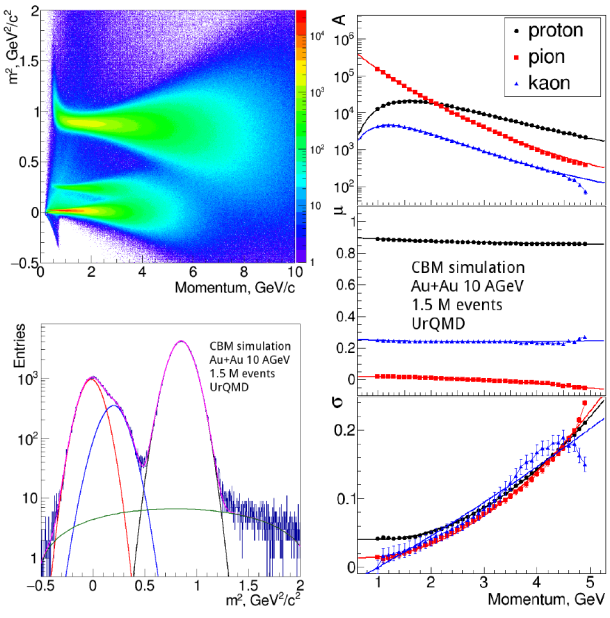

Figure 1: Distribution of m^2 versus p (top left) and for p = 4.0-4.1 GeV/c (bottom left) for positively charged hadrons. Magenta line shows the combined fit, green line shows background, others colors show contributions from different particles (π, K, p). (right) Parametrization of m^2 spectra in different momentum bins.

PID procedure is similar to that developed in ALICE [4]:

1. Fill m^2 vs p distribution for a pure sample of π, K and p (denoted below as 2D-(π,K,p)) and for all particles (2D-all). Pure sample of pions, kaons and protons can be obtained from decay daughters of K^0_s, Λ and ϕ using KF Particle Finder [3].
2. Parameterize m^2 distribution in slices of momentum:
   (a) Fit each slice of 2D-(π,K,p) using generalized Gaussian function $G(m^2) = Ae^{-(\frac{|m^2-\mu|}{\sigma})^k}(1 + Erf(s\frac{m^2-\mu}{\sqrt{2}\sigma}))$ with 5 paramemters abundance (A), mean (μ), sigma (σ), s and k are connected with skewness and kurtosis.
   (b) Fit each slice of 2D-all with a sum of generalized Gaussians $G(m^2, p)$ and polynomial function for background $BG(m^2, p)$.
3. Parametrize momentum dependence of the fit parameters. Repeat until parameters are stabilized.
4. Save fit parameters to the ROOT file for further use in the analysis.
5. Calculate a bayesian probability P_j for a given m^2 and p for a particle to be of type j:

$$P_j(m^2, p) = \frac{G_j(m^2, p)}{\sum_{i=\pi,p,K} G_i(m^2, p) + BG(m^2, p)}.$$

This procedure should be applied in different centrality classes [5]. In Fig. 1 an illustration of PID determination procedure using Gaussian fit function ($k = 2$ and $s = 0$ in $G(m^2)$) is shown. A pure sample of particles is obtained using MC-true information.

In summary, procedure for particle identification was developed for CBM. Bayesian approach allows to select sample of high-purity charged hadrons as a function of centrality and momentum and to unfold the measured observables based on parametrization of abundances of each particle. In future the efficiency, purity and misidentification of the PID method will be investigated.

References

[1] N. Herrmann et al. [CBM Collaboration], TDR for the CBM TOF, http://repository.gsi.de/record/54798.

[2] M. Bleicher et al., J.Phys. G25, 1859 (1999).

[3] M. Zyzak, PhD Thesis, http://publikationen.ub.uni-frankfurt.de/frontdoor/index/index/docId/41428

[4] J. Adam *et al.* [ALICE Collaboration], Eur. Phys. J. Plus **131**, no. 5, 168 (2016)

[5] V. Klochkov and I. Selyuzhenkov, GSI Scientific Report 2015 p.23 (2016) http://repository.gsi.de/record/189686

DOI:10.15120/GR-2017-1

Neutron shielding for PSD readout by SiPM*

O. Svoboda†[1], *F. Guber*[3], *A. Kugler*[1], *and A. Senger*[2]
[1]NPI CAS, Rez, Czech Republic; [2]GSI, Darmstadt, Germany; [3]INR RAS, Moscow, Russia

Radiation damage of the components of the CBM Projectile Spectator Detector (PSD) is an important issue. High intensity beams at the FAIR SIS100 will cause fast degradation of currently available types of SiPM planned for the detector readout. Parallel to the search for more radiation hard SiPM also the ways to reduce the neutron doses were investigated and polyethylene based neutron shielding was developed.

Radiation sensitive SiPM readout

The PSD is a compensating lead-scintillator calorimeter designed to measure the energy distribution of the projectile nuclei fragments (spectators) and forward going particles produced close to the beam rapidity [1]. Beams at FAIR SIS100 of up to 1E7 interactions/s will lead to a high radiation emission to the PSD producing a high neutron fluence of up to 4E12 n/cm^2 accumulated during one year of the experiment operation. Silicon photomultipliers (SiPM, sometimes marked also as avalanche photodiodes (APD)) are planned to be used for light readout from the wavelength shifting fibers (WLSF) connected to the plastic scintillators.

Although there is a relatively large number of SiPM manufacturers today, all types of SiPM suffer from low radiation hardness. In PSD, the SiPMs are the weakest component from the radiation hardness point of view. Intensive studies of SiPM radiation hardness are being performed at NPI Rez, see e.g. [2]. Currently available SiPMs from different vendors are irradiated with different neutron doses and their properties are studied in detail. Parallel to this, also the ways to reduce neutron dose are tested.

PSD as spallation target

Taking into account the composition of the PSD detector, namely lead and plastic, the PSD may be seen as a massive spallation target with neutron moderator. To see the "spallation" spectra at the end of the PSD setup, where the SiPMs are placed, a MCNPX 2.7 simulation was run [3]. One PSD module represented by an alternating lead-plastic structure of real dimensions was irradiated in the center with a white beam of 100 MeV - 10 GeV protons in the simulation. Neutron spectra were scored at the end of PSD and it was checked, that similar result will be obtained for the white spectra neutron beam of the same energy span. Gained neutron spectra were later used to fast simulate the efficiency of the proposed shielding.

MCNPX simulation

Several dimensions and boron enrichment of polyethylene neutron shielding were consequently tested in the MCNPX simulation. Neutron and proton spectra were calculated in the volume representing the SiPM diode, for results please see Figure 1. It was shown that even only 5 cm of 3 percent borated polyethylene can significantly lower the thermal neutron flux. Number of secondary protons created in this shielding is negligible. However, the MCNPX simulation was only an approximation due to unknown particle spectra hitting the PSD in real experiment.

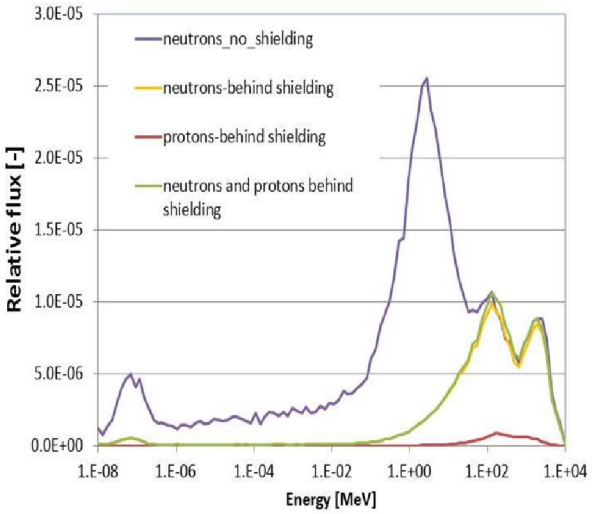

Figure 1: MCNPX 2.7 simulation of single PSD module with neutron shielding.

Fluka simulation

The proposed neutron shielding was tested also in the Fluka code [4], taking into account complex CBM setup and conditions. Fluka simulation proved significant decrease in neutron equivalent fluence at the position of PSD SiPM readout, especially for the most central modules, please see Figure 2. Differences in the neutron fluence with and without the polyethylene shielding are almost one order of magnitude. This might be the difference between slightly damaged SiPM, which can still read-out the light

* Work supported by Czech MEYS - LM2015049 , OP VVV - CZ.02.1.01/0.0/0.0/16_013/0001677
† svoboda@ujf.cas.cz

DOI:10.15120/GR-2017-1

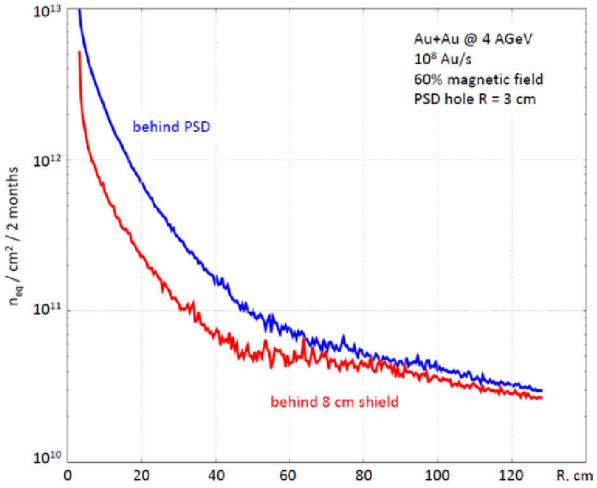

Figure 2: Fluka simulation of neutron shielding for PSD.

pulses from WLSF, and completely damaged SiPM with unacceptable high noise.

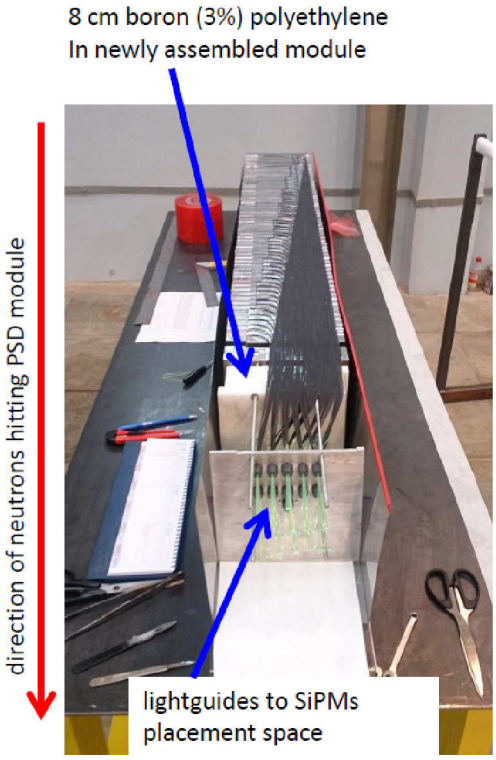

Figure 3: Assembly of PSD module including neutron shielding.

PSD module construction

Taking into account the results of MCNPX and Fluka simulations, it was decided to use neutron shielding of SiPM in PSD in the form of 8 cm thick polyethylene blocks, with three percent of boron. Shielding blocks are being mounted in the currently build PSD modules, see Figure 3. This shielding should provide additional safety reserve and lower the SiPM degradation in normal operation conditions.

Conclusion

Simple idea on significant reduction of neutron flux at the end of PSD was verified in MCNPX and Fluka simulations and successfully adopted in the construction of PSD modules. Lowering of especially thermal neutron flux can help together with the search on more radiation hard SiPM to build the PSD ready for SIS100 experiments and their high beam intensities.

References

[1] CBM collaboration, Technical Design Report for the CBM Projectile Spectator Detector (PSD), GSI Darmstadt 2015

[2] V. Kushpil et al., Neutron irradiation study of silicon photomultipliers from different vendors, NIM A (2016), http://dx.doi.org/10.1016/j.nima.2016.06.101

[3] MCNPX (Monte Carlo N-Particle eXtended), Los Alamos National Laboratory LA-CP-11-0438

[4] T.T. Bohlen et al., The FLUKA Code: Developments and Challenges for High Energy and Medical Applications, Nuclear Data Sheets 120, 211-214 (2014)

Status of micro-strip sensor development for the CBM Silicon Tracking System

J. M. Heuser[1], *C. J. Schmidt*[1], *C. Sturm*[1], *A. Lymanets*[1,5], *O. Bertini*[1], *M. Teklyshin*[2,5], *Ie. Momot*[3,1,5], *H. Malygina*[3,1,5], *P. Larionov*[3,4], *and Y. Murin*[6]

[1]GSI, Darmstadt, Germany; [2]FAIR, Darmstadt, Germany; [3]Goethe Universität, Frankfurt, Germany; [4]now at INFN-LNF, Frascati, Italy; [5]KINR, Kiev, Ukraine; [6]JINR, Dubna, Russia

Double-sided silicon microstrip sensor technology will be employed in CBM's Silicon Tracking System as one of the measures to achieve two-coordinate track-point determination with high spatial resolution and high momentum resolution through a minimized material budget [1]. Depending on their positions within the eight tracking stations, the sensors have been designed in four geometrical shapes. They have the same total width and numbers of strips but differ in the lengths of the strip-shaped electrodes, matched to the particle densities in the respective detector region. The main sensor parameters have been listed e.g. in reference [2]. Here shall be emphasized only: a) the thickness (285/320 $\pm$15 μm, vendor dependent), b) the outer dimensions (6.2 cm width; 2.2, 4.2, 6.2 and 12.4 cm height) and c) the strip lengths (2, 4, 6 and 12 cm), yielding 1024 strips of 58 μm pitch per sensor side. Front-and back-side strips are arranged under a 7.5 degree stereo angle. The short angled corner strips of the p-side are interconnected via routing lines on a second metal layer to allow read-out of the entire sensor from one sensor edge.

The production masks, established together with the two vendors, have been further advanced with respect to several important details. Small series of sensors have been realized through GSI and JINR purchase orders incorporating those improvements. They include e.g. multiple guard rings on the sensors' n-sides, with the intention to further increase operaration voltage limits, and perimeter lines being compatible with "stealth" laser dicing also at CiS to yield high-precision mechanical dimensions. Processing on 6" wafers, pre-requisite for fabricating the largest sensor, is standard at Hamamatsu and being put into operation at CiS next to the established 4" production line.

The assessment of the sensors has been advanced further. Quality assurance procedures, equipment and work sharing have been nearly finalized and documented. A test with non-irradiated sensors under anticipated thermal operating conditions (T=-5 °C) was carried out at COSY, Research Center Jülich, using a proton beam at close to minimum ionizing energy. Sensor samples have been altered with protons to beyond the end-of-life neutron equivalent fluence at the irradiation facility of the Karlsruhe Institute of Technology (KIT). The performance of the sensors with respect to ionizing radiation was addressed in a comprehensive CBM workshop at KIT bringing together silicon detector experts from different experiments and vendors. A STS project-internal workshop took place at GSI in March 2017 to define the roadmap for sensor production readiness. [1]

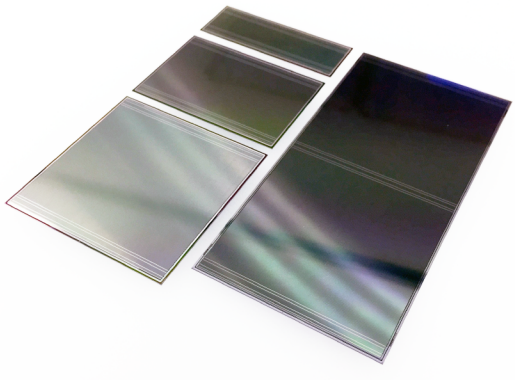

Figure 1: Microstrip sensors for the CBM Silicon Tracking System produced in the four major shapes (6.2 by 2.2, 4.2, 6.2 and 12.4 cm outer dimensions).

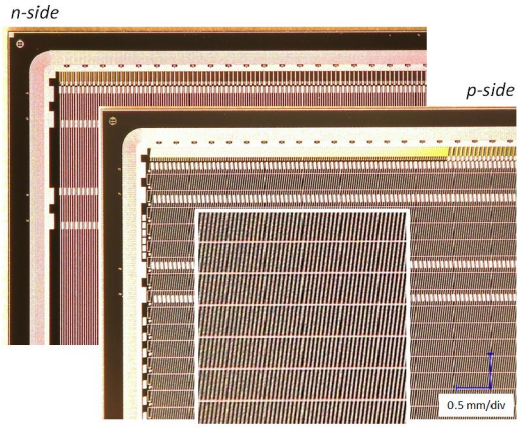

Figure 2: Close-up views of the most recent microstrip sensors, showing the strip segmentation on two sensor sides, the double-metal routing lines (magnified in the inlet) and sensor edge structures including multiple guard rings.

References

[1] GSI Report 2013-4 (2013), chapter 2.3

[2] CBM Progress Report 2015 (2016), p. 22

[3] http://www.cismst.org

[4] http://www.hamamatsu.com

[1] supported by HICforFAIR and EU-H2020 Project CREMLIN

DOI:10.15120/GR-2017-1

Test performance of the basic architecture for the inner zone of the CBM-TOF wall using heavy-ion beam at SPS-CERN *

M. Petriş[1], D. Bartoş[1], M. Petrovici[1], L. Rădulescu[1], V. Simion[1], J. Frühauf[2], M. Kiš[2], P-A. Loizeau[2], I. Deppner[3], N. Herrmann[3], and C. Simon[3]

[1]NIPNE, Bucharest, Romania; [2]GSI, Darmstadt, Germany; [3]PI, Heidelberg University, Germany

The Time Of Flight (TOF) subsystem is one of the core detectors of the CBM experiment. The TOF wall in conjunction with Silicon Tracking System (STS) is foreseen to identify charged hadrons, i.e. pions, kaons and protons, in the full acceptance of the system (the angular range covered by the STS detector of 2.5^0-25^0). It covers an active area of about 120 m^2 approximately rectangular in shape. A system time resolution of at least 80 ps including all possible contributions, such as electronics jitter and the resolution of the time reference system is needed. This requires a single channel time resolution better than 60 ps with an efficiency of at least 95%. Such a performance should be maintained up to a counting rate which, very close to the beam pipe, exceeds 30 kHz/cm^2 [1].

Our R&D activity has been focused on the development of a Multi-Gap RPC with Multi-Strip readout (MSMGRPC) for high counting rate and multiplicity environment, as it is anticipated to be in the inner zone of the CBM-TOF. Based on the good results obtained with the narrow strip pitch (2.54 mm) double stack counter (2 x 5 gas gaps of 140 μm), in terms of efficiency, time and two-dimensional position resolutions [2], a new prototype with the strip pitch equal with 7.4 mm (5.6 mm strip width) and a strip length of 96 mm was designed and built. Construction details of this prototype, called RPC2012, and its performance in the in-beam tests performed at CERN-PS accelerator together with the concept of the modular configuration of the CBM-TOF inner wall based on this RPC architecture were reported in [3].

The prototype was tested at H4 beam line of CERN SPS-facility, using reaction products produced by an Ar beam of 13A GeV energy incident on a Pb target. The average obtained cluster size was 1.6 strips per hit and the time resolution, including the electronics contribution, was of ~60 ps [4]. For all these tests mentioned above a front-end electronics based on 8 channel NINO chip [5] was used for signal processing.

Here we report the performance, in close to real conditions, of this architecture operated with a FEE based on a 32 channel motherboard [1] containing 4 PADI chips[7], the front-end electronics anticipated to be used for the CBM-TOF wall. The signals were digitized by 32-channel FPGA-TDCs [8] and readout via TRB3 [9] data hubs. The in-beam test were performed at CERN-SPS with a 30A GeV Pb ions incident on a Pb target.

The CBM-TOF experimental setup was divided in "low rate" and "high rate" branches, the last one being positioned at a polar angle of about 3^0 relative to the beam axis. A comprehensive description of the whole setup is given in [6]. Our prototypes were positioned in the high rate setup, the RPC2012 prototype being 'sandwiched' between RPC2015 [11] and RPCref prototypes. A diamond detector positioned in front of the target together with RPCref positioned at the end of the set-up, delivered the information for particle velocity measurement. A photo of the "high rate" branch is shown in Fig. 1. The spatial position along the

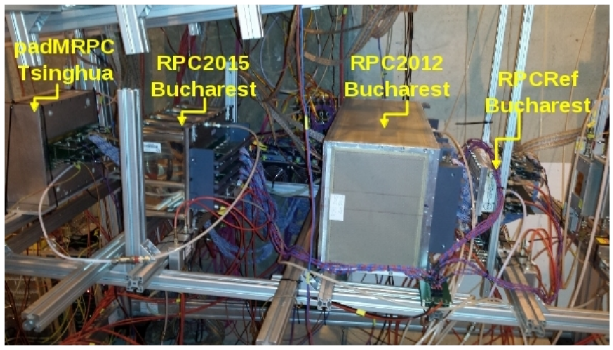

Figure 1: Photo of the high rate experimental set-up based on MGRPC prototypes used in the in-beam test.

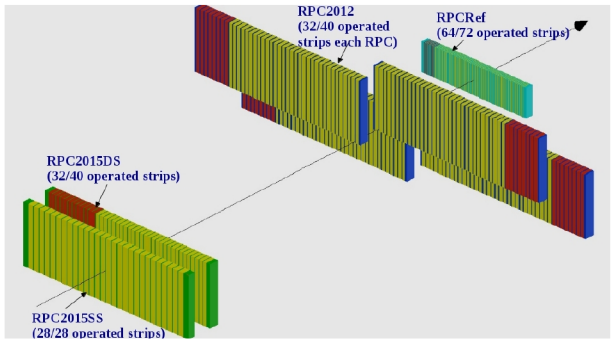

Figure 2: Sketch of the spatial position of the seven RPCs tested in the high rate setup at CERN-SPS.

*Romanian NASR/contract RO-FAIR F04 and NASR/NUCLEU Project PN16420104

beam line of the seven prototypes tested by our group and their operated area (green color) are presented in Fig. 2.

The principles of the data analysis starting from unpacking to calibration and corrections for slewing effect, position and reaction product velocity spread are described in [12]. In the left side of Fig. 3 is presented the time difference spectrum between one of the four counters positioned in the upper part of the text box (called RPC2012_3) and RPC2015DS (see reference [11]), with the same inner geometry and the same strip pitch. The 63 ps standard de-

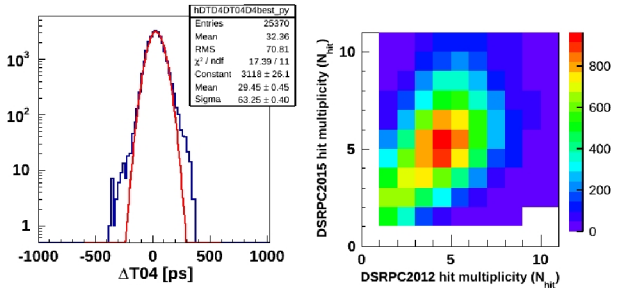

Figure 3: Time difference spectrum - left. Hit multiplicitiy correlation - right.

viation of the Gauss fit demonstrates the very good system time resolution. A single counter time resolution of 44 ps, including the electronic contribution is obtained supposing equal contributions of the two detectors. The comparison of the 63 ps standard deviation with the 71 ps RMS of the spectrum shows a non-significant contribution of the non-Gaussian tails. The correlation of the hit multiplicities in the two counters shows that in the most part of the events, almost the same multiple hits are incident on both detectors. The detectors were operated at 2 x 5.5 kV voltage. Due to their staggered positions, position cuts on both x and y directions were applied in the RPC2015DS, considered as reference counter, for efficiency estimation. However, due to a partial overlap of the active area of each of the four counters relative to the RPC2015DS, the obtained values are still affected by the hits lost at the edges of the overlaped area.

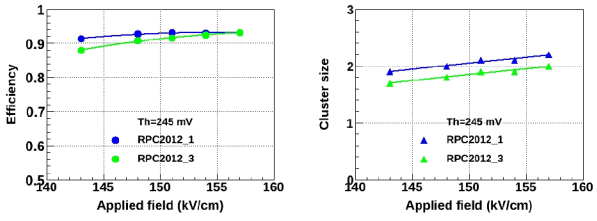

Figure 4: Efficiency - left and cluster size - right as a function of high voltage for RPC2012_1 and RPC2012_3.

In Fig. 4 is shown an expected behaviour of the efficiency and cluster size as a function of high voltage, for RPC2012_3 and RPC2012_1 (right mirrored relative to the axe shown in Fig. 2) for a PADI threshold of 245 mV. In the mentioned geometry of the experiment, a 93% efficiency for both counters was obtained. If we take into consideration the inner geometry of the RPC2012 counters of 2 x 5 gaps of 140 μm, the same as for RPC2015DS [10, 11], we could consider that at a nominal voltage of 2 x 5.5 kV the efficiency is in fact at the same value as for RPC2015DS (97%). The cluster size is of 2.2 strips for RPC2012_1 and of 2.0 strips for RPC2012_3 in the region of efficiency plateau. Average system time resolution of 73 ps for RPC2012_1 and of 67 ps for RPC2012_3 remain almost unchanged over the investigated high voltage range, as is shown in Fig. 5.

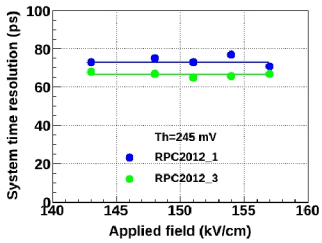

Figure 5: Time resolution as a function of high voltage for RPC2012_1 and RPC2012_3.

The single counter time resolution of 52 - 47 ps fullfils the single counter performance required for the inner zone of the CBM-TOF wall.

The results presented in the contributions to this Progress Report (present one and [11]), show that the MSMGRPC prototypes and the proposed basic architecture fulfill the requirements for the inner zone of the CBM-TOF wall.

References

[1] CBM-TOF Collaboration, CBM-TOF TDR, October 2014

[2] M. Petrovici et al, 2012 Journal Of Instrumentation, Volume 7, 2012 (2012 JINST 7 P11003).

[3] M. Petris et al., CBM Progress Report 2012 (2013), p.68

[4] M. Petriş et al., Journal of Physics: Conference Series 724 (2016) 012037

[5] F. Anghinolfi et al., Nucl.Instr.and Meth. A533(2004)183

[6] C. Simon et al., CBM Progress Report 2015, (2016), p.90

[7] M. Ciobanu et al., CBM Progress Report 2013, (2014), p.84

[8] C. Ugur et al., GSI Scientific Report 2014 (2015), p.212

[9] M. Traxler et al., GSI Scientific Report 2014 (2015), p.514

[10] V. Aprodu et al., CBM Progress Report 2015 (2016), p.98

[11] M. Petriş et al., this GSI Scientific Report

[12] M. Petriş et al., Journal of Instrumentation, Volume 11, September 2016 (2016 JINST 11 C09009)

DOI:10.15120/GR-2017-1

Prototype carbon fiber ladders for the CBM-STS made in industry

W. Niebur, M. Faul, and J. M. Heuser
GSI, Darmstadt, Germany

Carbon fiber support structures for the detector ladders of the CBM Silicon Tracking System are a central element for achieving a mechanically stable and, at the same time, low-mass detector [1].

Recently, prototype carbon fiber supports have been produced using an industrial process. That is based on winding high-modulus carbon fibers [2] around three support tubes. During this process, the tubes are installed on a hub that has been custom-designed at GSI and produced from Aluminum in precision mechanics industry [3]. The winding itself has been carried out in aerospace industry [4]. The hub is shown in Fig. 1. It consists of a core piece that can be installed on a rotating fixture, and three side pieces receiving the longitudinal support tubes. After winding and drying of the epoxy-clad fibers, the side pieces can be retracted and the hub removed from the produced structure. With a length of 130 cm, the hub allows producing carbon ladders of 110-120 cm length, matching the largest STS tracking stations. The base of the ladders is 6.1 cm wide, the height is 2.0 cm. The cell spacing realized by winding is ca. 4.0 cm. The tube support structure was chosen as it is best suited for overlaying it with the wound fibers, not risking sharp bends. With an outer/inner diameter of 1.5/0.5 mm, the tubes offer a low material cross section at essentially all particle crossing angles. Table 1 shows technical specifications of the three types of prototype ladders produced so far; they are depicted side by side in Fig. 2. The ladders differ in the carbon fiber used, both type and filaments contained, as well as the number of rovings per strud. A further, fourth prototype is being processed using fiber type M60J/3K with roving 4 or 5.

As the weight of the objects differ only slightly, the decision on which prototype to consider for further pre-series manufacturing will be based on the forthcoming analysis of the mechanical strength obtained, in terms of bending, twisting and squeezing. Sections of the carbon fiber ladders produced are already being employed in the ladder assembly tool that is currently under development [5].

Table 1: Specifications of the prototype ladders.

	prototype 1	prototype 2	prototype 3
support	CFK pipe	CFK pipe	CFK pipe
	0.5/1.5 mm ∅	0.5/1.5 mm ∅	0.5/1.5 mm ∅
matrix	L20/EPH960	L20/EPH960	L20/EPH960
fiber	M55J/6K	M55J/6K	M60J/3K
roving	1	2	3
weight	11.2 g	14.8 g	11.2 g

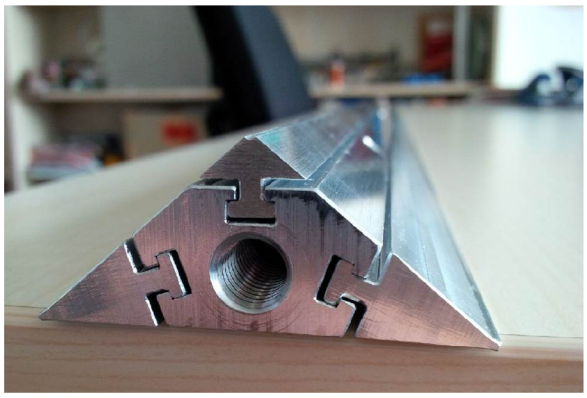

Figure 1: Hub made from Aluminum for the winding of carbon fibers around suport structures of different shapes.

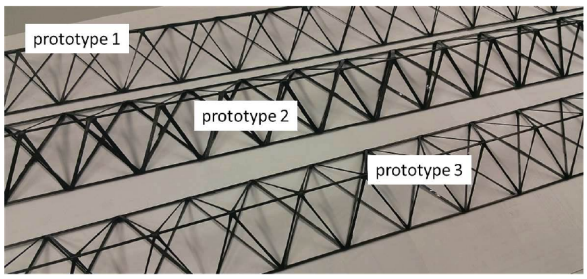

Figure 2: Prototype carbon fiber ladders produced according to the specifications shown in Table 1.

References

[1] Technical Design Report for the CBM Silicon Tracking System, GSI Report 2013-4 (2013), chapter 5.4

[2] Toray Industries Inc., www.toray.com

[3] Frühwein Mechanik GmbH & Co. KG, 64839 Münster/ Dieburg, Germany; www.mechanik-fruehwein.de

[4] xperion GmbH & Co. KG, Performance Polymer Composites, 88677 Markdorf, Germany; www.xperion-ppc.de

[5] U. Frankenfeld et al., Ladder assembly concept and tool, this report

DOI:10.15120/GR-2017-1

A data model for time slices and events in `cbmroot`

V. Friese
GSI Helmholtzzentrum für Schwerionenforschung GmbH, Darmstadt, Germany

The data interface of experiment and reconstruction software in CBM is the so-called time slice, a container comprising the complete detector raw data within a given time interval. These data are not associated to "events" (beam-target interactions) by a hardware trigger. It is the task of the reconstruction software to establish events out of this data stream. Thus, reconstruction starts from time slices and ends with events, which are either used for online data selection or given offline to the high-level physics analysis. The simulation faces the reverse challenge: Starting from modeling physical events by some suitable event generator, the detector response has to generate a data stream equivalent to that in the real experiment. The `cbmroot` framework thus has to provide an environment which allows to handle time slices and events at the same time.

Historically, `cbmroot` evolved along the lines of a classical, event-based framework, using the `FairRoot` layer on top of `ROOT` as a platform. Events were naturally represented by entries of a `ROOT TTree`, with event data in TClonesArrays as branches of the tree. Tasks operated on these data arrays event by event, triggered by each new entry of the `TTree`. Meanwhile, a complete reconstruction chain is available for this event-based mode.

The necessity to go beyond the event-by-event data processing towards the real, free-streaming data flow was clear from the beginning, and developments in this direction started many years ago by extensions of the framework [1, 2]. This was accompanied by the development of the DAQ software and the time slice data format [3] and by corresponding developments of the `FairRoot` software layer supporting the treatment of free-streaming data [4]. However, the necessity to define a data format suitable to the specific CBM needs remained. Such a data model was developed, tested and implemented in the year 2016.

The new data model closely resembles the old one on a formal level. It continues relying on the `ROOT TTree`, but one tree entry now represents one entire time slice, containing data from many physics events. Data are again arranged in TClonesArrays as branches of the tree, one array per data type (e.g, digi, cluster, hit, track). Events are represented by the dedicated data class `CbmEvent` in their own TClonesArray. The event class does not contain the data themselves, but a collection of indices of the associated data objects in their respective array (Fig. 1). Based on this scheme, the reconstruction can be divided into three parts:

1. Tasks before event building ("time-based tasks") operate on the entire time slice without information on events. Such time-based reconstruction was already developed for cluster-, hit- and track-finding in the STS.
2. The event-building task associates data to events by the method `CbmEvent::AddData(Cbm::DataType, UInt_t)`, with the type and index of the data object as argument. Event-building can be done on any data level, e.g., based on digis (raw data) or on already reconstructed tracks.
3. Tasks after event building ("event-based tasks") operate on data previously associated to events by the event-building task. They thus involve at each call a loop over all events within the current time slice. All already developed event-based tasks can be used here with only minor modifications in the data interfaces.

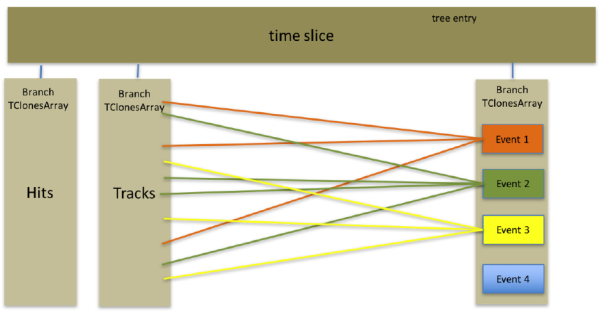

Figure 1: Event representation in the new data model. In this example, events are defined from reconstructed tracks.

The chosen approach fulfills the requirements outlined above. Besides being simple and requiring minimal intervention to the existing code base, its advantages are manifold. First, no data copy is required when associating a data object to an event. Second, the scheme provides the flexibility to define events based on any data level, e.g., with digis before any reconstruction or with reconstructed tracks. Both time-based and event-based algorithms can easily be integrated. The old, event-based simulation and reconstruction can be used within the same framework for reference; formally, this merely constitutes a special case with exactly one event per time slice. The price to pay are one additional integer (for the index) per data object and an additional (event) loop for event-based tasks. Performance checks up to now did not show a significant impact on the computing speed.

References

[1] V. Friese, J. Phys. Conf. Ser. **331** (2011) 032008
[2] V. Friese, Springer Lect. Notes Comp. Sci. **7125** (2012) 17
[3] J. de Cuveland and V. Lindenstruth, subm. to J. Phys. Conf. Ser. (proceedings CHEP 2016)
[4] M. Al-Turany *et al.*, J. Phys. Conf. Ser. **396** (2012) 022001

DOI:10.15120/GR-2017-1

Time-based selection of $J/\psi \rightarrow \mu^+\mu^-$ decays with the CBM-MUCH

T. Ablyazimov[1,2], *V. Friese*[1], *and V. Ivanov*[2,3]

[1]GSI Helmholtzzentrum für Schwerionenforschung GmbH, Darmstadt, Germany; [2]LIT JINR, Dubna, Russia;
[3]National Research Nuclear University "MEPhI", Moscow, Russia

The detection principle of the CBM muon system (MUCH) suggests to derive a software trigger on high-mass muon pairs using data from the MUCH alone, without a prior, compute-expensive reconstruction of tracks in the main tracking system (STS). A library of algorithms suitable for standalone track reconstruction in MUCH is being developed by the authors starting from 2013 [1]. It also comprises an approach suitable for the selection of $J/\psi \rightarrow \mu^+\mu^-$ decays based on reconstructed MUCH tracks with good efficiency and a suppression ratio exceeding 10^3 [2–4].

The results described in the referenced articles were obtained with simulated data which were separated into distinctive portions corresponding to collision events. For application in the real experiment, the triggering software must be able to work with bunches of measured data ("time slices") containing measurements from many different events.

The introduction of this paradigm entailed two aspects. First, the time attribute of the measurements had to be taken into account for the association of hits to tracks. This could be realised in a straightforward way by an upgrade of the data structures with the new attribute and its use in the determination of the measurement vicinity. The second consequence of the time-based approach is that the algorithms have to deal with severely increased combinatorics when the input data chunks contain many events instead of just one. Coping with this situation required to completely revise the search data structures and the corresponding algorithms.

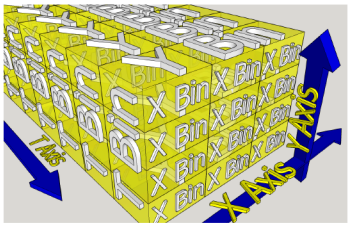

Figure 1: Bin hierarchy in the x, y and time space

All measured hits were placed into 3-dimensional binned structures, where "bins" are cuboids in the 3-dimensional space of the x-, y- and time coordinates. Each "bin" contains only a very limited number of hits or is even empty. The procedure of finding the corresponding bin for a given point in the x-, y- and time space is simple and straightforward. Each MUCH station is represented as a 3-dimensional, hierarchically organized array of bins (Fig. 1).

Although the main goal of the library is to trigger on $J/\psi \rightarrow \mu^+\mu^-$ decays, it is also considered to use it for the selection of the decays of lighter vector mesons. In previous versions, the track reconstruction started from the last MUCH station, to reduce combinatorics as much as possible. This approach excluded the reconstruction of low-mass vector meson decays, the daughter muons of which do not pass the last absorber. Thus, the approach was changed for the current library version: reconstruction now starts from the station before the last absorber. This enables the reconstruction of a sufficient share of low mass vector meson decays into the di-muon channel.

The tracks reconstructed in this way are later checked for the possibility to prolong them up to the last station. In the SIS-100 CBM muon setup, the last MUCH station is a TRD station with 4 detecting layers. The reconstructed tracks are checked for matching with hits in TRD as schematically shown in Fig. 2. Only tracks fulfilling this criterion are used for triggering on $J/\psi \rightarrow \mu^+\mu^-$.

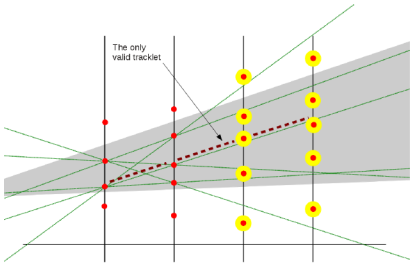

Figure 2: Matching a MUCH track with TRD hits

The performance of the algorithm was assessed by simulations for Au+Au collisions at 10A GeV from UrQMD. The reconstruction efficiency for J/ψ embedded into central events is 83%. The average reconstruction time for minimum-bias events is 4 μs on an Intel Xeon 3.1 GHz processor. The event number is reduced by a factor of 3,800; the data suppression factor is 1,700.

References

[1] T. O. Ablyazimov and V. V. Ivanov, CBM Progress Report 2014, GSI-2015-01521, p. 117

[2] T. O. Ablyazimov and V. V. Ivanov, CBM Progress Report 2014, GSI-2015-01521, p. 119

[3] T. O. Ablyazimov and V. V. Ivanov, Phys. Part. Nucl. Lett. **12** (2015) 559

[4] T. O. Ablyazimov and V. V. Ivanov, Eur. Phys. J. Web Conf. **108** (2016) 02001

DOI:10.15120/GR-2017-1

Time-based MUCH digitizer

V. Singhal[1], *S. Chattopadhyay*[1], *and V. Friese*[2]
[1]Variable Energy Cyclotron Centre, Kolkata, India; [2]GSI, Darmstadt, Germany

The task of the MUCH digitization is to calculate the detector response to a track traversing an active detector element. Inside `cbmroot`, this means creating `CbmMuchDigi` objects (representing the smallest unit of raw data) from `CbmMuchPoint` objects, which store the geometrical information of the track intersection with the detector obtained from transport simulation. MUCH digitization was developed previously for event-by-event simulations. This report describes the modifications to the MUCH digitization software in order to describe the self-triggered, free-streaming readout of the detector.

The task class for MUCH digitization is `CbmMuchDigitizeGem`. This task class and related data classes were re-written to cope with the requirements to a) work both in event mode and time-based (free-streaming) mode; b) be compatible with the framework scheme of `CbmReadoutBuffer`; c) properly treat interference of tracks in a given readout channel both in the event mode (interference within one event) and in the time-based mode (interference within the dead time of the electronics, within or across events).

The modified Much Digitizer iterates over each MuchPoint and correspondingly calculates the charge deposition in terms of the number of primary and secondary electrons. The number of primary electrons is simulated based on the energy, track length, particle type information and specification of the gas mixture. Then for each primary electron, the number of secondary electrons is determined based on the gas gain setting. The charge in each channel/pad is determined based on the segmentation of each layer and a spot radius of the electron avalanche. Noise and electronics effects are added afterwards [1].

For each channel/pad a `CbmMuchSignal` is generated, which describes the analogue response. It contains the unique detector address, the signal time, the time until the signal is active and can be influenced by subsequent signals (stop time), and the signal time shape represented by a `TArrayD` in steps of nanoseconds. The time of the signal, which is crucial for the correct description of the free-streaming behaviour, is calculated from the event start time (obtained from `FairRunAna`), the time of the `CbmMuchPoint` (time-of-flight from event start to detector) and the drift time in the GEM. A random factor for the time resolution of the detector is added.

The created signals are buffered in the `CbmMuchReadoutBuffer` singleton object, deriving from the `CbmReadoutBuffer` template. This buffer is responsible for dealing with pile-up. In case a second signal arrives in a given readout channel (pad) within its dead time, the `Modify()` function is called. This method merges the two signals into one. The start time of the resulting signal is the minimum of the start times of the merged signals, the stop time the maximum of the two stop times. The new signal shape is obtained by bin-by-bin addition of the two merging signal shapes.

After processing all `CbmMuchPoint` objects of one event in this manner, the readout buffer releases all buffered signals with stop time before the current event time, since they cannot be influenced by following signals any more. In case of event-by-event simulation, the entire buffer is read out irrespective of time, which excludes interference of tracks from different events.

`CbmMuchSignal` objects released by the readout buffer are converted into digital information (`CbmMuchDigi`) taking into account the properties of the readout ASIC like number of ADC bins, dynamic range and threshold. The digis are delivered to the `CbmDaq` software instance, which aggregates digis from all detector systems, builds time slices and stores then in the output tree. In case of event-by-event simulation, the digis are directly written into the output tree. The work flow for digitization in MUCH is schematically shown in Fig. 1.

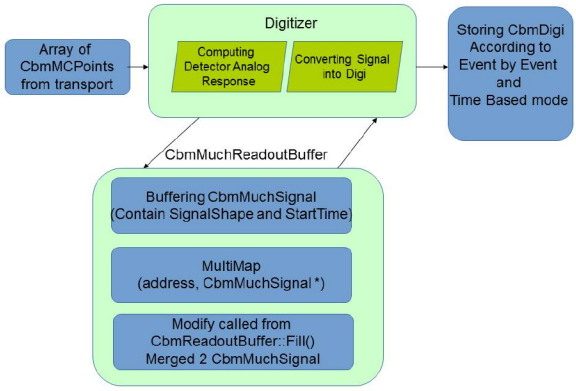

Figure 1: Scheme for time-based digitization in MUCH

All newly developed and modified classes are available in the trunk version of `cbmroot`. A detailed study is in process to test the performance of this newly developed scheme. Future plans include the reconstruction of dimuon signals in the time-based mode, the inclusion of detector inefficiencies, and others.

References

[1] V. Friese and E. Kryshen, CBM Progress Report 2010, GSI-2013-04801, p. 74

DOI:10.15120/GR-2017-1

An estimate of the required data bandwidth for the sensors of the CBM-MVD*

P. Sitzmann[1,2] and the CBM-MVD collaboration[2]
[1]GSI, Darmstadt, Germany; [2]Goethe Universität, Frankfurt am Main, Germany

The Micro Vertex Detector (MVD) of CBM is designed to operate at rates of up to 100 kHz Au-Au collisions and up to 10 MHz p-Au collisions. The CBM experiment will run with a free streaming triggerless readout. The limited time resolution of the CMOS Monolithic Active Pixel Sensors (MAPS) foreseen for this detector creates a pile-up in the detector. This will lead to a maxium of processeable hits per readout and complicates the track reconstruction, especially in the first station.

Recent progresses in CMOS industry allow for integrating discriminators into the pixel cell of MAPS. Therefore one may replace the previously considered rolling shutter readout by a priority encoder. This modification accelerates the time resolution of the sensors by about one order of magnitude, which has the potential to alleviate the pile-up problem substantially. It was decided to derive the CBM sensor MIMOSIS from a first related sensor design, which was developed for the ALICE ITS upgrade [1]. The radiation tolerance and rate capability of the ALICE sensor has to be improved by about one order of magnitude to match the more demanding requirements of CBM. The necessary modifications are carried out by the IPHC Strasbourg, which include adapting the sensor to the mechanical integration concept of the MVD.

To do so, a new internal readout structure is being designed for MIMOSIS (see Fig. 1). It foresees three stages of data buffering. The 64, so-called, region buffers receive each discriminated digital data from 16 columns of 504 pixels. Four neighbouring region buffers concentrate their data toward one super region buffer, which forwards it to one central elastic buffer. This solution balances the inhomogeneous occupancy of the sensors. Moreover, the elastic buffer flattens peaks in the data rate as caused by fast beam fluctuations are averaged out. Both steps reduce the required external bandwidth of the sensors to a maximum of eight parallel 320 Mbps data links. Some of the links may be deactivated in order to reduce the power dissipation of sensors with low occupancy.

The validity of the concept was confirmed with CBMRoot simulations for collision rates of 100 kHz (10 AGeV Au+Au) and 10 MHz (30 GeV p+Au). A security margin of a factor of three was considered in order to account for beam fluctuations. The delta electrons kicked out by the beam from the target was found to dominate the sensor occupancy. The required buffer memory was computed assuming a 5 µs readout time. The bandwidth of the data

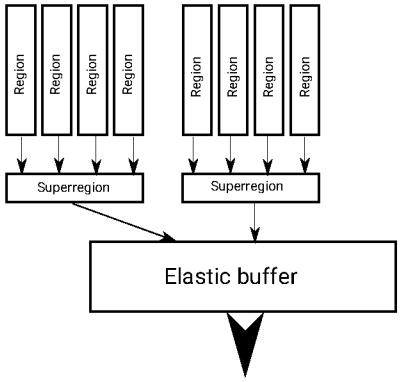

Figure 1: Sketch of the new readout layout in MimoSIS sensors

Component	average	3x av.	available
Region	10	30	100
Superregion	37	111	400
El. buffer input	345	1035	3200
Ext. links	345	–	800

Table 1: Required and available buffer memory and bandwidth in units of 16 bit words.

links (except for the external link) was assumed to allow for evacuating the full buffer during one frame time. The overhead caused by headers and trailers has been accounted for.

The results of the study are listed in Tab. 1. The results hold for the most exposed sensor of the first MVD station. The entries labelled "3x av." represent avarage peaks in the data rate as caused by beam intensity fluctuations. The memory and bandwidth foreseen is found sufficient for a reliable operation at the anticipated collision rates.

However, this promising result holds so far only for a detector operation with full magnetic field. Some physics cases call for reducing this field. This turns into a reduced deflection of delta electrons and thus to a higher occupancy. The consequences of this is currently being studied. First and preliminary results suggest that the occupancy increases by a factor of 2 reaching the limits of the capabilities of the sensor.

References

[1] D. Kim et al., 2016 JINST 11 C02042 and references therein

* Work supported by GSI(SIS)/HIC4FAIR/HGS-HIRE and Strategic Cooperation Contract GSI-Frankfurt

Online data preprocessing for the CBM Mirco Vertex Detector *

Qiyan Li[1], *M. Deveaux*[1], *J. Michel*[1], *C. Müntz*[1], *J. Stroth*[1,2], *and the CBM-MVD Collaboration*
[1]Institut für Kernphysik, Goethe-Universität Frankfurt, Germany; [2]GSI, Darmstadt, Germany

The CBM Micro Vertex Detector (MVD) is being designed to handle 10^5 Au+Au or 10^7 p+Au collisions/s. Weakly decaying particles like Hyperons or D Mesons will be identified in real time by means of a free streaming DAQ system, the FLES, which includes stages for event reconstruction and decay topology identification. To fulfill this task with the available computing resources, each processing step has to be optimized for low CPU load and bandwidth consumption. This does also hold for the cluster finding of the MVD. The current CBMRoot/C++ code was estimated to consume up to 80% of the CPU-power of the FLES once being confronted with a realistic data rate. To reduce this load, we tested strategies to perform preprocessing of the data before sending it to the computing farm.

A first stage of the proposed preprocessing is already integrated in the CMOS Monolithic Active Pixel Sensors used in the MVD. The MIMOSA-26 pixel sensor used for our test includes circuits for signal discrimination, on-chip zero suppression and one-dimensional cluster finding. The second stage as discussed in this work comprises full cluster finding and encoding on free resources of the FPGAs controlling the sensors. The related algorithm was required to match the available FPGA resources and to keep all information on cluster shapes without increasing the data volume and bandwidth.

In a first step, we found a way to encode reconstructed clusters into one 32 bit word per cluster. Tests showed that the protocol encodes 99.99% of the clusters recorded during beam test data of the MVD-prototype with MIMOSA-26 without loss of information [1, 2]. A VHDL module doing cluster finding and encoding was designed and tested successfully with the TRB2 board [3]. Real time cluster finding was demonstrated by operating it with a MIMOSA-26 sensor, which was illuminated with a β-source. To test the accuracy of this cluster finding, the output was stored together with its raw data, which was processed with the C++ reference code in a next step. The clusters recorded with both chains were compared for 260k frames. They were found to agree for physics data while some pathological signatures, as e.g. caused by a broken line, were rejected by the FPGA code. The output of the FPGA showed a mild compression of 14% w.r.t. the raw data (see Figure 1), which matches our requirements. The CPU time for the remaining steps to be done with C++ at the FLES (C++ cluster finding vs. unpacking of the encoded cluster information) was compared. Note that in both cases the first processing stage was carried out by the sensor . The low occupancy reached with the β-source causes a bias in favor of the offline processing. Nevertheless, the FPGA-processing reduces the remaining CPU load by a factor of four (see Figure 2).

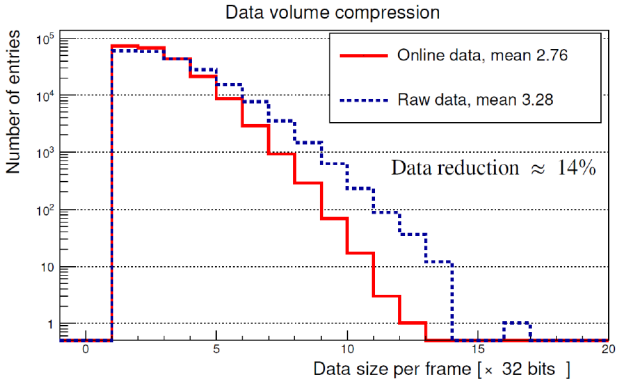

Figure 1: Data size per frame for a MIMOSA-26 exposed to β-rays (raw data vs. FPGA-encoded clusters).

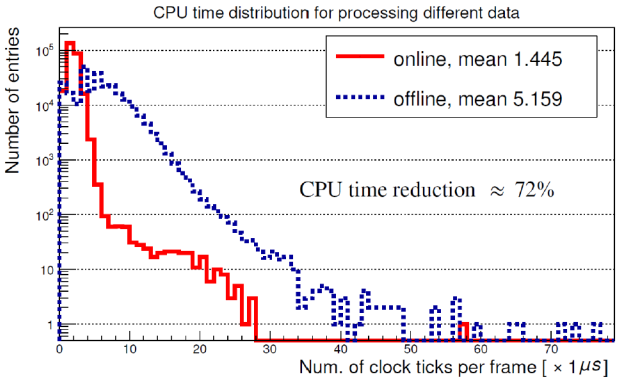

Figure 2: The CPU time per frame (decoding of FPGA-encoded clusters vs. C++ cluster finding).

The explorative study presented here demonstrates that the proposed strategy is suited to reduce the load of the FLES. It remains to be adapted to the internal data processing of the final MVD sensor, which is currently under design.

References

[1] Qiyan Li et al., GSI Scientific Report 2012 (2013) 56
[2] Qiyan Li et al., J. Phys.: Conf. Ser. 513 (2014) 022021 (Proceedings of CHEP-2013)
[3] Qiyan Li et al., GSI Scientific Report 2014

* supported by BMBF (05P15RFFC1), HIC for FAIR and GSI.

DOI:10.15120/GR-2017-1

Radiation damage caused by neutron capture in boron doped silicon sensors*

B. Linnik, T. Bus, M. Deveaux†, D. Doering, A. Yazgili, and J. Stroth
Goethe University, Frankfurt, for the CBM-MVD Collaboration

The active medium of CMOS Monolithic Active Pixel Sensors (MAPS), as foreseen for the CBM Micro Vertex Detector (MVD), is formed from p-doped silicon. Besides being affected by fast hadrons, this medium might subject to damage from thermal neutrons, which dissociate the boron dopands via the reaction n + ^{10}B $\rightarrow$^{7}Li + ^{4}He + 2.8 MeV. The consequences of this effect was tested experimentally and found being incompatible with the Non Ionizing Energy Loss (NIEL) hypothesis, which is commonly used for dosimetry.

The tolerance of MAPS to non-ionizing radiation damage has been extensively studied with fast $\sim$ 1 MeV reactor neutrons in accordance with the NIEL (Non-Ionizing-Energy-Loss) model [1]. This model assumes that radiation damage, which is caused by the neutrons removing atoms from their location in the silicon crystal, scales with the radiation energy. Despite the validity of the model is known to be limited by its ignorance to defect chemistry, it is commonly used for doing dosimetry for silicon sensors. Tables [2] are used to normalize the damage caused by different sources of radiation with respect to the one of 1 MeV neutrons, the so-called neutron equivalence.

The large cross sections of neutron induced fission of ^{10}B is not considered in those tables. We studied, if potential additional radiation damage may occur, which might e.g. endanger the operation of the CBM-MVD. The study was performed with MIMOSA-19 sensors provided by the PICSEL group of IPHC Strasbourg. The sensors were manufactured in the 0.35 μm AMS OPTO process and feature a 14 μm thick epitaxial layer with an anticipated P-doping of few $10^{15}/\mathrm{cm}^3$. The 196 $\times$ 196 3T-pixels with 12x12 μm^2 pitch have L-shaped diodes with 39.6 μm^2 surface. The doping of the substrate of the P-Well is likely $\sim 10^{19}/\mathrm{cm}^3$. Fission products created in the P-well can travel into and damage the epitaxial layer as our simulations showed.

The sensors were irradiated with neutrons at the FRM II research reactor in Garching. The irradiation was done at room temperature. Either a direct fission spectrum (MEDAPP beam line, $E_{\mathrm{peak}} = 2$ MeV) or cold neutrons (PGAA beam line, $E_{\mathrm{peak}} = 1.8 \times 10^{-3}$ eV) were used for irradiation, the sensors were bonded hereafter for testing. During our tests, they were illuminated with X-ray sources (^{55}Fe$\rightarrow$ 5.9 keV, ^{109}Cd$\rightarrow$ 22.1 keV) and the amplitude spectrum was obtained. This amplitude is typically reduced with increasing radiation dose as the radiation damage reduces the charge collection efficiency (CCE) of MAPS. The CCE is deduced from the Amplitude spectrum [3]. In accordance with the NIEL hypothesis, we assumed that this would be observed also for the sensors exposed to cold neutrons.

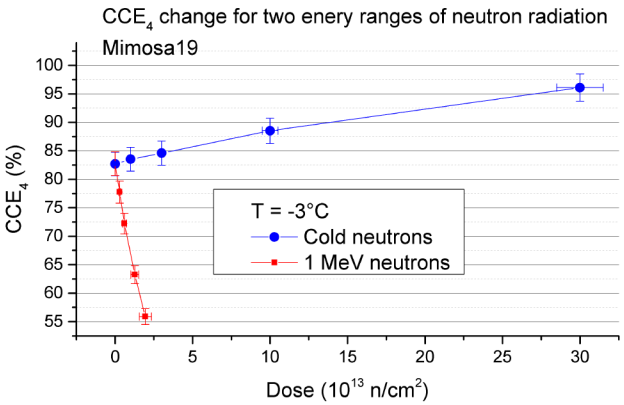

Figure 1: The charge collection efficiency for the four most significant pixel in a 5x5 cluster.

The results are displayed in Figure 1. The sensors irradiated at MEDAPP (1 MeV n) display the expected *decrease* of the the average CCE with increasing radiation dose. The the sensors irradiated at PGAA (cold n) show an unexpected *increase* of the CCE, which cannot be explained within the NIEL model. A more detailed study of out experimental data revealed that the sensors irradiated with cold neutrons show signatures of a strong acceptor removal. This reduces the doping of the sensing volume, which is known to increase the CCE [3]. This is not observed for the fission neutrons up to the highest doses applied.

The results prove that cold and thermal neutrons do not endanger the operation of the CBM-MVD. More importantly, they suggest that the response of sensors with p-doped sensing volume to neutron radiation changes in a qualitative way depending on the neutron energy. This creates a so far unknown exception for the NIEL model, which is likely of general interest in silicon detector physics.

References

[1] A. Vasilescu, ROSE/TN/97-2, CERN (1997)

[2] A. Vasilescu, G. Lindstroem, http://rd50.web.cern.ch/RD50/NIEL/default.html

[3] M. Deveaux et al., JINST 6.02 (2011): C02004.

* Work supported by BMBF (05P15RFFC1), GSI and HIC for FAIR.
† deveaux@physik.uni-frankfurt.de

Geometry database development for the CBM experiment

E. P. Akishina[1], *E. I. Alexandrov*[1], *I. N. Alexandrov*[1], *I. A. Filozova*[1], *V. Friese*[2], *and V. V. Ivanov*[1,3]
[1]LIT JINR, Dubna; [2]GSI, Darmstadt, Germany; [3]National Research Nuclear University "MEPhI", Moscow, Russia

The geometry of the CBM detector systems ("modules") is described in the ROOT TGeo format, with one separate file for each system. An entire CBM geometry is defined by a set of such geometry files with given versions.

Currently, the geometry files are stored and distributed through the CBM software repository. Setups as combinations of geometry files are defined on the ROOT macro level. This situation is rather complicated and error-prone.

The CBM Geometry Database (DB) is designed and implemented as a part of the CBM Databases project [1] according to the User Requirements Document [2]. A simplified object model of the CBM Geometry DB is shown in Fig. 1.

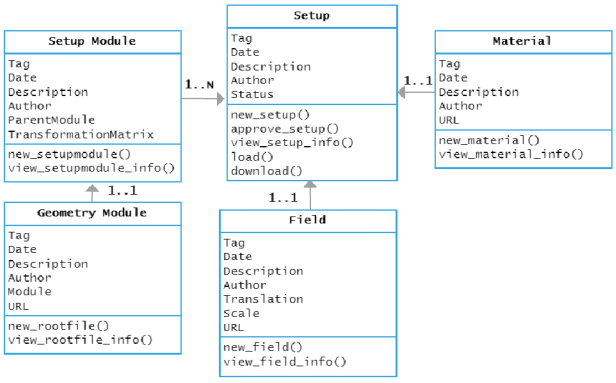

Figure 1: Object model of the CBM Geometry DB

Each object has a unique tag that can be used as a key for searching. Any object has the parameters: Description, Author and Date. Description is a short description of the object, Author is the user who created the object and Date is the time of object creation. The parameter URL is a string with the full path to the data file. This file is accessible from the Geometry DB. It should store geometry data in ROOT format if there is a link to the Geometry Module object, materials if there is a link to the Material object, and magnetic field if there is a link to the Field object.

The CBM geometry database is realized as a tree structure. The top-level object is the Setup. It has relations with one Material object, one Field object and several Setup Module objects. A Setup Module object has relation with one Geometry Module object. The Geometry Module object contains information about the sub-detector and its geometry data. The Setup Module object has a link to the mother Setup Module. Its Transformation Matrix parameter describes the placement of the module in the mother module.

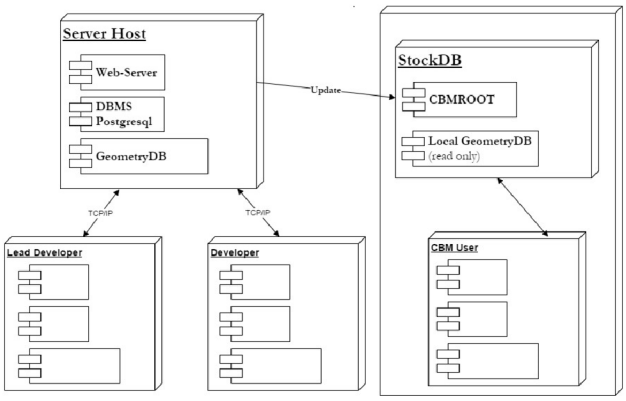

Figure 2: General architecture of the CBM Geometry DB

The Geometry DB has three type of users: Lead Developer, Developer and CBM User. The Lead Developer is a coordinator and the responsible person for the Setups. He/she can upload new versions of Setup and materials file. The Developer is a person responsible for a Setup Module and its Geometry Module. The CBM User has only read access.

The General architecture of the CBM Geometry DB is shown in Fig. 2. The Geometry DB consists of a Central DB and Local DB components. The Central DB keeps primary data and is unique within the entire CBM environment. Lead Developers and Developers use the Central DB in order to update Setups and corresponding data. Updates can be done through both web server and API modules. A Local Geometry DB is a copy or several copies of the Central DB. Local copies are implemented in SQLite. Any Local Geometry DB is updated after a change to the Central DB. It is available for CBM users via their local file system.

The API and GUI accesses are designed and implemented. The API is implemented as macros in the `cbmroot` environment.

References

[1] E. P. Akishina *et al.*, *Conceptual Considerations for CBM Databases*, JINR Communications E10-2014-103, JINR, Dubna

[2] E. P. Akishina *et al.*, *User Requirements Document of the Geometry DB for the CBM experiment*, http://lt-jds.jinr.ru/record/69336?ln=e

DOI:10.15120/GR-2017-1

CERN-SPS in-beam performance test of the new strip readout MRPC prototypes for the inner zone of the CBM-TOF wall *

M. Petriş[1], D. Bartoş[1], M. Petrovici[1], L. Rădulescu[1], V. Simion[1], J. Frühauf[2], M. Kiš[2], P-A. Loizeau[2], I. Deppner[3], N. Herrmann[3], and C. Simon[3]

[1]NIPNE, Bucharest, Romania; [2]GSI, Darmstadt, Germany; [3]PI, Heidelberg University, Germany

Due to the high interaction rates of 10^7 interaction/s at which the CBM experiment is anticipated to run the readout will be based on a free streaming concept. This imposes to the MSMGRPCs (Multi-Strip, Multi-Gap RPCs), a perfect matching of the characteristic impedance of the signal transmission line to the input impedance of the front-end electronics, in order to reduce fake signals produced by reflections [1].

Two new MSMGRPC prototypes, based on low resistivity glass ($\sim 10^{10}$ Ωcm) from China, match the characteristic impedance of the RPC signal transmission line to the input impedance of the front-end electronics ([2, 3]). They have also the granularity required by the inner zone of the CBM-TOF wall through a proper adjusting of their strip length. The transmission line impedance of a single readout channel of each prototype was estimated using APLAC Software. The first prototype has a classical single stack architecture (RPC2015SS) with 8 gas gaps of 140 μm. The pitch size (10.16 mm) and strip width (8.63 mm) are the same for both high voltage and readout electrodes. The second prototype has a double stack configuration (RPC2015DS) of 2 x 5 gas gaps of 140 μm, with the same pitch size (7.2 mm) for both high voltage and readout electrodes, but with different values of the strip widths: 1.3 mm for readout electrodes and of 5.6 mm for high voltage ones. This gives the possibility to exploit in an innovative way the advantage of having a strip structure for both readout and high voltage electrodes. Thus the tuning of the characteristic impedance of the signal transmission line to the value of the input impedance of the front-end electronics can be decoupled by the granularity adjustments. With the described geometrical parameters both counters have a characteristic impedance of the transmission line of 100 Ω.

The prototypes were tested in-beam at SPS-CERN with a 30A GeV Pb ions incident on a Pb target in conditions similar with those expected at SIS100, or even closer to those anticipated for SIS300. Our prototypes were positioned in the "high rate" branch of the CBM-TOF experimental setup, a comprehensive description of the whole set-up being given in [4]. The two described prototypes are positioned one behind the other (see Fig.1), in the same housing box, identified as RPC2015 Bucharest [5]. They were followed by four MSMGRPCs mounted in the same gas tight box, called RPC2012 and a narrow strip pitch (2.54 mm) MSMGRPC called RPCRef, the last one in the experimental set-up. A 16 strip polycrystalline diamond detector and a 4-pad single crystal diamond detector were positioned in front of the target, providing a start time for particle velocity measurements between the diamond detector and the RPCRef counter. The signals delivered by the RPCs were fed to PADI fast amplifiers [6] and processed by the same electronics chain described in [5].

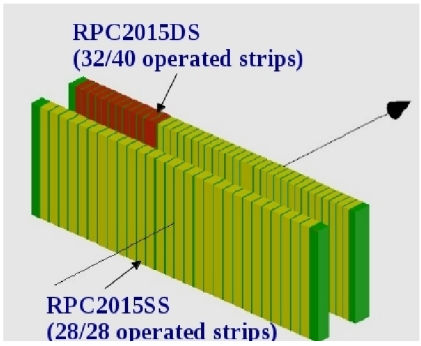

Figure 1: Overlap of the active area of the two RPC2015 prototypes.

We report here the performance of the RPC2015 prototypes, the results obtained with RPC2012 prototype being reported in detail in [5]. The principles of the data analysis starting from unpacking to calibration and corrections are presented in [7].

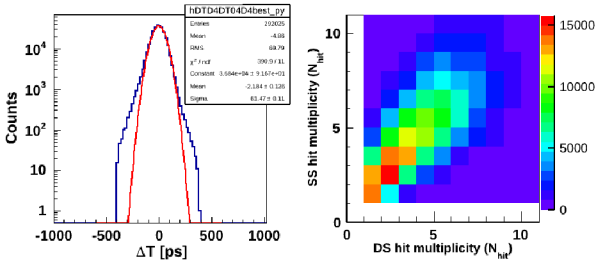

Figure 2: Time difference spectrum - left. Hit multiplicity correlation - right.

The time difference spectrum between RPC2015DS and RPC2015SS, for operation of RPC2015DS at 2 x 5.5 kV (157 kV/cm) and of RPC2015SS at 2 x 9 kV (161 kV/cm), with the PADI threshold set to 245 mV is presented in Fig.2, left side. A very good system time resolution of

* Romanian NASR/contract RO-FAIR F04 and NASR/NUCLEU Project PN16420104

61 ps, including the contribution of the electronics, was obtained. The correlation plot from the right side of Fig.2 shows that the two counters were exposed to almost the same hit multiplicities. If we consider equal contributions of the two counters, a single counter resolution of 43 ps is obtained. The observed tails in the time spectrum are negligible, if we compare the obtained 61 ps σ of the Gaussian fit with 69 ps RMS value of the spectrum. The obtained efficiency for this run, was of 97% for the RPC2015DS and of 98.5% for the RPC2015SS. The slight difference could be due to the difference in the applied potentials and also in the overlapped operated area, as is shown in Fig.1. The

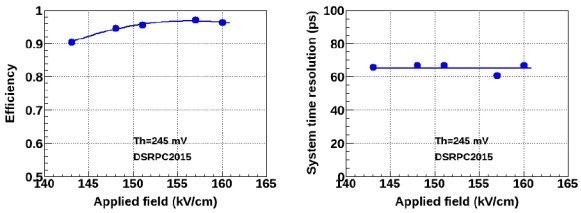

Figure 3: Efficiency - left and time resolution - right as a function of high voltage for RPC2015DS.

obtained detection efficiency and time resolution as a function of applied high voltage for RPC2015DS are shown in Fig. 3. An average system time resolution of 65 ps corresponds to the efficiency plateau, reached at applied electric fields in the gas gap larger than 157 kV/cm. The efficiency

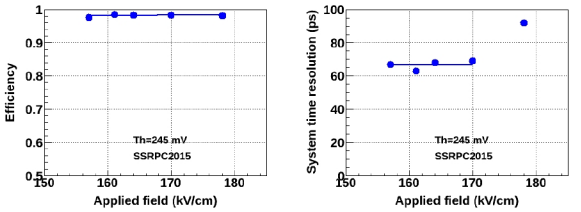

Figure 4: Efficiency - left and time resolution - right as a function of high voltage for RPC2015SS.

and system time resolution obtained for RPC2015SS are presented in Fig. 4. As can be observed, the counter was operated at the efficiency plateau of ~98%, with an average system time resolution of 66 ps. The larger value of the time resolution observed for operation at 178 kV/cm is due, most probable, to the operation at a too high electric field which pushes the counter in a streamer regime. The

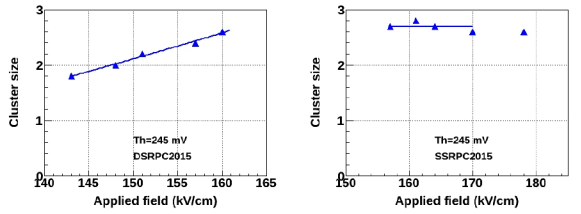

Figure 5: Cluster size for RPC2015DS - left and RPC2015SS - right as a function of high voltage.

obtained cluster size (number of strips with signal in a single hit) for the two counters is presented in Fig. 5. The cluster size is increasing for RPC2015DS as a function of applied potential while for RPC2015SS in the same high voltage range is almost constant. It slightly decreases at the largest applied fields due to possible distortions of the electric field produced by the space charge inside the gas gaps. The obtained values of the cluster size are larger than the one expected from the values of pitch sizes for the two counters. Previous obtained results for RPC2012 with a pitch size of 7.4 mm and the same inner geometry, showed a cluster size of the order of 1.4 - 1.5 strips [8] for single hit. These larger values can be due to large ionization created by heavy reaction products crossing the detector.

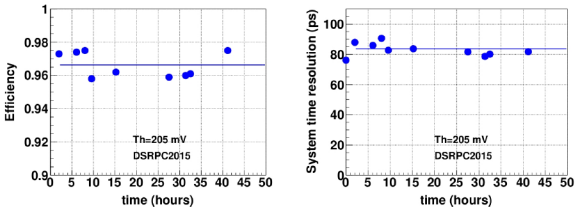

Figure 6: Aging effect for RPC2015DS for 40 hours operation with the same high voltage and threshold settings.

The detector performance stability was checked for a period of operation of about 40 hours with the same settings (RPC2015 at 157 kV/cm, RPC2015SS at 178 kV/cm). The efficiency and system time resolution were evaluated for the runs acquired over this period at similar counting rates. The stability of the detectors is demonstrated by the plots shown in Fig. 6. The obtained ~80 ps system time resolution is affected by the operation of the RPC2015SS at a too high electric field, (178 kV/cm), in a region of the working curve where its time resolution started to deteriorate (see Fig. 3). The operation of the detectors at a PADI threshold of 205 mV does not not influence the time resolution performance, as it is shown in [7, 9].

The performance of the RPC2015DS with the innovative adjustable characteristic transmission line impedance was demonstrated. The obtained results show that the two new prototypes with characteristic transmission line impedance matched to the input impedance of the front-end electronics, fulfill the challenging requirements of the inner zone of the CBM-TOF wall.

References

[1] CBM-TOF Collaboration, CBM-TOF TDR, October 2014

[2] V. Aprodu et al., CBM Progress Report 2015 (2016), p.97

[3] V. Aprodu et al., CBM Progress Report 2015 (2016), p.98

[4] C. Simon et al., CBM Progress Report 2015, (2016), p.90

[5] M. Petriş et al., this GSI Scientific Report

[6] M. Ciobanu et al., CBM Progress Report 2013, (2014), p.84

[7] M. Petriş et al., Journal of Instrumentation, Volume 11, September 2016 (2016 JINST 11 C09009)

[8] M. Petriş et al., Journal of Physics: Conference Series 724 (2016) 012037

[9] M. Petriş et al., GSI Scientific Report 2015 (2016), 32

DOI:10.15120/GR-2017-1

4-dimensional reconstruction of time-slices

V. Akishina[1,2,3], *I. Vassiliev*[1], *I. Kisel*[1,2,4], *and M. Zyzak*[1]

[1]GSI, Darmstadt, Germany; [2]Goethe-Universität, Frankfurt am Main, Germany; [3]JINR, Dubna, Russia; [4]Frankfurt Institute for Advanced Studies, Frankfurt am Main, Germany

Traditional latency-limited trigger architectures, typical for conventional experiments with a hardware trigger, are inapplicable for CBM. Instead, the experiment will ship and collect time-stamped data into a readout buffer in a form of a time-slice of a certain length with no isolated collisions, and deliver it to a large computer farm, where online event reconstruction and selection will be performed. Grouping of measurements into physical collisions must be performed in software and requires reconstruction not only in space, but also in time, the so-called 4-dimensional track reconstruction and event building.

Table 1: Track reconstruction efficiency in mbias Au+Au collisions at 10 AGeV in case of event-by-event reconstruction and 4-D reconstruction at different interaction rates.

Efficiency, %	3-D	0.1 MHz	1 MHz	10 MHz
All tracks	92.5	93.8	93.5	91.7
Prim. high-p	98.3	98.1	97.9	96.2
Prim. low-p	93.9	95.4	95.5	94.3
Sec. high-p	90.8	94.6	93.5	90.2
Sec. low-p	62.2	68.5	67.6	64.3
Clone level	0.6	0.6	0.6	0.6
Ghost level	1.8	0.6	0.6	0.6

The core of reconstruction in CBM is the Cellular Automaton (CA) based track reconstruction in the Silicon Tracking System (STS). This algorithm was modified to enable time-based reconstruction. It takes as input hits produced with the time-based cluster and hit finding algorithms from the time-slices, simulated in the `cbmroot` framework. Time-based detector response simulations in CBM take into account the anticipated timing behavior of detectors and readout electronics like e.g. time resolutions and strip dead times. Due to the self-triggered digitization and readout scheme, simulation has to take into account that signals of particles from different collisions can interfere in a detector volume. Thus, it puts the reconstruction chain in a more challenging condition.

Since the triplets are to be built of three hits potentially produced by the same particle, these hits should correlate in time. All combinations of hits with difference in time measurements exceeding the expected STS time resolution are rejected. The resulting reconstruction efficiencies of the 4-D CA track finder for various interaction rates are given in Table 1. For comparison, the corresponding values for the event-by-event analysis ("3-D") are included. Only a slight deterioration w.r.t. event-by-event is observed at the highest interaction rate of 10 MHz.

After the stage of the CA track finder is finished, all

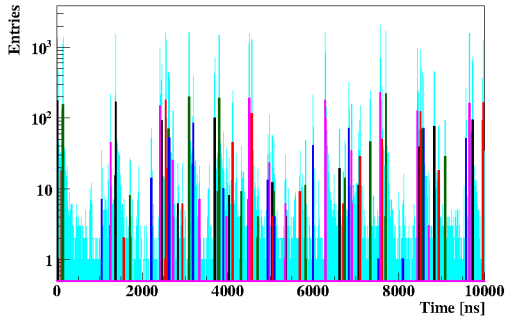

Figure 1: Distribution of reconstructed track time in a part of time-slice at 10 MHz interaction rate: hits (light blue) and tracks (different event-corresponding colors).

tracks found in the time-slice are fitted in 4-D space. Time was added as a parameter to the track state vector with the covariance matrix modified accordingly. Thus, both spacial and time track parameters are treated equally by the reconstruction chain. An event-building algorithm based on the reconstructed tracks was developed. The time distribution of hits is shown in Fig. 1 with light blue colour, illustrating the complexity of defining event borders in a time-slice. The time distribution of reconstructed tracks is shown in the same plot with different colours. The tracks clearly form groups corresponding to events. Tracks are combined into event-corresponding clusters according to the estimated time at the target position and its errors.

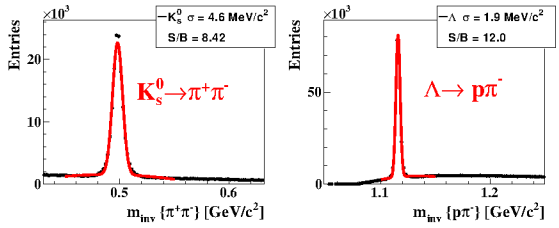

Figure 2: Performance of short-lived particle reconstruction on the example of K^0_s and Λ for time-slices with 0.5M mbias Au+Au events at 10 MHz interaction rate.

The obtained events were given as an input to the KF Particle Finder package for reconstruction of short-lived particles. A primary vertex is constructed in each event. Since TOF is not yet included into the time-based reconstruction, Monte-Carlo information for the identification of charged particles was used. The obtained K^0_s and Λ mass spectra are shown in Fig. 2. The combinatorial background for short-lived particles is similar to the event-based analysis, showing high values for the signal to background ratio.

DOI:10.15120/GR-2017-1

J/ψ interaction in nuclear matter at FAIR SIS100

P. P. Bhaduri[1], *M. Deveaux*[2], *and A. Toia*[3]

[1]Variable Energy Cyclotron Centre, 1/AF Bidhan Nagar, Kolkata-700 064, India; [2]Goethe-Universität Frankfurt, 60438 Frankfurt am Main, Germany.; [3]GSI, 64291 Darmstadt, Germany

J/ψ suppression in relativistic heavy-ion collisions is considered as an indicator for the formation of quark-gluon plasma (QGP). This is as the formation of the $c\bar{c}$ bound states is hampered by Debye screening in a deconfined medium. However, some J/ψ suppression was also observed in proton induced ($p + A$) collisions, which are not considered to form a deconfined medium. Isolating the genuine effects of the hot and dense medium of heavy-ion collisions requires a precise knowledge on the J/ψ dissociation in cold hadronic matter as produced in $p + A$ collisions.

J/ψ production in hadronic collisions is generally believed to be a factorizable two step process. The first step is the production of a color octet $c\bar{c}$ pair, which requires $\tau_0 \simeq 0.25$ fm in the rest frame of the pair and can be described by perturbative QCD (pQCD). This is followed by the non-perturbative formation of the color singlet resonance from the initially compact $c\bar{c}$ pairs, which is considered to require $\tau_R \simeq 0.35$ fm in the case of the J/ψ. In the nucleus and laboratory frame, the formation times are extended by Lorentz dilation. A conclusive experiment requires to chose a beam energy, which allows to create J/ψ particles without giving them a too high velocity. Otherwise, the $c\bar{c}$ pair will scatter or leave the nuclear core before the formation is completed. In both cases, the results will reflect the properties of the $c\bar{c}$ instead of providing the wanted information on the properties of the fully formed J/ψ. This consideration hampered a measurement of the hadronic dissociation of J/ψ e.g. with a 160 GeV/c proton beam the CERN-SPS [1].

CBM will be able to produce and detect J/ψ mesons in $p + A$ collision systems with unprecented rates at very low beam energies of $15 - 30$ GeV. We checked if those kinematic conditions would be suited to measure the interactions between fully formed J/ψ - mesons and cold nuclear matter. We consider this fulfilled if i) the formation path of the J/ψ in the rest frame of the nucleus remains below the ~ 2 fm distance between two nuclei and ii) the survival probability of the J/ψ is significantly modified by the medium. As shown in Fig. 1, the first condition is fulfilled for a beam energy of 15 GeV.

The J/ψ survival probability was calculated for three assumptions on the absorption cross section inside the nuclear medium. An estimate of the geometric cross-section (σ_{abs}^{Geo}), an estimate relying on perturbative QCD [2] (σ_{abs}^{QCD}), and a prediction of hadronic models based on meson exchange [3] (σ_{abs}^{Had}) were considered. The results of the calculations are displayed in Fig. 2. They suggest that

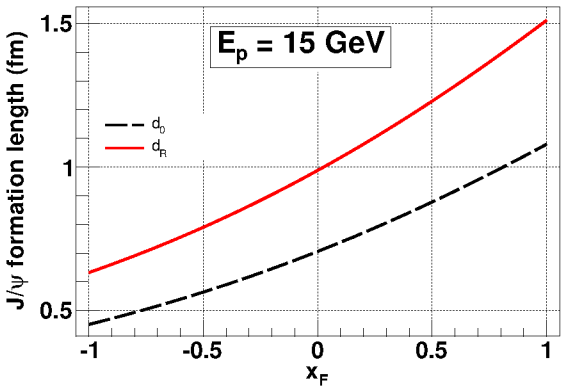

Figure 1: x_F dependence of the formation length of J/ψ mesons, in the laboratory frame, in 15 GeV p+A collisions.

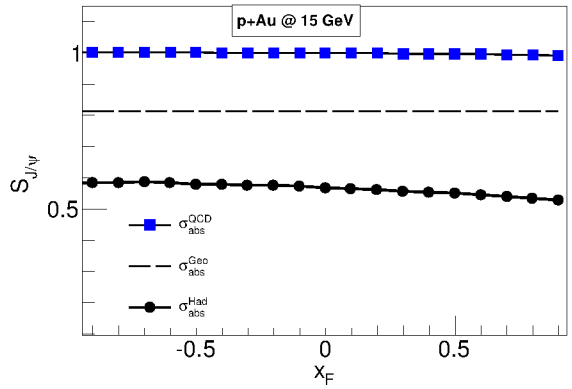

Figure 2: x_F dependence of the J/ψ survival probability in 15 GeV $p + Au$ collisions at FAIR.

the J/ψ yields will depend strongly on the anticipated scenario, which will allow to separate them by experiment. Measuring charmonium at CBM would thus be highly rewarding in terms of performing pioneering studies on the interaction of the physical resonances in the baryonic matter.

References

[1] D. Kharzeev and H. Satz, Phys. Lett. B **356** (1995) 365.

[2] D. Kharzeev and H. Satz, Phys. Lett. B **334** (1994) 155.

[3] R. Molina, C. W. Xiao and E. Oset, Phys. Rev. C **86** (2012) 014604; nucl-th/12030979

DOI:10.15120/GR-2017-1

Systematic study of sensor properties

O. Bertini[1] *and A. Lymanets*[1]
[1]GSI, Darmstadt, Germany

The Silicon Tracking System (STS) is main tracking detector of the Compressed Baryonic Matter (CBM) experiment providing tracking information of charged particles trajectories. The STS will consist of about 900 double-sided silicon microstrip sensors in four different sizes. Complicated fabrication technology of double-sided silicon sensors and large-scale production requires a solid and efficient quality assurance procedure of every sensor before connecting it to readout electronics [1].

The vendors of the present prototype sensors, CiS and Hamamatsu, provide results of bulk electrical tests. Since the leakage current value strongly depends on the temperature during the measurement, a calibration procedure has been developed in order to compare the results. As it is shown in Fig. 1 leakage current measurements after being scaled to 20°C are in good agreement with vendor's data.

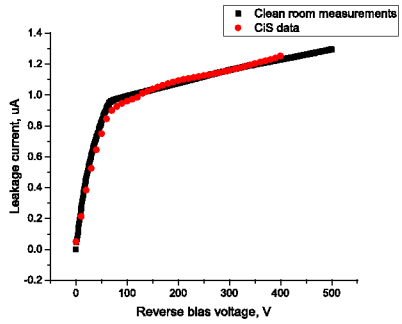

Figure 1: Comparison of leakage current measurements provided by a vendor (CiS) with tests performed at GSI, here for sensor type CBM06C2, batch 350714, wafer 18.

Another parameter which demonstrates functionality of the sensors is called slope and is defined as the ratio of the leakage current at 150 V to the current at 100 V. It provides information about how the leakage current changes between the depletion voltage (max. $\sim$ 100 V) and the expected operation voltage ($\sim$ 150 V). If the slope is steep, the sensor is already in a hard breakdown. The comparison of the slope between vendor's data and measurements at GSI is presented in Fig. 2. Compared to the direct leakage current measurements, the slope demonstrates the health of the sensors independently of the temperature measurement.

The strip quality tests are particularly important for identifikation of strip defects that can develop during fabrication, transportation or handling of sensors. The results of pinhole test of coupling capacitors are provided by the vendors as well. An automated strip test procedure has been developed and the test stand assembled in the clean room environment at GSI [2]. Newest prototype sensors of type

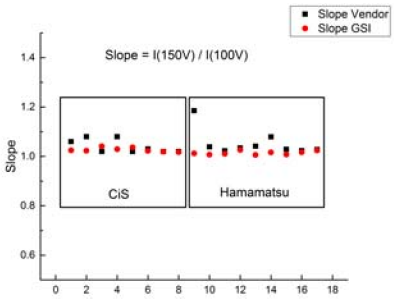

Figure 2: Measured slope compared with vendors' data.

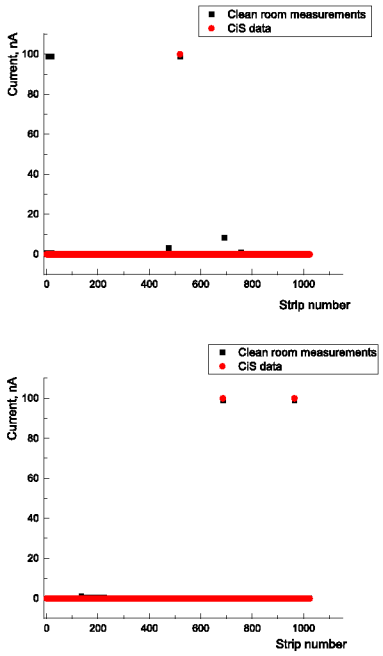

Figure 3: Comparison of the pinhole tests with vendor information for the latest prototype sensor CBM06. Top: N-side; bottom: P-side.

CBM06 have been tested there; the results for one sensor are shown in Fig. 3. New pinholes have been detected on the N-side of the sensor (Fig. 3, top) which demonstrates the necessity of sensor parameters verification shortly before sensor will be connected to readout electronics.

References

[1] P. Larionov and P. Ghosh, GSI Scientific Report 2012, p.47

[2] P. Larionov, CBM Progress Report 2015, p.24

DOI:10.15120/GR-2017-1

Investigation on low mass copper flex micro-cables for the STS detector

T. Blank[1], *M. Caselle*[1], *C. J. Schmidt*[2], *and M. Weber*[1]
[1]KIT, Karlsruhe, Germany; [2]GSI, Darmstadt, Germany

The silicon sensors of the Silicon Tracking System (STS) will be connected to the read-out chips (ROC) by means of up to 0.5 m long high-density and low-capacitance flex cables. Two flex micro-cable designs are currently under investigation. The first one is based on a stack of two single layer flex cables with aluminium traces, the second is a double-sided flex cable with copper traces on the top and bottom side. First 18 cm long samples of the copper flex cables have been delivered and electrically characterized. The measured capacitance of the copper cable surrounded by air was found to be 0.44 pF/cm. Finite Element (FE) simulation yields a capacitance value of 0.41 pF/cm. A parametric sweep of the geometric design parameters reveals the relationship between the capacitance and the design parameters of the cable.

Copper Micro Cable Design and Production

The copper flex micro-cable is produced utilizing advanced PCB production technologies. Thus, the signals can be routed over two planes resulting in a reduction of the amount of micro-cables by a factor of two compared to single layer aluminum cables. Figure 1 schematically shows a proposed high-density interconnection scheme between the micro-cable and die.

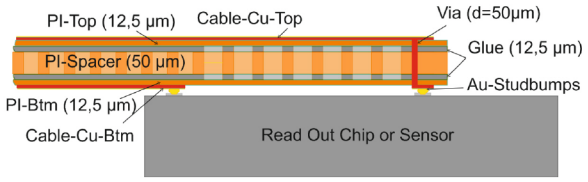

Figure 1: Cross section through the copper cable mounted on the ROC or sensor.

Owing to the PCB-processes, many cables can be manufactured in parallel on a panel. In a first test run, all cables for three sensors were produced on one panel. Figure 2 shows a set of cables with a length of 186 mm and 200 mm. They can be used to contact the top or bottom side of the sensor and the front-end electronics. The cables are delivered on a release tape (Fig. 2 – right), which eases the handling of the micro-cables.

The assembly process of the cables to the ROC chips includes a gold stud bump process on the ROC chips. The gold stud bumps are formed by means of an automated gold wire bonding machine (Fig. 3). The process is fast and reliable. More than 15 bumps can be deposited per second. The gold stud bumping process is an alternative to galvanic metallization processes to provide a solderable pad metallization on the ROC and sensor chips.

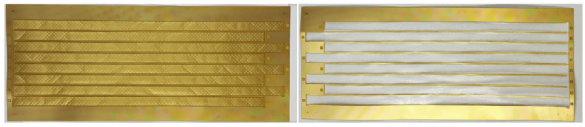

Figure 2: Eight copper micro cables (left) are required to connect the top or bottom side of the sensor to the ROC chips. The cables are delivered on a release tape (right).

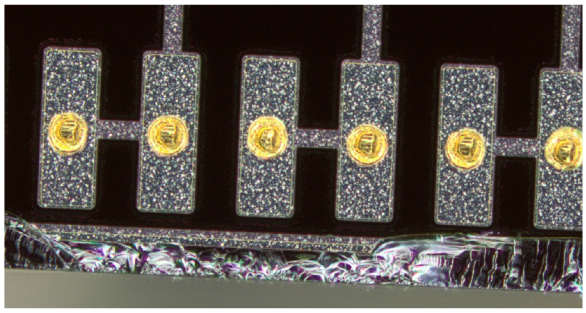

Figure 3: Gold stud bumps placed on a test ROC chip.

The stud bump process is followed by dispensing or printing anisotropic conducting epoxy glue onto the cable. The ROC is picked up from a tray or wafer and placed with a flip-chip machine on the contact pads of the cable. The glue on the cables is snap cured at a temperature of 150 °C for 10 seconds inside the flip-chip machine by means of a heated pick head. Figure 4 shows a ROC-dummy mounted onto a cable (left) and an X-ray image, revealing the placement accuracy of the process.

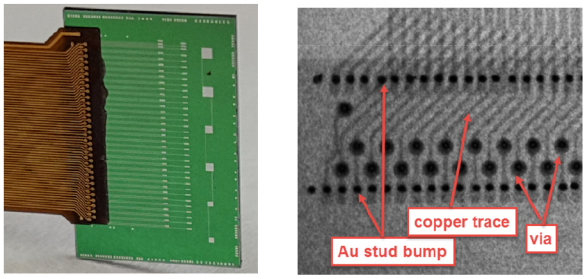

Figure 4: A dummy ROC is mounted to the cable (left), X-ray of the cable glued on the ROC (right).

DOI:10.15120/GR-2017-1

Electrical Characterization and Simulation

The total electronic noise in a detector channel strongly depends on the capacitance of the cable. Thus, the capacitance of the cable has been measured on a SUESS probe station. One copper trace on the top side was set to HIGH voltage. Both neighbouring lines on the top layer and four lines located directly underneath the "HIGH-line" on the bottom layer were connected to ground. The capacitance measured was 8.8 pF for a 20 cm long copper cable (0.44 pF/cm). In order to minimize the cable capacitance an FE simulation was performed. Geometric design parameters of the micro-cable like the copper trace width and the height of the meshed polyimide interposer were varied. The trace width changed from 18 μm to 36 μm, the height of the meshed interposer from 25 μm to 100 μm.

The FE-simulation results for the capacitance in dependence of the "Meshed Polyimide Layer" (MPL) are summarized in Fig. 5. The simulated capacitance for the real cable with a 50 μm thick meshed polyimide layer and 36 μm wide copper traces results in a capacitance of approximately 0.41 pF/cm. This value is in good agreement with the simulation results given in [1, 2], and the measured results of 0.44 pF/cm. The next generation of micro-cables will be realized with a 75 μm meshed interposer and 24 μm wide traces. Thus, a capacitance reduction of 18% down to 0.34 pF/cm might be possible.

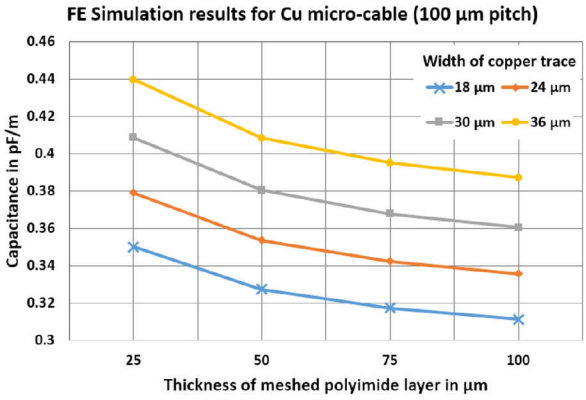

Figure 5: Simulation results of the capacitance over the thickness of the MPL and for varying copper traces width.

Figure 6 shows the electrical potential of a one cm long piece of cable within air. Additional grounded shielding layers were not considered for these simulation runs.

Status and outlook

From the first production run of the copper cable promising conclusions could be derived:

- High production yields can be reached with up to 20 cm long cables.
- The capacity of the copper cable is comparable to the cables comprising aluminium traces.

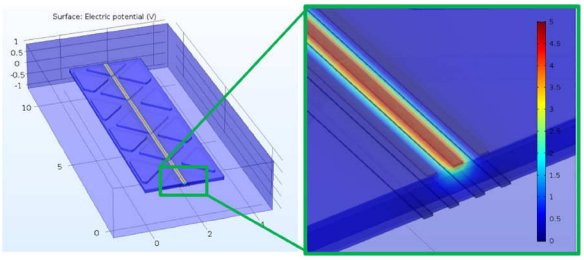

Figure 6: Simulation results of the capacitance over the mesh thickness and a varying copper traces width.

- The amount of production processes for the sensor-cable-ROC sub-system can be reduced by at least a factor of two due to the doubled number of signal layers in the copper cable.

However, the mounting processes for the cable needs further research. The glue process on the sensor side might be tricky, hence, alternative technologies based on small solder ball interconnects will be evaluated.

References

[1] T. Blank et al., Investigation on low-mass copper flex cables for the STS detector, CBM Progress Report 2015, ISBN 978-3-9815227-3-0

[2] D. Soyk et al., Capacity studies of CBM STS micro-cable stack-up, this report

Assembly of dummy modules for a STS test unit

C. Simons[1], *R. Visinka*[1], *O. Vasylyev*[1], *and I. Tymchuk*[2]
[1]GSI, Darmstadt, Germany; [2]LTU Ltd, Kharkov, Ukraine

With the construction of a demonstrator for the CBM Silicon Tracking System a lot of questions in matters of assembly techniques, cooling and cabling can be answered. Dummy-modules for this unit are assembled to gain experience with the longest microcables, the biggest sensors (62 mm by 124 mm), the ladder assembly, and to be able to fix the total cable lengths.

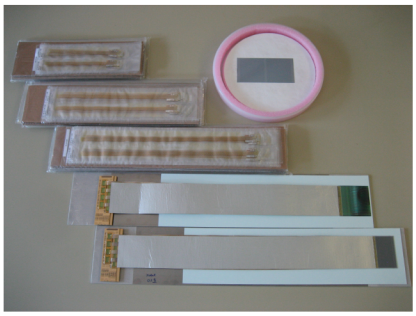

Figure 1: Dummy-modules for quarter unit 7.

The longest sensor modules

Unit 7, as the biggest unit, needs the longest microcables. For the n-side of the inner 42 mm silicon sensor, microcables of about 495 mm length are necessary. Until now the longest microcables delivered had a length of 250 mm and therefore important experience could be gained during the module-assembly with cables of up to such length. The storage plates and storage systems had to be adapted.

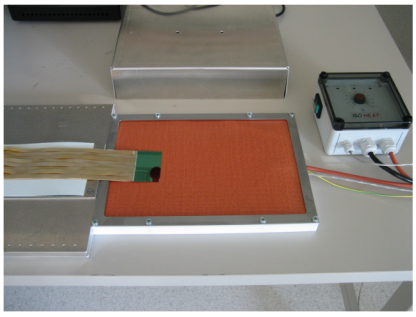

Figure 2: Dummy-module on the heating mat.

Since these longest modules do not fit in the oven for the curing process, a heating mat has been acquired. The mat can be placed next to the assembly tables, helps to avoid longer transport ways for the module and offers heating only in the glued area (sensor, ASIC or FEB).

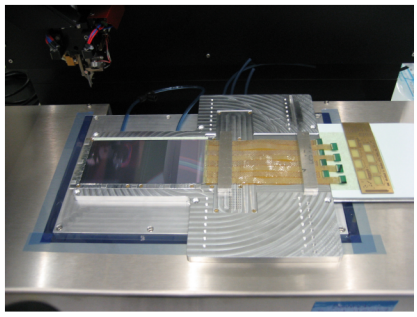

Figure 3: TAB-bonding on a 124 mm sensor.

The vacuum plates were adapted for the 124 mm sensors and the handling procedures were optimized (see Fig. 3).

The total cable lengths

The microcable lengths measured in the CATIA-model result from different factors: sensor position on the ladder, position of the sensor bonding rows, position of the ASIC bonding rows, overlap of the sensors, bending radius of the microcable, etc..
On one hand the aim is to pack the microcable stacks of the five modules closely and to avoid cable loops. On the other hand the mounting of the front-end-boards in the electronic boxes has to be considered (Fig. 4). The p-side-FEB is fixed on the bottom side of the cooling plate, the n-side-FEB on the top side.
Based on the microcables lengths measured in the CATIA-model the length for the module-cables have been increased in little steps to gain experience during the assembly-procedures and to find the optimal lengths.

Figure 4: Microcables in electronic box.

The dummy-modules for unit 7 will be used to test the ladder assembly tool with regard to functionality and accuracy.

DOI:10.15120/GR-2017-1

Capacitance studies of the CBM STS microcable stack-up

D. Soyk, H. Faber, and C. J. Schmidt
GSI, Darmstadt, Germany

Several studies with FEM tools have been made to find a thin microcable stack-up with a reduced capacitance and good assembly properties.

Discussion of parameters

The capacitance of a simple flat capacitor is calculated as follows:

$$C = \epsilon_r \epsilon_0 \frac{Lb}{d} \quad (1)$$

The vacuum permittivity ϵ_0 is a natural constant. If we assume that the capacity is directly proportional to the length L three parameters are left to optimize:

1. the relative permittivity ϵ_r depends upon the material.
2. the distance d between two layers of metal strands or the ground layer of the microcable. (N.B.: the pitch between two strands must be kept to avoid mismatch between sensor and microcable or between microcable and chip.)
3. the width b of the metal strands.

Choice of simulation tool

Two software tools were available to generate this study. The first was Ansys and the second was the Transmission Line Electromagnetic Modeling Tool - called TNT. Ansys employs the finite element method (FEM), TNT the near element boundary method (NEBEM). Some comparision studies were done to avoid errors due to systematical errors in the calculation method or simple software errors. For theses studies a defined layer stack was used and the permittivity ϵ_r of the spacer was varied. The stack consisted of the following materials above a metallic plane: 100 μm spacer, 10 μm polyimid, 14 μm aluminium outer signal layer; 50 μm spacer, 10 μm polyimid, 14 μm aluminium inner signal layer and 100 μm spacer. In the table below the results obtained with TNT and Ansys are displayed in comparison.

ϵ_r	TNT outer layer [pF/cm]	Ansys outer layer [pF/cm]	TNT inner layer [pF/cm]	Ansys inner layer [pF/cm]
3.5	0.91	0.99	0.89	0.94
2.25	0.68	0.72	0.66	0.69
1.5	0.53	0.55	0.51	0.52

Both simulation tools show the same trends: higher ϵ_r effects higher capacitance and the outer layer has a higher capacitance than the inner layer. Both trends are expected from equation (1). The results differ less than 1/10. Therefore both tools seems to be sufficent for our needs, and we chose the TNT tool for further studies.

Stack and material variations

In [1] a cable stack for the CBM STS readout was proposed. Further investigation especially concerning the produceability and the handling of the different layers of the micro-cable required some modifications. First the central spacer had to be split in two halfs to result in a symmetrical stack of the micro-cable for the p- and n-side of the sensor. Additionally the polyimid layer between the grounds and the outside spacer was suppressed to avoid the lamination of 2 flimsy, 10 μm thick polyimid layers during the production process. It turned out that at least the spacer under each signal layer should be the same to make the laboratory assembly procedures easier. The modified cable stack is shown in Fig. 1.

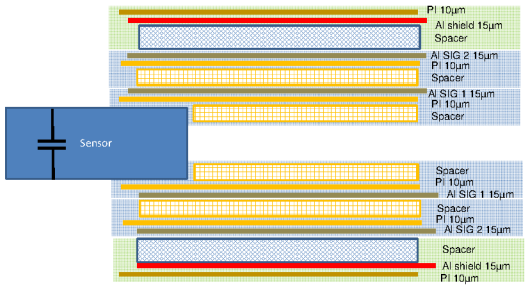

Figure 1: Modified CBM STS microcable stack-up

Variation of the spacer material and thickness give possibilities to influence the capacity of the cable. There were 6 material options to investigate:

material	ϵ_r	thickness [μm]
polyimid 5/10 filled	2.25	50
polyimid 5/10 filled	2.25	100
polyimid 3/10 filled	1.8	50
polyimid 3/10 filled	1.8	75
polyimid 3/10 filled	1.8	100
Foamtak II	1.5	165

DOI:10.15120/GR-2017-1

Possible stack-ups were chosen. In the following table one half of the symmetric stack-ups are described (from the outer layer to the plane of symmetry where the sensor is located):

No.	Layers
1	10μm polyimid,14μm aluminium,100μm polyimid 5/10, 14μm aluminium,10μm polyimid,50μm polyimid 5/10, 14μm aluminium,10μm polyimid,50μm polyimid 5/10
2	10μm polyimid,14μm aluminium,100μm polyimid 3/10, 14μm aluminium,10μm polyimid,50μm polyimid 3/10, 14μm aluminium,10μm polyimid,50μm polyimid 3/10
3	10μm polyimid,14μm aluminium,165μm Foamtak II, 14μm aluminium,10μm polyimid,50μm polyimid 5/10, 14μm aluminium,10μm polyimid,50μm polyimid 5/10
4	10μm polyimid,14μm aluminium,165μm Foamtak II, 14μm aluminium,10μm polyimid,50μm polyimid 3/10, 14μm aluminium,10μm polyimid,50μm polyimid 3/10
5	10μm polyimid,14μm aluminium,165μm Foamtak II, 14μm aluminium,10μm polyimid,75μm polyimid 3/10, 14μm aluminium,10μm polyimid,75μm polyimid 3/10
6	10μm polyimid,14μm aluminium,165μm Foamtak II, 14μm aluminium,10μm polyimid,100μm polyimid 3/10, 14μm aluminium,10μm polyimid,100μm polyimid 3/10
7	10μm polyimid,14μm aluminium,165μm Foamtak II, 14μm aluminium,10μm polyimid,165μm Foamtak II, 14μm aluminium,10μm polyimid,165μm Foamtak II

These 7 stack-ups were simulated for a strand width of 46 μm. The results for the inner and outer signal layer were calculated.

No.	inner layer [pF/cm]	outer layer [pF/cm]	thickness [μm]
1	0.715	0.724	544
2	0.615	0.620	544
3	0.715	0.613	674
4	0.615	0.566	674
5	0.569	0.534	774
6	0.548	0.518	874
7	0.468	0.476	1134

Stack no. 1 and no. 2 differ only by the polyimid material for the spacer used. No. 2 uses the polyimid 3/10 filled mesh with a mean ϵ_r of 1.8 instead of 2.25. An improvement of the strand capacitance for both layers is observable. No. 3 and 4 have the same structure as No. 1 and 2 between the signal layers, but the spacer between shielding and outer signal layer is thicker and with lower ϵ_r. This has mainly an influence on the capacitance of the outer signal layer, not on the inner signal layer. If the capacitance of both layers is to be improved the structure between the signal layers also needs improvement. No. 5 and 6 has the same stack of materials as no. 4, but the thickness of the polyimid 3/10 filled spacer is increased to 75 and 100 μm. The capacitance consequently decreases with the increasing thickness of the spacer as anticipated. No. 7 contains only 165 μm thick Foamtak II spacers. The low ϵ_r and the high thickness of the material results in a low capacitance of the signal layers.

Due to mechanical space restrictions in the CBM STS detector the "best" micro cable stack-up is not the one with the lowest capacitance, but the one with the lowest capacitance fitting in the foreseen space. In the final detector 5 microcable stack-ups will be adjacent and the overall thickness of these 5 stacks should be less than 5 mm (with some safety margin). Therefore the stack no. 5 was chosen. Now 2 of 3 parameters are optimized, namely the relative permittivity ϵ_r and the distance d between the signal layers (in other words the thickness of the spacer). To reach the design goal of a capacitance of less than 0.5 pF/cm, the last parameter must be modified: the width b of the metal strands of the signal cable. The strand width is reduced to a width of 30 μm and the calculation for the stack no. 5 is done. The following values are obtained for 30 μm strands:

inner layer [pF/cm]	outer layer [pF/cm]
0.387	0.367

For comparison, these are similar to the values obtained from the measurements of a realistic stack-up, where the width of the strands was 35 μm. The simulation is something like 1/10 off the measurement.

Conclusion

As shown above it is possible to obtain a thin microcable stack for the CBM STS detector with a relative capacitance lower than 0.5 pF/cm. In the real world the measured values for the capacitance should be well under the simulations, because the stack-up is in general not tightly laminated so that the average distance between the layers is generally larger. Also the layers of glue are assumed to be equal to zero and are neglected in the simulation.

References

[1] D. Soyk et al., "Modification of the CBM-STS micro-cable stack-up", CBM Progress Report 2014

DOI:10.15120/GR-2017-1

Optimization of multi-strange hyperons cuts in KF Particle Finder

H. Cherif[1,2], *A. Toia*[1,2], *and I. Vassiliev*[2]
[1]Goethe University Frankfurt am Main, Germany; [2]GSI, 64291 Darmstadt, Germany

One of the main goals of the CBM experiment is the measurement of very rare probes and the investigation of possible signatures of the phase transition from nuclear matter to deconfined phase and formation of the Quark Gluon Plasma (QGP). The enhanced production of multi-strange (anti)particles is one among those signatures, thus we investigate the performance of multi-strange hyperons measurement in the CBM experiment. Multi-strange (anti) hyperons are reconstructed via their weak decay into charged hadrons ($\Lambda \rightarrow p\pi, \Xi \rightarrow \Lambda\pi, \Omega \rightarrow \Lambda K$) measured by the Silicon Tracking System (STS) detector installed in a large acceptance dipole magnet. Identification of the decay products is performed by a time-of-flight measurement with TOF detector located at a distance of 6 to 10m behind the target. The analysis is performed by the KF Particle Finder (KFPF) package [1].. In order to reduce the combinatorial background, three selection criterias are applied in the reconstruction of multi-strange (anti)hyperons:

- χ^2_{geo} : To ensure that the trajectories of the daughter particles intersect within their errors.
- χ^2_{topo}: To ensure that the particle is produced in the primary vertex region.
- $l/\Delta l$: Distance from the decay point of the candidate to the primary vertex normalized on the error.

The values of these cuts are optimized by a scan over the whole set of selection criteria with a requirement to maximize the signal-to-background ratio with a minimal loss of efficiency. Specifically we studied the efficiency and significance of the signal in central Au+Au collisions at 10 AGeV simulated with the UrQMD event generator, coupled to a Geant3-based description of the CBM detector. The significance is defined as $S/\sqrt{S+B}$, where S and B are total numbers of signal and background of the candidate from Monte Carlo. We distinguish two types of efficiency, which are defined as:

- The efficiency of KF Particle Finder package which is the efficiency of the method followed in the reconstruction of particles, including the topological cuts and the Particle Identification in the ToF.
- The total efficiency in the 4π solid angle which, in addition to the previous, take into account the acceptance of the detector and the inefficiencies of track reconstruction and PID algorithms.

Fig. 1 shows the variation of the significance and the 4π efficiency as function of the cut values for the different cuts mentioned above. Then the default value is optimized for

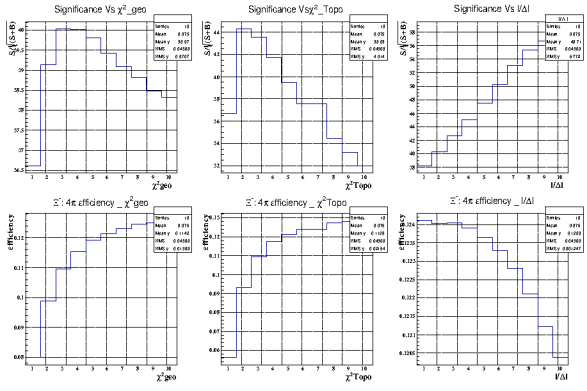

Figure 1: Significance and 4π efficiency as a function of cuts for the reconstruction of Ξ^-

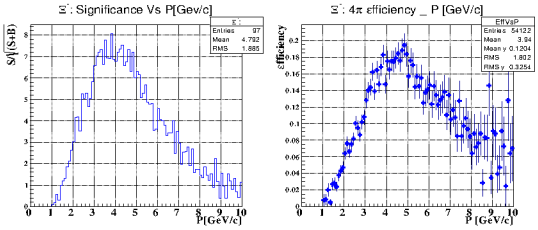

Figure 2: Significance and efficiency vs p for Ξ^-

each cut, taking into account the best arrangement between the significance and the efficiency. Table 1 shows the mean efficiency calculated with the default optimal cut values for all hyperons. Since the background as well as the selections

Hyperons	Λ	$\bar{\Lambda}$	Ξ^-	$\bar{\Xi}^+$	Ω^-	$\bar{\Omega}^+$
KFPF efficiency(%)	70.7	43.6	47.6	30.6	15.9	12.9
4π efficiency (%)	26.6	16.5	10.2	6.8	4.6	3.9

Table 1: Efficiency of reconstruction of multi-strange hyperons in the CBM experiment:

used for the reconstruction, depend on the average particle momenta, efficiency and significance are studied as a function of the particle momentum. The significance and the efficiency as function of momentum for Ξ^- is shown in Fig. 2. The high quality of these parameters demostrate the capability of CBM to reconstruct strange particles both with a high signal to background ratio and efficiency.

References

[1] M. Zyzak (2016), PhD thesis, Goethe University Frankfurt.

DOI:10.15120/GR-2017-1

Reconstruction of π^0 via double conversion method *

I. Kres[1], *C. Pauly*[1], *and K.-H. Kampert*[1]
[1]Department of Physics, University of Wuppertal, Germany

The CBM experiment is designed to study heavy ion collisions at high net-baryon densities and moderate temperature, at high interaction rates. Under these conditions, heavy particles containing charm quarks, like J/ψ, are produced, but also vector mesons ω, ρ, ϕ will be created, and detected via their rare dileptonic channel $\omega/\rho/\phi \rightarrow e^+e^-$. As leptons are not affected by hadronic interaction with the dense medium, the dileptonic decay channel offers the possibility to look into the early, dense phase of the fireball evolution. Due to their comparatively small production cross section, together with small branching ratio (BR) into e^+e^- a precise understanding of background is needed. A major source of this background are π^0, which have two main decay channels: $\pi^0 \rightarrow \gamma + \gamma$ with BR of 98.8% and $\pi^0 \rightarrow e^+ + e^- + \gamma$ (Dalitz decay) with BR of 1.1%.

Instead of measuring directly photons, using an electromagnetic calorimeter, the CBM-RICH detector is able to measure photons indirectly by detecting e^+e^--pairs stemming from conversion $\gamma \rightarrow e^+e^-$ in the target or in the material of the detectors. Two such reconstructed photons are then further combined to form a π^0.

In previous work this study was done for cases, when both photons from π^0 underwent conversion only in the target [1]. Using the secondary vertex finder included in the KFParticle package [2], one can reconstruct conversion vertices also outside the target, which will increase statistics by about a factor of 5, because the probability for conversion outside the target compared to conversion inside the target is roughly 50:50, as shown in figure 1.

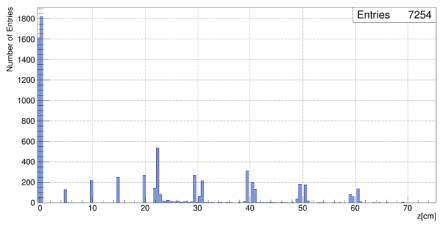

Figure 1: Distribution of z-position of reconstructed $\gamma \rightarrow e^+e^-$ vertices. The spikes correspond to the target (0 cm), MVD stations (5, 10, 15, and 20 cm), and STS (22, 30, 40, 50, and 60 cm) positions.

This previous study is now extended, including reconstruction of conversion vertices outside the target. The results shown here are based on 5×10^6 simulated UrQMD events of central Au+Au collisions at beam energy of 8 AGeV. The detector simulation includes the Micro Vertex Detector (MVD), Silicon Tracking System (STS), and Ring Imaging Cherenkov detector (RICH). The magnetic field has its nominal value 100%. The RICH geometry was used with the new cylindrical shaped photon detection plane.

In the first analysis step, all charged tracks are reconstructed in STS, and only lepton tracks are selected based on particle identification (PID) in the RICH. Since the leptons from $\pi^0 - e^+e^-e^+e^-$ signal events have in most of cases small momenta, half of them are outside of acceptance of the RICH detector, which makes the probability to register all four leptons from π^0 very low. A less restrictive requirement of at least two (one from each pair) out of four are identified in the RICH as leptons, helps to increase statistics by about factor of 10, compared to full identification in RICH.

When only one lepton of a potential e^+e^- pair is identified in the RICH, then the second candidate must not necessarily be a lepton as well. Applying additional cuts on the invariant mass of γ (< 10 MeV) and opening angle between charged particles ($< 1°$), one can exclude most of situations, where the second particle is not an electron. For all γ candidate events surviving these cuts, the invariant mass spectrum of π^0 is calculated and shown in figure 2.

The background was estimated with Event Mixing Technique (EMT) and was substracted from the spectrum. The subtracted spectrum was fitted using a Gaussian and the number of reconstructed π^0 is determined to be 4404 ± 82.

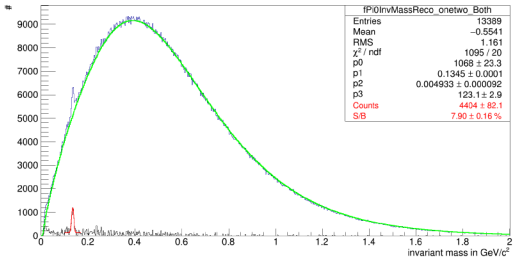

Figure 2: Invariant mass spectrum of reconstructed π^0 with double conversion method (blue), estimated background from EMT (green), background-substracted spectrum (black), Gaussian fit (red).

References

[1] Dissertation of Sascha Reinecke, Wuppertal, 2016.

[2] Dissertation of Maksym Zyzak, Frankfurt am Main, 2015.

* Work supported by BMBF 05P15PXFCA, and GSI

DOI:10.15120/GR-2017-1

CBM operation at low SIS100 beam energies

A. Senger[1]
[1]GSI, Darmstadt, Germany

Motivation

The CBM physics program covers the full beam energy range of SIS100. The operation of the CBM experiment at low beam energies has to be optimized with respect to the setting of the magnetic dipole field which deflects the beam. One condition for save operation is that the beam has to hit the beam dump which is located about 20 m downstream the target. Moreover, the beam should stay within the beam pipe, and should not directly hit the detectors. In order to fulfil these requirements, the magnetic field of the CBM dipole has to be reduced for operation at low beam energies. However, a reduced dipole field might have severe consequences for the tracking performance of the experiment. This report presents a study of a CBM operation scenario at low beam energies together with the resulting tracking performance. Simulations have been performed with the FLUKA package ([1], [2]), and with the FLAIR interface ([3]) for visualization of the results. Multi-scattering of the Au beam in in the Au target (1% interaction length) is included in the FLUKA calculations. A typical beam divergence is also taken into account, however, the width of the beam profile is dominated by multiple scattering.

Beam position in the beam dump

The beam profile for different Au beam energies at the entrance of the CBM iron beam dump (25.75 m downstream the target) is shown on figure 1. At the full magnetic field and a beam energy of 2 AGeV the maximum of the beam intensity is deflected by more than 1 m which is already outside the iron core of the beam dump (total width 2 m). Moreover, the width of the beam at 2 AGeV increases up to factor of 2 in comparison to 8 AGeV. The beam positions in the region of beam dump for different energies and scaled magnetic field are shown on figure 2. The symbols indicate the position of the maximum of the beam intensity, whereas the circles describe the width of the beam containing 99% of the intensity. In order to catch the beam for both polarities of the dipole magnetic field, the horizontal size of the beam dump was chosen to $\pm$100 cm (red dashed line in figure 2). Nevertheless, the magnetic dipole field has to be reduced to about 70% of the nominal value in order to dump 99% of the beam particles with an energy of 2 AGeV into the iron beam stopper.

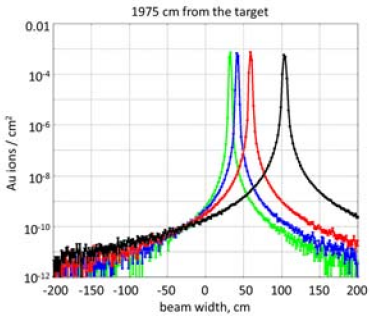

Figure 1: Beam profile at the region of the CBM beam dump for different Au beam energies: black - 2 AGeV, red - 4 AGeV, blue - 6 AGeV, green - 8 AGeV.

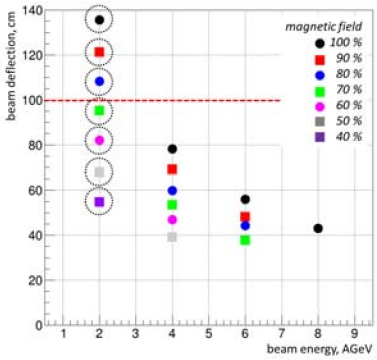

Figure 2: The beam positions at the iron beam dump for different energies and scaled magnetic field: black symbols - 100% magnetic field, red - 90%, blue - 80%, green - 70%, magenta - 60%, gray - 50%, and violet - 40% magnetic field. The circles indicate the beam width corresponding to 99% of the beam intensity for an energy of 2 AGeV. The red dashed line shows the horizontal width of the beam dump.

Beam position at the detector stations

As examples, we study the beam positions in the STS region (20-120 cm downstream the target) and the horizontal beam profile at the position of the TRD (5 m downstream the target) for an Au beam with an energy of 2 AGeV. Figure 3 illustrates the beam deflection in the region of the STS for different magnetic fields. The black dashed line depicts the radius of the beam pipe. At 60% of the nominal field value the beam still is very close to the beam pipe edge, and, hence, it seems preferable to reduce the magnetic field

DOI:10.15120/GR-2017-1

to 50% of the nominal value. In figure 4 the horizontal beam profile is shown at the position of the TRD. The red histogram in figure 4 corresponds to the beam profile for 100% magnetic field. The dashed black lines illustrate the central hole in the detector required for the beam pipe. As shown in figure 4, in case of 100% magnetic field the beam fully hits the detector area. In order to reduce the number of beam particles hitting the detector to 10^{-6} of the full beam intensity, the magnetic field has to be reduced to 50% of the nominal value. The resulting beam profile is shown in figure 4 as a light blue line.

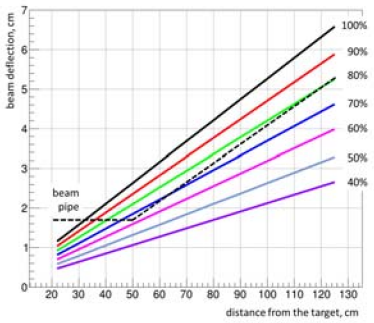

Figure 3: Beam position in the region of the STS (20-120 cm downstream the target) for Au beam at 2 AGeV for different magnetic field scaling (see explanation on picture). The black dashed line illustrates the radius of the beam pipe.

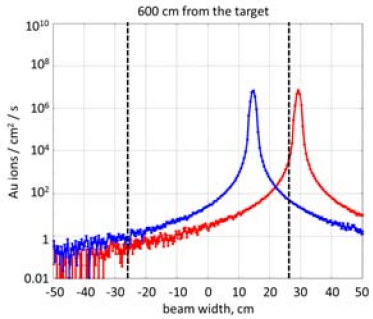

Figure 4: Horizontal beam profile at the position of the TRD (5 m downstream the target) for Au beam at 2 AGeV for 100% magnetic field (red line) and for 50% magnetic field (blue line). The black dashed lines illustrate the size of the detector hole for the beam pipe.

Particle reconstruction performance with reduced magnetic dipole field

The effect of a reduced magnetic dipole field on the particle reconstruction performance was studied using the cbmroot software and the KFParticle package. The simulated setup consists of STS and ToF. The particle reconstruction efficiency for Au beam energy of 2 AGeV with full and reduced magnetic field is shown in figure 5 (left panel). For the reduced magnetic field, the reconstruction efficiency for low momentum particles increases due to the increased acceptance. The momentum resolution for the same beam energy with full and reduced magnetic field is shown in figure 5 (right panel). At an Au beam energy of 2 AGeV and a magnetic field of 40% nominal value, the momentum resolution decreases by a factor of 2.

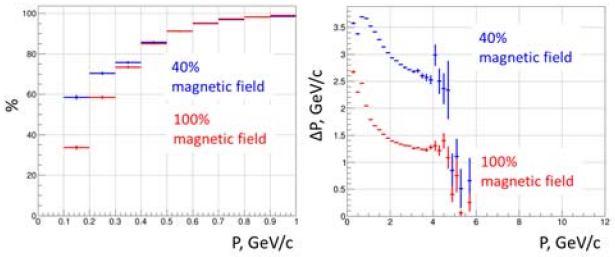

Figure 5: The particle reconstruction efficiency as function of particle momentum (left) and the momentum resolution versus momentum (right) for Au beam energy of 2 AGeV with full (red) and scaled (blue) magnetic field.

In order to study the effect of a reduced magnetic field on particle mass resolution and signal-to-background ratio, simulations have been performed for Λ and K^0_S mesons. The results on reconstruction efficiency, mass resolution and signal-to-background ratio for Λ and K^0_S are presented in figure 6.

Magnetic field	100%	40%	100%	40%	100%	40%
	Reconstruction efficiency		Mass resolution		Signal-to-background ratio	
Λ	6.0%	9.0%	1.7 MeV	3.4 MeV	4.7	2.0
K^0_S	2.8%	3.6%	4.0 MeV	9.0 MeV	25.0	20.7

Figure 6: The reconstruction efficiency of Λ and K^0_S, mass resolution and signal-to-background ration for reconstruction for Au beam energies of 2 AGeV with full and reduced magnetic field.

References

[1] "The FLUKA code: Description and benchmarking" G. Battistoni, S. Muraro, P.R. Sala, F. Cerutti, A. Ferrari, S. Roesler, A. Fasso', J. Ranft, Proceedings of the Hadronic Shower Simulation Workshop 2006, Fermilab 6–8 September 2006, M. Albrow, R. Raja eds., AIP Conference Proceeding 896, 31-49, (2007)

[2] "FLUKA: a multi-particle transport code" A. Fasso', A. Ferrari, J. Ranft, and P.R. Sala, CERN-2005-10 (2005), INFN/TC_05/11, SLAC-R-773

[3] "FLAIR: A Powerful But User Friendly Graphical Interface For FLUKA" V. Vlachoudis, Proc. Int. Conf. on Mathematics, Computational Methods & Reactor Physics (M&C 2009), Saratoga Springs, New York, 2009

DOI:10.15120/GR-2017-1

Hypernuclei reconstruction at the CBM experiment *

I. Vassiliev[1], *I. Kisel*[1,2,3], *and M. Zyzak*[1]

[1]GSI, Darmstadt, Germany; [2]Goethe-Universitaet Frankfurt, Frankfurt am Main, Germany; [3]Frankfurt Institute for Advanced Studies, Frankfurt am Main, Germany

In the CBM experiment at FAIR high net-baryon densities and moderate temperatures will be reached in heavy-ion collisions. Model calculations predict structures in the QCD phase diagram at large baryon chemical potentials, like the critical endpoint followed by a first order phase transition. Moreover, new phases are predicted, such as quarkyonic matter. Experimental discovery of these landmarks and regions in the QCD phase diagram would be a major breakthrough in our understanding of properties of strongly interacting matter at extreme conditions, with fundamental consequences for our knowledge on the structure of neutron stars, chiral symmetry restoration, and the origin of hadron masses. The aim of the CBM experiment is the measurement of very rare probes including multi-strange hyperons and hypernuclei at interaction rates of up to 10 MHz.

Theoretical models predict that single and double hypernuclei can be produced via coalescence in heavy-ion collisions with the maximum yield in the region of SIS100 energies [1, 2]. This is due to the superposition of two effects: the increase of light nuclei production with decreasing beam energy, and the increase of hyperon production with increasing beam energy. The CBM experiment at SIS100 will measure hydrogen and helium hypernuclei in huge amounts. To study the performance of multi-strange hyperon and hypernuclei reconstruction, several sets of $5 \cdot 10^6$ central Au+Au UrQMD events (Fig. 1) at the FAIR energy range 2-10 AGeV have been simulated.

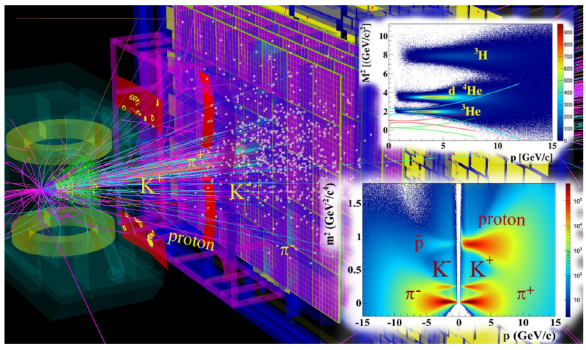

Figure 1: A simulated CBM event of a Au+Au collision. Reconstructed in the STS tracks propagated via RICH and TRD to the TOF detector. The TOF detector identifies hadrons i. e. pions, kaons, protons and fragments.

The combination of Micro Vertex Detector (MVD) and fast segmented strip detectors of the Silicon Tracker System (STS) with cables and support frames was used for event simulation and reconstruction. The TOF detector identifies hadrons i.e. pions, kaons, protons, and fragments, i. e. d, t, ^{3}He and ^{4}He in the angular range covered by the STS detector.

The current KF Particle Finder package includes search of Lambda hypernuclei: the bound state $\{\Lambda n\}_b$, ${}^3_\Lambda$H, ${}^4_\Lambda$H, ${}^4_\Lambda$He, ${}^5_\Lambda$He and corresponding anti-particles and double Lambda hypernuclei: ${}^4_{\Lambda\Lambda}$H, ${}^5_{\Lambda\Lambda}$H and ${}^6_{\Lambda\Lambda}$He. Hypernuclei will be reconstructed in the CBM experiment by their decays into charged hadrons and fragments, like d, t, ^{3}He and ^{4}He, which are detached from the primary vertex. As an example reconstructed ${}^4_\Lambda\text{He}\rightarrow{}^3\text{He}p\pi^-$ decay is shown in Fig. 2.

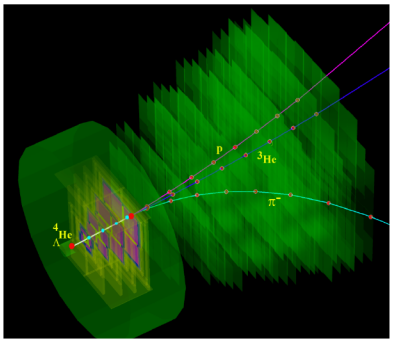

Figure 2: A reconstructed ${}^4_\Lambda\text{He}\rightarrow{}^3\text{He}p\pi^-$ decay topology.

${}^4_\Lambda$He hypernuclei are created at the primary vertex and decay to ${}^3\text{He}p\pi^-$ several centimeters downstream of the target. Presence of the ^{3}He fragment in a 3-prong vertex is a unique signature of such decay. The reconstructed invariant-mass spectrum of ${}^3\text{He}p\pi^-$ is shown in Fig. 3.

Small amount of background events in the high-mass region is due to misidentified high-momentum hadrons in the sample of ^{3}He selected particles.

Assuming the ${}^4_\Lambda$He production multiplicity for minimum bias Au+Au events at 10 AGeV about $5 \cdot 10^{-4}$ [1, 2], the branching ratio of 20% to ${}^3\text{He}p\pi^-$ decay [3], taking into account the 14.7% ${}^4_\Lambda$He detection efficiency, one would expect the ${}^4_\Lambda$He extremely high collection rate of up to $5.4{\cdot}10^5$ per hour.

Moreover, the experiment has a substantial discovery potential for light double Lambda hypernuclei. The topology of double-Lambda hypernuclei decay is complicated. For example ${}^6_{\Lambda\Lambda}$He first decays to ${}^5_\Lambda\text{He}p\pi^-$ several centimeters downstream of the target, then single-Lambda hypernuclei ${}^5_\Lambda$He weekly decays to ${}^4\text{He}p\pi^-$. In order to reconstruct

* Work supported by HICforFAIR, FIAS and HGS-HIRe for FAIR.

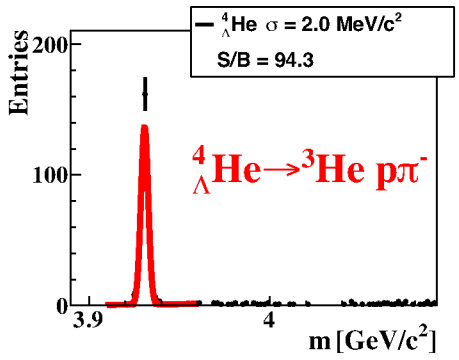

Figure 3: The reconstructed invariant-mass spectrum of ^{3}He$p\pi^-$ in $5 \cdot 10^6$ central Au+Au collisions at 10 AGeV. The red line indicates the signal plus background fit by a polynomial plus Gaussian function.

such a complicated topology KF Particle Finder first reconstructs detached 3-prong decay of $^5_\Lambda$He combining secondary ^{4}He, p and π^-, then a mass constraint is applied to selected $^5_\Lambda$He candidates, and $^6_{\Lambda\Lambda}$He particles are constructed as combination of secondary $^5_\Lambda$He, p and π^-. Finally the reconstructed $^6_{\Lambda\Lambda}$He candidates checked to be primary.

In the Table 1 the multiplicities, branching ratios, decay modes, efficiencies and collection rate per week at 10 MHz interaction rate of selected single- and double Lambda hypernuclei for the CBM experiment are shown.

particle	multiplicity	decay	BR	$\varepsilon_{4\pi}$%	yield/week
$^3_\Lambda$H	$0.9 \cdot 10^{-2}$	^{3}Heπ^-	0.25	19.2	$2.6 \cdot 10^9$
$^4_\Lambda$He	$0.4 \cdot 10^{-3}$	^{3}He$p\pi^-$	0.32	8.9	$6.9 \cdot 10^7$
$^5_\Lambda$He	$1.0 \cdot 10^{-5}$	^{4}He$p\pi^-$	0.4	7.9	$1.9 \cdot 10^6$
$^4_{\Lambda\Lambda}$H	$3.7 \cdot 10^{-5}$	$^4_\Lambda$Heπ^-	0.06	2.6	$3.8 \cdot 10^5$
$^5_{\Lambda\Lambda}$H	$5.0 \cdot 10^{-7}$	$^5_\Lambda$Heπ^-	0.08	2.0	$4.9 \cdot 10^3$
$^6_{\Lambda\Lambda}$He	$2.5 \cdot 10^{-8}$	$^5_\Lambda$He$p\pi^-$	0.08	1.3	160

Table 1: Multiplicities, branching ratios, decay modes, efficiencies and collection rate per week at 10 MHz interaction rate of single- and double Lambda hypernuclei for the CBM experiment.

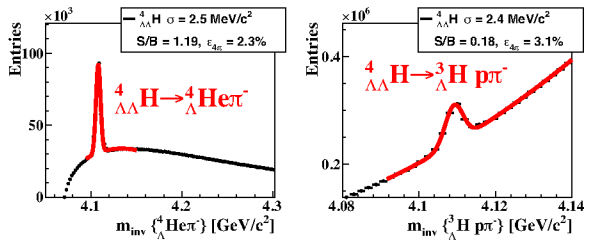

Figure 4: The reconstructed invariant-mass spectra of $^4_\Lambda$Heπ^- (left) and $^3_\Lambda$He$p\pi^-$ (right) in 10^{12} central Au+Au collisions at 10 AGeV. The red lines indicate the signal plus background fit by a polynomial plus Gaussian function.

The invariant-mass spectra of $^4_\Lambda$Heπ^- and $^3_\Lambda$He$p\pi^-$ are shown in Fig. 4. Left plot is obtain by combination of secondary $^4_\Lambda$He and π^-. Three particle invariant-mass spectrum of $^3_\Lambda$He$p\pi^-$ is shown in the right plot. The simulated amount of $5 \cdot 10^6$ central Au+Au collisions at 10 AGeV is not enough for determination of the background shape, so we use typical shapes of two or three particle background for hypernuclei scaled to simulated number of entries in the corresponding histogram. Assuming a reaction rate of 10^7 Au+Au minimum bias events/s (MVD will be removed from the setup), production multiplicity about $3.7 \cdot 10^{-5}$ and $2.5 \cdot 10^{-8}$ [1, 2], the branching ratios of 6.4% and 2.3% [3], one would expect to measure within one week about $3.8 \cdot 10^5$ and $1.8 \cdot 10^5$ $^4_{\Lambda\Lambda}$H, respectively.

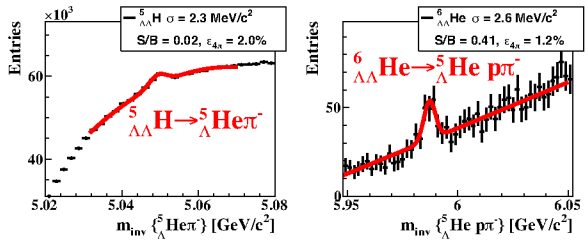

Figure 5: The reconstructed invariant-mass spectra of $^5_{\Lambda\Lambda}$He (left) and $^6_{\Lambda\Lambda}$He (right) in 10^{12} central Au+Au collisions at 10 AGeV. The red lines indicate the signal plus background fit by a polynomial plus Gaussian function.

With extremely low production multiplicity $2.5 \cdot 10^{-8}$ of $^6_{\Lambda\Lambda}$He and small branching ratio of 8% [3], one would expect to measure within one week about 160 $^6_{\Lambda\Lambda}$He (see Fig. 5). Such measurements would represent a breakthrough in hypernucleus physics, as up to now only very few double-Lambda hypernuclei events have been found [4]. The discovery of double lambda hypernuclei and the determination of their life-times will provide information on the hyperon-nucleon and hyperon-hyperon interactions, which are essential ingredients for the understanding of the nuclear matter equation-of-state at high densities, and, hence, of the structure of neutron stars [5].

Discovery and investigation of new hypernuclei and of hypermatter will shed light on the hyperon-nucleon and hyperon-hyperon interactions, which are essential ingredients for the nuclear equation-of-state at high densities and moderate temperatures. The CBM experiment will provide a unique machinary for their study.

References

[1] A. Andronic et al., Phys. Lett. **B697** (2011) 203.

[2] H. Stoecker et al., Nucl. Phys. **A827** (2009).

[3] H. Kamada et al., Phys. Rev., Ser. C **57** (1998) 1595.

[4] J. K. Ahn et al., Phys. Rev. C**88** (2013) 014003

[5] A. S. Botvina et al., Phys. Lett. B**742** (2014) 7

DOI:10.15120/GR-2017-1

Towards full event topology reconstruction with KF Particle Finder *

M. Zyzak[†1], *I. Kisel*[1,2,3], *and I. Vassiliev*[1]

[1]GSI, Darmstadt, Germany; [2]Goethe-Universitaet Frankfurt, Frankfurt am Main, Germany; [3]Frankfurt Institute for Advanced Studies, Frankfurt am Main, Germany

Physics analysis requires the cleanest possible samples of reconstructed particles. Therefore background for them should be suppressed. An independent analysis of each decay separately cannot guarantee this, since abundant particles can contribute to the background generation for all other particles. Thus, to solve the problem full event topology reconstruction is required.

We started the development of full event topology reconstruction at the example of $K^0_s \to \pi^+\pi^-$ and $\Lambda \to p\pi^-$. At first, all possible particle candidates are constructed in a usual manner (see Fig. 1, blue line). We would like to notice, that charged particles without PID are participating in reconstruction of both decays with the corresponding mass hypothesis.

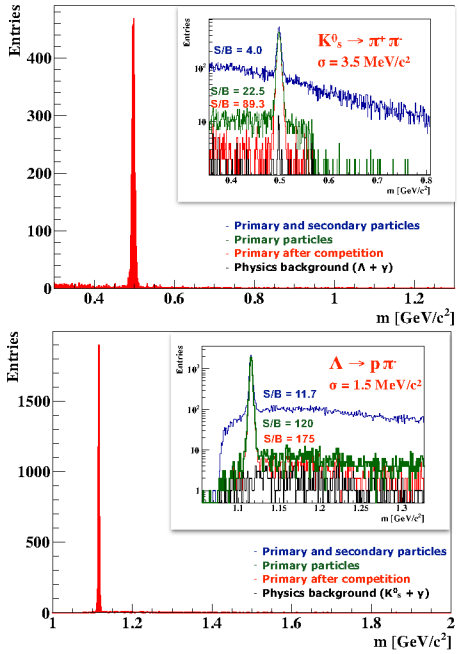

Figure 1: Full event topology reconstruction at an example of $K^0_s \to \pi^+\pi^-$ and $\Lambda \to p\pi^-$ decays reconstruction in 10k mbias UrQMD AuAu events at 10 AGeV with ToF PID

Only primary particles, which are produced directly in the collision, should be selected for physics analysis, since secondary particles produced as a result of a decay or interaction with the material of the detector do not carry information of the collision. The obtained spectra of the primary candidates are shown with a green line. We would like to notice, that the signal to background (S/B) ratio improved by about one order at this step, because the most of the background is due to the random combinatorial intersections of charged particles, that do not point to the primary vertex.

Candidates constructed with the incorrect mass hypothesis of the charged daughters but corresponding to the real primary particles (K^0_s, γ) cannot be rejected at this step. Since the mass of the daughters is assigned incorrectly, such candidates do not form a peak, but a broad structure at the mass spectrum (see Fig. 1, green line). However, candidate from the same daughter particles but with the correct mass hypothesis should be constructed, and it will contribute to the signal peak at the corresponding spectrum. Thus, from the particle candidates with the same set of daughters but different mass hypothesis only one can be selected. Currently, if at least one candidate lies within 3σ from the corresponding mass peak, the distances to the peaks normalised to the peak width are calculated for all candidates, and only the closest candidate is stored. As a result, background formed by the real short-lived particles can be suppressed, that additionally increases the S/B ratio (see Fig. 1, red line). The residual physics background is formed by γ and candidates with the incorrect mass hypothesis that are accidentally closer to the incorrect peak, it is shown with the black line in Fig. 1.

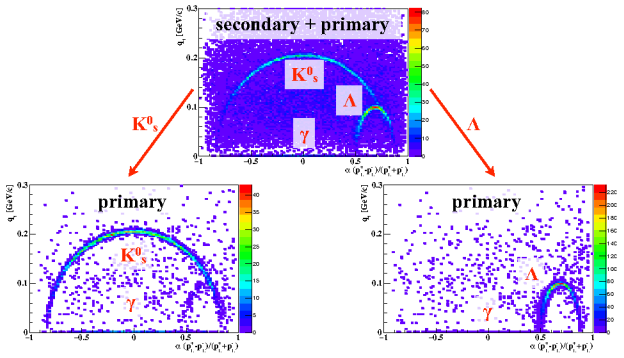

Figure 2: Illustration of the full event topology reconstruction with the Armenteros-Podolanski plots.

The procedure is illustrated by the Armenteros-Podolanski plots in Fig. 2. It is clearly seen, that initial spectra can be significantly cleaned up by the topology reconstruction.

Providing clean particle samples, full event topology reconstruction is a powerful tool for the physics analysis.

* Work supported by HICforFAIR, FIAS and BMBF.

† m.zyzak@gsi.de

Reconstruction of resonances with KF Particle Finder *

M. Zyzak[†1], *I. Kisel*[1,2,3], *and I. Vassiliev*[1]

[1]GSI, Darmstadt, Germany; [2]Goethe-Universitaet Frankfurt, Frankfurt am Main, Germany; [3]Frankfurt Institute for Advanced Studies, Frankfurt am Main, Germany

The main task of the CBM experiment is investigation of hot and dense matter created in the collision of heavy ions. One of the possible observables for such study are resonances. Comparison of the line shape of resonances together with their yields in pp and AA collisions are of the physics interest of CBM.

Resonances decay in the vicinity of the collision point. The main part of particles created in a heavy ion collision are originated there as well. Thus, fake particle-candidates produced as a result of random combination of primary tracks can not be separated from the real particles, for instance, by the decay topology. Thus, such random combinations create a huge background for resonances.

One of the possible ways to describe the background shape is fitting the spectrum with a smooth function, that is widely used to study, for example, ρ, K^*, ϕ, and Λ^* resonances [1]. Other methods, like mixed-event and like-signed techniques, will be studied further. We would like to notice, that the function should not have a peak-like structures not to distort the physics signal. In our studies we found an empirical function that satisfies our requirements:

$$f(x) = Ae^{(a_1x^2+b_1x)}(B - e^{(a_2x^2+b_2x)})^p, \qquad (1)$$

which reasonably describes the shape of the background. Here the first exponential term stands for description of the decreasing right part of the spectrum, the second term — for the left edge. Since the rice of the left edge and fall of the right edge are faster than exponential, the second order polynomials are used in the power of the exponents. The Function 1 is empirical and can be further improved.

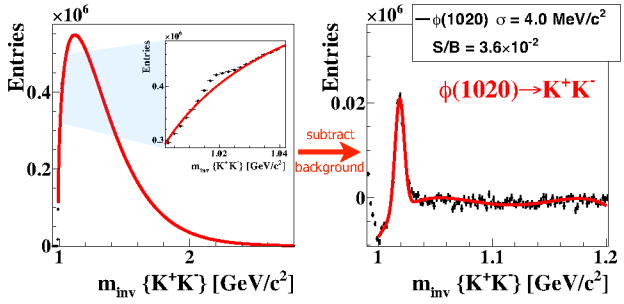

Figure 1: Illustration of the background fit procedure on the example of the ϕ meson spectrum reconstructed in 5M central AuAu UrQMD events at 10 AGeV with ToF PID.

The procedure for extraction of the resonance signal is illustrated on the example of $\phi \to K^+K^-$ spectrum obtained for 5M central AuAu UrQMD events in Fig. 1. At first, the spectrum is fitted with the Function 1. Then the background function is extracted from the total spectrum and the residual spectrum is fitted with a sum of Gauss and polynomial functions. The signal to background ratio is calculated in the region of $\pm 2\sigma$ of the Gauss fit tacking into account the total background.

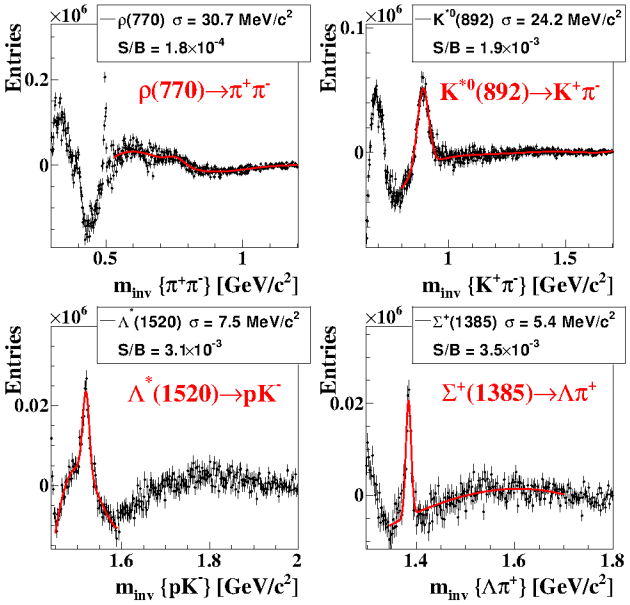

Figure 2: Spectra of resonances with the fitted background subtracted and a signal peak with a residual background shown.

The same procedure can be applied for background fit of other resonances. In Fig. 2 spectra of light vector mesons are shown at the example of $\rho(770) \to \pi^+\pi^-$, excited states of strange mesons — at the example of $K^0(892) \to K^+\pi^-$, excited states of hyperons — at the example of $\Lambda(1520) \to pK^-$ and $\Sigma^+(1385) \to \Lambda\pi^+$.

Summarising, the particles with a very low signal to background ratios down to 10^{-4} can be analysed even in central AuAu events in CBM.

References

[1] M. Aguilar-Benitez *et al.*, "Inclusive particle production in 400 GeV/c pp-interactions," Z. Phys. C — Particles and Fields 50, 405 426 (1991)

* Work supported by HICforFAIR, FIAS and BMBF.

† m.zyzak@gsi.de

DOI:10.15120/GR-2017-1

Σ^+ and Σ^- reconstruction by the missing mass method*

I. Kisel[1,2,3], *P. Kisel*[† 1,2,4], *P. Senger*[1], *I. Vassiliev*[1], *and M. Zyzak*[1]

[1]GSI, Darmstadt, Germany; [2]Goethe-Universität Frankfurt, Frankfurt am Main, Germany; [3]Frankfurt Institute for Advanced Studies, Frankfurt am Main, Germany; [4]Joint Institute for Nuclear Research, Dubna, Russian Federation

Properties of the quark-gluon plasma (QGP) can be studied using the idea of strangeness enhancement, since strange quarks are not brought into the reaction by the colliding nuclei. Any strange quarks or antiquarks observed in experiments are produced in the collision of heavy ions. Therefore, the abundance of strange quarks is sensitive to the conditions and dynamics of the deconfined matter phase, and strangeness enhancement can be indicating that deconfinement conditions were reached. Being abundant particles, Σ^+ and Σ^- carry out large fraction of produced strange quarks. Reconstruction of Σ together with other strange particles completes the picture of strangeness production and allows to compare yields of Σ and Σ^*. Reconstruction of Σ-particles will open a possibility to investigate H-dybarion objects, if such exist, by the decay channel $\Sigma^- p$, which is expected to be the dominant one.

All strange mesons and hyperons, except Σ-particles, can be either registered directly by the tracking system and identified by the PID detectors or have decay modes with all charged particles and, as a result, can be reconstructed through their daughters. Σ^+ and Σ^- have all decay modes with at least one neutral daughter, which can not be registered by the CBM detector at all (decay modes with n or ν) or can be registered with an efficiency on the 10^{-7} level (decay modes with π^0).

Having a lifetime sufficient to be registered by the tracking system ($c\tau_{\Sigma^+} = 2.4$ cm and $c\tau_{\Sigma^-} = 4.4$ cm), these particles can not be identified by the PID detectors. The missing mass method can be applied for their identification. Let us consider it at an example of $\Sigma^- \to n\pi^-$. Tracks of the mother (Σ^-) and the charged daughter (π^-) particles are reconstructed in the tracking system; the neutral daughter particle (n) is reconstructed from these tracks; a mass constraint is set on the reconstructed neutral daughter, that modifies also its momentum; the mother particle is constructed out of the charged and reconstructed neutral daughter particles and the mass spectrum is obtained, by which the particle can be identified.

Investigation of the Σ decays has shown that a large fraction of the background comes from misinterpretation of the tracks, which were reconstructed in two parts (clones). The problem is illustrated in Fig. 1 at an example of π^0 reconstruction from the $\Sigma^+ \to p\pi^0$ decay. Since the reconstructed momentum of both parts is the same, the resulting values of rapidity and momentum for π^0-candidate are close to zero and are nicely separated from the signal

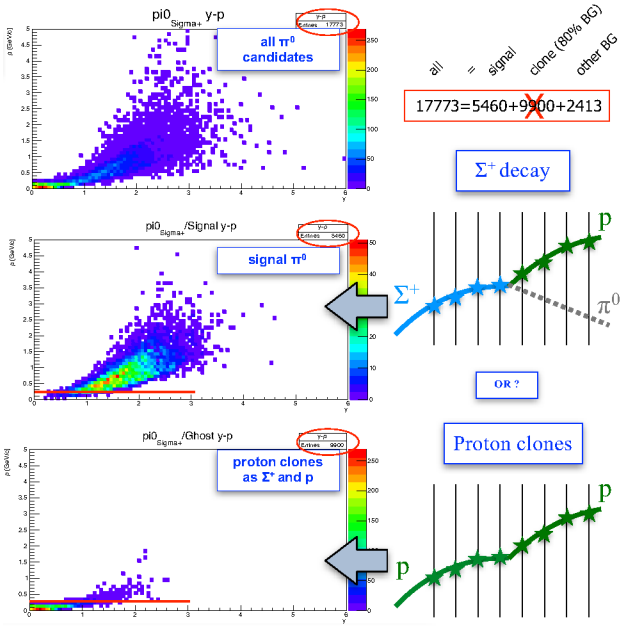

Figure 1: Momentum-rapidity distribution of reconstructed π^0 candidate in $\Sigma^+ \to p\pi^0$ decay.

region. Thus, such fake candidates can be strongly suppressed by cutting on the low momentum of the neutral candidate.

The topology of decays alows to require the decay point to be positioned after the last hit of a mother track and before the first hit of a daughter track. A cut on z-position of the reconstructed decay point reduces a significant part of the combinatorial background.

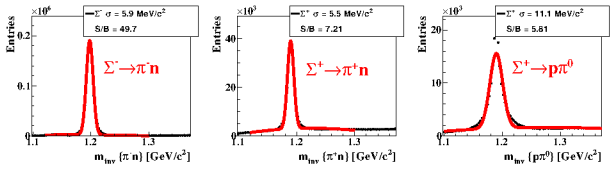

Figure 2: Mass distributions of reconstructed $\Sigma^- \to n\pi^-$, $\Sigma^+ \to n\pi^+$ and $\Sigma^+ \to p\pi^0$.

These cuts have been added to the KF Particle Finder package. Corresponding mass distributions of Σ decays with TOF PID are shown in Fig. 2. As a result of the study the signal to background ratios have been significantly improved, keeping the efficiencies at the same level.

* Work supported by BMBF, HICforFAIR and HGS-HIRe for FAIR.

† P.Kisel@gsi.de

Development of a CO_2 - based cooling demonstrator for the CBM STS

K. Agarwal, E. Lavrik, and H. R. Schmidt
Universität Tübingen, Tübingen, Germany

As the core detector of the CBM experiment, the Silicon Tracking System (STS) located in the dipole magnet provides track reconstruction and momentum determination of charged particles from beam-target interactions. Due to the expected irradiation damage, the sensors will dissipate some power and have to be kept at or below -5°C by complete removal of the heat dissipated by the front-end electronics (FEE) boards (total power load $\sim$ 40 kW). The heat must be removed to avoid thermal runaway and reverse annealing of the irradiated silicon sensors. Therefore, the STS will be operated in a thermal insulation box and will use bi-phase CO_2 cooling system for the FEE to maintain the desired environment for optimal detector operation at all times [1]. The effort presented in this report is aimed towards building a cooling demonstrator for two STS half-stations to show that the CBM-STS cooling concept is viable.

This work is an extension of the previous R&D conducted on bi-phase CO_2-cooling for CBM-STS aimed at FEE box design optimization where up to 200 W/FEE box heat was removed by keeping it at -15 °C for -40 °C coolant temperature [2]. Additionally, a 1 kW bi-phase CO_2 test cooling system, TRACI-XL [3] will be used for completing the demonstrator.

Thermal Interface Material (TIM) Studies

The CO_2 cooling system for the FEE primarily removes heat via conduction from FEE boxes mounted tightly on to the cooling plate. Since the mating surfaces are not absolutely flat and have micro-level imperfections, there is a presence of air-filled gaps with very low thermal conductivity (0.026 W/m·K at room temperature) acting as a thermal barrier. Hence temperature measurements are conducted by using different thermal-interface materials to replace all the space that otherwise would be occupied by air. Since heat transfer measurements are relative in nature, water will be used as the coolant for initial studies as it is easier to handle and has simpler experimental setup than CO_2 cooling. Later these results will be verified by using bi-phase CO_2.

Finite Element Method (FEM) Simulations

In order to understand the process, a series of FEM studies was performed using Solidworks Flow Simulations by keeping the component geometries as realistic as possible. The water inlet temperature was kept at 15 °C with a mass flow rate of 40 l/hr. Ceramic surface resistors are used as heat producing FEE components (2 W/resistor; 160 W/FEE box) glued on Aluminium Nitride (AlN180) plates attached to the FEE box fins. Table 1 describes all the TIMs that were used to fabricate the FEE boxes previously and the same are used for simulations for consistency. The annotations used are:

Interface 1: FEE Box - Cooling Plate
Interface 2: FEE Box Fin - AlN Plate
Interface 3: Resistor - AlN Plate
k: Thermal Conductivity of TIM
d: Thickness of TIM
RΘ: Distributed Thermal Resistance

Interface	TIM	k W/m·K	d μm	RΘ m^2·K/W
1 & 2	KP97	5.0	30	6.0×10^{-6}
	QGF-G03	16.0	125	7.8×10^{-6}
3	WLK 10	0.836	30	3.6×10^{-5}
	Arctic Silver	7.5	30	4.0×10^{-6}
	WLK DK 10	1.0	30	3.0×10^{-5}

Table 1: TIM Properties used for FEM Simulations.

Please note that the layer thickness of glue and grease is variable in reality, but it is taken as 30 μm for simulation purpose only which is consistent with the results presented in [2]. Additionally, since the specific heat capacity of none of the Interface 3 materials is available, it has been taken as 1000 J/kg·K which is of the same order as rest of the TIMs. Also note that QGF-G03 exhibits biaxial thermal conductivity with in-plane k = 470W/m·K and its effect is a subject of further simulations.

Interface 1	Interface 2	Interface 3	Max. Setup Temp ^{0}C
KP97	KP97	WLK 10	52.74
		Arctic Silver	52.16
		WLK DK 10	52.56
	QGF-G03	WLK 10	51.99
		Arctic Silver	51.33
		WLK DK 10	51.86
QGF-G03	KP97	WLK 10	52.80
		Arctic Silver	52.16
		WLK DK 10	52.70
	QGF-G03	WLK 10	52.14
		Arctic Silver	51.52
		WLK DK 10	52.03

Table 2: FEM simulation results.

Table 2 presents the simulation results for different interface combinations already fabricated. It shows that KP97,

DOI:10.15120/GR-2017-1

QGF-G03 and Arctic Silver as Interface 1, 2 and 3 respectively cools the FEE box to the lowest temperatures. It is evident, however, that the differences between the various interface materials are relatively small.

Experimental Readout Development

The experimental setup shown in Fig. 1 is adopted from the setup in [2]. PT100 temperature sensors will be installed on the cooling plate, on the aluminum fins of the FEE box and on the heat producing resistors to monitor the heat transfer, hence indicating the setup performance. Since the temperature sensors give an absolute value at a particular location rather than giving a temperature gradient, an overhead IR Camera has been installed to obtain a complete picture, thus verifying the results from the sensors. Since it is difficult to remove all the reflections in the camera's field of view, differential measurements of two images at different setup conditions is a proposed solution to analyze temperature change across the whole setup.

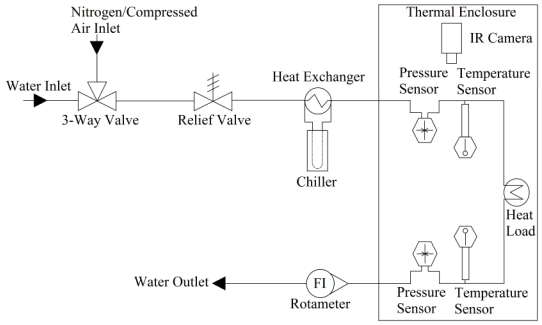

Figure 1: Experimental setup for TIM studies.

STS Thermal Insulation Box Development

The requirements for the STS thermal enclosure are:

- Large volume of ∼4m ^{3} with highly thermal insulating walls (maximum thickness 20 mm).
- Mechanically stable to hold the STS weight (maximum allowed deformation of 100 μm for ∼2 t).
- Electrical and light shielding.
- Feedthroughs for cables and pipes such that the vapor barrier is maintained (∼0.5% RH at room temperature to avoid condensation).
- Easy to assemble and disassemble for detector maintainence tasks.

As the first step, a smaller insulation box (0.75 × 0.50 × 1.50 m^3) will be fabricated from *Carbon Faserverstärkter Kunststoff* (CFK) sandwiches. Rohacell-51 (Polymethacrylimide) has been chosen as the foam because of its superior mechanical properties (compressive strength = 0.9 N/mm^2) and low thermal conductivity (0.036 W/m.K). Given the space constraints, calculations for thickness optimization were done keeping in mind that the outer wall temperature must be higher than the dew point of the surrounding environment. The following calculations have been done by taking [4] as a reference.

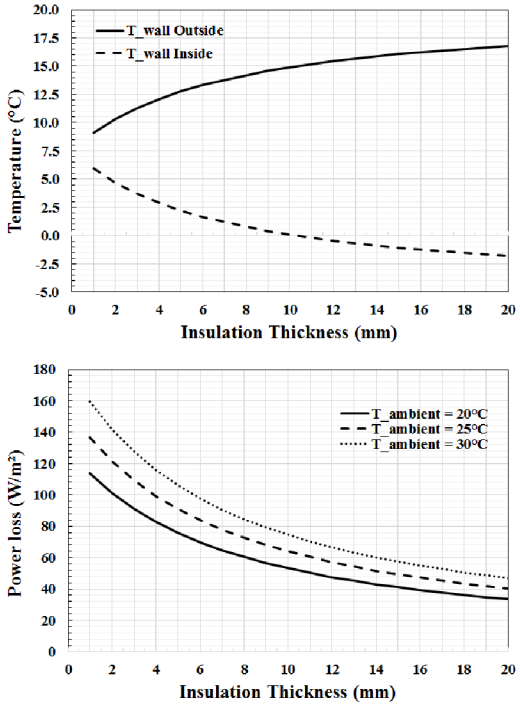

Figure 2: Insulation thickness optimisation

For the upper panel in Fig. 2, T$_{ambient}$ = 20 °C and RH = 50% which corresponds to T$_{dewpoint}$ = 9.27 °C. So 16 mm insulation thickness is safe as the temperature of outside wall is 16 °C which is fairly above the dew point.

The lower panel in Fig. 2 tells the additional power that has to be removed because of heat transfer from the outside environment to the box. The temperature inside the box has been taken as -5 °C and the power transferred per unit area has been studied for different ambient temperatures. At 16 mm insulation thickness, 40 W/m^2 of power has to be removed for T$_{ambient}$ = 20 °C, which increases to 47 W/m^2 for T$_{ambient}$ = 25 °C and 55 W/m^2 for T$_{ambient}$ = 30 °C. So the ambient temperature should also be considered with the heat dissipated from the sensors and FEE for determining the cooling efficiency of the setup.

Eventually 16 mm Rohacell-51 sheets are sandwiched from all sides with CFK of 2 mm thickness for adding mechanical strength.

References

[1] J. Heuser *et al.*, Technical Design Report for the CBM Silicon Tracking System, GSI Report 2013-4

[2] E. Lavrik *et al.*, CBM Progress Report, 2014 (2015) 52

[3] J. Sanchez *et al.*, CBM Progress Report, 2012 (2013) 21

[4] F. Lehner *et al.*, LHCb Silicon Tracker 2002-066

Pre-series production of ultra-light microcables for STS detector modules at LTU Ltd

V. M. Borshchov[1], *C. J. Schmidt*[2], *Yu. A. Murin*[3], *M. A. Protsenko*[1], *I. T. Tymchuk*[1], *R. A. Kushniruk*[1], *M. S. Tykhomirova*[1], *C. Simons*[2], *K. M. Liholitova*[1], *L. V. Klimova*[1], *and J. M. Heuser*[2]

[1]LED Technologies of Ukraine (LTU) Ltd, Kharkov, Ukraine; [2]GSI, Darmstadt, Germany; [3]JINR, Dubna, Russia

More than 1000 microcables for CBM-STS detector modules and demonstrators have been developed, manufactured and delivered to date. They are being used for verification of the work flow and tooling for STS detector module assembly and for investigations of possible read-out schemes at GSI and JINR. The work was carried out partly within the STCU project P635 by the partners GSI and LTU, partly within the contracts between LTU and GSI and also JINR.

Ultra-light microcables for STS detector modules

Ultra-light micro-cables are a key component for the CBM-STS. They are employed to realize the analog signal interconnection between silicon sensors and readout electronics, providing minimized material budget. Few different microcable types are foreseen to be used for STS detector modules [1]. They are composed of a stack of analog signal cables, meshed spacers and shield layers. The required total amount of microcables and meshed spacers for the STS is more than 75 thousands. Basically, the ultra-light analog cables are realized using aluminium-polyimide adhesiveless dielectric with 14 μm thick aluminum, and include 64 signal lines. The length of the cables ranges from about 100 mm up to about 500 mm. Within the performed works we have developed, manufactured and delivered pre-series batches of microcables for two purposes:

- pre-series microcables – for verification of work flows and tooling for STS detector module and ladder assembly;
- test microcables – for investigations of possible read-out schemes.

Pre-series microcables

Taking into account the different designs of the detector modules, the different lengths of the microcables involved, and further complications due to ladder assembly we have developed, manufactured and delivered 27 batches of microcables (about 900 pcs) for the verification of work flows and tooling used during STS detector module and ladder assembly. Batches of microcables were realized in the whole range of cable lengths from 100 mm up to 500 mm. A photo of a typical analog microcable is depicted in Fig. 1.

Also a new type of microcable has been developed, manufactured and delivered in several batches. It is intended

Figure 1: Analog connecting cable with meshed spacer.

for shielding of STS-XYTER ASICs which are covered by analog microcables.

The delivered cables allow to gain practical experience with module and ladder assembly and to apply further modifications to their design if required. The manufactured and delivered microcables allow to identify the production yield and define ways for increasing the yield at forthcoming pre-production and production stages. This includes studies of the reproducibility of the lithographic process, also involving new high-resolution masks, from where specifications towards the final production could be deduced.

Test microcables

For investigations of different possible read-out schemes (Fig. 2) we have developed, manufactured and delivered batches of microcables for demonstrators, as well as several assembled demonstrators with different length of cables and different types of microstrip sensors. The total amount of delivered and tested microcables, like the one shown in Fig. 3, is about 100 pcs.

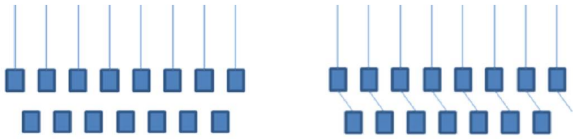

Figure 2: Read-out schemes: Every second strip (left) and two neighboring strips in parallel (right).

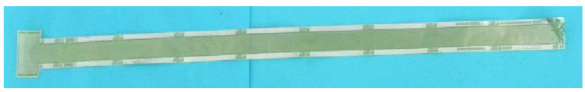

Figure 3: Test microcable for investigations of different readout schemes.

References

[1] V. M. Borshchov et al., CBM Progress Report 2015, p. 36

DOI:10.15120/GR-2017-1

Misalignment effects on track reconstruction for CBM-STS

S. Das and H. R. Schmidt
Universität Tübingen, Tübingen, Germany

The alignment uncertainties of the CBM-STS detector, made from silicon strip sensors with excellent position resolution, affect the performance of the track reconstruction. The basic sources of these uncertainties are the limited mechanical mounting precision ($\sim$ 100 μm) during the assembly of the detector, deformations of the detector elements due to temperature effects, and (or) influence of the magnetic field; so, during the experiment, we cannot rely on the mechanical mounting or the detector geometry alone to yield the required spatial resolution of the STS. Therefore, our approach is to use track based alignment methods (relying on tracks only) to determine the exact positions of the silicon sensors ($\sim$ 10 μm). In this report, we will address the effects of misalignment on the track reconstruction along with the discussion of the possibility to recover the alignment.

Misalignment Scenarios

For this report three misalignment scenarios have been introduced in the STS geometry on hierarchial basis (i.e., to the sensors, ladders, and then to the stations). A Virtual technique has been used for misalignment, i.e., according to the misalignment scenarios, the transformations have been applied on the STS hits at the time of track reconstruction without modifying the ideal geometry (Scenario_0). We have used the STS geometry (version 15b) to apply the misalignment scenarios. But in future the same implementation can be done easily on the updated geometry. The applied misalignment scenarios are detailed in the following table.

Element	Sensor	Ladder	Station
X	10 μm	50 μm	200 μm
Y	10 μm	50 μm	200 μm
α	50 μrad	250 μrad	1000 μrad
β	50 μrad	250 μrad	1000 μrad
γ	50 μrad	250 μrad	1000 μrad

Table 1: Summary of applied misalignment.

All the data (standard deviation to the distribution) have been diced using Gaussian distribution to make the transformations random. All the transformations (translations and rotations) have been applied to the detector elements as per the above data table.

- On the first scenario (Scenario_1), transformed data have been applied at the local sensor level to the ideal geometry (Scenario_0).
- On the second scenario (Scenario_2), in addition to the sensor level modifications, transformed data have been applied to the local ladder level.
- On the third scenario (Scenario_3), in addition to the last two scenarios, transformed data have been applied to the local station level.
- Important assumption: The Z-value has been kept constant throughout, as the projection has always been taken to the X-Y plane.

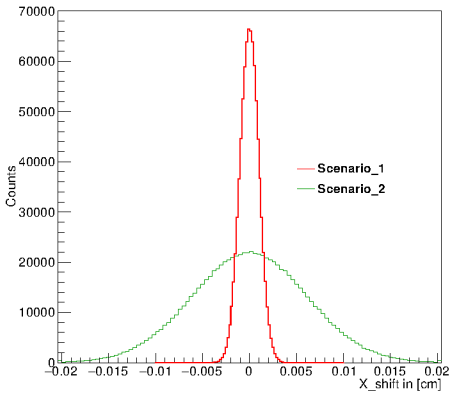

Figure 1: Resulting misalignment shifts on STS hits in X direction (example) for Scenario_1 and Scenario_2.

Effect of misalignment on track reconstruction

The investigation of the effect of the misalignment of the STS on primary track properties is performed using 200 UqQMD events under SIS100 energy. The track reconstruction is performed in several steps: Track seeding from the STS hits, trajectory building using combinatorial Cellular Automaton, track fitting and smoothing using Kalman Filter. The error on the hit position in the track fit is obtained by combining the spatial resolution of the detector with the applied misalignment uncertainty. The effect of the STS misalignment results in deterioration of the momentum resolution (Fig. 2).

Standard rules for matching a reconstructed track with the MC track have been performed. The effect of misalignment can also be seen for the primary track efficiency (quality of matching reconstructed tracks with MC tracks) plotted against momentum (Fig. 3).

DOI:10.15120/GR-2017-1

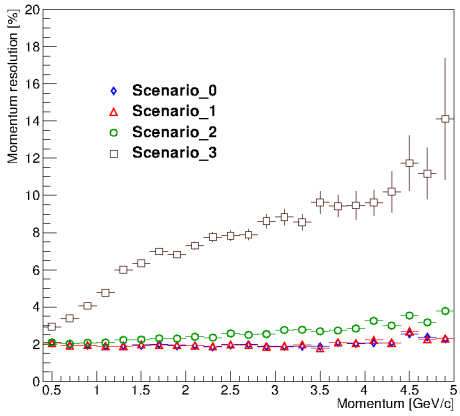

Figure 2: Momentum resolution for UrQMD events.

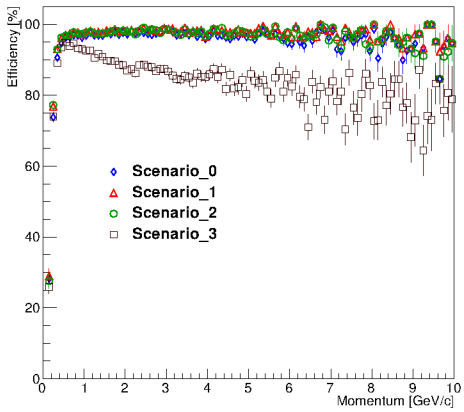

Figure 3: Primary track efficiency for UrQMD events.

Comparisions of track fit quality in terms of χ^2/NDF have also been plotted for ideal and misaligned cases for UrQMD events (Fig. 4). A clear deterioration of track fit quality can be seen with higher level misalignment.

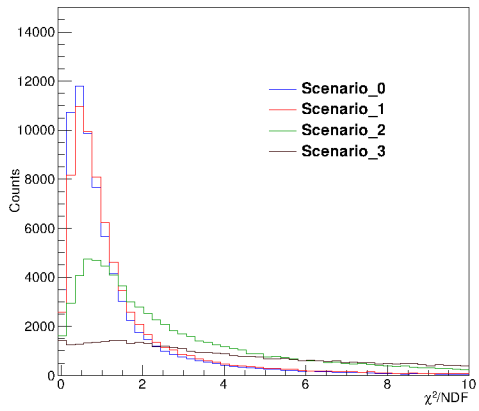

Figure 4: Track fit quality for UrQMD events.

Effect of misalignment on invariant mass

Figure 5 depicts the impact of misalignment on reconstructed invariant mass of the particle, based on decay topology (from the reconstructed secondary vertex).

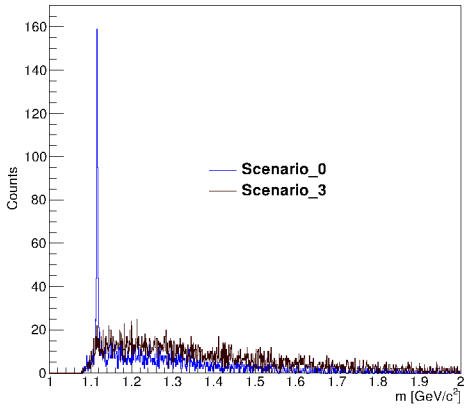

Figure 5: Invarint mass of Lambda (example) reconstructed from for UrQMD events.

Conclusion

This study has been the first attempt to misalign the STS components in order to check the effects on tracking and the physics observables. The obtained results are clearly indicating the direct influence on track and vertex reconstruction and emphasize the necessity of precise alignment of STS detector to achieve high spatial resolution. As a next step, the MILLEPEDE software package will be used to recover the alignment from the applied misalignment scenarios by computation. This will allow us to determine the limits of the required mechanical precision, during the assembly, as well as the overall precision required of the whole mechanical setup, to apply MILLEPEDE successfully [1, 2, 3, 4, 5].

References

[1] V. Blobel and C. Kleinwort, A New Method for the High-Precision Alignment of Track Detectors (2002), arXiv:hep-ex/0208021

[2] V. Blobel, Millepede II. Institut für Experimentalpyhsik, Universität Hamburg (2007), http://www.desy.de/ blobel/mptalks.html

[3] R. Frühwirth, Nucl. Instr. and Meth. A 262 (1987) 444

[4] Impact of CMS silicon tracker misalignment on track and vertex reconstruction, Nucl. Instr. and Meth. A 566 (2006) 45–49

[5] http://aliceinfo.cern.ch/Offline/Activities/Alignment.html

DOI:10.15120/GR-2017-1

Construction of a neutron source for radiation hardness tests of silicon strip detectors

E. Friske and H. R. Schmidt
Universität Tübingen, Tübingen, Germany

Radiation tolerance requirements

The microstrip detectors to be used in the Silicon Tracking System (STS) of CBM are expected to experience a non-ionizing radiation dose of up to 10^{14} n_{eq}/cm^2 [1] over the projected lifetime of $\approx$ 6 years, mainly causing lattice defects in the detector material. The detectors are read out as self triggering sensors, which sets high demands on their performance, particularly on the charge collection efficiency. Since this figure of merit will decrease over the course of the irradiation, subsequent properties like the signal-to-noise ratio will also be affected. To anticipate these changes and to give a realistic lifetime estimation of the sensors several irratiation campaigns have been, and are being, performed [2].

Long term irradiation

Non-ionizing radiation damage is caused by high energy particles expelling atoms from their lattice spaces, creating both lattice vacancies and interstitial atoms, which act as additional dopants and scattering centers, thus changing the electrical properties of the bulk material. Since neutrons are not charged and interact mostly with the nucleus by collisions they are a prime tool to study this phenomenon separately.
In addition to the actual damage, there are both annealing and reverse annealing effects present. These contribute on a timescale of days and depend on temperature, so an ideal simulation should recreate these conditions as closely as possible and reasonable.

Neutron source

As described in the preceding Progress Report [3], a Van-de-Graaf ion accelarator is used to generate a deuteron beam which is targeted at a deuterium gas cell. The neutrons generated from this deuterion fusion are used to irradiate the sensor material as sketched out in Fig. 1. The cell itself is shown in Fig. 2.

Since the accelerator used is limited in beam energy (2.4 MeV deuteron energy is the maximum we have been able to achieve) and beam current (a few μA), the setup needs to be as efficiently as possible in creating neutrons and irradiating the sensors. As the deuterium fusion cross section peaks at around 2 MeV and drops sharply toward lower energies, energy losses passing the gas cell entrance foil have to be minimized while maintaining a high gas density within the cell.

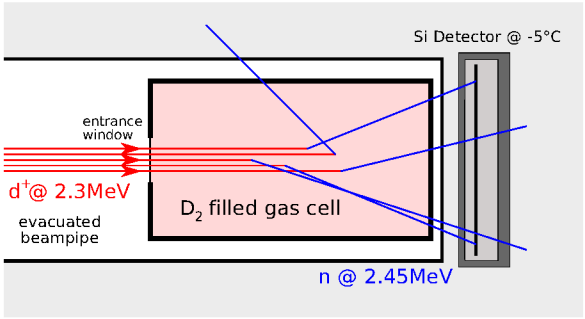

Figure 1: Schematic view of the cryogenic source.

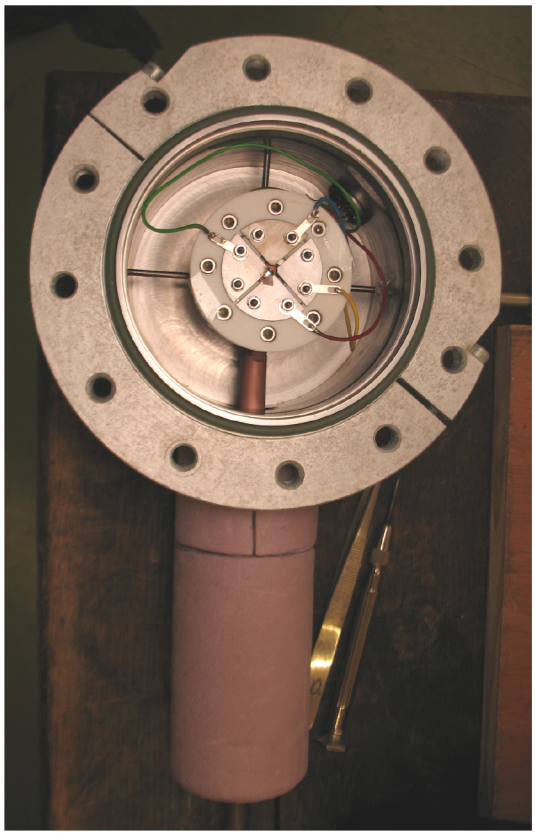

Figure 2: Photo of the manufactured cell with beam monitoring metal plates arranged around the titanium window.

Therefore, the entrance window has to be mechanically durable at a thickness of less than 5 μm, and consist of light elements to minimize scattering of the incident deuteron beam. Several materials were considered, including Havar®, aluminum, titanium and mica. TRIM simula-

DOI:10.15120/GR-2017-1

tions of the energy losses (Fig. 3) show that Havar, consisting mostly of heavier elements, has the strongest restrictions regarding material thickness, and has turned out to be unusable as a result. Aluminum alloy cannot be reasonably manufactured to the desired dimensions, and pure aluminum cannot withstand the 2-3 bars of pressure difference required. Tests with Mica were abandoned as it is a rather brittle material and very difficult to work with. In the end, a titanium foil with a thickness of 2.5 μm was successfully tested against a 3 μm beam while maintaining a pressure difference of 4 bar. Figure 2 shows the cell after a beamtime; one can see the burn traces from a badly aligned beam on the lower metal plate. The simulated average energy loss of this window for a 2.4 MeV beam is 0.14 MeV.

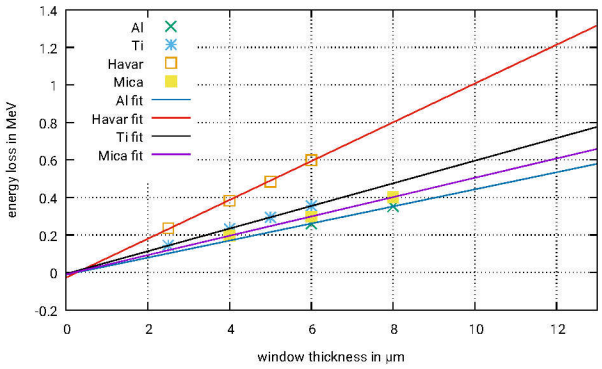

Figure 3: TRIM simulations showing the average energy losses of a 2.4 MeV deuteron beam.

Detector holder

To closely match the environment with the later in the experiment, in particular the operating temperature of -5 °C, a steel enclosure has been manufactured to house the sensor itself, the Alibava readout board and the trigger system. Although the Alibava system also provides self-triggering readout boards, an external trigger consisting of a plastic scintillator and a small photomultiplier tube has been chosen as the more reliable solution. Figure 4 shows the arrangement; the frame housing the actual sensor has been removed to allow a view onto the internal components.

Since the neutrons themselves do not generate signal in the silicon detector, a collimated beta source is currently being commissioned to provide both the signal in the detector and a trigger signal in the scintillator.

Next steps

The readout chains for the sensors, environment and enutron flux monitoring have to be established, tested and calibrated before the actual sensor irradiation can commence.

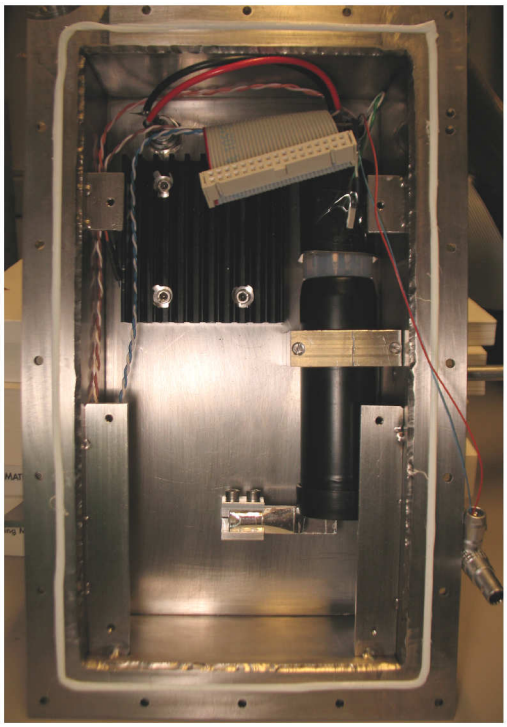

Figure 4: Photo of the sensor box with cooling fins, electrical feedthroughs and the photo multiplier tube with attached scintillator encased in reflective foil.

References

[1] I. Sorokin, Characterization of silicon microstrip sensors, front-end electronics, and prototype tracking detectors for the CBM experiment at FAIR, PhD thesis, Univ. Frankfurt, April 2014

[2] J. Heuser et al., Performance of neutron irradiated prototype sensors for the CBM Silicon Tracking System, CBM Progress Report 2013, p. 25

[3] E. Friske and H. R. Schmidt, A scalable neutron source for STS detector radiation hardness tests, CBM Progress Report 2015, p. 25

[4] W. von Witsch and J. G. Willaschek, High-pressure gas target for the production of intense fast-neutron beams, Nuclear Instruments and Methods Vol. 138 (1976) p. 13-17

DOI:10.15120/GR-2017-1

Optical quality assurance procedures for the STS detector

E. Lavrik[1], *I. Panasenko*[1,2], *and H. R. Schmidt*[1]
[1]Universität Tübingen, Tübingen, Germany; [2]KINR, Kiev, Ukraine

The CBM Silicon Tracking System (STS) is a compact detector built from about 900 double sided silicon microstrip sensors. The sensors will be delivered in 4 different form factors [1]. Current prototypes are from Hamamatsu, Japan, and CiS, Germany. In order to assure the quality of these sensors, highly efficient and automated optical quality assurance methods and procedures should be developed. For this purpose a metrology and quality assurance test station has been built at the University of Tübingen, which allows to measure various QA parameters for the sensors such as surface conditions (scratches, durst grains, photoresist residues, etc.) and geometry (wafer thickness and warp, edge (non-)parallelity and profile etc.) [2]. Having the sensor quality assured at a very early stage allows tp reject the faulty sensors as well as providing input data for further control stages such as electrical control.

The test station consists of an XY-inspection table with a replaceable vacuum chuck mount. Currently a custom-built three-zone chuck for sensor and a porous aluminum chuck for cable inspection are used. On the Z-stage a microscope camera and an optical assembly with motorized zoom and focus are mounted. The XY-stage allows to inspect sensors up to a size of 12.4 $\times$ 6.2 cm^2. A highly customizable software solution, which allows the adaptation to other hardware as well as other inspection objects like sensor micro-cables and detector modules, has been developed as a part of the project.

Sensor warp inspection

The methods for a non-destructable contactless way of sensor warp measurements based on focus adjustment developed in [3] were further improved and optimized. The accuracy of the method has been characterized by a calibration against a certified gauge block set from Mitutoyo Corp. (Fig. 1). The extracted height measurement accuracy is estimated to be 1 μm. Especially important was, given the fact of the upcoming mass inspection of sensors arriving from vendors, to reduce the measurement times without negatively impacting the measurement precision. With the development of new methods we were able to reduce the measurement times by a factor of up to 30.

Figure 2 shows the warp of both sides of a prototype CBM06C6 sensor. The warp of all available (25) prototype sensors has been measured; it ranges from 6 to 78 μm.

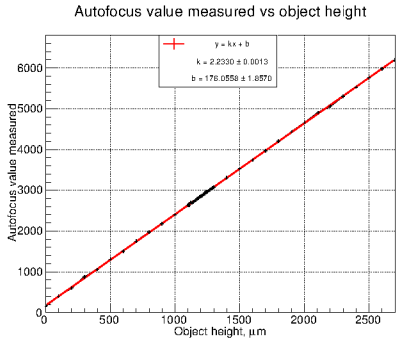

Figure 1: Fitted calibration curve for the height measurements.

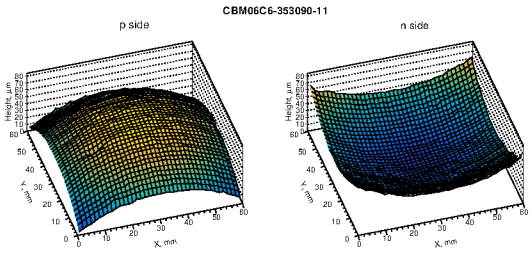

Figure 2: Warp of a prototype CBM06C6 sensor.

Edge parallelity inspection

The sensor's cutting edge profile inspections presented previously have been improved and extended with edge parallelity inspection. In this type of analysis, the distances between the sensor's features and the cutting edges are measured. The alignment marks being the outermost features on the sensor's surface are taken as reference. Figure 3 shows the measurement principle. First the center of the alignment mark (denoted with a red square on the figure) is located with pattern matching algorithms, then it is perpendicularly projected to both fitted edges of the sensor and the distances are measured. By comparing the distances measured at one corner with others, one extracts the information of the sensor's edge parallelity.

The distribution of the values extracted for the available sensors' edge parallelity is shown in the Fig. 4. The precision of the method is estimated to be better than 1 μm. This measurement shows that the sensor edge could be used for the sensor alignment during assembly yielding a precision better than 10 μm.

DOI:10.15120/GR-2017-1

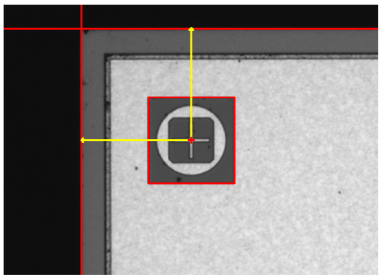

Figure 3: Detection principle for edge parallelity analysis.

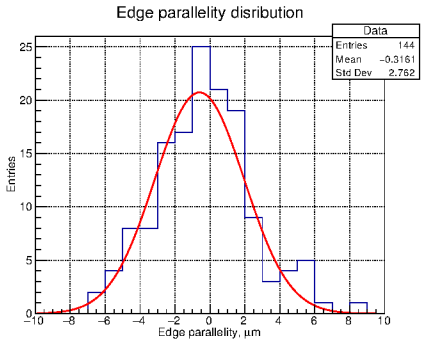

Figure 4: Edge parallelity distribution from the prototype sensors.

Micro-cable inspection

Figure 5 shows the schematics of the micro-cable stack as a part of the module, in which individual signal micro-cables are separated by meshed spacers and enclosed within an aluminum shield and polyimide coat. The optical inspection of micro-cables is only possible before their assembly into a stack, thus it should be best done at the production site.

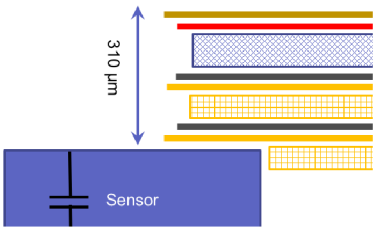

Figure 5: A schematic view of a micro-cable stack with signal cables in dark gray color.

We already reported on the micro-cable inspection R&D in [3]. These automated QA methods and procedures were developed for a certain type of illumination - ring light source. Since then, the setup was upgraded to use a direct light source, which has changed the approach to the cable inspection - aluminum traces reflect much more direct light, which "blinds" the camera. For this reason an alternative approach has been developed to perform two pass measurements with higher and lower camera sensors light exposure values. The first pass allows to detect the "silhouette"-type defects such as trace breaks, cut-offs, thinnings and lift-offs. The second pass allows to look at the aluminum surface defects such as foreign objects etc. This method change required the adaptation of the detection procedures and software algorithms.

Figure 6 shows the same region of interest under different exposure settings of the camera. What appears to be a trace break at low exposure (left panel) is identified as a dust grain at high exposure (right panel).

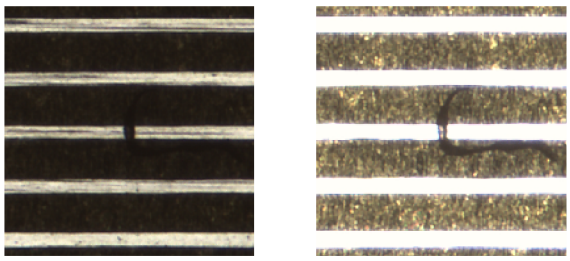

Figure 6: Images of the same region of interest taken with different exposure values allow to detect the defect.

A batch of 10 prototype micro-cables provided to GSI from LTU for tab-bonding tests were inspected. The defects listed in Table 1 had been successfully detected together with a small number of others (possibly introduced by handling or misidentification) in a fully automated scan mode.

Eventual reintroduction of the ring light source and replacement of the vacuum chuck with a back-lit pair of transparent glass sheets to clamp the cables between should further improve the performance of the inspection.

Cable number	Defects on the cable
40-2	1 break, 2 traces cut-off, 2 thinned traces
186-2	2 breaks, 2 traces cut-off, 1 thinned trace
163-3	1 break, 2 traces cut-off, 1 trace lift-off
181-1	Hole in Pi, deformation in the bond area
116-3	2 breaks, 1 trace cut-off, 1 trace lift-off
176-2	1 trace cut-off, 2 thinned traces
192-2	2 trace cut-off
194-2	1 thinned trace, deformation in bond area
168-1	5 traces cut-off
169-2	1 break, 3 traces lift-off

Table 1: Cable defects information from manual inspection enclosed in the package.

References

[1] Technical Design Report for the CBM Silicon Tracking System, GSI Report 2013-4, p. 23

[2] E. Lavrik et al., CBM Progress Report 2014, p.30

[3] E. Lavrik et al., CBM Progress Report 2015, p.23

DOI:10.15120/GR-2017-1

Microcable quality assurance: capacitance measurements

I. Panasenko[1,2], *H. R. Schmidt*[1], *E. Lavrik*[1], *C. Simons*[3], *and C. J. Schmidt*[3]
[1]Universität Tübingen, Tübingen, Germany; [2]KINR, Kiev, Ukraine; [3]GSI, Darmstadt, Germany

Ultra-light micro-cables are the key component for the CBM Silicon Tracking System. However, in addition to the total strip capacitance, microcables also contribute to the load capacitance seen by the FEE. Therefore it is important to know the total parasitic capacitance of the single trace (C_{tot}). For the module assembly a micro-cable stack which consists of 4 signal and 2 shield layers will be used. A schematic view of such a stack is depicted in Fig. 1. Here we report on the measurements of C_{tot} for an aluminum microcable stack # 2-11 (N-Top layer is 28.1 cm long, P-Top layer is 27.1 cm long) manufactured by LTU Ltd (Kharkov, Ukraine) [1].

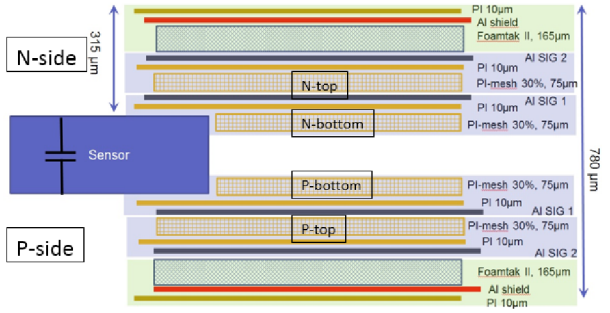

Figure 1: Schematic side view of the micro-cable stack for one CBM module.

Measurements were carried out on a custom, fully automated probe station developed at University Tübingen [2]. A 3-needle configuration was used to measure the capacitance of a single trace to two neighbors and a small extra fraction. The network simulator SPICE [3] was used to estimate the contribution of all other traces to the measured value in a 3-needle configuration and thus to derive C_{tot} of a single trace, and also to extract other capacitances (like trace-to-trace) which are impossible to measure directly. Because the microcable stack can be considered as an array of capacitors , without resistors, the measured capacitance does not depend on the frequency of the applied test signal.

Fig. 2 shows the results of measurements for all 64 traces of one layer of the microcable stack. Such measurements were performed for all 4 layers. Then the total trace capacitance was derived and the results are plotted in Fig. 3.
The capacitance measurements are summarized as follows:

$$C_{tot} = 0.382 \pm 0.020 \text{ pF/cm},$$
$$C_{TT} = 0.094 \pm 0.008 \text{ pF/cm},$$
$$C_{LL} = 0.083 \pm 0.010 \text{ pF/cm},$$
$$C_{TS} = 0.090 \pm 0.009 \text{ pF/cm},$$

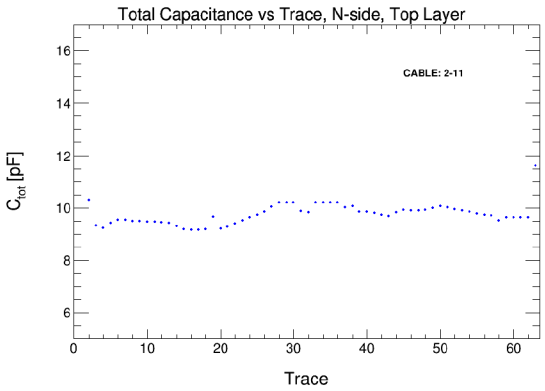

Figure 2: Measurements of C_{tot} for every trace of the 28,1 cm long microcable.

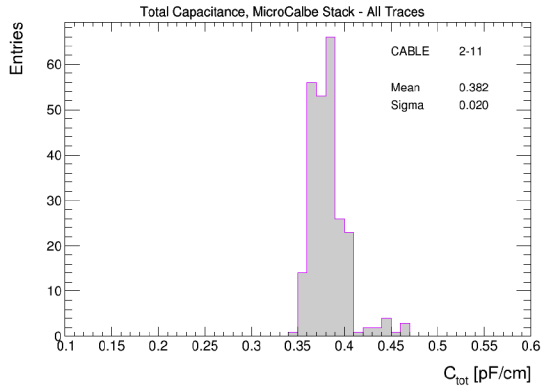

Figure 3: Measured total trace capacitance of the microcable stack.

where C_{TT} is the capacitance between two adjacent traces of a single layer, C_{LL} – the capacitance between two nearest traces of adjacent layers, C_{TS} – the capacitance between single trace and shield layer.

References

[1] V. M. Borshchov et al., Pre-series production of microcables for STS detector modules at LTU Ltd, CBM Progress Report 2015 (2015) 36

[2] I. Panasenko et al., Equipment and procedures for electrical quality assurance of CBM-STS silicon microstrip sensors, CBM Progress Report 2015 (2015) 25

[3] http://www.linear.com/designtools/software/#LTspice

DOI:10.15120/GR-2017-1

Sensor quality assurance: capacitance measurements

I. Panasenko[1,2], *H. R. Schmidt*[1], *E. Lavrik*[1], *and J. M. Heuser*[3]
[1]Universität Tübingen, Tübingen, Germany; [2]KINR, Kiev, Ukraine; [3]GSI, Darmstadt, Germany

We already reported [1] on the development of a custom-built automatic probe station for the microstrip sensors quality assurance (QA) of the CBM experiment. It was used to perform in-depth measurements of the capacitances which are important for the operation of double-sided microstrip sensors. Sensors of the CBM06 type from CiS [2] and Hamamatsu [3] were under investigation.

Experimental set-up

We have measured interstrip, coupling and backplane capacitances as a function of strip number, frequency and bias voltage using the experimental set-up and techniques described in [4]. In total 7 sensors were tested and 9 more sensors are currrently being measured.

Results

Backplane capacitance

The capacitance between a single implant strip and the backplane of the sensor can be obtained from CV measurements. Also, this measurement was used to determine full depletion voltage (V_{FD}). The results are summarized in the table below where H and C in the sensor type correspond to Hamamatsu and CiS, respectively.

Sensor ID	Type	V_{FD}, V	C_b, pF/cm
10938-1609-5	H04DM	70.2	0.18
10938-2695-2	H06SM	67.0	0.17
10938-4440-58	H06DM	74.3	0.18
10938-4440-60	H06DM	67.4	0.18
331827-3	C06SM	78.1	0.21
350714-06-1	C02DM	70.2	0.22
351139-23	C04DM	70.2	0.21

Coupling capacitance

The coupling capacitance C_c is the capacitance between the strip implant and the read-out aluminum strip. Measurements have shown that coupling capacitance has a strong frequency dependence. It can be explained considering the sensor as an extended network of capacitors and resistors [5, 6]. The network simulator SPICE [7] was used to reproduce and understand frequency dependence of the measured capacitance and to extract frequency independent values. The experimental and simulated results are plotted in Fig. 1.

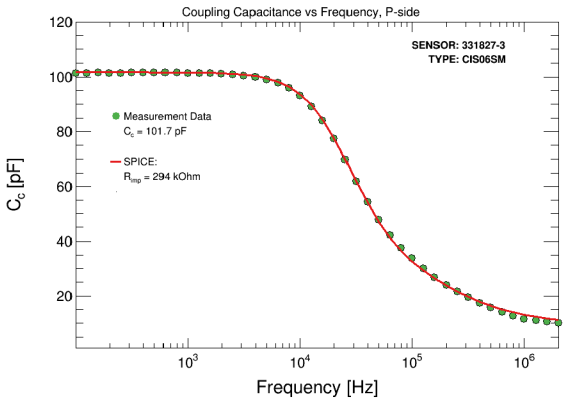

Figure 1: Coupling capacitance for p-side strips of a CiS 6x6 cm^2 sensor as function of frequency (measurements and SPICE simulation).

The strip implant resistance was also extracted from the simulation and is 92 kOhm/cm and 49 kOhm/cm for Hamamatsu and CiS sensors, respectively. A bias voltage scan of the coupling capacitance showed that it is practically independent of the biasing conditions for p-side strips and saturates after full depletion for n-side strips. The coupling capacitance was measured for all 1024 strips on each side of every sensor (14336 strips in total) and the experimental results are summarized in Fig. 2.

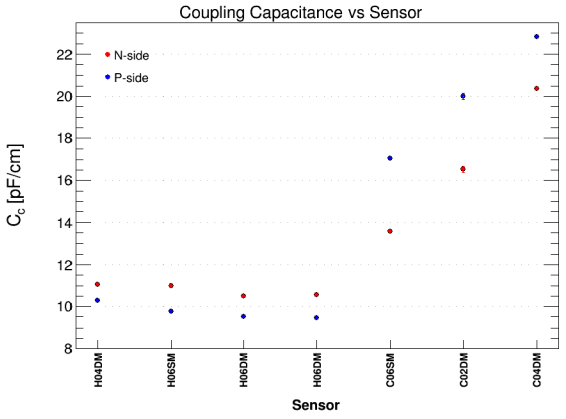

Figure 2: Experimental values of the coupling capacitance for all tested sensors.

DOI:10.15120/GR-2017-1

Interstrip capacitance

The interstrip capacitance C_{is} is the main contribution to the input capacitance of the FEE, therefore it determines the noise performance of the FEE. Figure 3 shows the experimental and simulated results for frequency dependence of the interstrip capacitance (between two adjacent strips including metal and implant contributions, the other strips are grounded).

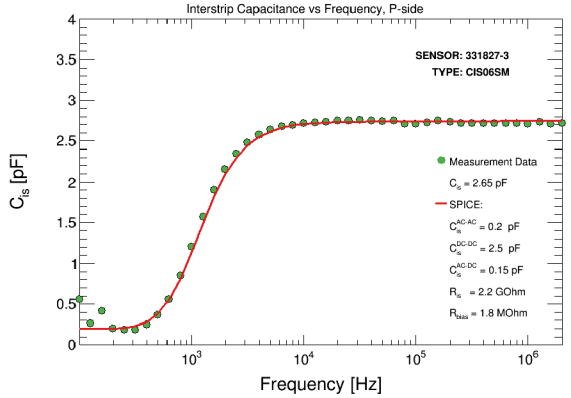

Figure 3: Interstrip capacitance for p-side strips of a CiS 6x6 cm^2 sensor as function of frequency (measurements and SPICE simulation).

The bias voltage scan of the interstrip capacitance showed that C_{is} becomes constant beyond full depletion for all tested sensors but an overdepletion of +40 V is suggested.

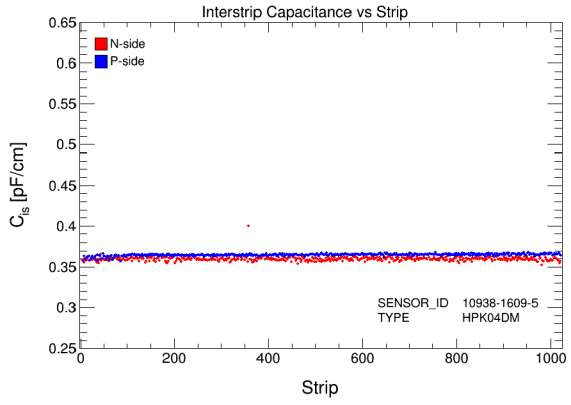

Figure 4: Automated strip scan: the interstrip capacitance for p- and n-sides of a Hamamatsu 6x4 cm^2 sensor.

An example of the interstrip capacitance measurements across the entire sensor is given in Fig. 4. The measured C_{is} for the tested Hamamatsu sensors is uniform over all strips, for CiS sensors small deviations were observed [6]. The average value of C_{is} is 0.36 pF/cm for Hamamatsu sensors and it is slightly higher for CiS sensors: 0.43 pF/cm and 0.57 pF/cm for p- and n-sides, respectively.

Total strip capacitance

The total strip capacitance C_{tot} is defined as the sum of the capacitance of the strip to the backplane and the interstrip capacitance to adjacent strips [4]:

$$C_{tot} = C_b + 2C_{is} + C_{rs}, \quad (1)$$

where C_{rs} is a contribution to interstrip capacitance due to remaining strips. C_{rs} was estimated experimentally and is about 10% of C_{is}. The total strip capacitance is dominated by the interstrip capacitance and the backplane capacitance contributes only 15–25% to the total one. Figure 5 show the total strip capacitance of p- and n-side strips for all tested sensors. The avarage value of C_{tot} for Hamamatsu sensors is 1 pF/cm for both sensor sides. We observed a higher C_{tot} for CiS sensors especially from n-side in comparison with Hamamatsu sensors. For both vendors total strip capacitance is significantly smaller than coupling capacitance which insures a good charge collection:

$$C_c/C_{tot} > 10. \quad (2)$$

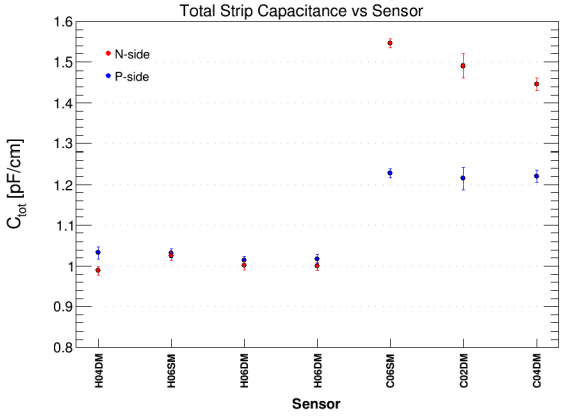

Figure 5: Total strip capacitance for all tested sensors.

References

[1] I. Panasenko et al., Equipment and procedures for electrical quality assurance of CBM-STS silicon microstrip sensors, CBM Progress Report 2015 (2015) 25

[2] http://www.cismst.org

[3] http://www.hamamatsu.com

[4] STS Note 2016-1, Specifications for Quality Assurance of Microstrip Sensors in the CBM Silicon Tracking System (2017) 22

[5] E. Barberis, Nucl. Instr. Meth. A342 90-95 (1994)

[6] I. Panasenko, Capacitance Measurements of Microstrip Sensors, Workshop on radiation induced surface effects in double-sided silicon microstrip sensors, Karlsruhe, 3 Nov. 2016

[7] http://www.linear.com/designtools/software/#LTspice

Ladder assembly concept and tool

U. Frankenfeld[1], *H. R. Schmidt*[2], *C. Simons*[1], *O. Vasylyev*[1], *and R. Visinka*[1]
[1]GSI, Darmstadt, Germany; [2]Universität Tübingen,Tübingen, Germany

Ladder assembly

The sensors of the Silicon Tracking System (STS) are mounted onto a carbon fibre structure (CF-ladder). Before the mounting, the sensors are assembled with read-out cables and the front-end electronic (module assembly [1, 2]). The task of the ladder assembly is to mount the modules with a sensor position precision better than 100 μm.

Concept and tool

The CF-ladder is mounted into a supporting fixture. In order to be able to reproduce the positioning the fixture has to be kept at a constant temperature in a controlled environment. In a first step the holding structure (L-leg [3]) is positioned with a tool (Fig. 1) and glued onto the CF-ladder.

The concept is based on positioning the sensor with a vacuum holder (Fig. 3). The position of the sensor is defined by the surface of the vacuum-holder and the two ledges (Fig. 2). This implies that corners of the sensors have to be cut precisely since the edges define the position of the sensor. The vacuum holder is positioned onto the jig with dowel pins.

A concept tool has been designed and produced to study the feasibility of the assembly procedure. The size of the tool has been chosen to mount two 6.2 $\times$ 6.2 cm^2 sensors on a CF-ladder. The surface of the sensor holder has been lapped to avoid scratches to the surface of the sensor. An alternative approach is the usages of a protecting layer (e.g. paper) between the sensor and the vacuum holder. The positioning tool for the L-legs is made from plastic in 3D-printing; for a final tool the precision can be enhanced.

Feasibility tests

Several gluing test of the L-legs have been performed to ensure the mechanical properties of the structure. The first ladder will be assembled with two non-functional sensors to measure the precision of the mounting. Finally a ladder with functional sensors will be assembled and tested to ensure that the handling and gluing of the sensors has no influence of the performance of the detector.

Further developments

Further developments will be the optimization of the shape of the L-leg to avoid glue spreading onto the edges of the sensor. After proving the concept of the ladder assembly a full-scale prototype tool will be designed and build to assemble a large ladder with ten modules. A transfer tools to take the ladder out of the mounting jig is under development. It will also be used to store the ladders before installing them into the STS. For the quality assurance and to measure the sensor positions after assembly an optical inspection system has to be established.

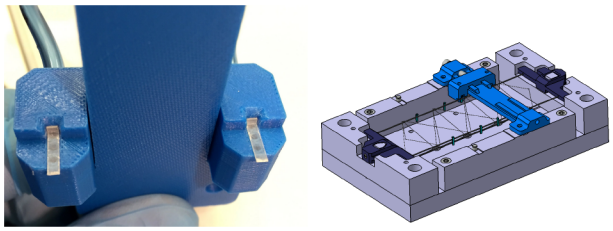

Figure 1: Positioning tool to holde two L-legs with vacuum (left). The mounting height of the L-leg is defined by the tool, in lateral direction they are moved onto the CF-ladder structure (right).

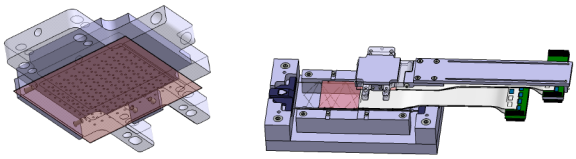

Figure 2: The vacuum tool to position the sensor; the position is defined by the ledges and dowel pins (left). A module is positioned onto the ladder (right).

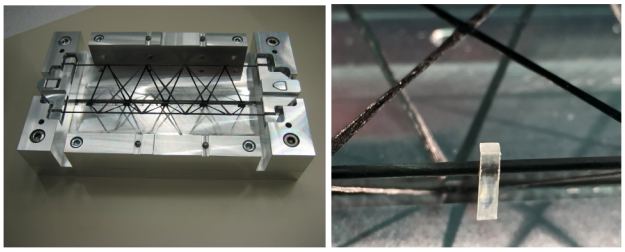

Figure 3: The CF-ladder is placed into the mounting fixture (left). One L-Leg is glued with the tool onto the CF-ladder (right).

References

[1] C. Simons et al., CBM Progress Report 2015, p. 38
[2] A. Sheremetev et al., CBM Progress Report 2015, p. 40
[3] A. Voronin et al., this report

DOI:10.15120/GR-2017-1

3D calculation for the CBM magnet quench protection system.

P. Kurilkin[1], P. Szwangruber[2], E. Floch[2], F. Toral[3], A. Bychkov[1], Yu. Gusakov[1], V. Ladygin[1], A. Malakhov[1], and A. Shabunov[1]

[1]LHEP-JINR, Dubna, Russian Federation; [2]GSI, Darmstadt, Germany; [3]CIEMAT, Madrid, Spain

CBM dipole magnet

The H-type superconducting magnet [1] of the CBM experiment is designed to provide a vertical magnetic field with bending power of 1 Tm over a length of 1 m from the target. The maximum energy storage is evaluated as 5.15 MJ when the operating current of the CBM magnet is rated at 686 A. A 3D model of the magnet with the support is presented in figure 1. Calculations have been performed to design the coil case, the coil vessel, the support links and the quench protection scheme for the CBM superconducting dipole magnet [2]- [8]. The code TOSCA [9] was used for calculating electromagnetic forces exerted on the coil, while the structural analysis was made using the code ANSYS [10].

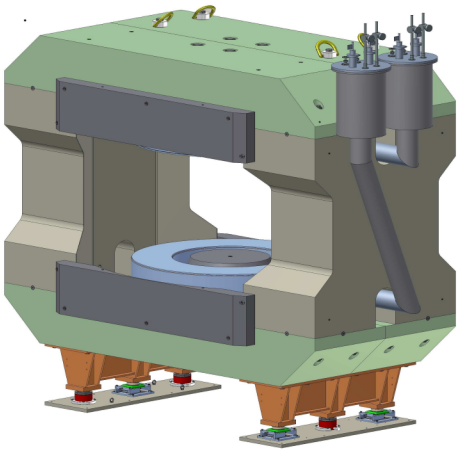

Figure 1: 3D view of CBM dipole magnet with the support.

3D Quench simulation for CBM magnet

The 3D quench calculations for the CBM magnet coil have been carried out by two numerical programs based on the finite-difference method. One of them is used currently at GSI and its detailed description can be found in [11].The other (SQUID) based on CIEMAT numerical code [12] was adapted to perform the quench simulation for the CBM magnet. The magnet coil is represented as a straight slab with a length equal to the average turn length. A regular mesh is applied to the slab so that the cross section of the one mesh element equal to the cross-section of the insulated conductor. Longitudinally, the coil is divided into a number of slices which define a mesh element size. The material properties are homogeneous within each mesh element.

The calculations take into account the inductance function $L_d(I)$[1]. The 3D SQUID program takes into account the real field map distribution in the coil and two layer of conductor insulation (0.1 mm Kapton, 0.2 mm G10).

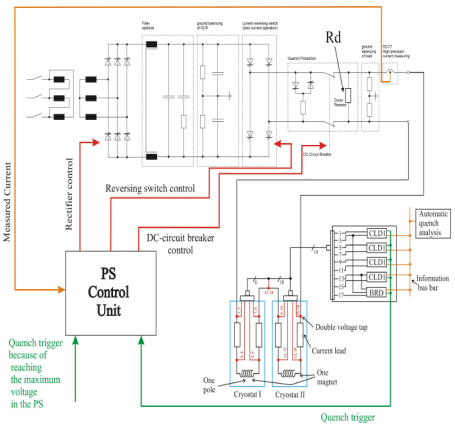

Figure 2: Quench detection and protection scheme (including power supply and voltage taps.

Quench protection system

Earlier, the 3D quench calculations [6]- [8] have been performed to optimize the behavior of the winding of the magnet during the quench. The quench protection system for the CMB magnet will be based on the extraction of the energy stored in the magnet via a dump resistor Rd (see figure 2). The details can be found in [1]. The dump resistor is connected in parallel to the magnet and it is always on.

In case of the quench the magnet will be disconnected from the power supply and the magnet current will be

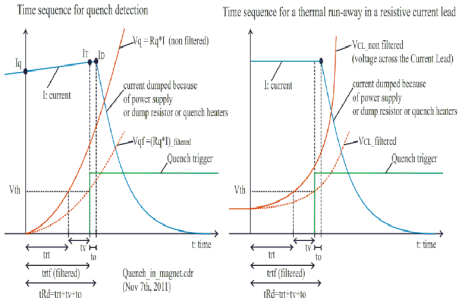

Figure 3: Quench detection time sequence.

DOI:10.15120/GR-2017-1

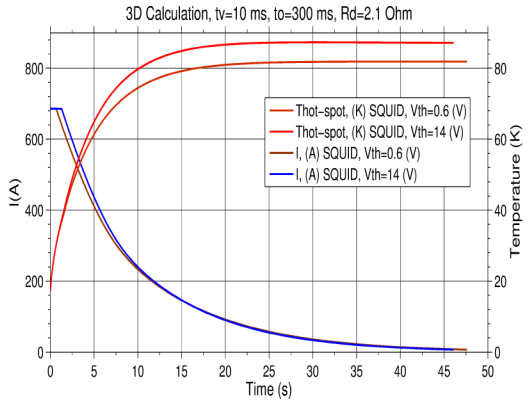

Figure 4: 3D quench calculation of the CBM dipole magnet – the magnet current and the hot-spot temperature.

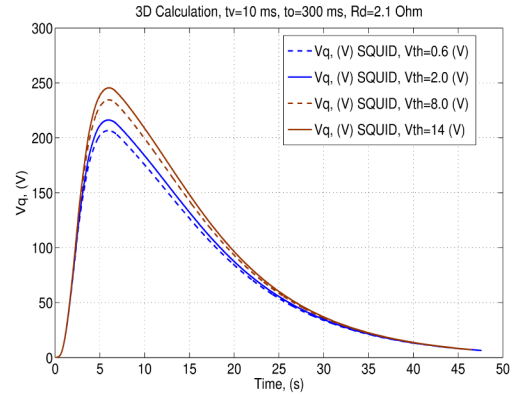

Figure 5: 3D quench calculation of the CBM dipole magnet – the quench voltage.

dumped via the dump resistor. The quench detection time sequence is presented schematically in figure 2. A few calculations were performed for the power supply team, which works on the power converter specification. The detection voltage threshold (Vth) was varied from 0.6 V to 14 V. The favored mechanical switch has an opening time (to) of 300 ms. Validation time (tv) is equal to 10 ms. Figure 4 presents the time dependence of the magnet current and hot-spot temperature with the use $Vth = 0.6V$ and $Vth = 14V$. The 2.1 Ohm dump resistor is also taken into account in the calculations. The maximal "hot-spot" temperature in the coil is about 87 K, when $Vth = 14V$. The time dependence of quench voltage is shown in figure 5. The quench voltage does not exceed the 250 V using the $Vth = 14V$. The maximum voltage across the magnet (1441 V) occurs when the dump resistor turns on.

Conclusion

The designed superconducting dipole magnet will be a unique component of CBM detector setup due to a large pole gap and wide horizontal opening.

The quench protection system will be based on the energy evacuation from the 2.1 Ω dump resistor. The 3D calculations were made for the several values of the detection voltage threshold to estimate the behavior of the magnet coil during the quench.

References

[1] P. Akishin et al., The CBM collaboration, *Technical Design Report for the CBM Superconducting Dipole Magnet* (2014).

[2] A. Bychkov et al., *CBM Progress Report 2014*, (Darmstadt, 2015) 12.

[3] Yu. Gusakov et al., *CBM Progress Report 2015*, (Darmstadt, 2016) 4.

[4] Yu. Gusakov et al., *CBM Progress Report 2015*, (Darmstadt, 2016) 5.

[5] P. Akishin et al., *CBM Progress Report 2013*, (Darmstadt, 2014) 5.

[6] P. Kurilkin et al., *CBM Progress Report 2015*, (Darmstadt, 2016) 7.

[7] P. Kurilkin et al., *CBM Progress Report 2013*, (Darmstadt, 2014) 8.

[8] P. Kurilkin et al., J. Phys.: Conf. Ser. **742**, 012017 (2016).

[9] Vector Fields Ltd., *Tosca. 3d electromagnetics code*, Kidlington (1984).

[10] http://www.ansys.com/

[11] P. Szwangruber et al., IEEE Trans. Appl. Supercond., **23** 4701704 (2013).

[12] F. Toral, *Design and Calculation Procedure for Particle AcceleratorSuperconducting Magnets: Application to an LHC Superconducting Quadrupole*, Ph. D. Thesis. (Madrid) (2001).

DOI:10.15120/GR-2017-1

Tests of the STS-XYTER v2 ASIC for the CBM STS readout

A. Rodriguez Rodriguez[1], *J. Lehnert*[2], *V. Kleipa*[2], *C. Simons*[2], *R. Visinka*[2], *and C. J. Schmidt*[2]
[1]Goethe Universität, Frankfurt, Germany; [2]GSI, Darmstadt, Germany

The STS-XYTER frontend ASIC for the readout of the CBM silicon tracking system (STS) provides self-triggered hits for 128 channels with 5-bit flash ADC charge information and 14-bit timing information with a resolution of < 5 ns. Version 2 of the ASIC from AGH Cracow[1] is available since fall 2016 and implements a large number of optimizations in the analog frontend such as lower noise, larger signal range and improved radiation hardness. The digital backend for control and data readout is completely revised [2], now implementing a custom protocol optimized for readout via the CERN GBTX data aggregation ASIC.

The test setup at GSI

A test system has been set up at GSI for initial ASIC characterization and tests of operation. The setup (Fig. 1) features a frontend board (FEB) with a single STS-XYTER v2 ASIC, the common CBM data processing board (DPB) prototype (AFCK) [3] and a gDPB FMC card from the CBM TOF as connector interface. The AFCK firmware reuses the functionality of the STS protocol tester [4] backend implementation, which allows a quick transition from an ASIC emulation to the real hardware device. Up to three FEBs can be connected to a single gDPB FMC, allowing to test multi-ASIC operation as well as parallel tests on multiple devices.

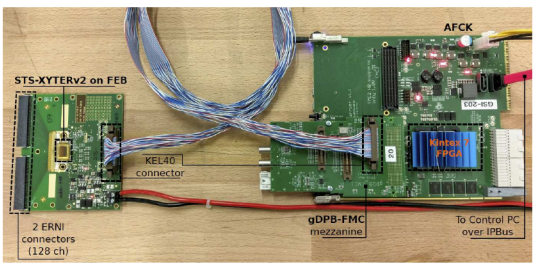

Figure 1: STS-XYTER version2 test setup

Operational tests

The STS-XYTER was brought into operation, the synchronization procedure used to initiate communication with the ASIC was successfully tested and basic control access established. Multiple test modes which produce hits at different stages of the analog and digital processing chain were used and data generation, processing and readout of hit data and control information over a configurable set of AC coupled SLVS links were tested. Using internally generated analog calibration pulses, the full internal processing chain was operated and basic settings for hit generation were exercised.

ADC trim procedure

A reliable ADC calibration procedure is a prerequisite for reading real sensor data. The 5-bit ADC implements a set of 31 discriminators for the ADC values with a subsequent thermometric encoding. Discriminator reference thresholds are provided by a resistor chain; the individual thresholds can be adjusted by trim voltages provided by 8-bit DACs. Trim values can modify discriminator thresholds over a large range, allowing also to set up non-linear responses of desired. A procedure was developed to determine the individual trim values required to achieve a predefined ADC response characteristics. Figure 2 shows the result of a trim procedure. The uncorrected discriminator thresholds which exhibit even a non-monotonous behavior are corrected to a linear response over a predefined signal range.

ASIC characterization in various lab setups and in beam tests will continue in 2017.

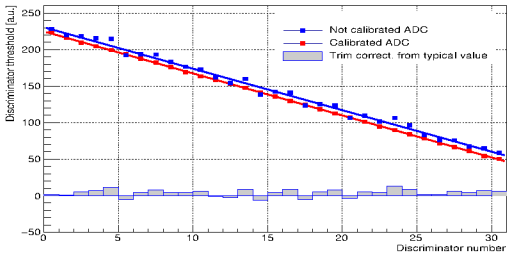

Figure 2: Single 5-bit ADC channel before and after threshold trim.

References

[1] K. Kasinski, R. Kleczek, R. Szczygiel, Front-end readout electronics considerations for Silicon Tracking System and Muon Chamber, JINST 11 (2016) C02024, doi:10.1088/1748-0221/11/02/C02024

[2] K. Kasinski, R. Szczygiel, W. Zabolotny, Back-end and interface implementation of the STS/MUCH-XYTER2 prototype ASIC for CBM experiment, JINST 11 (2016) C11018

[3] W. Zabolotny et al., Versatile prototyping platform for Data Processing Boards for CBM experiment, JINST 11 (2016) C02031 (Proceedings of TWEPP-2015)

[4] W. Zabolotny et al., Design of Versatile ASIC and Protocol Tester for CBM Readout System, JINST (2017) (Proceedings of TWEPP-2016)

DOI:10.15120/GR-2017-1

Charge collection studies of silicon microstrip sensors with different read-out bonding configurations using perpendicular β-particles

Ie. Momot[1,3,4], *M. Teklishyn*[2,4], *C. Simons*[3], *and J. M. Heuser*[3]

[1]Goethe Universität, Frankfurt, Germany; [2]FAIR, Darmstadt, Germany; [3]GSI, Darmstadt, Germany; [4]KINR, Kiev, Ukraine

The STS design aperture covers the polar angles 2.5° to 25°. A read-out strip pitch of 58 μm was chosen to match the design requirement of spatial resolution. About 900 sensors will be installed in the 8 stations of the STS, which translates into $\sim 1.8 \times 10^6$ of read-out channels [1].

To increase signal from charged particles in the outer aperture, where tracks are inclined with respect to the sensor surfaces, different read-out configurations between the sensor strips and electronics are considered. Three types of connections were realized on a test board with a double-sided Si sensor: when each strip is read out by one electronics channel, when only every second strip is read out, and when two strips are bonded to one read-out channel. On the board, 384 sensor strips were divided in 7 groups and bonded to 256 read-out channels applying those three patterns.

For the study, a dedicated setup was built in the STS laboratory. The sensor with the acquisition system was mounted inside a light tight aluminum box, which has a movable support for a radioactive source on the top and a trigger on the bottom. A scintillator connected to a photomultiplier tube is used as a trigger system. The scintillator, sensor and collimated source are aligned in such way that mostly perpendicular particles can penetrate. The source and the scintillator are mechanically interconnected and can move simultaneously in X and Y direction. The height of the source above the sensor can be adjusted independently. For sensor readout the Alibava system [2] was used. It employs the Beetle chip which was developed for the tracker system of the LHCb experiment [3].

Electrons with energies between 1 and 2.28 MeV (^{90}Y β-decay energy) can be considered as minimum ionizing particles. In order to avoid triggering on the also occuring soft component < 1 MeV, a threshold was applied for the signals from the photo multiplier. During analysis a time cut was applied, edge channels of each connection were considered as noisy and removed. After obtaining reliable data, a simple clustering was applied. The resulting spectrum was fitted with a Landau-Gaussian convolution and the most probable value interpreted as collected charge. Noise was calculated as an average fluctuation of the signal baseline. An example of the obtained spectra is depicted in Fig. 1 (top). The dependence of the charge collection on the applied reverse bias in steps of 20 V is shown in Fig. 1 (bottom). The signal-to-noise ratio (S/N) for one-strip clusters was calculated for all connections: (1) for one to one connection: S/N $\backsim$ 26; (2) every second r/o: S/N $\backsim$ 25; (3) two to one: S/N $\backsim$ 22.

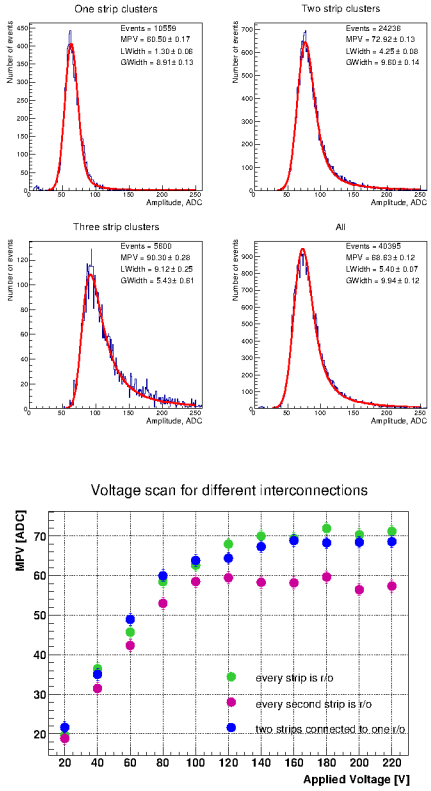

Figure 1: ^{90}Sr spectra fitted with Landau-Gauss convolution for one-to-one connection (top). Charge collection dependence from applied voltage for three configuration schemes (bottom).

Three types of connection schemes have been studied with perpendicular penetrating particles. For each of them, the analysis yields S/N > 20. A further study with inclined beam to mimic the real experiment was made at the COSY facility, Jülich, in August 2016 with 1.6 GeV/c proton beam. Results are forthcoming.

References

[1] J. Heuser et al., Technical Design Report for the CBM Silicon Tracking System, GSI Report 2013-4, http://repository.gsi.de/record/54798

[2] http://www.alibavasystems.com

[3] S. Löchner and M. Schmelling, *The Beetle reference manual for Beetle version 1.3/1.4/1.5*, LHCb note 2005-105, August 22, 2006.

DOI:10.15120/GR-2017-1

Studies of the charge collection efficiency of the prototypes of the silicon microstrip sensors for the STS with 1.7 GeV/c protons

M. Teklishyn[1,2], *O. Bertini*[3], *J. M. Heuser*[3], *A. Lymanets*[3], *H. Malygina*[4,3,2], *and I. Momot*[4,3,2]
[1]FAIR, Darmstadt, Germany; [2]KINR, Kiev, Ukraine; [3]GSI, Darmstadt, Germany;
[4]Goethe Universität, Frankfurt, Germany

Motivation for the proton beam tests

There is a large variety of prototype silicon microstrip sensors for the CBM Silicon Tracking System (STS). The key quantity to be tested is the ratio of the signal over the noise, which makes a direct impact on the detection efficiency of the whole system. The amplitude of the signal itself is directly linked to the ability of the sensor to collect an electrical charge, produced by an interaction with a charged particle. We study the charge collection efficiency by irradiating our sensors with the beam of monochromatic relativistic protons: in this way we expect an equal amount of energy being deposited in the sensor sensitive volume per interaction. It allows us to study systematically what fraction of the deposited energy is transformed to the electrical charge which is then later being collected by the read-out electronics.

The charge in the sensitive volume of the silicon microstrip sensor can be induced by different sources, including an infrared laser, cosmic muons and relativistic electrons from β isotopes. However, the beam of the high momentum protons allows us to perform ultimate tests with the conditions that approach to those in the CBM experiment. Meanwhile, due to the very low momentum spread of the proton beam at COSY accelerator in Jülich, Germany [1], one can perform precise studies of the angular dependence of the sensor response.

The proton kinetic energy is known within 0.1% precision. It allows us to calculate a correction factor of the deposited energy comparing to the minimum ionizing particle (MIP):

$$\Delta E(1.7\,\mathrm{GeV}/c)/\Delta E_{\mathrm{MIP}} = 1.08(4) \qquad (1)$$

The dependency of the energy losses on the incident particle energy is shown in Fig. 1. Values of the mean energy losses in silicon are taken from the NIST Standard Reference Database [2].

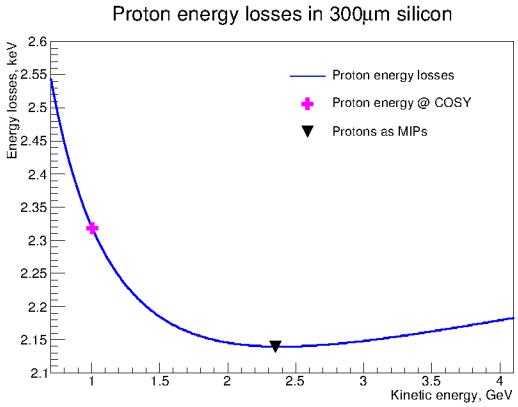

Figure 1: Mean energy losses of protons penetrating a 300 μm thick silicon sensor.

Setup description

We selected 7 sensors to be tested at the COSY accelerator during one week from August 24 till September 4, 2016. Two sensors with the double metallization, two single-metal sensors and two single-metal with oxygenation for better radiation tolerance were fixed in sandwich PCBs and then attached to the read-out electronics via 68-pin ERNI connectors. One single-metal non-oxygenated sensor was directly wire bonded to the read-out electronics. For the latter one we had an access to the 256 read-out channels, merged in 5 groups representing different connection schemes. For the PCB-mounted sensors we used two kinds of interconnectors, which also allowed us to test various connection schemes.

The main cryostation was placed on the movable platform, which allowed a manual vertical adjustment. The platform was equipped with two step motors in a way that one could remotely control the transverse position and the azimuth angle of the cryostation. The latter feature was used for the angular scan procedure.

Two rectangular ($5 \times 20 \times 100\,\mathrm{mm}^3$) plastic scintillators with the photomultiplier tubes were involved in the trigger chain. They were mounted on two aluminium frames upstream and downstream the cryostation. The scintillators were positioned cross-like in plastic holders; in that way they constrained a square cross-section of $5 \times 5\,\mathrm{mm}^2$ for the incident particles.

During the preparation phase in the first two days several configurations of the sensors and stations were tried. Initially, it was foreseen to measure two PCB mounted sensors in the cryostation at once. However, it was observed, that two sensors, being close in one aluminium box together with corresponding electronics, suffered from severe noise.

Thus it was decided to operate only one sensor in the cryostation per run during the first phase of tests. Meanwhile, we put a warm aluminium box mounting a direct-bonded single-metal sensor to the upstream aluminium frame just behind (few millimeters) the plastic holder of the

DOI:10.15120/GR-2017-1

scintillator. In this configuration a series of measurements were performed during the next three days. The sensors in the cryostation were mainly operated at the temperature $T = -10\,^{\circ}\mathrm{C}$ to reduce noise and approach to the final conditions of the future experiment.

In the second phase of measurements we decided to dismount the warm aluminium box, to remove it from its cover and to place it inside the cryostation. The latter was then operated at $T \simeq 10\,^{\circ}\mathrm{C}$ due to the limited thermal coupling through the thick aluminium walls of the partially disassembled warm station. In such a configuration a set of angular scans was performed with the direct-bonded sensor.

Read-out electronics

Due to significant technical issues that occurred with the `nXYTER v.1` based read-out chain [3], we had to find an alternative option for reading out signals from the silicon microstrip sensors during the proton beam tests. We stopped at the `Alibava` system [4], based on the *Beetle* chip [5], initially developed for the tracking system of the LHCb experiment. The read-out chain of the Alibava system consists of two PCBs: the Daughter Board, attached directly to the sensor under the test, and the Mother Board, which performs the digitization and communication with the PC via the USB protocol.

The chosen electronics showed a good performance during the test in the STS laboratory. Since it could be only operated in the external trigger mode only, we designed a trigger chain based on the pair of plastic scintillation detectors. The requirement of the coincidence of two signals within a window of $40\,\mathrm{ns}$ was performed with a NIM crate electronics. Then the logical signal was feed to the two Alibava Mother Boards, thus we triggered a signal read-out from two sensors at once.

The time to digital converter of the Alibava system provides us a relative time between the trigger occurrence and the snap shot of all read-out channels within the $25\,\mathrm{ns}$ time window. Thus before the main measurements we had to make a latency scan, studying the signal amplitude with respect to the time delay.

Data analysis status

Considering complicated structure of the beam time profile, mainly its significant non-uniformity, the main task of the current stage of the data analysis is selection of the events that can be further analyzed. We develop algorithms which should allow us to reject noisy events and events with multiple interactions (thus one can not associate a time-stamp to a given interaction) without significant suppression of the acquired statistics.

Particularly, one procedure has been developed for effective off-line noise reduction. We implement a median correction for every 64 channels for a given event. It allows us to reduce a noise level almost by $1/3$ for some data sets. Typical histograms before and after median correction

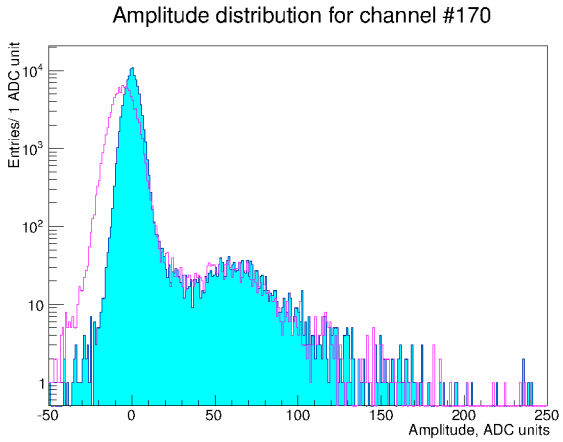

Figure 2: An example of the amplitude distribution in a single channel before (magenta histogram) and after (filled cyan histogram) correction to the common mode.

are shown in Fig. 2.

Further investigations will touch a cluster finding algorithm. This task becomes nontrivial due to complex read-out scheme implemented differently in different set of data taking. A set of the transitional matrices M_{ij} may be implemented to transform data from the channel basis to strip basis:

$$M_{ij} \times C_i = S_j,\ i = 0..255,\ j = 0..1023 \qquad (2)$$

With the properly reconstructed cluster we will be able to proceed to the comparison of signal strength in different conditions which will link us to the charge collection efficiency and the signal over noise ratio.

References

[1] R. Maier, Cooler synchrotron COSY — Performance and perspectives, Nuclear Instruments and Methods in Physics Research Section A: Accelerators, Spectrometers, Detectors and Associated Equipment, Volume 390, Issues 1—2, 1 May 1997, Pages 1-8, ISSN 0168-9002

[2] M.J. Berger, J.S. Coursey, M.A. Zucker and J. Chang (2005), ESTAR, PSTAR, and ASTAR: Computer Programs for Calculating Stopping-Power and Range Tables for Electrons, Protons, and Helium Ions (version 1.2.3). [Online] Available: http://physics.nist.gov/Star [2017, February 10]. National Institute of Standards and Technology, Gaithersburg, MD.

[3] A.S. Brogna et al. 2006. N-XYTER a CMOS read-out ASIC for high resolution time and amplitude measurements on high rate multi-channel counting mode neutron detectors, Nucl. Instrum. Meth. Phys. Res. A568 301

[4] Alibava Systems, http://www.alibavasystems.com

[5] S. Löchner and M. Schmelling, The Beetle reference manual for Beetle version 1.3/1.4/1.5, LHCb note 2005-105, August 22, 2006.

DOI:10.15120/GR-2017-1

A thermal enclosure for microstrip sensor tests in laboratory and beam

A. Lymanets[1,4], *M Teklishyn*[2,4], *O. Bertini*[1], *H. Malygina*[3,1,4], *I. Momot*[3,1,4], *and J. M. Heuser*[1]
[1]GSI, Darmstadt, Germany; [2]FAIR, Darmstadt, Germany; [3]Goethe Universität, Frankfurt, Germany;
[4]KINR, Kiev, Ukraine

A shielded thermal enclosure has been developed that allows for testing silicon microstrip sensors of different sizes from different vendors under temperature conditions as later in the CBM experiment. The enclosure can be operated in the laboratory as well as in the beam and provides integrated cooling infrastructure that is required to operate irradiated sensors at below room temperature. It has been successfully used during the August 2016 beam time at COSY (Reserach Center Jülich) [1] where sensors with different strip readout schemes have been operated and parameter scans, such as beam incidence angle and temperature scan, have been performed. A key design requirement addressed in the thermal enclosure is the minimal cool-down time that would facilitate the measurements of irradiated sensors.

Experimental setup

The enclosure consists of a shielding *Al* box that is nested in a plastic box with styrofoam isolated walls and windows for the beam. It has separate cooling circuits for front-end electronics and dry nitrogen that is blown into the box in order to reduce humidity and prevents possible water vapor condensation. In order to speed up cooling of nitrogen gas, a forced convection is provided by the built-in fans that are switched on during the cooling time only. The setup provides simultaneous operation of two sensor boards read out by two ALIBAVA [2] daughter boards equipped with BEETLE [3] front-end chips (see Fig. 1).

In order to control the experimental conditions, temperature and humidity has been measured inside and outside the enclosure using a custom microcable resistive temperature detector (RTD) as well as combined temperature and humidity sensors (Honeywell HIH-3602-C). Environment parameters outside the box have been used to calculate the dew point. The sensor data have been acquired and stored using custom LabVIEW-based software. Figure 2 shows the temperature and relative humidity trend recorded over a time period of above 11 hours. A cool-down time from room to operation temperature of -5.7° is below 2 hours. The nitrogen flow during the measurements was 150 l_n/min which kept the relative humidity in the enclosure well below 30%.

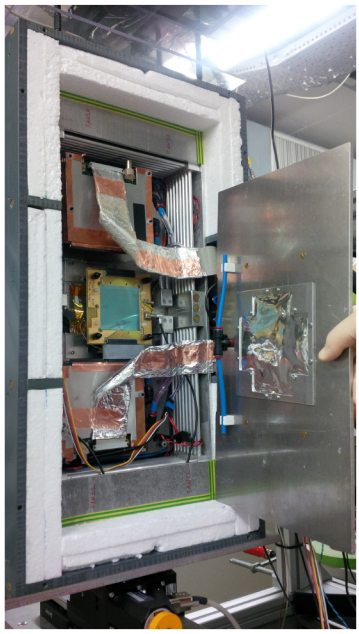

Figure 1: Thermal enclosure with cooling lines at the perimeter of the core part and two ALIBAVA daughter boards.

Conclusions

The constructed enclosure has provided stable and low-noise operation conditions during the beam test at COSY (Jülich) in 2016. Fast cool-down time allowed to test many microstrip sensors in various configurations and to study the effect of operation conditions on the system performance.

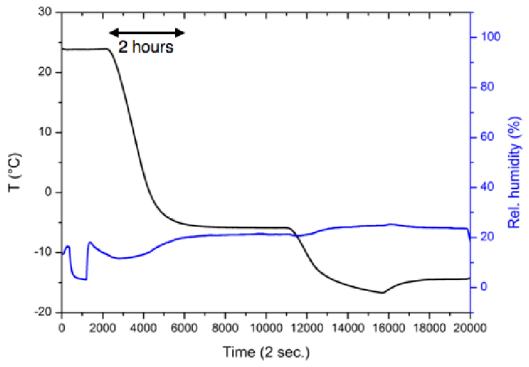

Figure 2: Temperature and humidity trend during the cool-down cycle.

References

[1] R. Maier, NIM A 390 (1997) 1-8

[2] http://www.alibavasystems.com, Feb. 10, 2017

[3] S. Löchner and M. Schmelling, LHCb note 2005-105, Aug. 22, 2006

DOI:10.15120/GR-2017-1

Control software for the DPB based readout chains and related beamtime activities

P.-A. Loizeau[1], *D. Emschermann*[1], *and the CBM DAQ working group*
[1]GSI, Darmstadt, Germany

Since 2015, several of the CBM sub-detectors groups are starting to use new readout chains based on the AFCK FPGA board, on the IPbus system for slow-control communication and on the FLES system for data acquisition. For the configuration and control of these new chains, a set of libraries and binaries based on IPbus was developed. The first step in 2015 was the conversion of tools from the previous chains to support the readout of a single nXYTER front-end board through the control path (Control DAQ or CDAQ) [1]. This set of tools is now expanded for multi-boards operations and synchronized data taking with different CBM sub-detectors (TOF, MUCH, STS).

The *dpbcontrols* software is available to all CBM members [2] with support for the following firmware modules: (i) FEB-F: nXYTER v2 ASIC front-end board, (ii) PADI-GET4: PADI 6 or X board associated with GET4 v1.23, v1.3 or v2.0 board, (iii) CDAQ: data readout through the IPbus control path, (iv) FLIM: data readout in Micro-Slice containers (μS) through the 10 Gb FLES link [3], (v) TS slave: receiver part of the Time Synchronization (TS) system used for multi-boards systems in the CBM 2016 beamtimes with Data Processing Boards (DPBs) [4].
AFCK boards loaded with a CBM firmware are tagged *xDPB*, with *x* a letter corresponding to the firmware type. Two DPB firmware systems are currently in use: nDPB for STS and MUCH with FEB-F + CDAQ + FLIM + TS slave modules and gDPB for TOF with PADI-GET4 + CDAQ + FLIM + TS slave modules. For each of these systems, a Command-Line-Interface binary (CLI) is provided to the users, with access to low level commands (e.g. registers setting) but also higher level operations such as the automatic calibration of front-end parameters using data samples acquired through the CDAQ. The two CLI programs also support the execution of configuration scripts to simplify the operation of systems with hundreds of channels.

For quick monitoring and debugging, the CDAQ data can be either sampled and directly printed out in the CLI tools as text or integrated in simple ROOT monitoring macros for continuous readout. One limitation of this CDAQ is that in most operating conditions data are lost between two readout cycles. It is therefore mostly a tool for setup tuning and not for detector characterization.

In order to operate experimental setups with multiple DPBs or multiple DPB types, all boards need to use a common clock and some commands need to be executed synchronously on all targets. The TS system provides to all DPBs a 40 MHz clock and a synchronization pulse locked to it with a period of $1024 * 2^{15}$ cycles or 0.8388608 s. Before sending a command needing synchronous execution, the time elapsed since the last synchronization pulse is readout to ensure that all targets can receive the command before the next pulse. Three programs are used with this method to perform the synchronization procedure of the current prototype systems: 1) one to reset all DPBs in the setup in a synchronized way and prepare them for configuration, 2) one to reset and synchronize the clock counters of all DPBs and reset the μS counter of their FLIM module (timing synchronization) 3) one to enable data emission in a synchronized way (data synchronization: all DPBs start sending their data at the same μS).

All these tools were used during a beamtime in the H4 cave at CERN SPS in November 2016 [5]. Two prototypes from the MUCH sub-detector were readout with the FEB + nDPB system (7 nDPBs with up to 4 FEBs per board) and multiple RPC prototypes from the TOF sub-detector were readout with the PADI-X + GET4 + gDPB system (6 gDPBs with up to 3 front-end boards each).
During this beamtime, an online monitor was developed based on CBMROOT [6]. It allowed the shift crew to check on a web page with interactive histograms and in real time the status of all front-end boards and of the DAQ system.

Another test setup was installed for the TOF sub-detector group in the STAR experiment at BNL [7], with a single gDPB. No CBM expert will be on-site when beam will be available during the STAR 2017 run. Therefore, the integration of the tools and configuration files in simple scripts was pushed further, to the point where a reboot of the DAQ computer triggers a full automatic reconfiguration, followed by the execution of the FLES DAQ and the CBMROOT online monitor.

References

[1] P.-A. Loizeau *et al.*, "Configuration, monitoring and data acquisition with the IPbus-AFCK readout chains", CBM Progress Report 2015 (2016) 106

[2] "CBM GitLab repository", https://cbmgsi.githost.io/p.-a.loizeau/dpbcontrols

[3] D. Hutter *et al.*, "CBM FLES input interface developments", CBM Progress Report 2015 (2016) 112

[4] L. Meder *et al.*, "Timing synchronizer system developments for pre-production beam test setups", CBM Progress Report 2015 (2016) 109

[5] D. Emschermann *et al.*, "Common CBM beam test at CERN SPS 2016", this report

[6] F. Uhlig *et al.*, "Online monitoring with CbmRoot", this report

[7] I. Deppner *et al.*, "TOF Status Report", this report

DOI:10.15120/GR-2017-1

Design and development of the nDPB FPGA mezzanine card

C. de J. García Chávez[1], *D. Emschermann*[2], *and U. Kebschull*[1]
[1]Infrastructure and Computer Systems for Data Processing (IRI), Frankfurt University, Frankfurt/Main, Germany;
[2]GSI, Darmstadt, Germany

Introduction

With the introduction of the AFCK [1] as a Data Processing Board DPB, several CBM subsystems such as the Silicon Tracking System STS and the Muon Chamber MUCH require the integration of nXYTER-based front-end boards into the current CBM-DAQ. For this reason, an FPGA mezzanine card was developed in order to allow the interconnection of the front-end boards to the AFCK.

Design considerations

In order to achieve a correct time-stamping in a free-running data acquisition chain, a global synchronization system is necessary. Therefore a connection to an external synchronization system [2] is made through a RJ45 connector, which receives the synchronization signals from a tDPB. Given the fact that the nDPB is floating at the high-voltage bias level of the STS module, which is around +/- 150V, an isolation between the FPGA fabric and the RJ45 is mandatory. The isolation is made by a magnetic Ethernet isolator.

A Small Form Factor SFP optical transceiver module is also included on the nDPB-FMC to allow a 10 Gbps FLIM or 1Gpbs IPBUS communication between the AFCK and the DAQ-PC. Moreover, two KEL-68 connectors have been included on the nDPB-FMC to connect to the nXYTER front-end boards. Finally, in order to facilitate prototyping, three LVDS General Purpose Input/Output GPIO pins were also included on the FMC.

Because of the high speed signals and high pin-out density of the FMC design, an 8-layer PCB stack-up was selected. Five layers were used for high speed transmission lines while three layers where used as power planes. In order to reduce the high-frequency losses caused by the PCB dielectric material, a MEGTRON-6 material was selected for the *cores* and the *prepegs*. The final nDPB-FMC is shown in the Fig.1.

Closing notes

The nDPB-FMC was successfully used and tested during the CERN SPS 2016 beamtest [3]. The FLIM optical connection as well as the external synchronization by the RJ45 were also successfully tested. Moreover, the nDPB-FMC was shown to be also useful for the SPADIC 2.0 readout, as presented in [4]. Fig.2 shows the experimental nDPB setup used during the CERN SPS 2016 beamtest where multiple nDPB-FMC were used.

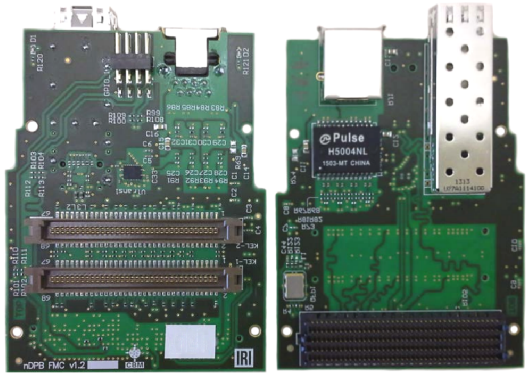

Figure 1: Left: Top side of the nDPB-FMC, two KEL-68 connectors are shown as well as the GPIO connector. Right: Bottom side of the nDPB-FMC, RJ45, magnetic isolator, FMC-HPC connector and the SFP with a cage are shown.

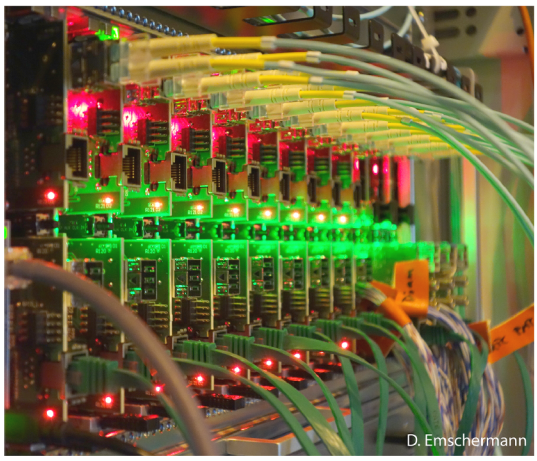

Figure 2: nDPB setup at CERN SPS 2016 beamtest

References

[1] W. Zabołotny et al., "The AFCK Board as the Data Processing Board prototype for the CBM experiment". CBM Progress Report 2015.

[2] L. Meder et al., "A timing synchronizer system for beam test setups requiring galvanic isolation". Real Time Conference (RT), 2016 IEEE-NPSS Conference Record, doi:10.1109/RTC.2016.7543119.

[3] D. Emschermann et al., "Common CBM beam test at CERN SPS 2016", this report.

[4] C. de J. García Chávez et al., "Development of the SPADIC v2.0 read-out chain at CERN SPS 2016". This report.

DOI:10.15120/GR-2017-1

Simplification of the TRD readout chain and related modification of the pad plane layout

D. Emschermann[1]
[1]GSI, Darmstadt, Germany

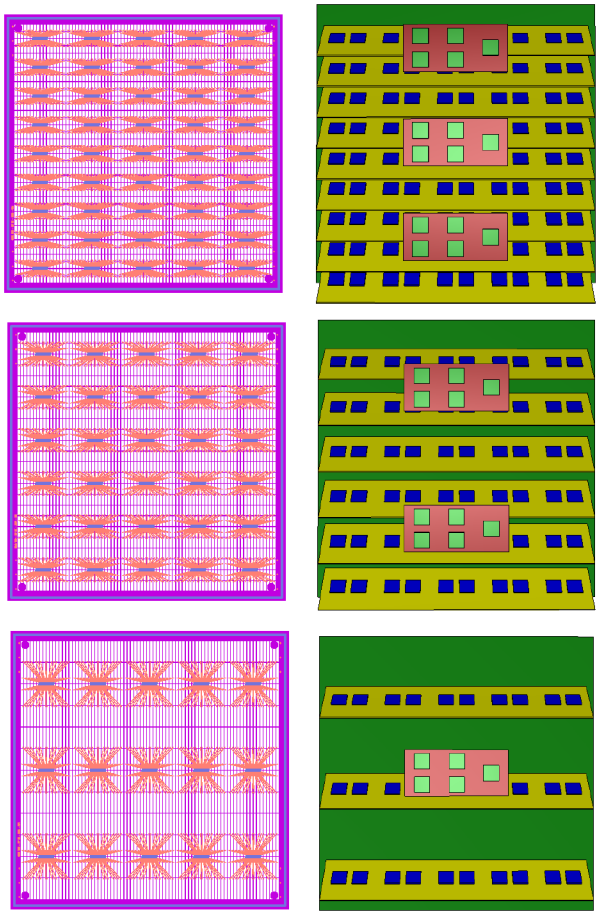

Figure 1: Pad plane layout of the small TRD module types 1, 2 and 3 (from top to bottom), with a respective pad length of 15.0 mm, 22.5 mm and 45.0 mm. The pad plane is interfaced with 9x, 6x or 3x FEB-5x2 and readout with 3x, 2x or 1x ROB-5.

The TRD v16a uses four different FEB types (FEB-5x3, FEB-5x2, FEB-5x1, FEB-8x1) and 3 ROB types (ROB-7, ROB-5, ROB-3). The detector layout was further optimised in TRD v17a, aiming at a reduction of the amount of different components in the readout chain. A modification of the pad plane layout for the three small 57×57 cm^2 TRD module types (1, 2, and 3), see Fig. 1, allows to equip all of them with a single FEB-5x2 type.

The modification consists in using the same 64-pin connector on all 3 module types. With increasing pad size the 64-pin footprint needs to be adapted to the related pad length. That is possible until the increase in pad capacitance deteriorates the signal-to-noise ratio below a given threshold value. As a result of this optimisation the FEB-5x3, FEB-5x1 and ROB-7 are no longer required.

module type	1	2	3	6	7	8
# of modules	32	24	40	24	32	48
ASICs / FEB	10	10	10	8	8	8
FEBs / module	9	6	3	8	4	3
# of FEBs	288	144	120	192	128	144
# of ROB-5	96	48	40	48	32	0
# of ROB-3	0	0	0	0	0	48

Table 1: Key numbers of the SIS100 TRD v17a detector, summarising to 9232 SPADIC and 1464 GBTx ASICs.

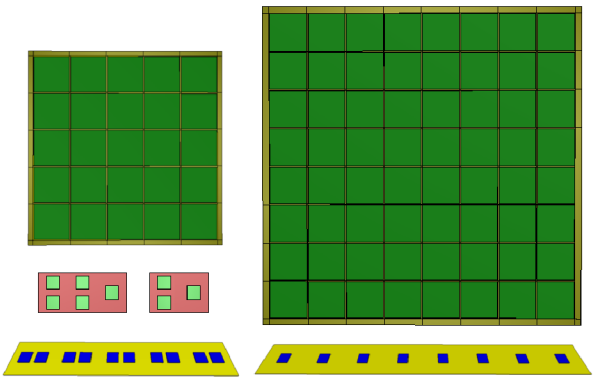

Figure 2: The building blocks of the TRD detector system: (green) modules of 2 different sizes, (yellow) 2 FEB types, 5x2 and 8x1, and (red) 2 ROB types, ROB-5 and ROB-3.

All 3 small module types are now based on an identical readout tree: a group of 30 SPADIC ASICs with 60 e-links is interfaced to a ROB-5 providing 70 e-link inputs. The module types 1, 2 and 3 consist of 3, 2 and 1 such readout trees, as detailed in Tab.1. The total number of ASICs sums up to 9232 SPADIC and 1464 GBTx.

Thanks to this simplification the TRD detector is built from only 2 FEB types (FEB-5x2, FEB-8x1) and 2 ROB types (ROB-5, ROB-3), see Fig. 2. Further benefits of a readout chain employing only the ROB-3 and no ROB-5 are currently under study.

References

[1] The CBM Collaboration, *Technical Design Report for the CBM Transition Radiation Detector (TRD)*, to be published

DOI:10.15120/GR-2017-1

Development of the SPADIC v2.0 readout chain at the CERN-SPS in 2016 *

C. de J. García Chávez[1], *C. Bergmann*[2], *D. Emschermann*[4], *P. Kähler*[2], *M. Kohn*[2], *P. Munkes*[2], *F. Roether*[3], *and U. Kebschull*[1]

[1]Infrastructure and Computer Systems for Data Processing (IRI), Frankfurt University, Frankfurt/Main, Germany; [2]Institut für Kernphysik, Münster, Germany; [3]Institut für Kernphysik, Frankfurt, Germany; [4]GSI, Darmstadt, Germany

Overview

By November 2016, front end boards equipped with the new SPADIC v2.0 chip have become available [1]. Together with the introduction of a new readout architecture based on the *AFCK*, the *FLIM* [2] data transmission protocol and the *IPBUS* protocol for slow-control and system configuration, a set of firmware and software designs were developed to enable the readout of the SPADIC v2.0 chips during the test beam at the CERN-SPS in 2016.

Experimental Setup

Two SPADIC v2.0 front end boards were installed on a 95×95 cm^2 MWPC of the CBM-TRD type-8 [3][4][5] at the CERN-SPS [6]. The location of components are shown in Fig. 1. On the left side of the image, the red squares denotes the location of the SPADIC v2.0 front end boards on the MWPC while on the right side, denoted by a yellow square, an *AFCK* installed in a *mTCA* is shown.

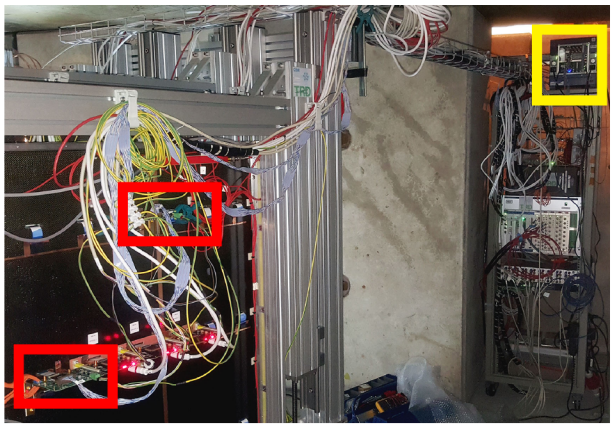

Figure 1: Experimental setup at the CERN-SPS in 2016.

Firmware Development

The readout architecture used during the CERN-SPS beam time in 2016 is represented by a diagram as shown in Fig. 2. The SPADIC v2.0 front end boards are connected to the *AFCK* by means of a *gDPB-FMC* mezzanine card. The SPADIC v2.0 uses the *STS-HCTSP* protocol [7] for data transmission and configuration. After the front end data is readout and processed by the *AFCK*, it is transmitted towards the *FLIB* installed in a *DAQ-PC* by an optical connection available at the *nDPB-FMC* [8] using the *FLIM* protocol. For future reference, this firmware architecture will be named *eDPB*, where *"e"* comes from the *e-link* transmission protocol used by the front-end and *DPB* as acronym for *Data Processing Board*.

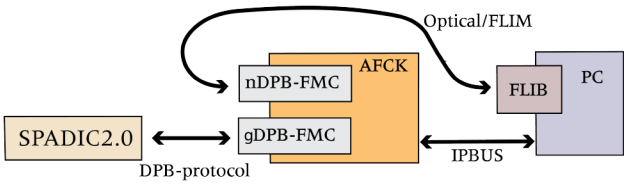

Figure 2: SPADIC v2.0 readout architecture.

An overview of the AFCK firmware design is shown in Fig. 3. Data coming from multiple SPADIC v2.0 front end boards is buffered and then pre-processed by a *Feature Extraction* core [9]. Finally, a simple timeslice building is performed before the data is sent to the *FLIB*.

Feature Extraction

Feature Extraction is required to process and extract as much valuable information as possible from the SPADIC chips with a minimum of data bandwidth. In the presented *eDPB* design, it is possible to either process data from SPADIC v2.0 front end boards or from a *StreamSim* device. A *StreamSim* device is basically an AFCK board working as a front end emulator, where SPADIC data recordings can be downloaded and then transmitted by a 3 Gbps optical line, built on top of a Xilinx Aurora protocol [10], towards the *eDPB*. Scenarios where testing and developing of feature extraction algorithms are required, can benefit from this configuration. For data integrity tests, two independent data streams are sent to the *FLIB*. An optical line would only transmit the original SPADIC messages without any pre-processing, while the second optical line would only transmit the data resulting after SPADIC messages are processed by the feature extraction core. The *eDPB* design has used the *nDPB* firmware design as basis, given its similarities, but differing in the front end and the configuration requirements.

Software Development

The *IPBUS* protocol has been used to transmit the configuration commands from the *DAQ-PC* towards the front end boards. For this purpose a software library was built to provide a feasible way to initialize the data transmission

* Work supported by BMBF No. 05P15RFFC1.

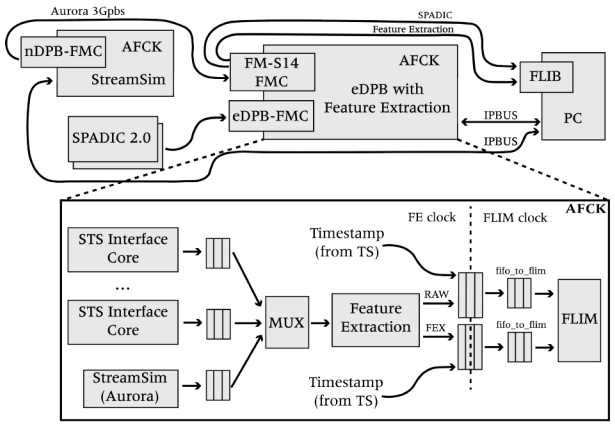

Figure 3: Up: DAQ diagram with SPADIC v2.0 as front end and a StreamSim device. Down: AFCK firmware design diagram.

from the SPADIC v2.0. Initialization and configuration scripts facilitates both the analog and digital configuration of the SPADIC v2.0 such as baseline adjustment and neighbour forced trigger matrix. A considerable contribution for the software stack has been developed by the *CBM-DAQ* group.

Current Status

The design and evaluation of the *eDPB* firmware design was successfully performed during the CERN-SPS test beam in 2016. Communication tests between the *eDPB* and the SPADIC v2.0 were as well successful. Configuration scripts that were developed during previous beam tests for the SPADIC v1.0 and SPADIC v1.1 were successfully ported to the SPADIC v2.0 in order to work with the new *eDPB* design by using the *IPBUS* protocol.

References

[1] M. Krieger et al., *Development of new SPADIC versions 1.1 and 2.0*, this report.

[2] D. Hutter et al., *CBM FLES input interface developments*, CBM Progress Report 2015.

[3] P. Kähler et al., *Operation and measurement programme of a SPADIC readout chain on type-8 CBM-TRD prototypes at the CERN-SPS 2016*, this report.

[4] F. Roether et al., *Construction of type-8 MWPCs for the CBM-TRD*, this report.

[5] *Technical Design Report for the CBM Transition Radiation Detector*, The CBM Collaboration, 2017 (to be published).

[6] D. Emschermann et al., *Common CBM beam test at CERN-SPS 2016*, this report.

[7] K. Kasinski et al., *A protocol for hit and control synchronous transfer for the front-end electronics at the CBM experiment*, NIM A835(2016)66 or doi:10.1016/j.nima.2016.08.005.

[8] C. de J. García Chávez et al., *Design and development of the nDPB FPGA mezzanine card*, this report.

[9] C. de J. García Chávez et al., *Status Update of the Feature Extraction Framework for Automatic FPGA Firmware Generation*, CBM Progress Report 2015.

[10] "Xilinx", http://www.xilinx.com.

DOI:10.15120/GR-2017-1

Status of the CBM-MVD station precursor PRESTO *

M. Koziel[1], *P. Klaus*[1], *C. Müntz*[1], *J. Stroth*[1,2], *and the CBM-MVD Collaboration*
[1]Institut für Kernphysik, Goethe-Universität Frankfurt, Germany; [2]GSI Darmstadt, Germany

Sensor Integration When integrating touchy sensors on carriers, the yield represents a vital assembly parameter and drives the optimization of quality assessment (QA). In 2015, the first side of the PRESTO module (comprising six 50 μm thin MIMOSA-26 AHR sensors) was assembled [1]. After assembly, five out of six sensors were functional. Note, all sensors have been subject to probe testing with dedicated needle cards and test procedures prior to integration. One half of the sixth sensor worked well while the remaining half did not produce any data. With time, an additional sensor started to exhibit malfunctioning. Despite visual inspection did not reveal problems with the sensors or wire bonding, we extensively examined our wire-bonding hardware and procedures. The latter pointed to a possible weakness originating from edging of bond wedges and Al-wire. After replacing the hardware components, wire-bonds from the two mentioned sensors were taken off and replaced. As a result, one of the two malfunctioning sensors was recovered. The other one, where output data were not produced, did not change its behavior.

We therefore associate the malfunction of this particular sensor to be caused by improper handling during the assembly process. After considering all tests related to the first side of PRESTO to be accomplished, we have focused meanwhile on the assembly of the second side. It hosts three rows of sensors, each populated with three 50 μm thin MIMOSA-26. For this side, sensors based on low- and high-resistivity substrates were chosen. The use of low-resistivity is motivated by reserving the high-resistivity based devices for other projects. Some sensors with minor malfunctions, revealed during the probe test campaign, were also placed on purpose. We hope to trace the possible development of these malfunctions during each of the integration steps. Figure 1 shows the newly equipped front side of PRESTO.

Continuous Operation and Control System The long-term operation of PRESTO was assessed in our vacuum vessel during summer 2016. A 24/7 readout was achieved for several weeks. This campaign helped us decide which metrics to monitor and which software and hardware interlock systems to employ to prevent system failure. During the run, a custom software solution was used to gather relevant metrics such as electrical sensor currents, module temperature, vacuum pressure, cooling system status. Some further metrics from the data stream that should be monitored include e.g. cluster multiplicities, local hit rates and occupied bandwidth. To do so, an EPICS based control and monitoring system is currently under planning and will soon put into operation in a pilot system to be evaluated when operating the then fully equipped PRESTO. Later, it shall serve the full CBM-MVD as control and monitoring solution.

Cooling System and Planning Systematic cooling studies are now under way for PRESTO and for the later full MVD. New equipment was put into operation to increase the performance and fully characterize the cooling system. This includes a water cooling pump for pressure boost, temperature sensors for the cooling medium, flow meters, and pressure gauges in the next expansion stage. Some of those systems might be excluded from the final MVD to make the cooling system less prone to malfunction. For now, they are required to fully characterize the properties of our system.

Figure 1: Configuration of sensors assembled on the front side of the PRESTO module. First side assembled with sensors and flex cables.

Conclusion Extensive tests of the first-side assembly of PRESTO were conducted in 2016. They triggered many activities, e.g. optimization of QA, development of the monitoring and control system for the MVD, and evaluations of the cooling system. The latest progress on PRESTO – the integration of the second side – is under way.

References

[1] M. Koziel et al., "Vacuum-compatible, ultra-low material budget Micro-Vertex Detector of the compressed baryonic matter experiment at FAIR", NIM-A 845 (2017) 110 (dx.doi.org/10.1016/j.nima.2016.05.093)

* supported by BMBF (05P15RFFC1), HIC for FAIR and GSI.

Online data preprocessing for the CBM Mirco Vertex Detector *

Qiyan Li[1], *M. Deveaux*[1], *J. Michel*[1], *C. Müntz*[1], *J. Stroth*[1,2], *and the CBM-MVD Collaboration*
[1]Institut für Kernphysik, Goethe-Universität Frankfurt, Germany; [2]GSI, Darmstadt, Germany

The CBM Micro Vertex Detector (MVD) is being designed to handle 10^5 Au+Au or 10^7 p+Au collisions/s. Weakly decaying particles like Hyperons or D Mesons will be identified in real time by means of a free streaming DAQ system, the FLES, which includes stages for event reconstruction and decay topology identification. To fulfill this task with the available computing resources, each processing step has to be optimized for low CPU load and bandwidth consumption. This does also hold for the cluster finding of the MVD. The current CBMRoot/C++ code was estimated to consume up to 80% of the CPU-power of the FLES once being confronted with a realistic data rate. To reduce this load, we tested strategies to perform preprocessing of the data before sending it to the computing farm.

A first stage of the proposed preprocessing is already integrated in the CMOS Monolithic Active Pixel Sensors used in the MVD. The MIMOSA-26 pixel sensor used for our test includes circuits for signal discrimination, on-chip zero suppression and one-dimensional cluster finding. The second stage as discussed in this work comprises full cluster finding and encoding on free resources of the FPGAs controlling the sensors. The related algorithm was required to match the available FPGA resources and to keep all information on cluster shapes without increasing the data volume and bandwidth.

In a first step, we found a way to encode reconstructed clusters into one 32 bit word per cluster. Tests showed that the protocol encodes 99.99% of the clusters recorded during beam test data of the MVD-prototype with MIMOSA-26 without loss of information [1, 2]. A VHDL module doing cluster finding and encoding was designed and tested successfully with the TRB2 board [3]. Real time cluster finding was demonstrated by operating it with a MIMOSA-26 sensor, which was illuminated with a β-source. To test the accuracy of this cluster finding, the output was stored together with its raw data, which was processed with the C++ reference code in a next step. The clusters recorded with both chains were compared for 260k frames. They were found to agree for physics data while some pathological signatures, as e.g. caused by a broken line, were rejected by the FPGA code. The output of the FPGA showed a mild compression of 14% w.r.t. the raw data (see Figure 1), which matches our requirements. The CPU time for the remaining steps to be done with C++ at the FLES (C++ cluster finding vs. unpacking of the encoded cluster information) was compared. Note that in both cases the first processing stage was carried out by the sensor . The

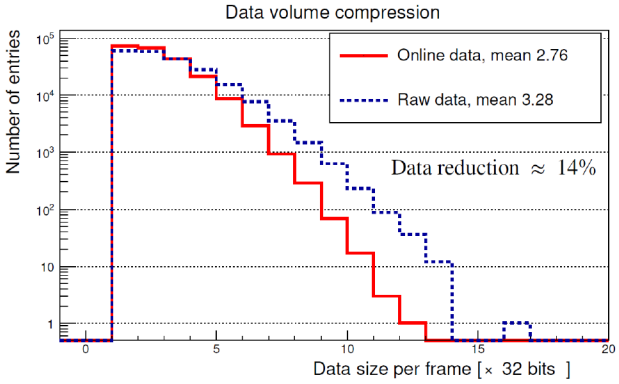

Figure 1: Data size per frame for a MIMOSA-26 exposed to β-rays (raw data vs. FPGA-encoded clusters).

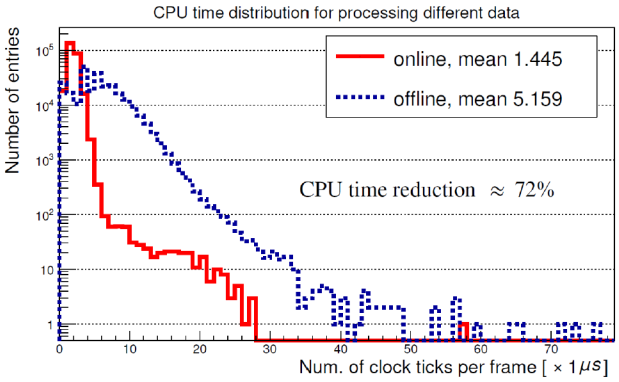

Figure 2: The CPU time per frame (decoding of FPGA-encoded clusters vs. C++ cluster finding).

low occupancy reached with the β-source causes a bias in favor of the offline processing. Nevertheless, the FPGA-processing reduces the remaining CPU load by a factor of four (see Figure 2).

The explorative study presented here demonstrates that the proposed strategy is suited to reduce the load of the FLES. It remains to be adapted to the internal data processing of the final MVD sensor, which is currently under design.

References

[1] Qiyan Li et al., GSI Scientific Report 2012 (2013) 56
[2] Qiyan Li et al., J. Phys.: Conf. Ser. 513 (2014) 022021 (Proceedings of CHEP-2013)
[3] Qiyan Li et al., GSI Scientific Report 2014

* supported by BMBF (05P15RFFC1), HIC for FAIR and GSI.

DOI:10.15120/GR-2017-1

Cooling studies with thermal pyrolytic graphite for the CBM-MVD *

D. Mijatovic[1], M. Koziel[1], P. Klaus[1], C. Müntz[1], J. Stroth[1,2], and the CBM-MVD Collaboration
[1]Institut für Kernphysik, Goethe-Universität Frankfurt, Germany; [2]GSI Darmstadt, Germany

The CBM Micro Vertex Detector (MVD) comprises four planar detector stations, each divided in quadrants, and equipped with dedicated pixel sensors. Their operation results in about 300 W of total heat input. The challenging material budget of the stations ($< 0.5\%$ X_0) in combination with the operation in vacuum asks for an elaborated cooling concept. It is based on conductive cooling inside the geometrical acceptance employing thin sheets of high-performance materials as sensors carriers, featuring heat conductivities in the order of four times the one of copper, like poly-crystalline CVD-Diamond and Thermal Pyrolytic Graphite (TPG) [1]. These carriers guide the heat to actively cooled heat sinks outside the acceptance. This report presents systematic studies on the in situ cooling performance of MVD quadrants, with a focus on assessing TPG carriers of different thicknesses. Note, the in-plane heat conductivity of TPG is about 1600 W/mK at room temperature, and less than 20 W/mK perpendicular to the surface. Figure 1 (left) depicts the setup geometry by showing the temperature distribution on a TPG sensor carrier of the 3rd station attached to a actively cooled Aluminum heat sink, measured by the IR camera (Vario Cam). The heat load (in the order of 700 mW/cm^2) was mimicked by sheets of Kapton heaters, operated in a standardized vacuum test stand. The thermal performance was

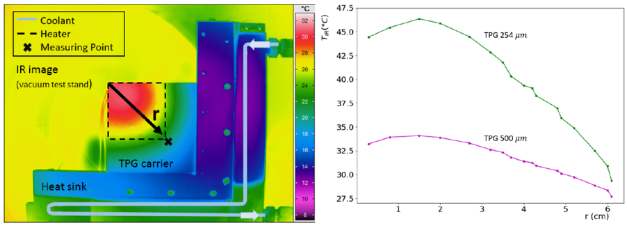

Figure 1: Left: IR image of a 500 µm thin 8×8 cm^2 TPG carrier attached to the heat sink, heat load of 15 W applied 180 s, $T_{cooling\ fluid} = 15$ °C, the heat sink was not corrected for emissivity. Right: Temperature along diagonal coordinate, both TPG thicknesses, $T_{cooling\ fluid} = 25$ °C, after 10 s of heating.

quantitatively characterized by analyzing temperature differences and heating curves of TPG sheets with different thicknesses (254 and 500 µm), shown in figures 1 (right) and 2, respectively. Fitting the temperature rise during the first 10 s ("fast") with $\propto (1 - \exp(-t/\tau))$ results in τ_{fast} of 3-4.5 s, almost independent of the TPG thickness. This

* supported by BMBF (05P15RFFC1), HGS-HIRe and GSI.

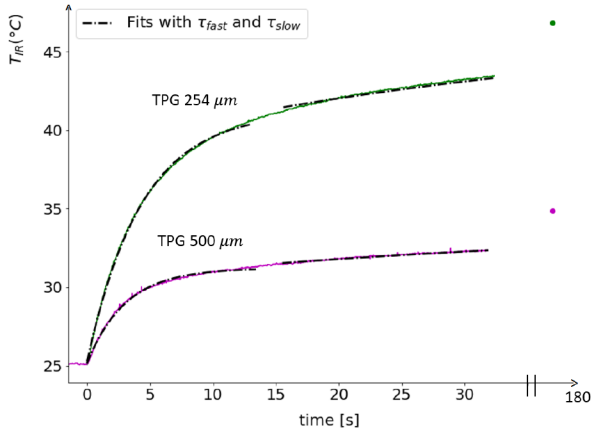

Figure 2: Heat-up curves of TPG carriers of two different thicknesses in vacuum, measured in the point depicted fig. 1, $T_{cooling\ fluid} = 25$ °C, relative adjustment of curves at $t = 0$ s. Broken lines: Exponential fits to initial and saturating time range, see text.

fast time constant is in agreement with the above mentioned outstanding in-plane heat conductivity of TPG, a result derived from solving the equation of heat conductivity [2]. A second common time constant of $\tau_{slow} \approx 45$ s characterizes the saturation phase.

In summary, a standardized test stand was set into operation to characterize the cooling performance of CBM-MVD quadrants. First results on the cooling performance, given by both, the material properties of TPG (τ_{fast}) and the power to evacuate the heat from the carrier (τ_{slow}), have been derived by measuring characteristic time constants of heating curves. The measured time constant τ_{fast} underlines the excellent thermal performance of this material. Temperature differences and τ_{slow} offer a quantitative assessment to further improve the heat evacuation and selecting the optimum TPG thickness. Next campaigns will focus on characterizing Parylen-coated TPG, even thinner pyrolytic graphite foils (PGS) and pCVD-Diamond. They will be complemented by and compared to thermal CAD simulations aiming at optimizing the contact to the heat sink and its design.

References

[1] Diamond Materials www.diamond-materials.com; Momentive momentive.com, Optigraph www.optigraph.eu

[2] P. Klaus, priv. communication

The TOF FAIR phase 0 project *

I. Deppner[1], *N. Herrmann*[1], *and the CBM-STAR eTOF working group*[1]
[1]Ruprecht-Karls-Universität Heidelberg, Heidelberg, Germany

The FAIR phase 0 project of TOF comprises the installation and operation of CBM TOF MRPCs (MRPC3a/b [1]) in the STAR experiment at BNL and the analysis of the data taken during the Beam Energy Scan (BESII) in 2019/20.

For BESII the STAR collaboration aims to increase the acceptance of their detector in the pseudorapidity range between $1.0 \leq \eta \leq 1.5$. Therefore an upgrade of the inner TPC (iTPC) is foreseen. The upgrade improves the momentum resolution for particle tracks pointing in forward direction. In order to improved also the particle identification (PID) capability in the same acceptance range an additional upgrade on the TOF system (eTOF) is intended. The impact of these upgrades are clearly visible in Figure 1 [2] showing the acceptance region and PID limitations for electrons (upper left), pions (upper right), kaons (lower left) and protons (lower right). The eTOF upgrade

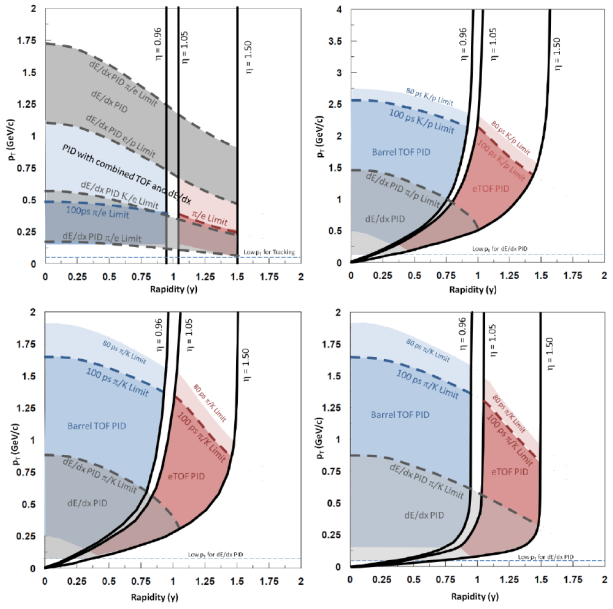

Figure 1: The $p_T - y$ acceptance region for electrons (upper left), pions (upper right), kaons (lower left) and protons (lower right) showing the limits due to tracking and PID.

requires the installation of a new TOF system in the abovementioned pseudorapidity range. This system will be provided by CBM TOF subgroups from China and Germany in the context of the CBM FAIR phase 0 program. It includes about 6 % of the CBM TOF MRPCs with the complete front end and readout electronics and the necessary software packages. The operation of this CBM TOF subsystem opens the opportunity to gain experience with the handling of the system, with the calibration procedures and data preprocessing leading to a reduced commissioning time within CBM later on. In addition the CBM members have access to the entire data set produced by STAR during BESII. After the BESII campaign in 2021 the full system will be dismantled and shipped to back FAIR where the componets will be used as part of the final CBM-TOF wall.

The conceptional design of the eTOF is depicted in Figure 2. Each STAR CBM TOF module contains 3 MRPC3a/b counters. The modules will be mounted on a frame sitting at the east side magnet pole tip of the STAR experiment forming a wheel. The modules are arranged in three layers grouped in 12 sectors which have full overlap with the TPC sectors. The eTOF wheel has in total an active area of about 9.3 m^2 and comprises 6912 readout channels. This geometry was implemented in CBM ROOT. Simulations show that in the fixed target mode which is also anticipated by the STAR collaboration a maximal particle flux of about 45 $\mathrm{Hz/cm}^2$ and a multi hit probability of 7.5 % is reached.

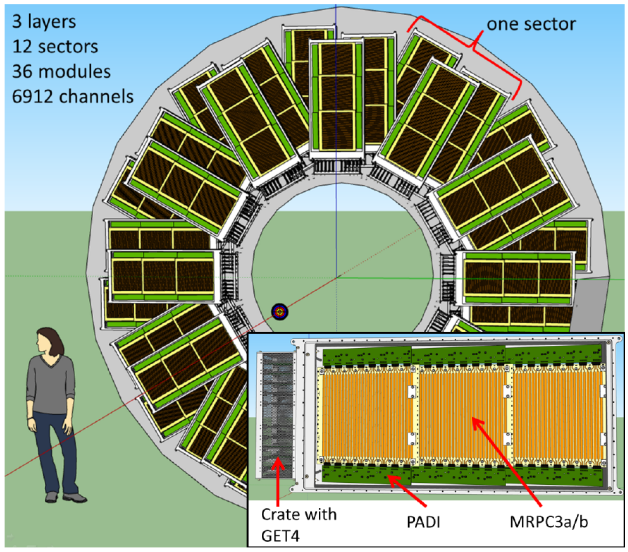

Figure 2: Illustration of the STAR eTOF wheel. The modules are arranged in 12 sectors and contain 3 MRPC3a/b each.

In order to make a first DAQ integration test a mod-

* This project was partially funded by BMBF 05P12VHFC7 and by EU/FP7-HadronPhysic3/WP19 and has received funding from the European Union's Horizon 2020 research and innovation program under grant agreement No 654168.

DOI:10.15120/GR-2017-1

ule (conf. Fig. 3) housing two MRPC3b counters produced at USTC was shipped to BNL and mounted at the 6 a clock position at the magnet pole tip in October 2016 (see Fig. 4). The goal is to participate in the physics run (Run17) starting in Feb. 2017 and test all components under real beam conditions. The counters were positioned behind each other in the module in order to find coincidences among themselves. The data readout is based on an AFCK

Figure 3: View inside the open STAR CBM TOF module.

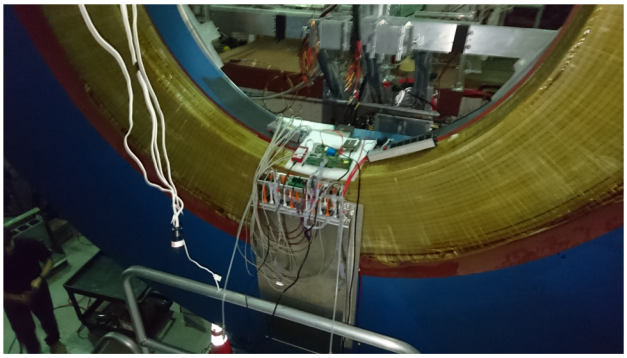

Figure 4: STAR CBM TOF module mounted on the east pole tip of the STAR experiment.

board and the FLES system as indicated in Fig. 5 which is in contrast to the triggered STAR DAQ free running. Since the AFCK is not magnetic field resistant it is placed in a region with very low field 6 m away from the module. The data are transmitted via 100 m long optical fibers to the FLIB of the DAQ-PC which is sitting in the STAR DAQ-room. A synchronization scheme has been developed for the clocking systems by locking our CLOSY system to the STAR TDC clock and the AFCK firmware was extended to interpret the trigger token sent by the STAR trigger system and inserting it into the data stream. If such a token word is detected in the data by the CBM monitoring system based on CBMROOT a window with a proper time shift is extracted from the data stream and the data are sent to the STAR event builder. The system can be inspected and monitored via the CBMROOT web-interface and in general is setup such that no CBM manpower is required to be present on site during data taking.

That the DAQ system and the interface to STAR indeed works can be seen in Figure 6. It shows the time difference between the MRPC hits and the STAR trigger. At a time difference of about 1.75 μs a correlation between trigger and MRPC hits is visible.

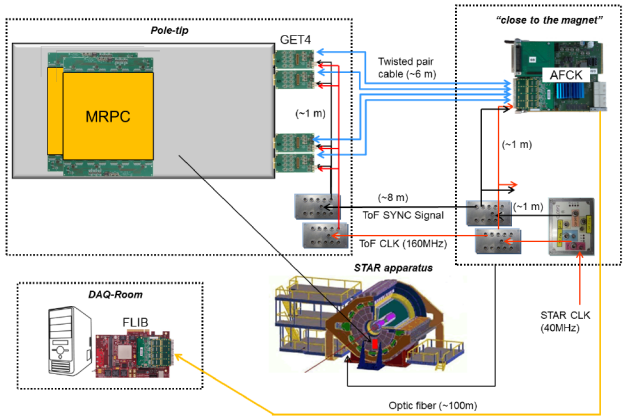

Figure 5: Overview of the CBM components used during the STAR physics run in 2017.

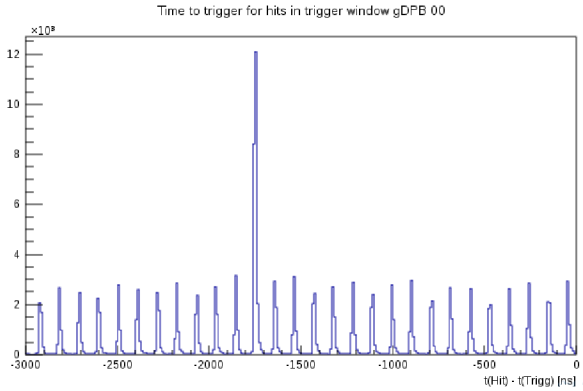

Figure 6: Time difference between the MRPC hits and the trigger token. At about 1.75 μs a correlation between trigger and MRPC hits is visible.

The time line for the next major steps are the following:

- Installation of a full sector (3 modules) in summer 2017,
- 2^{nd} system integration test with one full sector by participating in the physics run (Run18) in February 2018,
- shipping 36 modules including infrastructure to BNL in summer 2018,
- installation and commissioning in fall 2018,
- start of BESII campaign in February 2019,
- decommission and shipping all modules including infrastructure to FAIR in 2021.

DOI:10.15120/GR-2017-1

References

[1] N. Herrmann et al. “CBM-TOF Technical Design Report”, http://repository.gsi.de/record/109024/files/, October 2014

[2] “Physics Program for the STAR/CBM eTOF Upgrade”, arXiv:1609.05102

DOI:10.15120/GR-2017-1

Common CBM beam test at the CERN SPS 2016

D. Emschermann and the CBM collaboration
GSI, Darmstadt, Germany

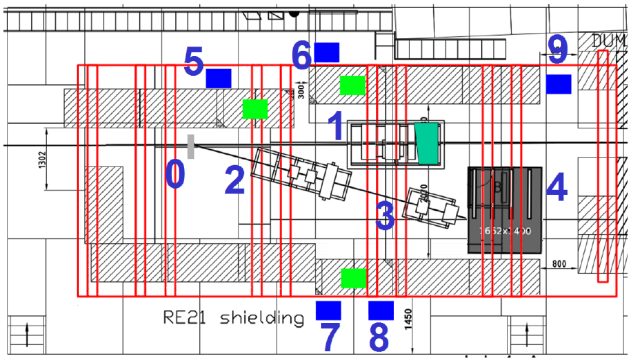

Figure 1: Layout of the RE21 experimental area. 0: Pb-foil target, 1: mainframe with TOF MRPC and MUCH GEM detectors, 2: Bucharest TRD setup, 3: Bucharest TOF MRPC setup, 4: Münster/Frankfurt TRD setup, 5: service rack for TOF/MUCH mainframe, 6: free-streaming DAQ rack, 7: service and readout rack for Bucharest detectors, 8: TRD gas analysis rack, 9: service and readout rack for Münster/Frankfurt detectors

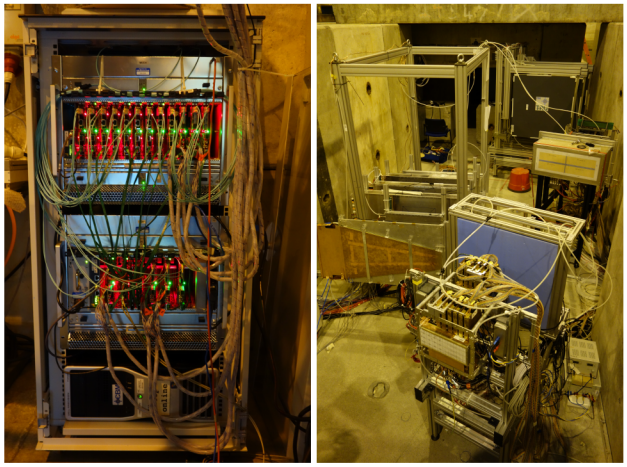

Figure 2: (left) The free-streaming DAQ system (6) for MUCH and TOF consisting of 18 AFCK boards operated in 2 microTCA crates in a common rack. (right) A downstream view of the RE21 detectors during the setup phase.

In November and December 2016 the CBM DAQ, MUCH, TOF and TRD subgroups gathered at the CERN SPS for the annual heavy ion run [1, 2, 3, 4, 5, 6]. A dedicated radiation bunker, see Fig. 1, was prepared along the H4 beamline in the North Area. A large number of full-size detector prototypes (MWPCs, GEMs, MRPCs, Bakelite RPCs and diamond counters) from pre-series production were installed in the zone, see Fig. 2 (right). The SPS accelerator delivered a primary Pb-beam at momenta of 13 AGeV/c, 30 AGeV/c and 150 AGeV/c which was impinging on a 1 mm thick Pb-foil as target. The CBM detectors were installed at small angles to the primary beam to measure the spray of secondary particles at hit rates of up to few kHz/cm^2.

A highlight of this beam test was the new, free-streaming DAQ system, see Fig. 2 (left). It was used to readout the TOF MRPCs equipped with GET4 electronics (using AFCKs with gDPB firmware), MUCH GEM detectors readout with NXYTER v2.0 ASICs (employing AFCKs with nDPB firmware). These two DAQ branches were kept in phase by the timing and synchronisation system [7] (made of AFCKs with tDPB firmware). In a separate TRD DAQ setup, the new SPADIC v2.0 was readout with an AFCK board connected to a FLIB node [8]. New hardware [9] and software tools for configuration and online monitoring for the DAQ system were developed for this beamtest [10, 11, 12]. The operation of CBM subsystems with a common DAQ system is a first step towards the future miniCBM@SIS18 setup [13].

References

[1] F. Fidorra et al., *Development and construction of a gas system for the CBM-TRD*, this report

[2] P. Kähler et al., *Operation and measurement programme of a SPADIC readout chain on type-8 CBM-TRD prototypes at the CERN-SPS in 2016*, this report

[3] F. Roether et al., *Construction of type-8 MWPCs for the CBM-TRD*, this report

[4] A. Kumar et al., *Beamtest of triple GEM prototypes with Pb+Pb collisions at CERN SPS*, this report

[5] A. Bercuci et al., *Bucharest RPC and TRD prototypes at the CERN-SPS test beam in 2016*, this report

[6] M. Petriş et al., *CERN-SPS in-beam performance test of the new strip readout MRPC prototypes for the inner zone of the CBM-TOF wall*, this report

[7] L. Meder et al., *Integration of the Timing Synchronizer System into the Readout System for the Beamtime at CERN SPS in 2016*, this report

[8] C. de J. García Chávez et al., *Development of the SPADIC v2.0 readout chain at the CERN-SPS in 2016*, this report

[9] C. de J. García Chávez et al., *Design and development of the nDPB FPGA mezzanine card*, this report

[10] P.-A. Loizeau et al., *Control software for the DPB based readout chains and related beamtime activities*, this report

[11] F. Uhlig, *Online monitoring with* `cbmroot`, this report

[12] M. Mitkov et al., *Prototype of EPICS based detector control system for the ToF test stand at CERN 2016*, this report

[13] C. Sturm et al., *mCBM@SIS18 - a CBM full system test in high-rate nucleus-nucleus collisions at GSI / FAIR*, this report

DOI:10.15120/GR-2017-1

DiRICH readout electronics - status and first measurements

V. Patel[1], *C. Pauly*[1], *J. Michel*[2], *P. Skott*[3], *M. Traxler*[3], *C. Ugur*[3], *and K.-H. Kampert*[1]
[1]Wuppertal university; [2]Frankfurt university; [3]GSI Darmstadt

The realization of the new DiRICH electronic readout chain for Hamamatsu H12700 MAPMTs (CBM- and HADES RICH detectors), as well as for Photonis MCP sensors (PANDA DIRC), has seen major progress over the last year. Since mid 2016, first prototype modules of all components are available for detailed testing and evaluation. Figure 1 shows photographs of a partly equipped 3x2 MAPMT module, and of the individual DiRICH, DiRICH-Combiner, and DiRICH-Power cards. All these modules seem to work as expected, no critical design flaws have been encountered yet.

The only major item still missing is a working FPGA design for the full 32ch TDC. The TDC base design (even with 64 channels) for the Lattice ECP3 platform of the HADES TRB3 "Trigger and Readout board" is in use since many years, and has to be adapted now to the Lattice ECP5 platform of the DiRICH module. Here, the loss of the main FPGA-TDC developer is causing a critical delay. So far, only a first 4 channel version of the TDC is available for the DiRICH, proving the principal feasibility of the project. However, all tests of the DiRICH readout chain so far look very promising, some first results are summarized below.

Testing of the full readout chain is carried out at two places: At GSI, in the HADES cave, a large test chamber has been installed, already carrying the new HADES RICH MAPMT photon detector flange (see Figure 2). This setup will later allow for a full size system test, when larger numbers of modules become available. After successful commissioning of the new photon detector, the whole detector flange will be craned to the HADES frame and mounted to the HADES RICH. At the moment, blind flanges cover all open module ports, allowing for tests with single MAPMTs and few modules. A pulsed laser system (Picoquant 630nm, 50ps pulse length, kindly provided by the GSI PANDA group) is installed in the tank, allowing for precise timing measurements based on single photons. An additional LED light source in the tank, connected to an adjustable DC current source, allows for high rate tests with uncorrelated photon rates (in addition to the triggered light source) of up to several 100 kHz per channel, comparable to the maximum photon rates expected for CBM SIS 100 high rate experiments.

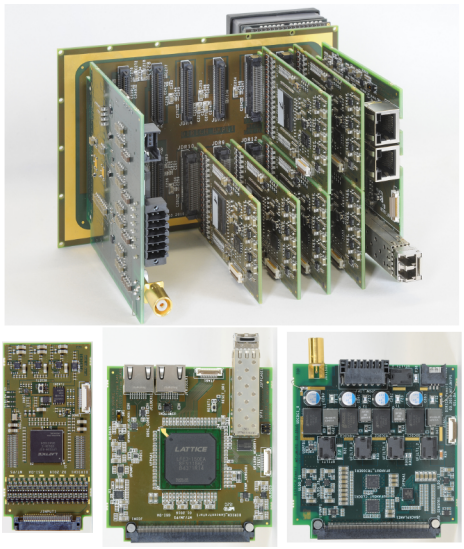

Figure 1: A 3x2 MAPMT readout module (top), with one out of 6 MAPMTs on front side, and few 32ch DIRICH FPGA-TDC frontend modules (lower left), a DiRICH-Power supply module (lower right), and a DiRICH-Combiner module (lower center).

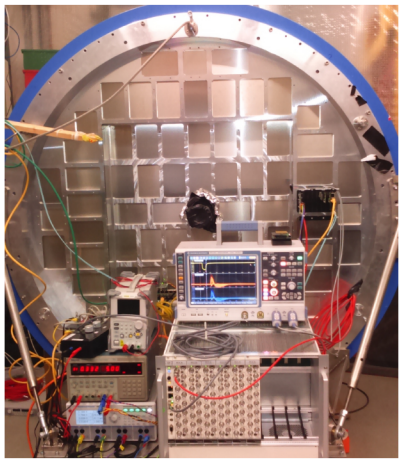

Figure 2: Test setup in the HADES cave, showing the new HADES RICH photon detector flange mounted to the test chamber, with one 3x2 readout module installed for testing.

The new CBM RICH prototype box for COSY beam tests is used for smaller scale tests of up to 2 fully equipped readout modules at Wuppertal university (see [1]).

The most critical part in the DiRICH design is the analog input stage. The input signals of the MAPMTs (few mV average amplitude for single photons) are galvanically decoupled using transformers, and then amplified ($\simeq \times 30$) in a single stage transistor amplifier operating at very low Vcc of only 1.1V to minimize power consumtion. The amplified signal is then discriminated and time stamped inside the FPGA.

DOI:10.15120/GR-2017-1

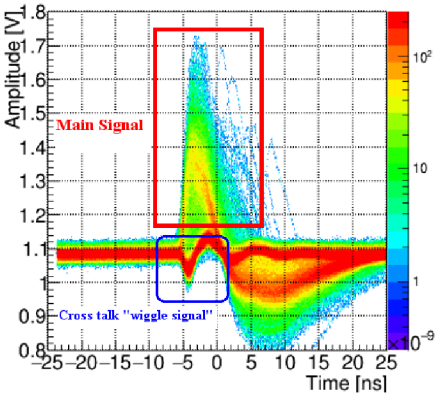

Figure 3: Typical MAPMT single photon signals from DIRICH after preamplification.

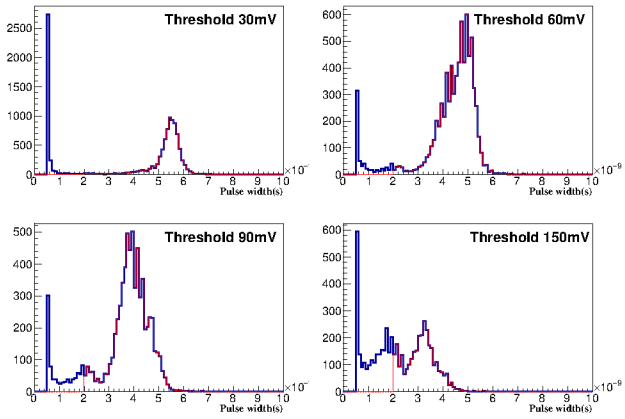

Figure 4: Time over threshold information for various software threshold settings

In order to test the analog part, we have equipped a single DiRICH module with two active, 4 GHz oscilloscope probes (input impedance 0.8 pF), read out by a fast digital oscilloscope. The probes are connected to the preamp output of two different channels. This setup serves to visualize the amplified input signals directly before entering the FPGA for discrimination and digitization. Moreover, the digital scope allows us to save the full signal traces of both channels for later offline analysis (with up to 100 events/second). Analyzing these data offline allows us to simulate the FPGA functionality (TDC and discrimination) in software, and to study the leading- and trailing edge timing precision, Time-over-Threshold measurement, threshold behaviour, efficiency, or noise, independant of the FPGA-TDC itself. In addition, one can also correlate these time-based measurements with signal amplitude or charge extracted from the scope traces (which are not available from the TDC measurement), for performance evaluation. This approach turned out to be extremely helpful not only for characterizing the analog input stage, but also for debugging of the FPGA-TDC design, since we know exactly what data to expect from the TDC measurement.

Figure 3 shows the preamplifier output signal for single photon pulses, directly before discrimination in the FPGA. After shaping, the photon signals have a mean positive amplitude of 250 mV (gain $\simeq \times$ 30), with a FWHM of 4-5 ns. A pronounced undershoot of the shaped signal is intentional in order to achieve a fast threshold crossing for trailing edge time measurement.

The laser intensity in these measurements was adjusted such, that only in 10% of pulses a single photon is detected in a given channel. In triggered events with no photon hitting the particular channel, a different signal shape can be observed, attributed to a capacitive coupling in the MAPMT anode plate. This "wiggle" signal is of opposite polarity, and comparatively small. The amplitude of this signal scales with the number of simultaneous photon hits on the full MAPMT surface, which is here in the order of 6-10, a realistic upper value for later detector operation. For low discriminator threshold settings, this cross talk signal could produce additional "ghost" hits, causing smearing of the Cherenkov ring pattern. This effect of strongly increased cross talk hits at lower thresholds has been already observed (though not fully understood at that time) in the last CERN test beam 2014, where the amplitude sensitive PADIWA readout chain was used, triggering on the leading edge of the signal only. In previous measurements using the charge-sensitive nXYter readout chain, this cross talk signal was much suppressed due to its bipolar shape in combination with the large integration time of the slow shaping amplifier input stage.

A powerful tool to effectively suppress these cross talk "wiggle" pulses in the DiRICH readout is provided by the simultaneous measurement of leading- and trailing edge time, i.e. by the Time-over-Threshold (ToT) of the signal. For relatively low thresholds (30-90 mV after preamp), the ToT of the wiggle signal is rather small (below 1-2 ns), where the single-photon pulses have a ToT in the order of 4-5 ns. The observed ToT distribution for various threshold settings (based on the offline analysis of the scope trace data) is shown in Figure 4. Applying a cut of ToT >2 ns (red graph), the pulses induced by crosstalk can be easily suppressed, as long as the threshold is reasonably low (<100 mV).

The effectiveness of the ToT cut can be clearly observed in the leading/rising edge arrival time distribution with respect to the trigger signal of the laser pulser, shown in Figure 5. Without ToT cut, two peaks are observed: The early peak around T=0 ns stems from real photon hits, where the hits induced by crosstalk cause a delayed signal around T=4 ns due to their opposite polarity. Applying the cut on ToT > 2 ns completely suppresses this delayed peak without loss of real photon events, even at very low thresholds (red graph). The width of the photon peak (RMS $\simeq$ 480 ps) corresponds well to the expected PMT timing precision (MAPMT Transit-Time-Spread TTS $\simeq$ 300 – 400 ps), in particular if keeping in mind that no walk correction is applied.

DOI:10.15120/GR-2017-1

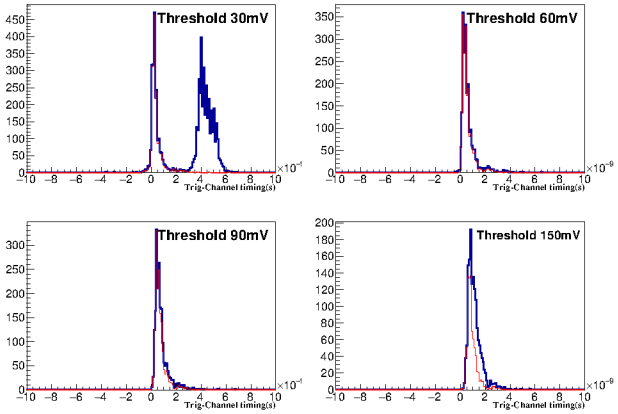

Figure 5: Leading edge timing difference between laser trigger and one of the channels

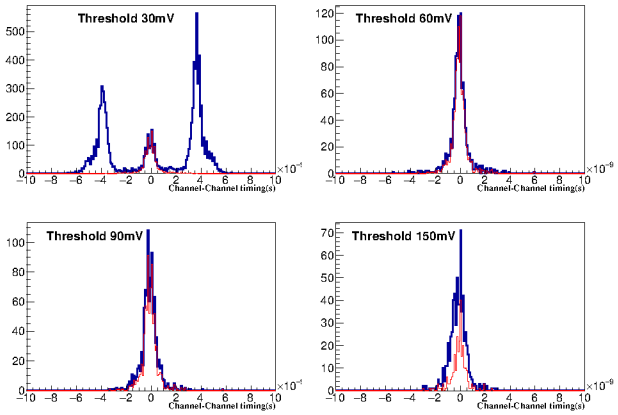

Figure 6: Leading edge timing difference between two channels

Figure 6 shows the leading edge time difference between the two channels equipped with the scope probes. This distribution, with its three distinct peaks in the time difference observed at low threshold, is well reproduced also in the first measurements with the full FPGA-TDC, but caused some confusion at first observation. It can now be fully understood based on the signal characteristics discussed above: The center peak, around ΔT=0, is caused by events, where both channels either detected one simultaneous photon each (laser pulse length 50 ps), or both channels only detected a cross talk signal (the latter is suppressed here by the scope acquisition trigger). The side peaks at +/- 4 ns correspond to events with a photon in one channel, and a cross talk signal in the other (blue distribution). Applying the ToT cut on both individual channels fully suppresses the side peaks (red distribution), and gives a nice single correlation peak close to $\Delta T \simeq 0$. The width of this peak (RMS $\simeq$ 650 ps) is again a good measure for the overall system timing precision, and is in fair agreement with the expected value of $\sqrt{2} \times TTS$=430–550 ps.

The DiRICH-Power module allows two different operation modes to provide LV power to all modules: Either

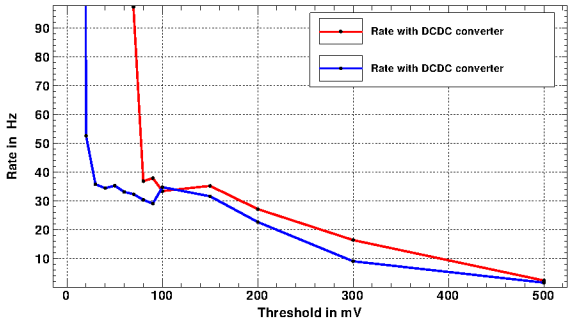

Figure 7: Rate using DCDC and without DCDC converter.

using on-board DCDC converters to generate the required 1.1 V / 1.2 V / 2.5 V and 3.5 V supply voltages out of a single low-current input at 20-30 V, or by external supply via 4 different input lines, providing only filtering and monitoring on the module itself. The second method avoids operation of noisy DCDC converters close to the sensitive analog input electronics of the DIRICH modules, but requires substantial cabling effort, in particular in view of the large required current (up to 15 A) on the 1.1 V supply line, where the voltage drop on the supply cables becomes substantial. A comparison of both operation modes is given in Figure 7, showing the detected hit rate of a single MAPMT channel as function of threshold. The observed plateau around 35 Hz corresponds to the MAPMT single photon dark rate in the given pixel. Without using the DCDC supply mode, threshold settings down to 20 mV can be achieved (after preamplification, corresponding to $<$1 mV MAPMT signal). In DCDC powering mode, the system noise kicks in at thresholds around 75 mV. However, additional cuts on the ToT will allow to partly suppress this noise in the offline analysis. Additional copper shielding enclosing the DCDC converters is already foreseen and will be tested.

The first tests of the new DiRICH readout concept look very promising, and seem to qualify the overall concept. In particular, the importance of the ToT-measurement for background suppression in comparison to simple leading edge measurement already became evident. A few minor design issues have already been found, and will be fixed in a second iteration of the DiRICH module, which is under production now.

For further validation of the concept a test beam at COSY/Jülich is scheduled for end of May, where two fully equipped 2x3 MAPMT modules will be put into operation. We hope, that a first 32ch FPGA-TDC design will become available until then. If everything goes well, we plan to start mass production of all modules end of 2017, in order to equip the full HADES RICH detector in time for the next HADES beamtime at SIS18 earliest mid 2018.

References

[1] C. Pauly et al., "A small RICH prototype for beam tests at COSY", this report.

DOI:10.15120/GR-2017-1

mCBM@SIS18 – a CBM full system test-setup for high-rate nucleus-nucleus collisions at GSI / FAIR

C. Sturm[1], J. de Cuveland[3], D. Emschermann[1], V. Friese[1], N. Herrmann[2], P.-A. Loizeau[1], W. Niebur[1], A. Senger[1], F. Uhlig[1] for the CBM collaboration

[1]GSI, Darmstadt, Germany; [2]Ruprecht-Karls-Universität Heidelberg, Germany; [3]Frankfurt Institute of Advanced Studies (FIAS), Frankfurt am Main, Germany

The Compressed Baryonic Matter experiment (CBM) is one of the major experimental projects at the upcoming FAIR facility. It will explore strongly interacting matter at highest net-baryon densities by investigating nucleus-nucleus collisions in fixed-target mode with extracted beams from the SIS100. The unique feature of CBM is its high-rate capability of up to 10^7 interactions per second, which will make it sensitive to extremely rare probes and, consequently, will give it a high discovery potential. In order to achieve these ambitious goals, CBM will employ fast and radiation-hard detectors and readout electronics. Moreover, a novel, free-streaming data acquisition system will be used, which aggregates the data sent by the self-triggered front-end electronics and push them to an online compute farm for data reconstruction and selection in real time.

By today, the design of the detector and electronics components for CBM is largely completed, and series production is going to start. The components were tested in the laboratory and in beam. However, it is highly desirable to test and optimize the operation of the full system of complex hard- and software components – from the detectors over the readout ASICs and the DAQ to on- and offline data processing and analysis – under realistic experiment conditions before the installation and commissioning of the full CBM detector setup.

We thus are going to install a full-system test-setup for CBM at the GSI/FAIR host lab site under the name *mCBM@SIS18* ("mini-CBM", later shortened to mCBM). The test setup shall include detector modules from all CBM detector subsystems (MVD, STS, RICH, MUCH, TRD, TOF, ECAL, see [1] - [5]) using (pre-)series production specimen. Hence, mCBM will allow to test and optimize

- the operation of the detector prototypes in a high-rate nucleus-nucleus collision environment,
- the free-streaming data acquisition system including the data transport to a high-performance computer farm located in the Green IT Cube,
- the online track and event reconstruction as well as event selection algorithms,
- the offline data analysis and
- the detector control system.

Commissioning and running mCBM in the first two years (2018 and 2019) will complete our knowledge on proper functioning as well as on the performance of the CBM detector systems and their associated Front-End Electronics (FEE) before the final series production starts. The experiences gained during the complete mCBM campaign will significantly shorten the commissioning period for the full CBM experiment at SIS100.

The mCBM test-setup will be positioned downstream a solid target under a polar angle of about 25° with respect to the primary beam (see Fig. 3 and 3). mCBM does not comprise a magnetic field, and, therefore, will measure charged particles produced in nucleus-nucleus collisions traversing the detector stations following straight trajectories. The tracking system comprises 2x STS (mSTS), 3x MUCH (mMUCH) and 4x TRD stations (mTRD) in total 9x track-

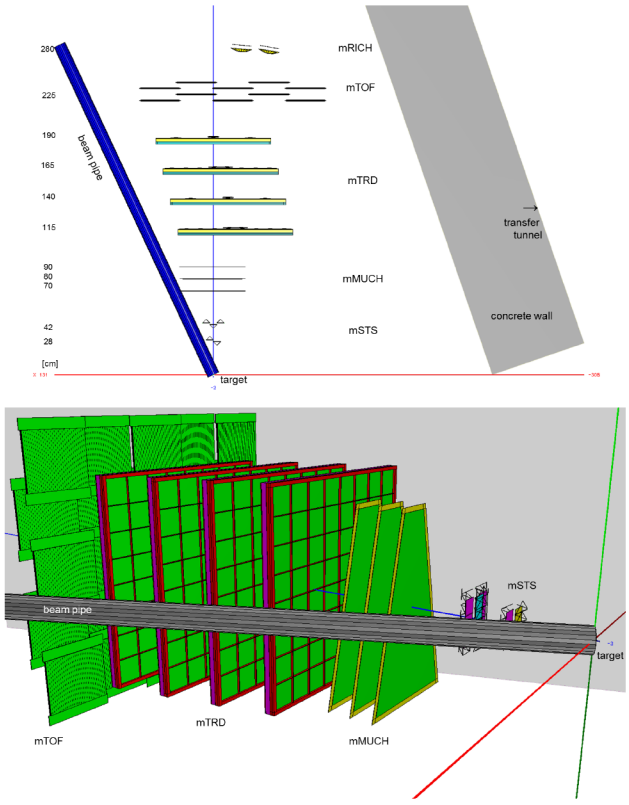

Figure 1: Top view (top panel) and side view (bottom panel) of the mCBM test setup at the HTD cave. The detector stations are aligned at an emission angle of about $\Theta_{lab} = 13°$ (beam pipe side, y = 0). Note, the GEM counters of the mMUCH subsystem are trapezoidal shaped (see lower panel), which is not visible in the top-view projection.

DOI:10.15120/GR-2017-1

ing layers which provide redundant position information and allow to perform tracklet searches. The setup will possess a high-resolution time-of-flight system consisting of a fast and segmented diamond counter for time-zero (T_0) determination in front of the target as well as a TOF stop wall (mTOF). Four RICH solid-state-modules forming the mRICH subsystem will be placed behind the mTOF detector and deliver a second measurement of the particle velocity in a selected acceptance window. A small calorimeter (mECAL) will also be mounted behind the mTOF covering a reduced acceptance. Additionally, 8x PSD prototype-modules (mPSD) will be used to characterize the collision geometry. In a later stage MVD stations (mMVD) will be included into the test-setup enabling a high-precision vertex reconstruction. For tracks passing the active area of the mSTS, mMUCH, mTRD and mTOF subsystems the covered Θ_{lab} range results to $13° - 37°$. According to the needs, the initial configuration of the mCBM test-setup is rather versatile and can be variably adapted.

The mCBM design focuses on the system performance aspect integrating existing (or currently under construction) prototype modules of all CBM detector subsystems into a common, high-performance free-streaming data acquisition (DAQ) system. The detector stations will be equipped with final readout electronics containing ultra-fast and radiation-tolerant ASICs as front-end chips followed by CERN GBTx-based radiation-tolerant data aggregation units. Further down-stream, the data streams are handled by Data Processing Boards (DPB) containing powerful FPGAs and are forwarded via FLES Input Boards (FLIB), a PCIe based FPGA board, to a large-scale computer farm, the First-Level Event Selector (FLES), which performs on-line track and event reconstruction and selection, see Fig. 2.

The installation site for the mCBM test-setup is the detector test area named HTD in the GSI nomenclature (see Fig. 3) situated at the beam entrance of the experimental area cave-C (HTC) hosting the nuclear structure experiment R^{3}B. Although the space is very limited in the HTD area, the compact mCBM setup measuring a full length of about 3 m will fit into the HTD cave.

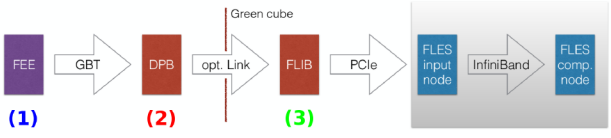

Figure 2: Envisaged mCBM readout chain for the startup phase, based on DPB and FLIB. The mCBM subsystems are equipped with individual front-end electronics FEE (1). These front-ends are interfaced by the GBTx ASIC, which forwards the detector data via optical GBT link. All GBT links are received by the DBP layer located at 50 m distance in the DAQ container (2). The DPB is a FPGA based board which allows for subsystem specific pre-processing of the arriving data stream. A long distance optical link connects the DPB output to the FLIB board installed in the FLES input node in the Green IT Cube (3).

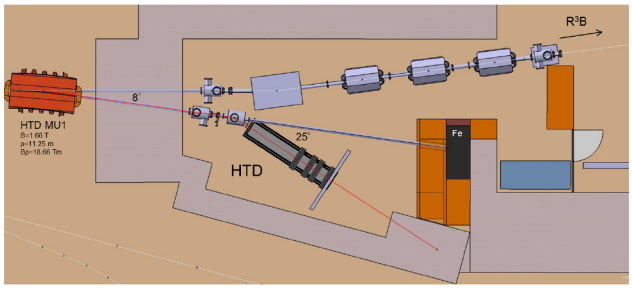

Figure 3: Design of the HTD site modified for the mCBM test-setup.

As illustrated in Fig. 3, the incoming beam will be either transported to the R^{3}B experiment or deflected to the detector test area HTD by a switching magnet (dipole magnet) mounted directly in front of cave-C carrying the name HTD MU1 in the GSI nomenclature. The design of the switching magnet HTD MU1 leads for the (design) track with a bending radius of $\rho = 6.25$ m to an effective deflection angle of 14.5°, corresponding to an magnetic rigidity of $B\rho = 10$ Tm. Using HTD MU1 as currently designed would substantially limit the projectile energy available at the HTD cave. Accordingly the maximum kinetic energy for heavy projectiles like Au would be limited to 0.45 AGeV generating unrealistic conditions due to a large number of low-momentum fragments emitted during the collision.

In order to exploit the full beam energy range of SIS18 we plan to bend the beam projectiles on the expanded track with a significantly larger bending radius ρ through the switching magnet HTD MU1. Choosing the expanded track with a radius of $\rho = 11.25$ m results for the top rigidity of the SIS18 synchrotron of 18.66 Tm in an effective deflection angle of 8.0°. The loss in horizontal aperture of 22 mm [6] is acceptable and will not limit the beam quality.

To verify the performance of the CBM data taking concept the mCBM setup will be used to reconstruct physics observables that can be compared to published data. A feasibility study with the mCBM setup was performed using the Λ production probability in heavy-ion collisions as a benchmark observable. At SIS18 beam energies Λ baryons are produced close to or below the free NN production threshold. Thus their production probability is rather small (see Table 1) posing a CBM-like challenge to the reconstruction and selection task.

	Ni + Ni at 1.93 AGeV	Au + Au at 1.24 AGeV
Λ production probability	$2.3 \cdot 10^{-2}$	$3.2 \cdot 10^{-2}$
signal counts	5645	2011
signal / background	8.4	0.24
significance	71.0	19.8
efficiency · acceptance	$1.7 \cdot 10^{-3}$	$7.0 \cdot 10^{-4}$

Table 1: Results of MC simulation of 10^8 UrQMD minimum-bias events with full mCBM detector response.

DOI:10.15120/GR-2017-1

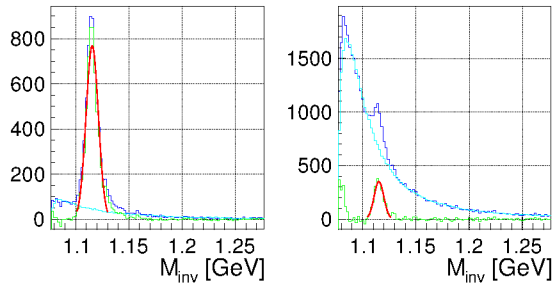

Figure 4: Λ-identification in UrQMD events in Ni + Ni collisions at 1.93 AGeV (left) and in Au + Au at 1.24 AGeV (right). Invariant mass distributions are shown for pair combinations (combinatorics) within events (dark blue), for pair combinations from mixed events (cyan) and for the subtracted distribution (green). Statistics information is obtained from a Gaussian fit to the subtracted distribution (red line) and is summarized in Table 1.

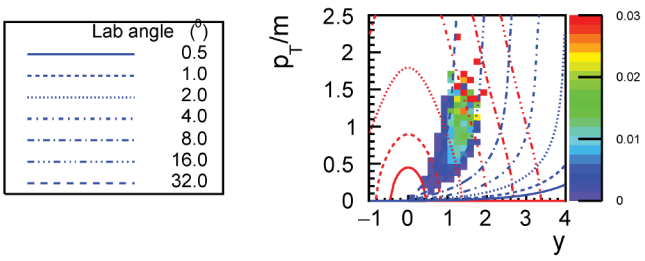

Figure 5: Efficiency of reconstructed Λ - baryons with mCBM produced in Ni + Ni collisions at 1.93 AGeV (input: events generated with UrQMD). Red and blue lines indicate constant laboratory momenta and laboratory polar angles, respectively.

Since mCBM does not include a magnetic field for momentum measurement, the reconstruction has to be done via time-of-flight (TOF) and track topology. That the limited information available is sufficient for Λ reconstruction is demonstrated by a MC simulation, modeling the full data analysis chain. For simplicity, only STS and TOF hits are considered for the reconstruction algorithm.

The result of the procedure for 10^8 minimum bias UrQMD events of the reactions Ni + Ni at an incident energy of 1.93 AGeV and Au + Au at 1.24 AGeV is shown in Fig. 4.

The phase space coverage is shown in Fig. 5 demonstrating that the acceptance of mCBM is limited to a small angular range close to mid-rapidity. In this range published data are available in [7] [1] that the mCBM results can be quantitatively compared to. It is worth noting that the technical goal and challenge is to reconstruct the invariant mass distributions shown in Fig. 4 within a time period of 10 s data taking at SIS18, assuming a beam intensity of 10^8 ions per second bombarded on a 10 % interaction target.

To get even closer to the load anticipated for CBM operation at SIS100 the feasibility of reconstructing Λ baryons in the heavier system Au + Au implying lower beam energies was investigated. Fig. 4 (right) presents the results of the analysis for the reaction Au + Au at an incident beam energy of 1.24 AGeV employing the same selection cuts that were used for the Ni + Ni analysis (see Fig. 4, left panel). After background subtraction a clear peak is visible albeit with a much worse signal to background ratio as compared to the Ni + Ni case (see Table 1). Improvements are certainly possible by tuning the selection cut values. However, at the current state of planning the presented performance obtained on a clean event based reconstruction is considered to be sufficient to demonstrate mCBM's capabilities.

Thus also all the background rejection strategies necessary to reconstruct rare probes with CBM at SIS100 can be prepared and exercised with mCBM. In addition, if the technical goals of mCBM are achieved a measurement of the Λ production excitation function should become feasible. This was not yet measured in the SIS18 beam energy range thus offering a unique opportunity to contribute to world data, although the covered phase space is limited and therefore systematic errors become large when extrapolating to unmeasured regions.

The successful implementation and demonstration of the technical capabilities would also open the road to more relevant physics observables like the measurement of light hypernuclei. The beam time request for more physics oriented observables will be placed in the next beamtime period from 2020 – 2021, once the preliminary results are supporting the high expectations.

References

[1] J. Heuser, W. F.J. Müller, V. Pugatch, P. Senger, C. J. Schmidt, C. Sturm and U. Frankenfeld, Technical Design Report for the CBM Silicon Tracking System (STS), GSI-2013-05499, http://repository.gsi.de/record/54798

[2] S. Chattopadhyay, Y. P. Viyogi, P. Senger, W. F.J. Müller and C. J. Schmidt, Technical Design Report for the CBM : Muon Chambers (MuCh), GSI-2015-02580, https://repository.gsi.de/record/161297

[3] C. Höhne, Technical Design Report for the CBM Ring Imaging Cherenkov Detector (RICH), GSI-2014-00528, http://repository.gsi.de/record/65526

[4] N. Herrmann, Technical Design Report for the CBM Time-of-Flight System (TOF), GSI-2015-01999, https://repository.gsi.de/record/109024

[5] F. Guber and I. Selyuzhenkov, Technical Design Report for the CBM Projectile Spectator Detector (PSD), GSI-2015-02020, https://repository.gsi.de/record/109059

[6] C. Mühle (GSI), private communication

[7] M. Merschmeyer et al. (FOPI collaboration), K^0 and Λ production in Ni+Ni collisions near threshold, Phys. Rev. C 76 (2007) 024906

[1] HADES results on Λ production in Au + Au collisions at 1.23 AGeV will be published soon.

A slow control system for the HADES and CBM RICH detectors *

A. Weber[1], *P. Zumbruch*[2], *and C. Höhne*[1]
[1]Justus-Liebig Universität, Giessen, Germany; [2]GSI, Darmstadt, Germany

An EPICS based slow control system for the HADES RICH700 upgrade and the future CBM RICH is developed. The slow control system is server-client-model based and highly flexible due to variations in the experimental setup. The control software for the ISEG HV power supply (see Fig. 1) is designed in a 3 layer outline. It allows the control of every channel of every module of the crate individually, but also the control of predefined groups of channels from different modules. In addition it is possible to group channels via the GUI, too. The ISEG HV crate (*ECH 44A*) has a *CC24* Master module which includes the EPICS IOC. This allows to run the slow control software of the crate without any additional computer. The HV crate has 6 *EHS F620n-F_SHV* modules with 16 channels each. The modules are limited to 1,5 kV and with single channel floating-GND.

Figure 1: The ISEG crate with 6 modules à 16 channels and a CC24 master.

To cope with low voltage a TDK Lambda Genesis 60-40 is used (see Fig.2). The EPICS IOC runs on an own computer which is connected to the TDK Lambda via LAN. The IOC uses `StreamDevice` with an own protocol for the device. It is possible to control the voltage, set current limits and control different statuses of the LV device.

Figure 2: The TDK Lamda low voltage power supply.

During the experiment the temperature and the humidity will be measured. The temperature is mapped with many DS18B20 1-Wire Sensors from *Maxim Integrated*. To measure the humidity HDC1000 humidity sensors from *Texas Instruments* are used. These sensors support the I^2C protocol and have address pins which allow to use up to 4 of these sensors at one port (see Fig.3). Both sensor types are connected to a HadCon2 Board which controls the pins. The HadCon2 is connected to a raspberry pi 2 model B via USB connection. The EPICS IOC runs on the raspberry pi and sends the HadCon2 the commands for the measurement of temperature and humidity.

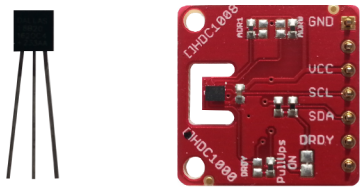

Figure 3: left: One DS18B20 1-wire sensor from Maxim Integrated. right: A HDC1000 sensor on a breakout board.

The HADES RICH upgrade will use many DIRICH boards which have a 1-wire temperature sensor. This temperature can be readout via the TrbNet. Therefore an EPICS IOC is written. It gets the value from many different boards with one call which reduces the traffic on the TrbNet. It is also possible to get more further status values from the TrbNet with the IOC.
The Control System Studio (CSS) is used as the GUI of the HADES RICH experiment and shows the EPICS process variables in a human readable, graphical layout (see Fig.4). It replaced the *Motif Editor and Display Manager* (MEDM) which is known from previous HADES running periods.

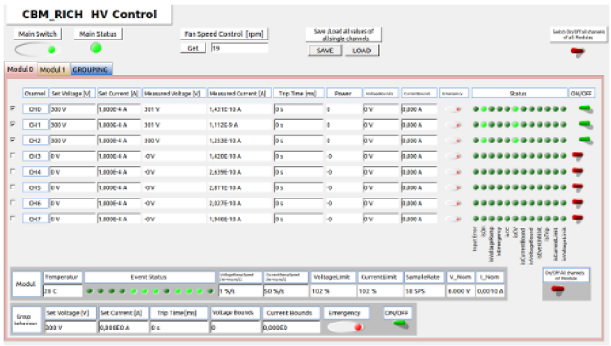

Figure 4: The CSS BOY GUI for the HV power supply.

* supported by BMBF grant 05P15RGFCA

DOI:10.15120/GR-2017-1

Performances of two strip-readout MRPC prototypes towards CBM-TOF *

P. Lyu[1], *Y. Wang*[1], *B. Guo*[1], *D. Han*[1], *Y. Li*[1], *N. Herrmann*[2], *I. Deppner*[2], *C. Simon*[2], *P. Weidenkaff*[2], *J. Frühau*[3], *P. Loizeau*[3], *and M. Kis*[3]

[1]Department of Engineering Physics, Tsinghua University, Beijing, China; [2]PI, Heidelberg University, Heidelberg, Germany; [3]GSI, Darmstadt, Germany

On basis of the strip-readout MRPC prototype produced and tested in 2014 [1], we have developed two new prototypes by improving original design aiming at the CBM-TOF's high rate situation [2]. They both apply double-stack structure, consisting of two mirrored stacks of resistive plates, which fit into the three parallel readout PCBs. In each stack, there are four 0.25 mm gas gaps divided by five resistive plates composed of the low-resistive glass [3]. The gas gaps are defined by nylon monofilaments spacers aiming at a more homogeneous gap width. On each readout PCB, the 32 readout strips are on a 10 mm pitch with 3 mm interval. Signals induced with both polarities are sent in differential fashion to the PADI front-end-electronics. Parameters of these two prototypes are shown in Fig.1. Among the two MRPCs, one is of the seal-sealed structure, which is named THU-DS. The other one is traditional unsealed MRPC, called THU-DU.

MRPC Parameter	Design Value/mm
PCB dimension	360 × 338
Glass dimension	330 × 276
Gas gap number	2 × 4
Gas gap width	0.25
Strip pitch	7 + 3
Strip length	270
Strip number	32
Detection area	317 × 270

Figure 1: Parameters of the strip-readout MRPCs.

The thought of self-sealed MRPC comes from the gas pollution caused by CBM-TOF's extremely high beam intensity. The gas exchange inside a gas box mainly occurs through diffusion which is dominated by several factors including boundary conditions. Less space for gas flowing outside the MRPC means the boundary is closer to the polluted gas area. We can infer that the gradient of impurities concentration is steeper, so the gas should exchange faster. A simulation was done to confirm this assumption [4]. The results are shown in Fig.2. In a horizontal transect inside a 100×100 cm^2 gas box under irradiated flux rate of 25 kHz/cm^2, Fig.2(a) demonstrates the concentration of pollutants produced in MRPC's effective area. In the 50×50 cm^2 MRPC area which is marked by the white dot line, there is a vortex caused by jet entrainment near the gas inlet at the left boundary, which results from pressure dropping around the inlet. The center of pollutants distribution is shifted to the vortex, and the maximum concentration is 20%. Then, the gas box volume is decreased to 60×60 cm^2, and the maximum value in the MRPC region drops by a great amount to 11.8% as shown in Fig.2(b). It is proved that small flow gas volume is propitious to weakening the influence of gas pollution.

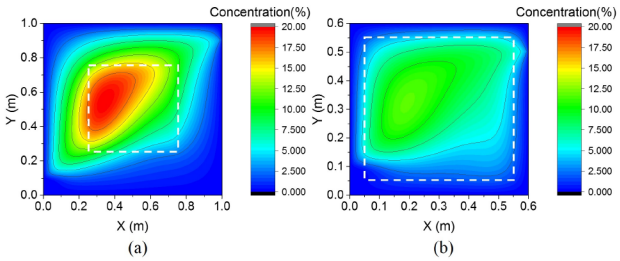

Figure 2: The simulated concentration distribution of gas pollutants produced by a 50×50 cm^2 MRPC (marked by white dot line) under 25 kHz/cm^2 particle flux.(a) The maximum concentraiton is 20% when putting this MRPC in a 100×100 cm^2 gas box. (b) The maximum concentration decreases to 11.8% when putting this MRPC in a 60×60 cm^2 gas box. [4]

To make the THU-DS self-sealed, two rectangular frames made of PMMA are inserted into the three readout PCBs as shown in Fig.3. Gas inlets and outlets are arranged on the two bars vertical to the direction of nylon monofilaments spacers. These frames are 5 mm in width and with the same height of each stack. They are fixed to the PCB surfaces with the silicon glue. When this MRPC is fully assembled, the silicon glue is again potted into outside edges in order to make the chamber gas tight.

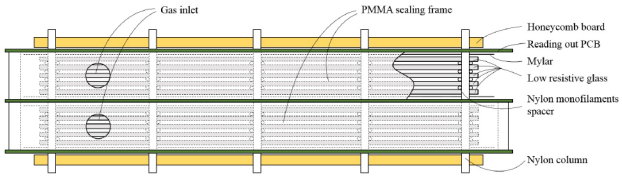

Figure 3: Sectional sketch of the THU-DS MRPC.

In order to further examine the performance of these two prototypes working under higher particle flux rate, they

* This study is supported by National Key Programme for S&T Research and Development under Grant No.2016YFA0400100, the Ministry of Science and Technology under Grant No.2015CB856905 and National Natural Science Foundation of China under Grant No.11420101004, 11461141011, 11275108.

have been tested in the 2015 November SPS beam time using the secondary particles from a 30 AGeV Pb beam hitting on a 1/2/3 mm Pb target. The layout of beamtest is shown in Fig.4 [5]. It contained two parts, the upper setting and lower setting. The THU-DS and THU-DU were installed among the upper setting. Theoretically the THU-DS could work independently, but for consistency with other chambers it was placed inside of the gas box together with THU-DU. The gas was injected first into the THU-DS directly from gas box inlet, and then it flew out from the prototype to the whole box. The gas mixture used was 90% $C_2H_2F_4$, 5% i-C_4H_{10} and 5% SF_6.

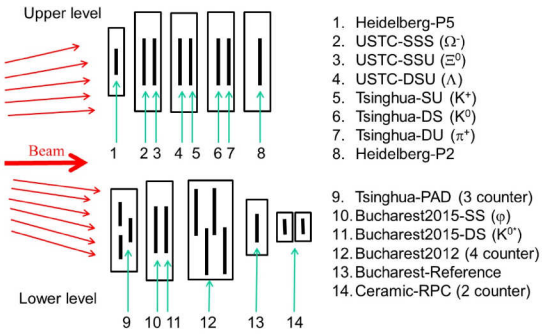

Figure 4: Setup sketch of TOF MRPCs in CERN SPS Nov 2015 beam time. The THU-DS and THU-DU were installed among upper level. [5]

The analysis on raw data from beam time was done with CBM-Root macros developed by TOF groups. In order to obtain the performance of each counter, one among them is taken as the reference of another. A series of calibration types, including strip alignment, velocity correction, gain correction and walk correction, were looped in an iterative way until the time of flight is no longer correlated to any of the interfering factors, and then the MRPCs' performances were obtained. An analysis scan of each 30-minute run throughout the beam time from Nov 28^{th} to Dec 1^{st} 2015 was completed. Data of efficiency scan and FEE threshold scan were selected and made the plots in Fig.5.

As shown in Fig.5(a), the efficiency of THU-DU enters into plateau region at 112 kV/cm and maintains around 98%. The THU-DS's efficiency is slightly lower at 97%. For the time resolution in Fig.5(b), it gets improved with higher applied voltage, and it decreases to 85 ps for both MRPCs when reaching nominal voltage. Assuming that the THU-DS and THU-DU are of the same time resolution, an independent value of $85/\sqrt{2} \approx 60$ ps for both counters is calculated. The cluster size grows with applied field in Fig.5(c) because of the expanded avanlanche. The THU-DS has a smaller value of 1.4.

A FFE threshold scan is demonstrated in Fig.5. Application of higher threshold helps to filter the noise, and thus we observe a better time resolution (Fig.5(f)). Signal loss caused by rising threshold, at the other hand, reduces the efficiency (Fig.5(e)) and cluster size (Fig.5(d)). All properties observed from THU-DS and THU-DU fit our expectation very well. Both of these two strip-readout MRPCs' performances prove that they are capable of requirements from the high-particle-rate TOF system include CBM TOF.

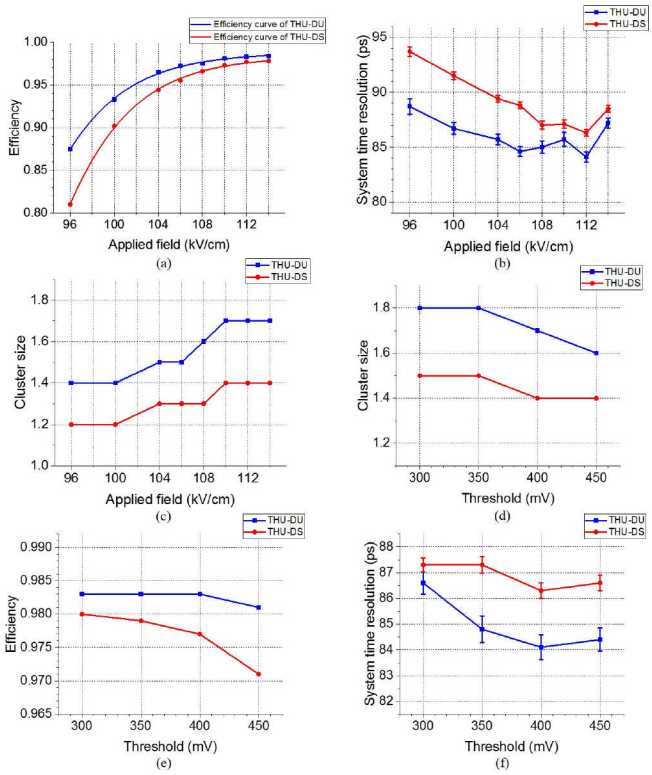

Figure 5: (a) Efficiency of THU-DS and THU-DU in HV scan. (b) System time resolution of THU-DS and THU-DU in HV scan. (c) Cluster size of THU-DS and THU-DU in HV scan. (d) Cluster size of THU-DS and THU-DU in FEE threshold scan. (e) Efficiency of THU-DS and THU-DU in FEE threshold scan. (f) System time resolution of THU-DS and THU-DU in FEE threshold scan.

However, neither obvious differences in the performances between the THU-DS and THU-DU nor the influences of gas aging have been found. At the moment, we are working on optimization of the sealed structure of THU-DS and confirmation on its recovering ability from higher rate condition. Further studies with the help of higher intensity beam is still necessary.

References

[1] Y. Wang, et al. JINST. 11 (2016) C08007.

[2] The CBM collaboration, Technical Design Report for the CBM Time-of-Flight System (TOF). (2014) 13.

[3] J. Wang, et al. Nucl. Instr. and Meth. A713 (2013) 40.

[4] P. Lyu, et al. JINST. 11 (2016) C11041.

[5] C. Simon, et al. CBM Progress Report 2015, 90.

DOI:10.15120/GR-2017-1

Prototype of EPICS based detector control system for the TOF test stand at CERN 2016

M. Mitkov[1], *P. Zumbruch*[1], *J. Frühauf*[1], *and I. Deppner*[2]
[1]GSI, Darmstadt, Germany; [2]Ruprecht-Karls-Universität, Heidelberg, Germany

During the Nov. beamtime 2016 at SPS/CERN, a setup with several ToF prototype detectors were controlled for the first time by an EPICS[1] based prototype **D**etector **C**ontrol **S**ystem (**DCS**). It featured full control, including software based open-loop control, monitoring, and alarming of the ToF Setup's devices operational parameters, which corresponds to a typical SCADA[2] System. In addition all relevant process variables (PVs) were archived for a long-term availability of data, e.g. for analysis.

Based on the open-sourced EPICS framework, i.a. featuring high scalability, modular design, and sustainability, this prototype consists of $\approx 10^3$ PVs and can almost freely be scaled up to larger experimental setups, e.g. in the FAIR phase 0 program at STAR/BNL and miniCBM or even the final CBM TOF wall, of up to 10^5-10^7 PVs. The communication between the different devices and the ToF DCS is based on Ethernet.

The current ToF DCS version supports the following devices:

- CAEN SY1527LC: High voltage power supply
- ISEG CC24: High voltage power supply
- TDK-LAMBDA GEN 90-8: Low voltage power supply
- Bronkhorst EL-Flow Series valve: Three input control valves and one output flow monitor
- ADAM CPWplus 150: Gas bottle scale for laboratory use

The headless CS-Studio[3] RDB[4] archiver application stores selected DCS detector control and monitoring values to a PostgreSQL Database. In our case those values are voltages and currents delivered by the high voltage (HV) and low voltage (LV) power supplies and the gas flow for 3 different gases delivered by the flow regulators of the gas-mixing station. With the CS-Studio Data Browser it is possible to visualize seamlessly historic and live data (see Fig. 1) in order to analyze the detector operation behavior.

The software open-loop control was programmed to protect the detectors from damages caused by e.g. a gas blockage by ramping down the HV but also to trigger an alert in order to inform the experimentalist in case e.g. of a gas leakage or a FEE power consumption mismatch.

All features are graphical visualized with CS-Studio. Figure 2 shows the main ToF DCS view, which contains

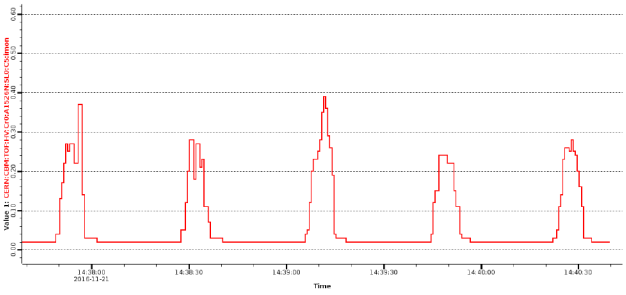

Figure 1: PV monitoring of the current of one high voltage channel af function of time. The spill structure of the beam is clearly reflected in the MRPC current.

a header monitoring the low voltages and the gas flows and a control part. The control part has different sub-menu tabs for getting access to each device or individual sub-detector, by default the high voltage tab is active.

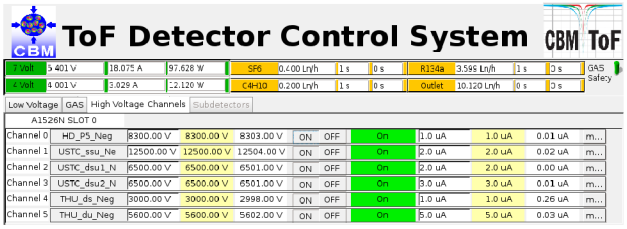

Figure 2: ToF DCS screenshot

We can conclude that the ToF DCS prototype successfully controlled, monitored and archived the ToF detector during the last beamtime 2016 at CERN. It can be extended for a larger setups, e.g. STAR at BNL, or final CBM. This current project of a ToF DCS prototype will be continued as a bachelor thesis' subject.

In the near future additional safety features will be implemented in the ToF DCS. One feature is a sound alarm informing the local operators if a value is not regular. A second feature could be to inform not present users an emergency case by email or sms[5].

References

[1] EPICS, http://www.aps.anl.gov/epics/

[2] K.Kasimir, G. Garcassi, Control System Studio Guide, 2016

[3] Time–of–Flight System(TOF), Technical Design Report for the CBM, 2014, Darmstadt

[1]Experimental Physics and Industrial Control System
[2]Supervisory Control and Data Acquisition
[3]Control System Studio is an Eclipse-based collection of tools to monitor and operate large scale control systems
[4]Relational Database
[5]Short Message Service

DOI:10.15120/GR-2017-1

Test performance of the basic architecture for the inner zone of the CBM-TOF wall using heavy-ion beam at SPS-CERN *

M. Petriş[1], *D. Bartoş*[1], *M. Petrovici*[1], *L. Rădulescu*[1], *V. Simion*[1], *J. Frühauf*[2], *P-A. Loizeau*[2], *I. Deppner*[3], *N. Herrmann*[3], *and C. Simon*[3]

[1]NIPNE, Bucharest, Romania; [2]GSI, Darmstadt, Germany; [3]PI, Heidelberg University, Germany

The Time Of Flight (TOF) subsystem is one of the core detectors of the CBM experiment. The TOF wall in conjuction with Silicon Tracking System (STS) is foreseen to identify charged hadrons, i.e. pions, kaons and protons, in the full acceptance of the system (the angular range covered by the STS detector of 2.5^0-25^0). It covers an active area of about 120 m^2 approximately rectangular in shape. A system time resolution of at least 80 ps including all possible contributions, such as electronics jitter and the resolution of the time reference system is needed. This requires a single channel time resolution better than 60 ps with an efficiency of at least 95%. Such a performance should be maintained up to a counting rate which, very close to the beam pipe, exceeds 30 kHz/cm^2 [1].

Our R&D activity has been focused on the development of a Multi-Gap RPC with Multi-Strip readout (MSM-GRPC) for high counting rate and multiplicity environment, as it is anticipated to be in the inner zone of the CBM-TOF. Based on the good results obtained with the narrow strip pitch (2.54 mm) double stack counter (2 x 5 gas gaps of 140 μm), in terms of efficiency, time and two-dimensional position resolutions [2], a new prototype with the strip pitch equal with 7.4 mm (5.6 mm strip width) and a strip length of 96 mm was designed and built. Construction details of this prototype, called RPC2012, and its performance in the in-beam tests performed at CERN-PS accelerator together with the concept of the modular configuration of the CBM-TOF inner wall based on this RPC architecture were reported in [3].

The prototype was tested at H4 beam line of CERN SPS-facility, using reaction products produced by an Ar beam of 13A GeV energy incident on a Pb target. The average obtained cluster size was 1.6 strips per hit and the time resolution, including the electronics contribution, was of ~60 ps [4]. For all these tests mentioned above a front-end electronics based on 8 channel NINO chip [5] was used for signal processing.

Here we report the performance, in close to real conditions, of this architecture operated with a FEE based on a 32 channel motherboard [1] containing 4 PADI chips[7], the front-end electronics anticipated to be used for the CBM-TOF wall. The signals were digitized by 32-channel FPGA-TDCs [8] and readout via TRB3 [9] data hubs. The in-beam test were performed at CERN-SPS with a 30A GeV Pb ions incident on a Pb target.

The CBM-TOF experimental setup was divided in "low rate" and "high rate" branches, the last one being positioned at a polar angle of about 3^0 relative to the beam axis. A comprehensive description of the whole setup is given in [6]. Our prototypes were positioned in the high rate setup, the RPC2012 prototype being 'sandwiched' between RPC2015 [11] and RPCref prototypes. A diamond detector positioned in front of the target together with RPCref positioned at the end of the set-up, delivered the information for particle velocity measurement. A photo of the "high rate" branch is shown in Fig. 1. The spatial position along the

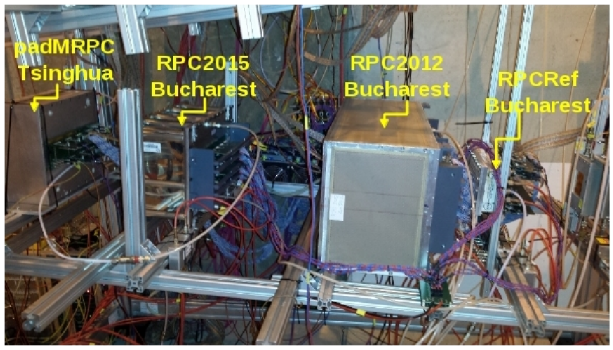

Figure 1: Photo of the high rate experimental set-up based on MGRPC prototypes used in the in-beam test.

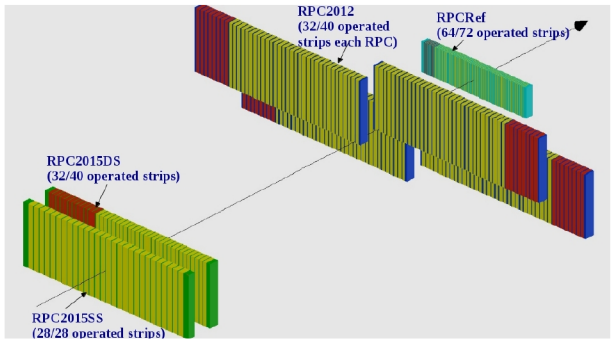

Figure 2: Sketch of the spatial position of the seven RPCs tested in the high rate setup at CERN-SPS.

*Romanian NASR/contract RO-FAIR F02 and NASR/NUCLEU Project PN09370103

DOI:10.15120/GR-2017-1

beam line of the seven prototypes tested by our group and their operated area (green color) are presented in Fig. 2.

The principles of the data analysis starting from unpacking to calibration and corrections for slewing effect, position and reaction product velocity spread are described in [12]. In the left side of Fig. 3 is presented the time difference spectrum between one of the four counters positioned in the upper part of the text box (called RPC2012_3) and RPC2015DS (see reference [11]), with the same inner geometry and the same strip pitch. The 63 ps standard de-

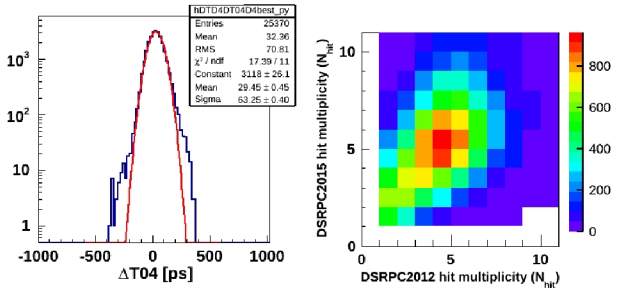

Figure 3: Time difference spectrum - left. Hit multiplicitiy correlation - right.

viation of the Gauss fit demonstrates the very good system time resolution. A single counter time resolution of 44 ps, including the electronic contribution is obtained supposing equal contributions of the two detectors. The comparison of the 63 ps standard deviation with the 71 ps RMS of the spectrum shows a non-significant contribution of the non-Gaussian tails. The correlation of the hit multiplicities in the two counters shows that in the most part of the events, almost the same multiple hits are incident on both detectors. The detectors were operated at 2 x 5.5 kV voltage. Due to their staggered positions, position cuts on both x and y directions were applied in the RPC2015DS, considered as reference counter, for efficiency estimation. However, due to a partial overlap of the active area of each of the four counters relative to the RPC2015DS, the obtained values are still affected by the hits lost at the edges of the overlaped area.

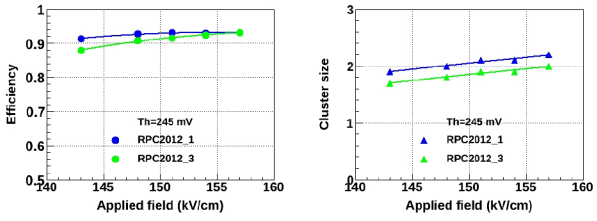

Figure 4: Efficiency - left and cluster size - right as a function of high voltage for RPC2012_1 and RPC2012_3.

In Fig. 4 is shown an expected behaviour of the efficiency and cluster size as a function of high voltage, for RPC2012_3 and RPC2012_1 (right mirrored relative to the axe shown in Fig. 2) for a PADI threshold of 245 mV. In the mentioned geometry of the experiment, a 93% efficiency for both counters was obtained. If we take into consideration the inner geometry of the RPC2012 counters of 2 x 5 gaps of 140 μm, the same as for RPC2015DS [10, 11], we could consider that at a nominal voltage of 2 x 5.5 kV the efficiency is in fact at the same value as for RPC2015DS (97%). The cluster size is of 2.2 strips for RPC2012_1 and of 2.0 strips for RPC2012_3 in the region of efficiency plateau. Average system time resolution of 73 ps for RPC2012_1 and of 67 ps for RPC2012_3 remain almost unchanged over the investigated high voltage range, as is shown in Fig. 5.

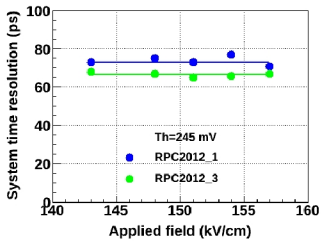

Figure 5: Time resolution as a function of high voltage for RPC2012_1 and RPC2012_3.

The single counter time resolution of 52 - 47 ps fullfils the single counter performance required for the inner zone of the CBM-TOF wall.

The results presented in the contributions to this Progress Report (present one and [11]), show that the MSMGRPC prototypes and the proposed basic architecture fulfill the requirements for the inner zone of the CBM-TOF wall.

References

[1] CBM-TOF Collaboration, CBM-TOF TDR, October 2014

[2] M. Petrovici et al, 2012 Journal Of Instrumentation, Volume 7, 2012 (2012 JINST 7 P11003).

[3] M. Petris et al., CBM Progress Report 2012 (2013), p.68

[4] M. Petriş et al., Journal of Physics: Conference Series 724 (2016) 012037

[5] F. Anghinolfi et al., Nucl.Instr.and Meth. A533(2004)183

[6] C. Simon et al., CBM Progress Report 2015, (2016), p.90

[7] M. Ciobanu et al., CBM Progress Report 2013, (2014), p.84

[8] C. Ugur et al., GSI Scientific Report 2014 (2015), p.212

[9] M. Traxler et al., GSI Scientific Report 2014 (2015), p.514

[10] V. Aprodu et al., CBM Progress Report 2015 (2016), p.98

[11] M. Petriş et al., this CBM Progress Report

[12] M. Petriş et al., Journal of Instrumentation, Volume 11, September 2016 (2016 JINST 11 C09009)

CERN-SPS in-beam performance test of the new strip readout MRPC prototypes for the inner zone of the CBM-TOF wall *

M. Petriş[1], D. Bartoş[1], M. Petrovici[1], L. Rădulescu[1], V. Simion[1], J. Frühauf[2], M. Kiš[2], P-A. Loizeau[2], I. Deppner[3], N. Herrmann[3], and C. Simon[3]

[1]NIPNE, Bucharest, Romania; [2]GSI, Darmstadt, Germany; [3]PI, Heidelberg University, Germany

Due to the high interaction rates of 10^7 interaction/s at which the CBM experiment is anticipated to run the readout will be based on a free streaming concept. This imposes to the MSMGRPCs (Multi-Strip, Multi-Gap RPCs), a perfect matching of the characteristic impedance of the signal transmission line to the input impedance of the front-end electronics, in order to reduce fake signals produced by reflexions [1].

Two new MSMGRPC prototypes, based on low resistivity glass ($\sim 10^{10}$ Ωcm) from China, match the characteristic impedance of the RPC signal transmission line to the input impedance of the front-end electronics ([2, 3]). They have also the granularity required by the inner zone of the CBM-TOF wall through a proper adjusting of their strip lenght. The transmission line impedance of a single readout channel of each prototype was estimated using APLAC Software. The first prototype has a classical single stack architecture (RPC2015SS) with 8 gas gaps of 140 μm. The pitch size (10.16 mm) and strip width (8.63 mm) are the same for both high voltage and readout electrodes. The second prototype has a double stack configuration (RPC2015DS) of 2 x 5 gas gaps of 140 μm, with the same pitch size (7.2 mm) for both high voltage and readout electrodes, but with different values of the strip widths: 1.3 mm for readout electrodes and of 5.6 mm for high voltage ones. This gives the possibility to exploit in an inovative way the advantage of having a strip structure for both readout and high voltage electrodes. Thus the tuning of the characteristic impedance of the signal transmission line to the value of the input impedance of the front-end electronics can be decoupled by the granularity adjustments. With the described geometrical parameters both counters have a characteristic impedance of the transmission line of 100 Ω.

The prototypes were tested in-beam at SPS-CERN with a 30A GeV Pb ions incident on a Pb target in conditions similar with those expected at SIS100, or even closer to those anticipated for SIS300. Our prototypes were positioned in the "high rate" branch of the CBM-TOF experimental setup, a comprehensive description of the whole set-up being given in [4]. The two described prototypes are positioned one behind the other (see Fig.1), in the same housing box, identified as RPC2015 Bucharest [5]. They were followed by four MSMGRPCs mounted in the same gas tight box, called RPC2012 and a narrow strip pitch (2.54 mm) MSMGRPC called RPCRef, the last one in the experimental set-up. A 16 strip polycrystalline diamond detector and a 4-pad single crystal diamond detector were positioned in front of the target, providing a start time for particle velocity measurements between the diamond detector and the RPCRef counter. The signals delivered by the RPCs were fed to PADI fast amplifiers [6] and processed by the same electronics chain described in [5].

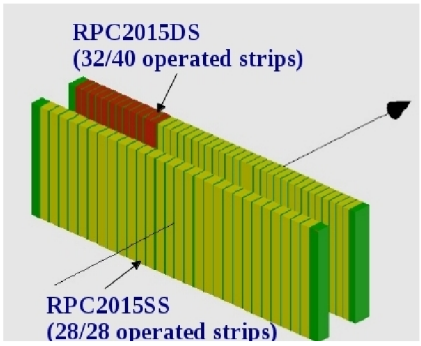

Figure 1: Overlap of the active area of the two RPC2015 prototypes.

We report here the performance of the RPC2015 prototypes, the results obtained with RPC2012 prototype being reported in detail in [5]. The principles of the data analysis starting from unpacking to calibration and corrections are presented in [7].

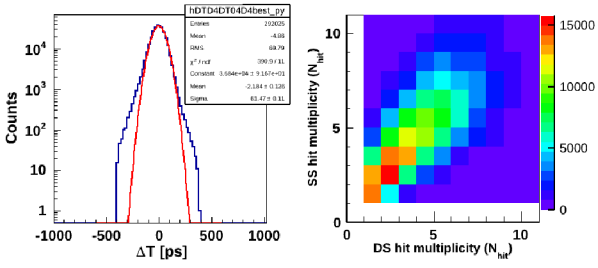

Figure 2: Time difference spectrum - left. Hit multiplicitiy correlation - right.

The time difference spectrum between RPC2015DS and RPC2015SS, for operation of RPC2015DS at 2 x 5.5 kV (157 kV/cm) and of RPC2015SS at 2 x 9 kV (161 kV/cm), with the PADI threshold set to 245 mV is presented in Fig.2, left side. A very good system time resolution of

* Romanian NASR/contract RO-FAIR F02 and NASR/NUCLEU Project PN09370103

DOI:10.15120/GR-2017-1

61 ps, including the contribution of the electronics, was obtained. The correlation plot from the right side of Fig.2 shows that the two counters were exposed to almost the same hit multiplicities. If we consider equal contributions of the two counters, a single counter resolution of 43 ps is obtained. The observed tails in the time spectrum are negligible, if we compare the obtained 61 ps σ of the Gaussian fit with 69 ps RMS value of the spectrum. The obtained efficiency for this run, was of 97% for the RPC2015DS and of 98.5% for the RPC2015SS. The slight difference could be due to the difference in the applied potentials and also in the overlaped operated area, as is shown in Fig.1. The

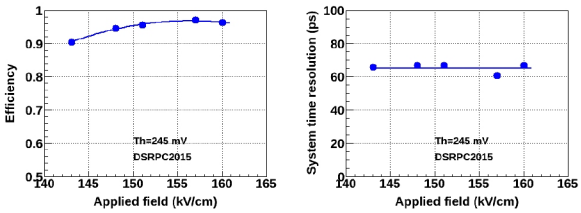

Figure 3: Efficiency - left and time resolution - right as a function of high voltage for RPC2015DS.

obtained detection efficiency and time resolution as a function of applied high voltage for RPC2015DS are shown in Fig. 3. An average system time resolution of 65 ps corresponds to the efficiency plateau, reached at applied electric fields in the gas gap larger than 157 kV/cm. The efficiency

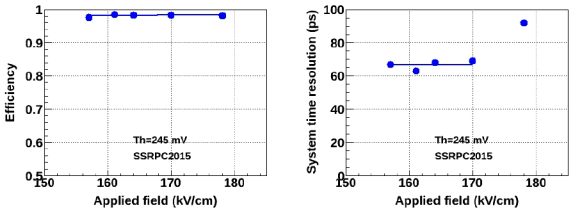

Figure 4: Efficiency - left and time resolution - right as a function of high voltage for RPC2015SS.

and system time resolution obtained for RPC2015SS are presented in Fig. 4. As can be observed, the counter was operated at the efficiency plateau of ~98%, with an average system time resolution of 66 ps. The larger value of the time resolution observed for operation at 178 kV/cm is due, most probable, to the operation at a too high electric field which pushes the counter in a streamer regime. The

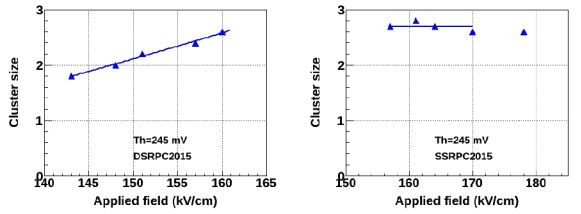

Figure 5: Cluster size for RPC2015DS - left and RPC2015SS - right as a function of high voltage.

obtained cluster size (number of strips with signal in a single hit) for the two counters is presented in Fig. 5. The cluster size is increasing for RPC2015DS as a function of applied potential while for RPC2015SS in the same high voltage range is almost constant. It slightly decreases at the largest applied fields due to possible distorsions of the electric field produced by the space charge inside the gas gaps. The obtained values of the cluster size are larger than the one expected from the values of pitch sizes for the two counters. Previous obtained results for RPC2012 with a pitch size of 7.4 mm and the same inner geometry, showed a cluster size of the order of 1.4 - 1.5 strips [8] for single hit. These larger values can be due to large ionization created by heavy reaction products crossing the detector.

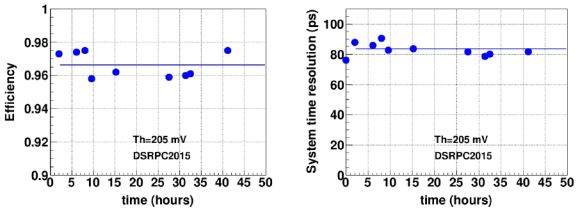

Figure 6: Aging effect for RPC2015DS for 40 hours operation with the same high voltage and threshold settings.

The detector performance stability was checked for a period of operation of about 40 hours with the same settings (RPC2015 at 157 kV/cm, RPC2015SS at 178 kV/cm). The efficiency and system time resolution were evaluated for the runs acquired over this period at similar counting rates. The stability of the detectors is demonstrated by the plots shown in Fig. 6. The obtained ~80 ps system time resolution is affected by the operation of the RPC2015SS at a too high electric field, (178 kV/cm), in a region of the working curve where its time resolution started to deteriorate (see Fig. 3). The operation of the detectors at a PADI threshold of 205 mV does not not influence the time resolution performance, as it is shown in [7, 9].

The performance of the RPC2015DS whith the inovative adjustable characteristic transmission line impedance was demonstrated. The obtained results show that the two new prototypes with characteristic transmission line impedance matched to the input impedance of the front-end electronics, fullfil the challenging requirements of the inner zone of the CBM-TOF wall.

References

[1] CBM-TOF Collaboration, CBM-TOF TDR, October 2014

[2] V. Aprodu et al., CBM Progress Report 2015 (2016), p.97

[3] V. Aprodu et al., CBM Progress Report 2015 (2016), p.98

[4] C. Simon et al., CBM Progress Report 2015, (2016), p.90

[5] M. Petriş et al., this CBM Progress Report

[6] M. Ciobanu et al., CBM Progress Report 2013, (2014), p.84

[7] M. Petriş et al., Journal of Instrumentation, Volume 11, September 2016 (2016 JINST 11 C09009)

[8] M. Petriş et al., Journal of Physics: Conference Series 724 (2016) 012037

[9] M. Petriş et al., CBM Progress Report 2015 (2016), 95

Simulation of the MRPC response degradation with increasing time in spill *

C. Simon[1], N. Herrmann[1], I. Deppner[1], A. Akram[1], E. Bao[1], P.-A. Loizeau[2], Ph. Weidenkaff[1], and the CBM ToF working group[1]

[1]Ruprecht-Karls-Universität Heidelberg, Heidelberg, Germany; [2]GSI, Darmstadt, Germany

Following avalanche formation in an MRPC gas gap, electrons and positively charged gas ions drift towards opposing glass plates, accumulate on the surfaces and—as a consequence—cause a local reduction of the electric field in the gap. These charges compensate one another by means of bulk and surface currents on relaxation time scales of $\mathcal{O}(ms) \leq \tau \leq \mathcal{O}(s)$, depending on the glass resistivity. The growth of subsequent avalanches in the very location is therefore influenced by the formation time and the charge content of the preceding ones.

The average effect of different recovery times for the electric field between events, i.e. of different incident particle fluxes, on MRPC performance criteria like detection efficiency, time resolution and mean cluster size has been extensively studied by the ToF working group on prototypes equipped with both float and low-resistive glass (cf. e.g. [1], [2] and [3]). In all these cases, detector data were averaged within spills and across spills. These measurements did therefore not address the question of how the degradation of the MRPC response evolves with increasing time in spill. Exposing the detector to a sustained particle flux should—regarding the operation principle—decrease its detection efficiency until local reduction and recovery of the electric field cancel out.

A self-triggered, front-end driven data acquisition with readout channel dead times of a few nanoseconds allows for studying the degradation and saturation of the MRPC response in unprecedented detail. Such a system was realized for the first time on a large scale in the GET4-AFCK-FLIB chain used in the 2016 heavy-ion beam time at CERN/SPS to read out multiple MRPC prototypes. This significant progress on the experimental hard- and software side has been accompanied by the development of a more realistic ToF digitizing scheme which the following parametrization of the MRPC response degradation builds upon.

Be $Q_{\mathrm{ind},0}$ a random variable which describes the total electric charge spectrum induced by avalanches in the readout plane of an unloaded MRPC. Be $q_{\mathrm{max},0}$ the highest possible value of $Q_{\mathrm{ind},0}$ and $q_{\mathrm{ind},i}$ the charge actually induced by the i-th avalanche at position $\mathbf{x}_i$ and time t_i. Be further r_{imp} an impact radius quantifying the spatial extent of an E-field reduction and τ_{MRPC} the relaxation time for field restoration. Then in this approach the induced charge spectrum accessible to the n-th avalanche at coordinates $(\mathbf{x}_n, t_n)$ follows the probability distribution of the random variable

$$Q_{\mathrm{ind},n} = \left[1 - \sum_{i=1}^{n-1} \left\{ \frac{q_{\mathrm{ind},i}}{q_{\mathrm{max},0}} \times \frac{1}{1 + \left(\frac{\mathbf{x}_n - \mathbf{x}_i}{r_{\mathrm{imp}}}\right)^2} \times \exp\left(-\frac{t_n - t_i}{\tau_{\mathrm{MRPC}}}\right) \right\}\right] Q_{\mathrm{ind},0} \quad . \tag{1}$$

In a Monte-Carlo parameter study the detection efficiency of a $1\,\mathrm{cm}^2$ spot in the center of an MRPC prototype with dimensions $32 \times 27\,\mathrm{cm}^2$ was simulated for low-resistive (cf. Fig. 1, left) and float glass electrodes (cf. Fig. 1, right) as a function of time in spill at three different incident particle fluxes. The impact radius r_{imp} of $100\,\mu\mathrm{m}$ is the same in both cases. With low-resistive glass the MRPC degrades efficiency rather slightly and reaches saturation quickly while preserving its operability even at $25\,\mathrm{kHz/cm}^2$. With float glass it shows a decline in efficiency of about 3 % already at $1\,\mathrm{kHz/cm}^2$ that might actually be observable in the 2016 test beam data.

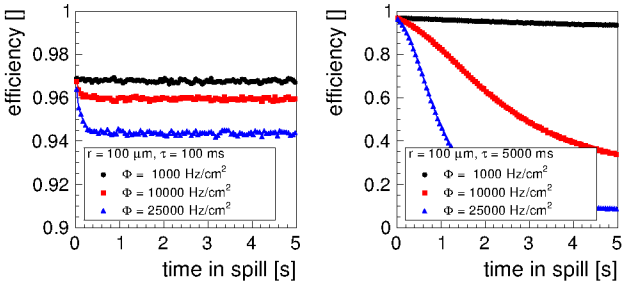

Figure 1: MRPC efficiency degradation (input efficiency: $\varepsilon_0 \approx 0.97$) as a function of time in spill with low-resistive glass (left) and with float glass (right) for different particle fluxes.

As the run time of the summation in Eq. (1) grows quadratically with the number of MRPC hits (about 8.5 hours for 1 million mutually interacting hits in a single-threaded process) possible applications of multi-threading and batch processing are under investigation.

References

[1] I. Deppner *et al.*, 2012 JINST 7 P10008

[2] M. Petriş *et al.*, J. Phys. Conf. 533 (2014) 012009

[3] Y. Wang *et al.*, JINST 9 (2014) C08003

* This project was partially funded by BMBF 05P2015 and by EU/FP7-HadronPhysic3/WP19.

DOI:10.15120/GR-2017-1

Observation of after-pulses in the detector response of MRPC prototypes for CBM-TOF

Ph. Weidenkaff[1], *A. Akram*[1], *I. Deppner*[1], *N. Herrmann*[1], *P.-A. Loizeau*[2], *and C. Simon*[1]
[1]Ruprecht-Karls-Universität, Heidelberg, Germany; [2]GSI, Darmstadt, Germany

First characterizations of CBM-ToF MRPC prototypes have been performed using the free-streaming time-to-digital converter Get4. The high double hit resolution of the Get4-TDC (better than $5\,ns$ [2]) allows to study effects in the detector response immediately after a primary hit. An series of after-pulses has been observed in the first 50 nanoseconds after a primary signal. The probability, multiplicity and temporal distribution of these after-pulses have been compared between six MRPC prototypes in a cosmic radiation test. A short description of all tested prototypes can be found in [1].

The MRPC read out chain consists of PADI as pre-amplifier, the Get4 TDC and the AFCK as data processing board. The slow-control interface IPbus was used as a read-out interface between AFCK and the data acquisition PC since a proper PCI-E based read-out interface was not available in time.

An example of the temporal distribution of after-pulses after a primary signal can be seen in figure 1a. Several common features can be observed on all prototypes:

No after-pulses in the first nanosecond followed by a steep rise of the time distribution. This feature originates from the double hit capability of Get4. In this time window after each hit in a channel, the TDC channel is either fully inactive or not completely efficient.

A rather flat maximum is seen between $5\,ns$ and $10\,ns$ after the primary signal. In this region the prototypes show either a flat distribution or a slight rise of the distribution.

The spectrum continuously decreases over time after the maximum. This decrease can be described reasonably well by an exponential decay. The shape as well as the length of the decline leads to the conclusion that the majority of the observed after-pulses are not caused by electronic reflections.

It is also observed that the time over threshold of the after-pulses is independent of the after-pulse delay with respect to the primary signal.

The likelihood to observe such after-pulses was significantly higher than the expected rate of random coincidences from the measured dark rate on all studied prototypes. A correlation between these after-pulses and the primary signal is therefore evident. The probability to observe any after-pulses after a primary signal is shown in figure 1b for the two prototypes from USTC.

A higher probability for multi-hit events is observed on the unmatched USTC-DSU prototype. However, also the impedance matched USTC-DSM prototype shows multiple hits on the same TDC channel in $10\% - 20\%$ of the events. In mean, such an event contains the primary signal

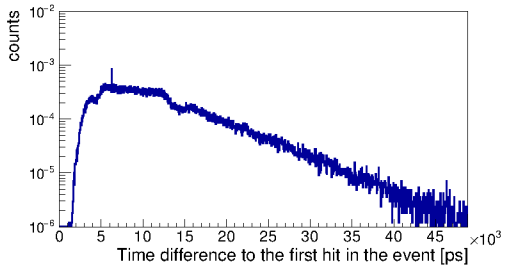

(a) *Temporal distribution of after-pulses after the primary hit on an example channel (Channel 16 of USTC-DSM). The distribution is normalized to the number of Events in which the TDC-channel detected at least one hit. Source: [3]*

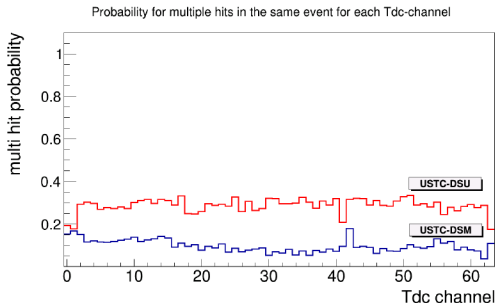

(b) *Probability to find after-pulses in an event in which a primary signal is found for each TDC channel of the prototypes USTC-DSU (red) and USTC-DSM (blue).*

and 1.12 after-pulses on USTC-DSM and 1.47 after-pulses on USTC-DSU. The tails of the after-pulse multiplicity distributions extent to up to 10 after-pulses.

Since the observed after-pulses are correlated with primary signals, it is expected that this problem persists also at high rates. For highest interaction rates, the influence of after-pulses on the physics performance of MRPCs has to be studied.

References

[1] I.Deppner et al, "Narrowing down the MRPC design with heavy ion beams at CERN/SPS", GSI Scientific Report 2015 (2016) p.90

[2] H. Deppe and H. Flemming, "The GSI Event driven TDC with 4 Channels Get4", Technical report, GSI, Darmstadt 2014

[3] Ph. Weidenkaff, "Characterizations of Multi-Gap Resistive Plate Chamber Prototypes in a Freestreaming Read-Out Environment", Master-thesis, Ruprecht-Karls Universität, Heidelberg 2017

DOI:10.15120/GR-2017-1

RICH geometry optimization*

I. Kres[1], *T. Mahmoud*[2], *and C. Höhne*[2]
[1]University of Wuppertal, Germany; [2]II. Physikalisches Institut, JLU-Gießen, Germany

Due to modifications of the CBM dipole magnet the overall RICH geometry has to be re-optimized. In previous reports [1,2] we described the optimization procedure and showed results with two-wing PMT-plane (left part in figure 1). Although the two-wing geometry showed very good performance in simulations, it is not realizable in the real experiment due to overlap of electronics modules in the center as illustrated in the figure. Therefore, in a second step a cylindrical shaped geometry of the MAPMT plane was investigated (right part in figure 1). This geometry not only overcomes the overlap problem, but also brings the PMTs closer to the focal plane of the mirrors.

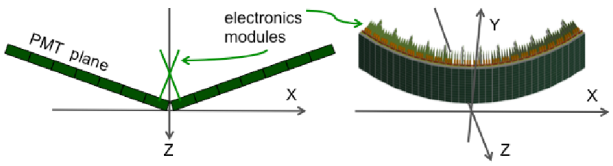

Figure 1: MAPMT plane geometries. Left picture represent two-wing geometry. Right picture represent cylindrical geometry.

The detailed optimization procedure is described in [1]. For the curved geometry the following parameters were optimized: rotation around the x-axis, radius of the cylindrical curvature, and y- and z-position coordinates. As for the two-wing geometry, two main criteria were optimized: the ratio of minor to major axis of an ellipse fit to the ring (B/A) and the RMS of the distribution of the distance between the fit and the individual hits forming the ring (dR). In the study single electrons and positrons were generated isotropically in space with a flat distribution in transverse momentum from 0 to 4 GeV/c.

The best integrated B/A and dR values are 0.93 and 2.8 mm respectively. They are achieved with a rotation angle $\theta = 16°$ around the x-axis, a cylindrical radius $r = 165\ cm$, and a position of plane center at $y = 158\ cm$ and $z = 218.6\ cm$ from the interaction point. The B/A distribution on the upper half of the PMT plane is shown in the upper panel of figure 2. For a wide area the B/A ratio is larger than 94% indicating a low grade of ellipticity and consequently high ring finding efficiency, which is found to be about 97% for Au-Au collisions at energies of 8 AGeV [3]. Compared to results with the two-wing

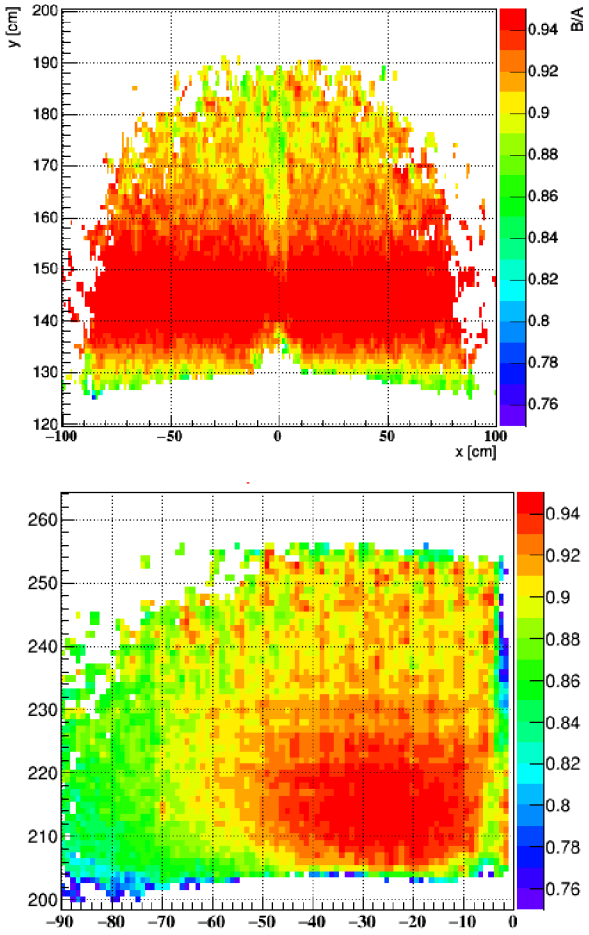

Figure 2: B/A ratio distribution versus position on the cylindrical (up) and the two-wing (low) MAPMT plane. Note that in the lower panel only one half of the plane is shown.

geometry (lower panel in figure 2), the B/A distribution with the cylindrical geometry is much more homogeneous. The dR distribution is shown in figure 3. It is distinctly low and homogeneous within a resolution of 1 mm, which is only 2% of the ring radius.With the two-wing geometry dR lay between 3 mm and 5 mm.

The plane dimensions of $111.3 \times 74.2\ cm^2$ were adjusted to cover the experiment acceptance and to be integer multiples of modules containing 2×3 PMTs each. The upper plane has 14 strips in the x-direction with 7 modules each

*Work supported by HIC for FAIR, by the GSI F&E- Cooperation with Giessen and Wuppertal, and by BMBF grants 05P12RGFCG and 05P15PXFCA.

DOI:10.15120/GR-2017-1

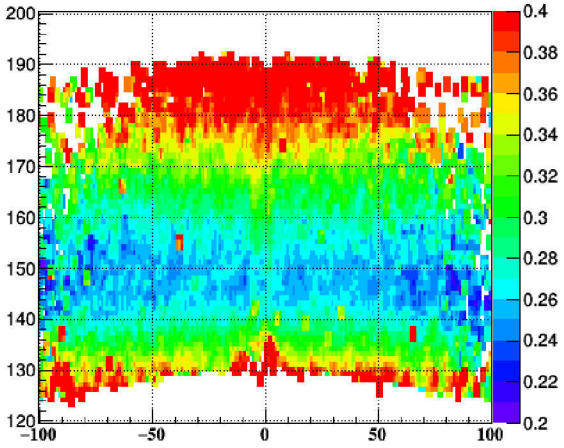

Figure 3: dR distribution versus position on the cylindrical MAPMT plane

(in the y-direction). This module structure was adopted due to electronics development considerations, see [4].

We recall that the RICH detector is designed to detect electrons stemming from vector mesons like ρ, ω, and ϕ. Their small production cross section, together with the small branching ratio into e^+e^-, is challenging in terms of the large (physical) background stemming from Dalitz decays of π^0 and γ-conversions.

To evaluate the optimal detector size of the new geometry, simulations of heavy-ion collisions were carried out aiming at localizing the rings stemming from low mass vector mesons and those from background. 2×10^6 events were simulated with PLUTO at a beam energy of 10 AGeV. We consider the Micro Vertex Detector (MVD), the Silicon Tracking System (STS), and RICH in the simulations. The magnetic field has its nominal value of 100%.

Figure 4 shows the results for electrons from ω decays. The same behaviour is observed for electrons from ρ decays. The corresponding rings are mostly concentrated in the middle of the PMT plane, which is comprehensible as these electrons have momenta of about 2 GeV/c and hence their tracks are less curved by the magnetic field.

The background electrons come to a large extend from conversion photons, which in turn come from π^0 decays: $\pi^0 \to \gamma + \gamma \to (e^+e^-) + (e^+e^-)$. The electrons have momenta of about 0.2 GeV/c and accordingly they populate the full MAPMT plane due to large deflection in the magnetic field. To be able to detect as many of these electrons as possible the PMT plane was enlarged by adding one additional strip (i.e. 7 modules along the y-axis) on each of its outer sides. This measure results in recording 10% of additional electrons originating from π^0 decays. This is particularly important when one considers the RICH contribution to the direct photon signal, where it is essential to understand the background from π^0 decays and to have

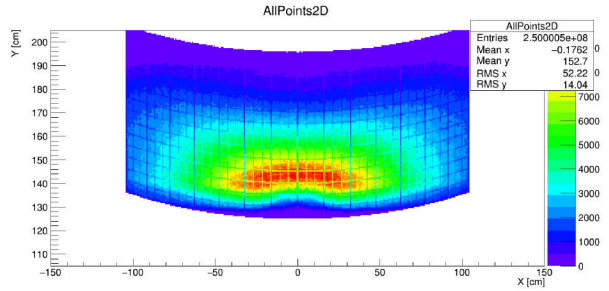

Figure 4: $x - y$ position of RICH hits from Cherenkov light on the upper PMT plane produced by e^+e^- from ω particles. Standard geometry (14 strips).

it under control. Figure 5 shows Cherenkov light on the extended PMT plane with 16 strips coming from from π^0.

Please note that not the whole PMT plane will be equipped with PMTs due to costs consideration (1344 PMTs in total for the 16-strip configuration). However, as clearly seen in the figures 4 and 5, the outer upper parts of the plane are not relevant for any of the signals.

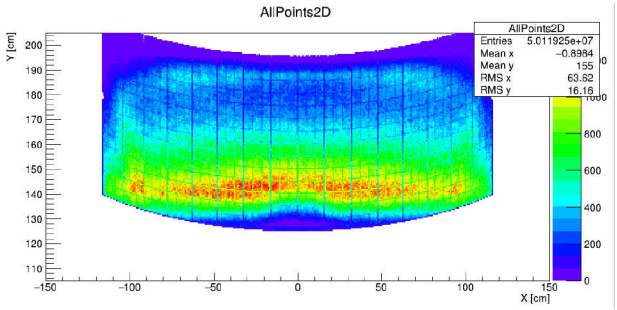

Figure 5: $x - y$ position of RICH hits from Cherenkov light on the upper PMT plane produced by e^+e^- from π^0 particles. Geometry with 16 strips.

For a better understanding of advantages and disadvantages of the 16-strips geometry feasibility studies with dielectrons are required. A detailed analysis shows how the extended geometry improves the π^0-reconstruction and accordingly the background suppression for dilepton analysis.

In summary, we state that the investigated cylindrical geometry not only solves the overlap problem of electronics boards, but also leads to better results in view of ring finding and fitting quality.

References

[1] T. Mahmoud and C. Höhne, CBM Progress Report 2014, Darmstadt 2015, p. 60

[2] T. Mahmoud and C. Höhne, CBM Progress Report 2015, Darmstadt 2016, p. 46

[3] S. Lebedev et al., this report

[4] V. Patel et al., this report

Cooling studies with Thermal Pyrolytic Graphite for the CBM-MVD*

D. Mijatovic[1], *M. Koziel*[1], *P. Klaus*[1], *C. Müntz*[1], *J. Stroth*[1,2], *and the CBM-MVD Collaboration*

[1]Institut für Kernphysik, Goethe-Universität Frankfurt, Germany; [2]GSI Darmstadt, Germany

The CBM Micro Vertex Detector (MVD) comprises four planar detector stations, each divided in quadrants, and equipped with dedicated pixel sensors. Their operation results in about 300 W of total heat input. The challenging material budget of the stations ($< 0.5\%$ X_0) in combination with the operation in vacuum asks for an elaborated cooling concept. It is based on conductive cooling inside the geometrical acceptance employing thin sheets of high-performance materials as sensors carriers, featuring heat conductivities in the order of four times the one of copper, like poly-crystalline CVD-Diamond and Thermal Pyrolytic Graphite (TPG) [1]. These carriers guide the heat to actively cooled heat sinks outside the acceptance. This report presents systematic studies on the in situ cooling performance of MVD quadrants, with a focus on assessing TPG carriers of different thicknesses. Note, the in-plane heat conductivity of TPG is about 1600 W/mK at room temperature, and less than 20 W/mK perpendicular to the surface. Figure 1 (left) depicts the setup geometry by showing the temperature distribution on a TPG sensor carrier of the 3rd station attached to a actively cooled Aluminum heat sink, measured by the IR camera (Vario Cam). The heat load (in the order of 700 mW/cm^2) was mimicked by sheets of Kapton heaters, operated in a standardized vacuum test stand. The thermal performance was

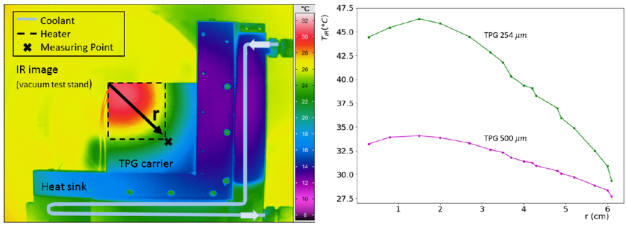

Figure 1: Left: IR image of a 500 µm thin 8×8 cm^2 TPG carrier attached to the heat sink, heat load of 15 W applied 180 s, $T_{cooling\ fluid} = 15$ °C, the heat sink was not corrected for emissivity. Right: Temperature along diagonal coordinate, both TPG thicknesses, $T_{cooling\ fluid} = 25$ °C, after 10 s of heating.

quantitatively characterized by analyzing temperature differences and heating curves of TPG sheets with different thicknesses (254 and 500 µm), shown in figures 1 (right) and 2, respectively. Fitting the temperature rise during the first 10 s ("fast") with $\propto (1 - \exp(-t/\tau))$ results in τ_{fast} of 3-4.5 s, almost independent of the TPG thickness. This fast time constant is in agreement with the above mentioned

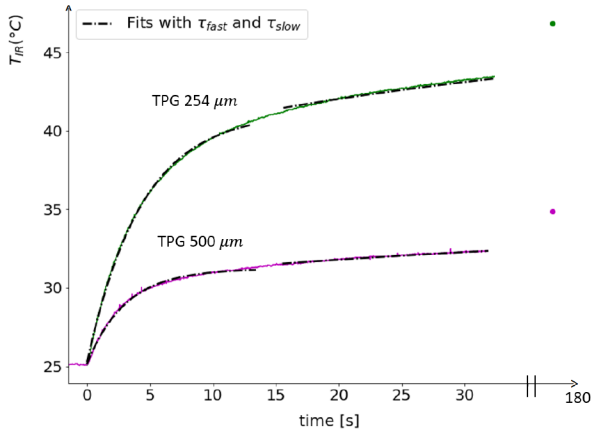

Figure 2: Heat-up curves of TPG carriers of two different thicknesses in vacuum, measured in the point depicted fig. 1, $T_{cooling\ fluid} = 25$ °C, relative adjustment of curves at $t = 0$ s. Broken lines: Exponential fits to initial and saturating time range, see text.

outstanding in-plane heat conductivity of TPG, a result derived from solving the equation of heat conductivity [2]. A second common time constant of $\tau_{slow} \approx 45$ s characterizes the saturation phase.

In summary, a standardized test stand was set into operation to characterize the cooling performance of CBM-MVD quadrants. First results on the cooling performance, given by both, the material properties of TPG (τ_{fast}) and the power to evacuate the heat from the carrier (τ_{slow}), have been derived by measuring characteristic time constants of heating curves. The measured time constant τ_{fast} underlines the excellent thermal performance of this material. Temperature differences and τ_{slow} offer a quantitative assessment to further improve the heat evacuation and selecting the optimum TPG thickness. Next campaigns will focus on characterizing Parylen-coated TPG, even thinner pyrolytic graphite foils (PGS) and pCVD-Diamond. They will be complemented by and compared to thermal CAD simulations aiming at optimizing the contact to the heat sink and its design.

References

[1] Diamond Materials www.diamond-materials.com; Momentive momentive.com, Optigraph www.optigraph.eu

[2] P. Klaus, priv. communication

* supported by BMBF (05P15RFFC1), HGS-HIRe and GSI.

DOI:10.15120/GR-2017-1

DiRICH readout electronics - status and first measurements *

C. Pauly[1], *K.-H. Kampert*[1], *J. Michel*[2], *V. Patel*[1], *P. Skott*[3], *M. Traxler*[3], *and C. Ugur*[3]
[1]Wuppertal university; [2]Frankfurt university; [3]GSI Darmstadt

The realization of the new DiRICH electronic readout chain for Hamamatsu H12700 MAPMTs (CBM- and HADES RICH detectors), as well as for Photonis MCP sensors (PANDA DIRC), has seen major progress over the last year. Since mid 2016, first prototype modules of all components are available for detailed testing and evaluation. Figure 1 shows photographs of a partly equipped 3x2 MAPMT module, and of the individual DiRICH, DiRICH-Combiner, and DiRICH-Power cards. All these modules seem to work as expected, no critical design flaws have been encountered yet.

A particular challenge in the development of the DiRCH readout module is the low signal amplitude of the MAPMT / MCP signals for single photons. With sensor gain in the order of 1×10^6, and a signal width in the order of few ns, a typical single photon pulse has an average amplitude of about 10 - 20 mV. In order to achieve good detection efficiency, this requires operation at thresholds down to the mV level. This poses particular challenges on the noise characteristic of the analog input stage of the DIRICH.

* Work supported by BMBF grants 05P15PXFCA, 05P15RGFCA, and GSI

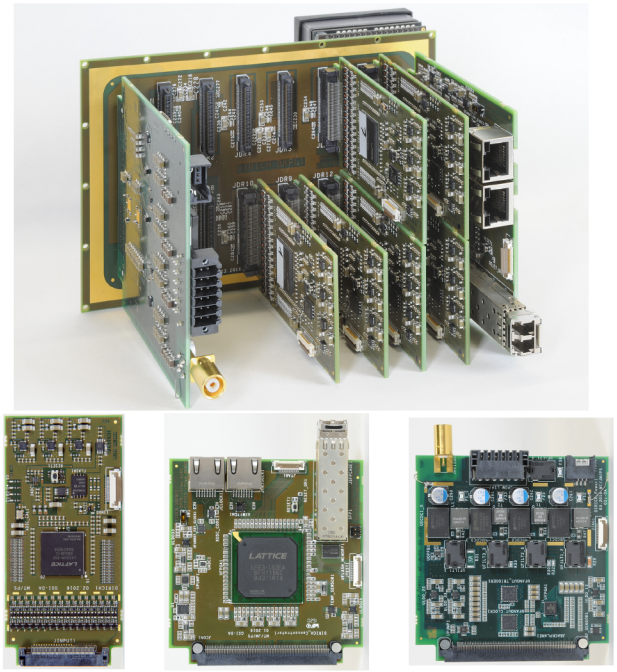

Figure 1: A 3x2 MAPMT readout module (top), with one out of 6 MAPMTs on front side, and few 32ch DIRICH FPGA-TDC frontend modules (lower left), a DiRICH-Power supply module (lower right), and a DiRICH-Combiner module (lower center).

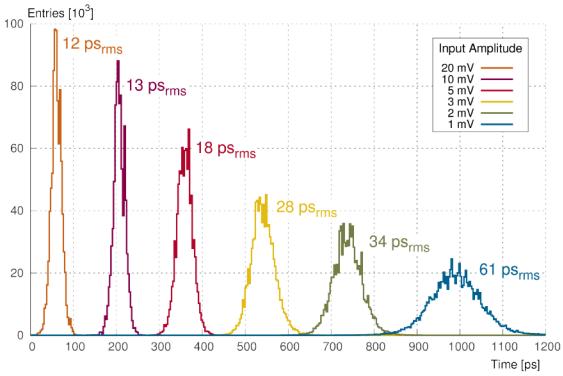

Figure 2: Achieved timing precision measured as time difference (RMS) for analog input pulses of varying amplitude. The absolute peak positions were artificially shifted for better differentiation.

The achieved performance in terms of timing precision for low amplitude signals is demonstrated in Figure 2. Here, a pulser was used to generate PMT like signals of varying amplitude down to 1 mV only. The signal was split into two identical signal paths, and injected into the DiRICH preamplifier. The timing precision was determined as RMS of the measured time difference of the leading edge threshold crossing of both channels. After proper TDC calibration, a timing precision down to 12 ps RMS could be observed, depending on input signal amplitude. Even at very low input amplitude of 2 mV, still a timing precision of 34 ps RMS could be demonstrated. This is fully sufficient given the internal timing accuracy of the photon sensors (PMT: 290 ps Transit time spread, MCP <100 ps).

The first tests of the new DiRICH readout concept look very promising, and seem to qualify the overall concept. A few minor design issues have already been found, and will be fixed in a second iteration of the DiRICH module, which is under production now.
For further validation of the concept a test beam at COSY/Jülich is scheduled for end of May, where two fully equipped 2x3 MAPMT modules will be put into operation. If everything goes well, we plan to start mass production of all modules end of 2017, in order to equip the full HADES RICH detector in time for the next HADES beamtime at SIS18 earliest mid 2018.

DOI:10.15120/GR-2017-1

Update on MAPMT delivery and series testing, interim results*

J. Förtsch †[1], *D. Pfeifer*[1], *C. Pauly*[1], *V. Patel*[1], *and K.-H. Kampert*[1]
[1]Bergische Universität Wuppertal, Germany

To cover the photo-detection plane of the CBM-RICH detector, 1100 HAMAMATSU H12700 MAPMTs were ordered by GSI in Summer 2015. The delivery starting in November 2015 consists of 50 delivered MAPMTs each month and will thus be finished late 2017. To ensure a high quality, all the MAPMTs need to fulfill certain requirements that are discussed in [1]. To measure these requirements and to fully characterize each 64 ch MAPMT, a single photon scanning test bench was built (see [2]).

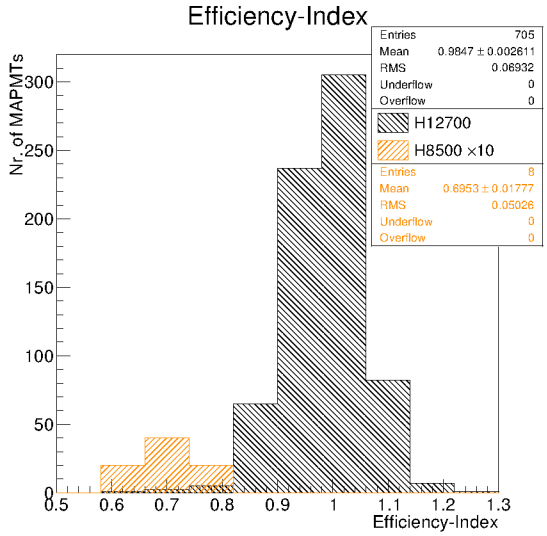

Figure 1: Efficiency-index distributions for the H12700 (black) and its predecessor H8500 (orange). The distribution of the H8500 is scaled by a factor of 10 for visibility. An efficiency-index of 1 states that the measured MAPMT is as efficient as the reference MAPMT averaged over its full surface.

Currently, 705 H12700 MAPMTs have been characterized using the test bench. This allows for a first broader look on the quality of the delivered MAPMTs. Therefore, the distributions of the 705 MAPMTs for parameters such as the efficiency-index, dark rate, gain, and skewness will be discussed in the following.

The efficiency-index uses a continuously measured reference-MAPMT as scale. The distributions of the efficiency-index for the H12700 MAPMTs and its predecessor, the H8500, are shown in figure 1. From the distributions it is clearly visible that the new H12700 has, in average, a 30% higher efficiency for single photons at 405 nm, as compared to the H8500. Furthermore, one can see that the distribution of the H12700's efficiency is rather narrow, featuring a RMS of 0.07.

In the RICH-detector each six MAPMTs will share one HV supply channel, distributed via a common backplane. To effectively group the MAPMTs and to reject MAPMTs not meeting the minimum gain requirements, a precise knowledge of the gain is important. Figure 2 shows the gain of all measured MAPMTs. The gain shows a rather broad distribution ranging from 1×10^6 up to 5×10^6, with all tested MAPMTs meeting the specified minimum gain of 0.8×10^6.

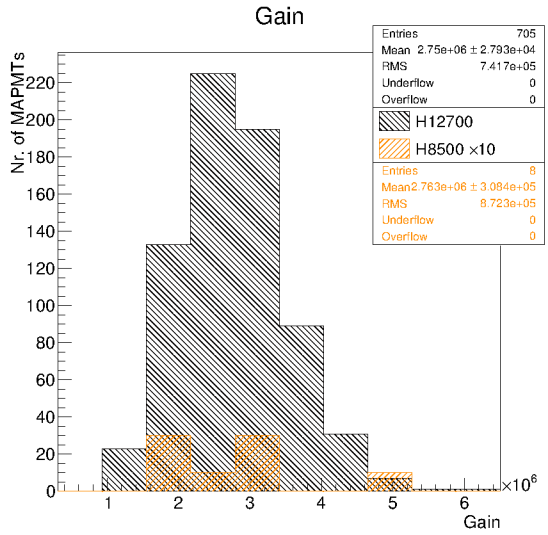

Figure 2: Gain distributions for the H12700 (black) and its predecessor H8500 (orange, scaled by a factor of 10).

As the CBM-RICH will consist of 1000 MAPMTs, being read out by a free streaming and self triggered DAQ, a requirement of less than 100 Hz dark rate per pixel has been set. To show the trend of the dark rate, the total dark rates of the different MAPMTs are shown in figure 3 and sorted by their production number. As the dark rate depends strongly on the temperature during the measurement, the temperature in the test bench was measured from mid of charge 11 onwards. The temperature was then taken into account following the extrapolation procedure described in [3]. Although no temperature measurement exists for the early measurements, one can still compare the measured dark rates to the recalibrated ones, as these measurements were done latest early summer, with a rather constant room temperature at around 25 °C. One can see that from the

* Work supported by GSI and BMBF contract No. 05P15PXFCA
† j.foertsch@uni-wuppertal.de

DOI:10.15120/GR-2017-1

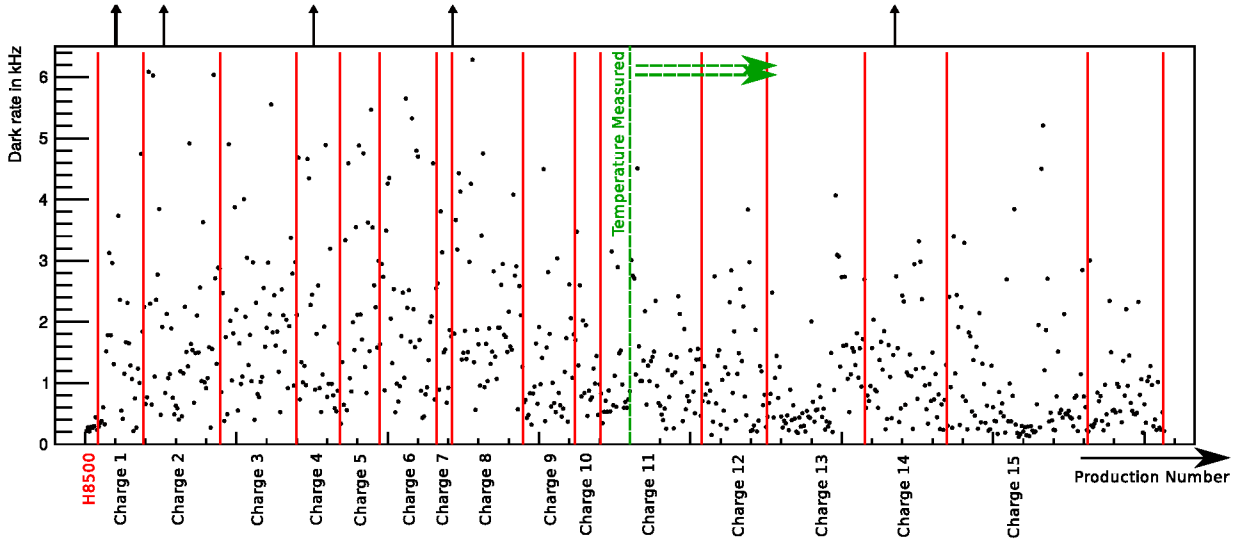

Figure 3: Dark rate in kHz vs. production number. The black arrows indicate MAPMTs having a dark rate higher than 6.4 kHz (specified maximum). The MAPMTs measured after the green dashed line are recalibrated to 25 °C using the measured temperature during the scan and the extrapolation procedure described in [3]. The red vertical lines indicate different delivery charges, with the first division being all the measured H8500 MAPMTs.

measured MAPMTs only very few do not fulfill the requirement of 6.4 kHz dark rate at maximum (black arrows in figure). Those MAPMTs are mainly found in the first few charges in which many MAPMTs show a tendency to higher dark rates. Furthermore one can see that the H8500 (first production numbers of fig. 3) show a much lower dark rate. This might be due to the H8500 MAPMTs being older and thus having a better alkali balance inside of the MAPMT. Still one can assume that the dark rate of the H12700 might remain slightly higher than that of the H8500.

A persistent feature one can observe for nearly all MAPMTs is a gradient in the efficiency from the left to the right side on the MAPMT surface. To better describe this feature the skewness parameter was introduced as the average efficiency of the MAPMT's left side (side of pixel 8) divided by the average efficiency of the MAPMT's right side (side of pixel 1). For the first 12 delivered charges an average skewness of 0.942 ± 0.002 was determined. This gradient was not observed for the H8500 having an average skewness of 1.007 ± 0.012. For newer charges (13-16) the feature seems to be slightly less prominent, as the average skewness for these charges is 0.951 ± 0.002.

From a sub-sample of 550 fully examined MAPMTs 27 MAPMTs were reclaimed. From these 27 MAPMTs, 13 were approved by HAMAMATSU to not meet the given requirements with six more MAPMTs still being analysed, and eight MAPMTs being rejected by HAMAMATSU for the time being. Nine out of these 13 MAPMTs missed the requirement on the dark rate[1]. The second most common failed requirement was the cathode uniformity, with six from 13 MAPMTs being too inhomogeneous. To prove the inhomogeneity of the photo-cathode an additional spatially resolved quantum efficiency-scan was carried out. An example for an accepted reclamation due to extreme inhomogeneity is shown in figure 4, where the spatially resolved quantum efficiency is compared to the spatially resolved efficiency measured by the single photon test bench.

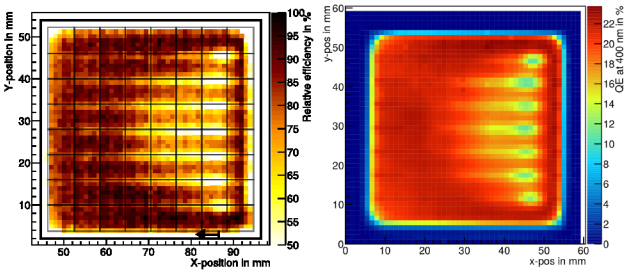

Figure 4: Left: Spatially resolved single photon efficiency. Right: Spatially resolved quantum efficiency.
The similar structure in both measurements suggests that the observed inhomogeneity stems from the photo-cathode.

[1] Maximum average dark rate 100 Hz per pixel with no pixel above 1 kHz maximum.

References

[1] J. Eschke et al., Ordering of 1100 MAPMTs H12700 for the CBM-RICH photon detector, CBM Progress Report 2015, Darmstadt 2016, p.57

[2] J. Förtsch et al., Development of a MAPMT test stand and first results, CBM Progress Report 2015, Darmstadt 2016, p.58

[3] V. Patel et al., Temperature dependence of dark noise for H12700 MAPMTs : A quantitative approach, this report

Radiation hardness tests of SiPMs for CBM PSD readout - in lab and at NA61@CERN beamtime*

V. Mikhaylov[†1,2], *A. Kugler*[1], *V. Kushpil*[1], *S. Morozov*[3], *and O. Svoboda*[1]
[1]NPI of CAS, Řež, Czech Republic; [2]CTU, Prague, Czech Republic; [3]INR RAS, Moscow, Russian Federation

PSD radiation environment

The Projectile Spectator Detector (PSD) of the CBM experiment is a compensating lead-scintillator calorimeter designed to measure the energy distribution of the forward going projectile nucleons and nuclei fragments (spectators) produced close to the beam rapidity [1]. High intensity beams at FAIR SIS100/300 up to 1E6/1E7 interactions/s lead to the high radiation emission to the PSD making it act as a spallation target producing the high neutron fluence up to 4E12 n/cm^2 accumulated during a year of the experiment operation. Studies of passive parts of PSD including the scintillators shown that it can work in this conditions. The radiation hardness of the Silicon Photomultipliers (SiPM, also called multipixel avalanche photodiodes (M-APD)) to be used for the light readout is the main topic to be discussed.

SiPM irradiation conditions

Several SiPM devices produced by different manufacturers were tested as options for the PSD readout: Zecotek MAPD-3A, Zecotek MAPD-3D, Hamamatsu S12572-010P, Sensl uF-C30020, uF-B30020 and Ketek PM-3350 [2]. SiPMs were irradiated at the cyclotron of NPI Řež with a "white" (2-35 MeV) and mono-energetic (22 MeV) neutron spectrum and total fluxes in the range of 2E10-1E13 n/cm2.

Choice of the SiPM device

The drastic change of the dark current was observed for all the SiPM samples after irradiation by total fluence around 4E12 n/cm^2 as shown at Figure 1. For the Ketek and Sensl devices, the change was the most abrupt requiring more than 1 mA of power supply for the operation making them inapplicable for the readout. Another factor to be mentioned is the dynamic range which is directly dependent on the square of SiPM pixel size. The Sensl and Ketek SiPMs are available on the market with the smallest size of 20-50 um, which compared to the Hamamatsu and Zecotek SiPMs available pixel size of 10 um shortens the dynamic range by 1-2 orders. The dark current of Hamamatsu and Zecotek SiPMs was found to be about an order of magnitude less than for Sensl and Ketek samples. However, Zecotek SiPMs available on the market have pixel recovery time about 2-10 us making them too slow for the PSD readout where hundreds or tens of nanoseconds are required for the operation at 1E6/1E7 interactions/s. Consequently, Hamamatsu S12572-010P was chosen as the best available candidate for the PSD readout in the high radiation environment of CBM experiment.

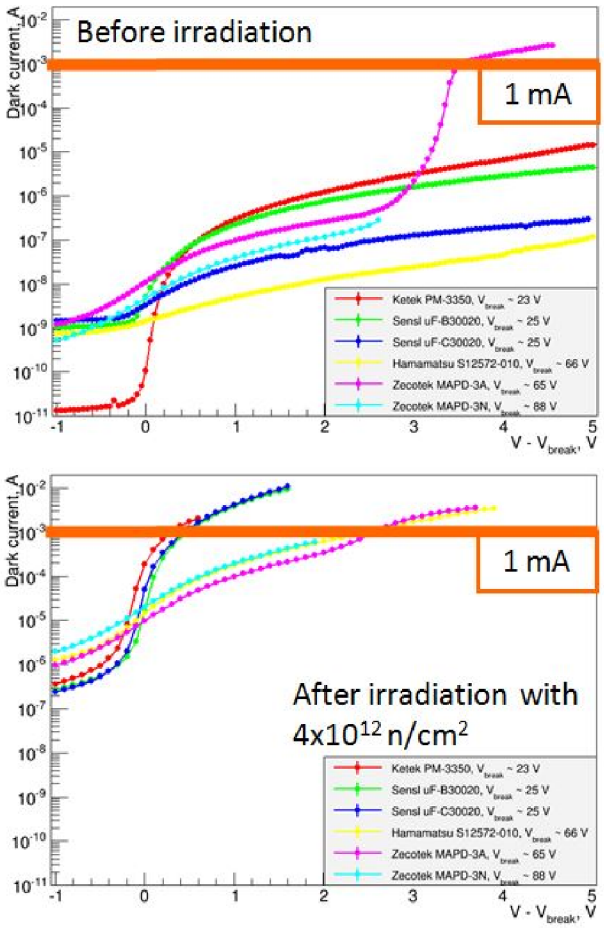

Figure 1: Dark current of SiPMs produced by various manufacturers. Top - before irradiation, bottom - after irradiation.

Investigation of Hamamatsu SiPMs

The change of dark current, breakdown voltage, noise and signal response to LED for Hamamatsu SiPMs was further studied at the lab. Variation of the breakdown voltage due to irradiation was found relatively small to be up to

* Work supported by Czech MEYS - LM2015049 , OP VVV - CZ.02.1.01/0.0/0.0/16_013/0001677
† mikhaylov@ujf.cas.cz

DOI:10.15120/GR-2017-1

0.5 V. This pose no problem for the operation of SiPM itself, but raise requirement of regular module recalibration as section response depends on the SiPM gain which is dependent on the breakdown voltage.

Figure 2 represents the results of SiPMs laboratory tests by the signal to noise ratio (SNR) for the SiPM response to same amplitude LED illumination. One can see the gradual decrease of the SNR with the increase of total absorbed neutron fluence. With neutron fluence up to 7E11 n/cm^2, SNR is dropping to value of 30 which is quite safe for the device operation. However, signals are still visible even for SiPMs irradiated by 1E13 n/cm^2 fluence. Generally speaking, the SNR degradation means the requirement for the regular module recalibration as well as inevitable shortening of the dynamic range.

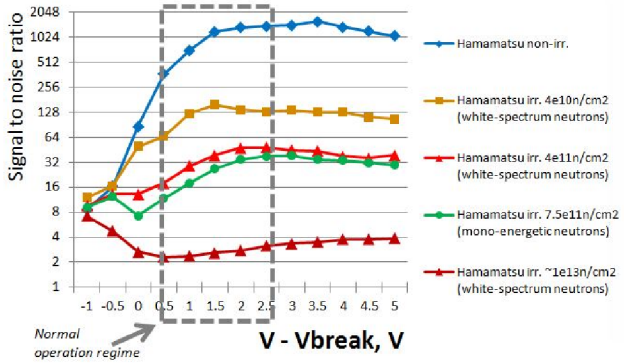

Figure 2: Signal to noise ratio for Hamamatsu SiPMs illuminated by LED.

Further studies were conducted at the NA61 CERN beamtime in summer 2016 with help of NA61 PSD calorimeter similar to CBM PSD with SiPM-based readout [3]. Three packs of 5 Hamamatsu SiPMs - non-irradiated, irradiated with 4E10 and 4E11 n/cm^2 ("white spectrum" of 2-34 MeV) were soldered to NA61 PSD readout boards and mounted to the calorimeter module. With the module equipped with SiPMs irradiated to the same dose, we estimated dependence of the proton energy determination resolution on the neutron fluence applied to SiPMs. First five sections of the module were equipped with the investigated SiPMs, so the achieved energy resolution values are greater than in the case of the full 10-sections operation.

The 80 GeV/c proton beam was utilized to access the calorimeter energy determination performance with irradiated SiPMs. Module energy resolution R_E was calculated from the deposited energy as the sigma of Gauss fit divided by its mean (see Figure 3). For the module equipped with non-irradited SiPMs R_E was equal to 16.5 %. For the SiPMs irradiated by total fluence of 4E10 n/cm^2 it remained the same; even though noise RMS of the module during the simple LED-test shown increase in 1.7 times, it was not visible during the proton beam tests probably due to to increased noise from the other electronic sources during the whole detector operation. Still, signal from muons was not possible to detect, which is not a problem for the detector operation, but makes muon-calibration impossible, so other calibration methods have to be employed. For the SiPMs irradiated by total fluence of 4E11 n/cm^2 R_E was equal to 21.1 %, meaning decrease in the energy resolution by 4.6 %.

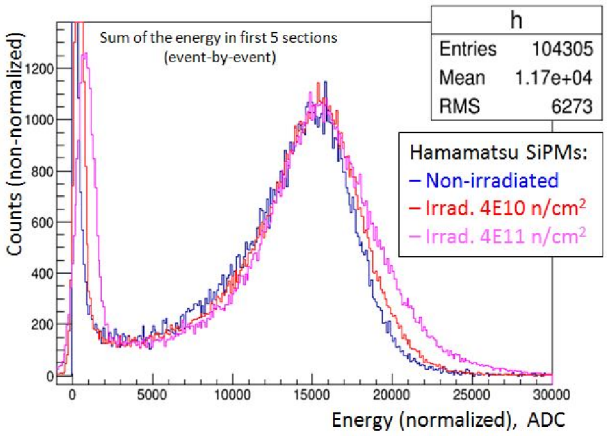

Figure 3: Energy resolution for 80 GeV/c proton beam with half of NA61 PSD module equipped with Hamamatsu SiPMs.

Conclusion

During the SiPM irradiation tests, Hamamatsu S12572-010P was chosen as the best available candidate for the PSD readout. Dark current increase with the absorbed fluence raises the requirement for the corresponding high-current power supply up to 1 mA per SiPM (channel). Gradual degradation of the SiPM signal to noise ratio with the absorbed fluence poses the requirement for the regular PSD module recalibration during the experiment operation. PSD energy resolution R_E studied at NA61 beamtime dropped only slightly - by 4.6 % for the SiPMs irradiated by total fluence of 4E11 n/cm^2.

References

[1] CBM collaboration, Technical Design Report for the CBM Projectile Spectator Detector (PSD), GSI Darmstadt 2015

[2] V. Kushpil et al., Neutron irradiation study of silicon photomultipliers from different vendors, NIM A (2016), http://dx.doi.org/10.1016/j.nima.2016.06.101

[3] V. Mikhaylov et al., Performance of the forward calorimeters for heavy-ion experiments at FAIR, NICA, and CERN SPS, Proceedings of Science, PoS(EPS-HEP2015)281.

DOI:10.15120/GR-2017-1

A slow control system for the HADES and CBM RICH detectors

A. Weber[1], *P. Zumbruch*[2], *and C. Höhne*[1]
[1]Justus-Liebig Universität, Giessen, Germany; [2]GSI, Darmstadt, Germany

An EPICS based slow control system for the HADES RICH700 upgrade and the future CBM RICH is developed. The slow control system is server-client-model based and highly flexible due to variations in the experimental setup. The control software for the ISEG HV power supply (see Fig. 1) is designed in a 3 layer outline. It allows the control of every channel of every module of the crate individually, but also the control of predefined groups of channels from different modules. In addition it is possible to group channels via the GUI, too. The ISEG HV crate (*ECH 44A*) has a *CC24* Master module which includes the EPICS IOC. This allows to run the slow control software of the crate without any additional computer. The HV crate has 6 *EHS F620n-F_SHV* modules with 16 channels each. The modules are limited to 1,5 kV and with single channel floating-GND.

Figure 1: The ISEG crate with 6 modules à 16 channels and a CC24 master.

To cope with low voltage a TDK Lambda Genesis 60-40 is used (see Fig.2). The EPICS IOC runs on an own computer which is connected to the TDK Lambda via LAN. The IOC uses `StreamDevice` with an own protocol for the device. It is possible to control the voltage, set current limits and control different statuses of the LV device.

Figure 2: The TDK Lamda low voltage power supply.

During the experiment the temperature and the humidity will be measured. The temperature is mapped with many DS18B20 1-Wire Sensors from *Maxim Integrated*. To measure the humidity HDC1000 humidity sensors from *Texas Instruments* are used. These sensors support the I^{2}C protocol and have address pins which allow to use up to 4 of these sensors at one port (see Fig.3). Both sensor types are connected to a HadCon2 Board which controls the pins. The HadCon2 is connected to a raspberry pi 2 model B via USB connection. The EPICS IOC runs on the raspberry pi and sends the HadCon2 the commands for the measurement of temperature and humidity.

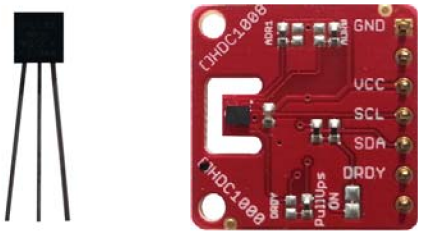

Figure 3: left: One DS18B20 1-wire sensor from Maxim Integrated. right: A HDC1000 sensor on a breakout board.

The HADES RICH upgrade will use many DIRICH boards which have a 1-wire temperature sensor. This temperature can be readout via the TrbNet. Therefore an EPICS IOC is written. It gets the value from many different boards with one call which reduces the traffic on the TrbNet. It is also possible to get more further status values from the TrbNet with the IOC.
The Control System Studio (CSS) is used as the GUI of the HADES RICH experiment and shows the EPICS process variables in a human readable, graphical layout (see Fig.4). It replaced the *Motif Editor and Display Manager* (MEDM) which is known from previous HADES running periods.

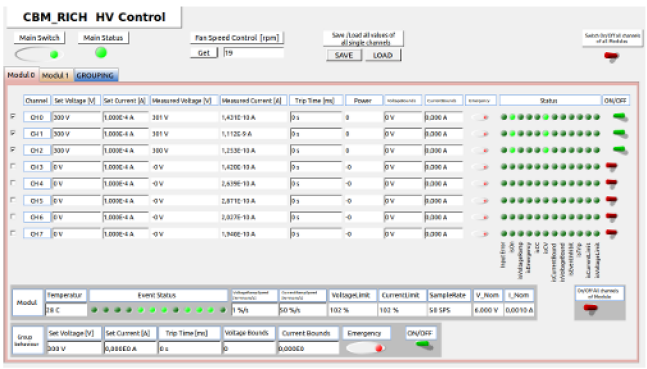

Figure 4: The CSS BOY GUI for the HV power supply.

DOI:10.15120/GR-2017-1

Laboratory tests of the Bucharest TRD prototype performance in High Counting Rate environment*

A. Bercuci[1], *G. Caragheorgheopol*[1], *V. Cătănescu*[1], *M. Petriş*[1], *and M. Petrovici*[1]
[1]National Institute for Physics and Nuclear Engineering (IFIN-HH), Bucharest, Romania

At collision rates of 10^7 $events/sec$ the inner zones of the CBM experiment will be exposed to $\sim$ 100 kHz/cm^2 [1]. This is beyond what was reached so far with current test setups at present irradiation facilities [2], [3]. Although the inverse of time difference between consecutive events, during CERN-SPS bunches, is compatible with or even higher rates [3], since they are not sustained for longer times make all tests done so far incomplete. The TRD prototype developed in Bucharest [4] and the FEE designed to operate it, the FASP [5], [6] and the motherboards housing it, were optimised for high-counting rate environment applications. An alternative to particles bombardment, although less complete, is the use of high flux X-ray tubes.

Experimental set-up

Our experimental setup was aimed to study the alterations of a known signal - in our case the ^{55}Fe detection rate - in the presence of a heavy X-ray detector irradiation. The experimental setup is sketched in Fig. 1 left.

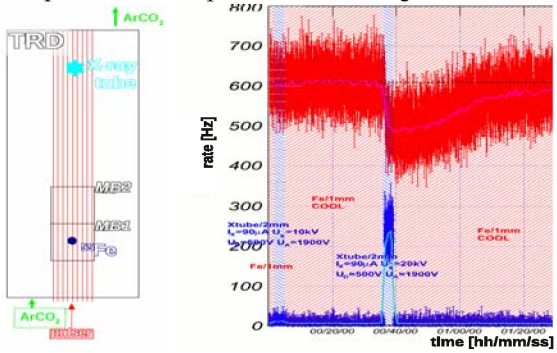

Figure 1: Left : The experimental setup including the position of the X tube and ^{55}Fe wrt TRD, the direction of $ArCO_2$ gas flow and the read-out areas (MB). Right : Monitoring of ^{55}Fe rate (red/magenta) before and after X-ray (blue shaded area) tube irradiation.

The collimated X-ray tube is placed at one end of the detector surface, close to the $ArCO_2$ outlet, while the witness ^{55}Fe source at the other end to assure that the gas flow will not have a detrimental influence. The distance between the center of the two irradiated areas is $\sim$ 20 cm.

^{55}Fe *rate variation after X-rays irradiation*

The measurement was done using 2 areas of $\sim$ 8 cm^2 each. The first is used to record ^{55}Fe rate (red in Fig. 1 right) while the other (blue same figure) the background. Blueish areas in the figure mark the X-ray tube irradiation, typical a couple of minutes. It was estimated that a current intensity on the tube (I_X) of 90 μA will produce in the current setup $\approx$ 100 kHz/cm^2. For U_X = 10 kV the X-ray spectrum is smooth and limited at 10 keV while U_X = 20 kV extends the X-ray spectrum up to 20 keV with pronounced Au L lines at 9.71, 11.44 and 13.38 keV. After the irradiation with the harder spectrum a noticeable degradation of efficiency is measured in the witness rate through a drop of more than 15 % which is recovered after $\sim$ 1 h probably through the gas flow. Less significant effects are produced by the soft spectrum.

Pulser signal monitoring after X-rays irradiation

Squared shaped signals injected on the anode wires are used to induce equal amplitude signals in all FEE channels They are sensitive to parasitic currents which may be produced on HV electrodes by heavy irradiation. In Fig. 2 the monitoring of such signals for all 16 FEE channels used in the setup of Fig. 1 left is shown.

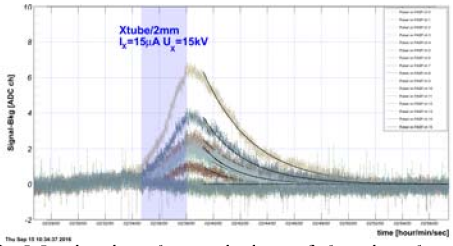

Figure 2: Monitoring the variation of the signal amplitude on different FASP channels before and after X ray (shaded area) tube irradiation.

During irradiation an increase of max. 6 ADC ch of the measured signal is recorded on some channels which represent at most 0.4 % of the standard signal. An exponential time decay of the amplitude excess is recorded with a time constant of $\approx$ 150 s depending on the FEE channel. Such electronic effects, although present in the detector are too low in magnitude to explain the large variations seen in the ^{55}Fe rate.

References

[1] CBM Technical Status Report.
[2] A. Bercuci et al., this report.
[3] A. Bercuci et al., this report.
[4] M. Petrovici et al., Nucl.Instr. and Meth. A579(2007)961.
[5] V. Cătănescu et al., CBM Progress Report (2009) 47.
[6] V. Cătănescu et al., CBM Progress Report (2014) 82.

* Work supported by Romanian ANCSI/CAPACITATI Modul III Contract F04 and NUCLEU Project Contract PN 16420104.

Tracking with the Bucharest TRDs at the CERN-SPS 2015 Testbeam * †

A. Bercuci[1], *D. Bartoş*[1], *G. Caragheorgheopol*[1], *V. Cătănescu*[1], *M. Petriş*[1], *and M. Petrovici*[1]
[1]National Institute for Physics and Nuclear Engineering (IFIN-HH), Bucharest, Romania

A main application of the TRD subsystem within the CBM experiment planned to be build at GSI-FAIR is prolonging tracks defined by the SPS subsystem and improve matching with TOF. The Bucharest TRD prototypes designed for the inner zone of the TRD wall are particular suited for such application as they are optimized for $2D$ position information [1] in high-counting rate environments. A testbeam organized at SPS-CERN was aimed to prove this using a beam of 30 $AGeV/c$ Pb on Pb target.

Experimental setup

A compact setup of 3 TRD prototypes was installed downstream of target at $\sim$ 2 m at an angle of $\sim$ 30^o. A sketch of the TRD read-out units - the triangular pads - and their relative alignment pointing to the target is shown in Fig. 1 with target position on the left side.

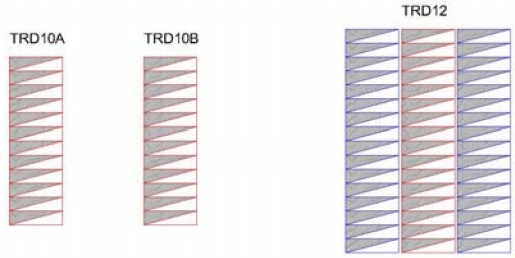

Figure 1: A sketch of the Bucharest TRD setup in which the alignment of pad-rows is emphasised in red for the 3 operated prototypes.

The TRD setup was operated with FASP[2] ASIC for the overlapped area. A MBS-DAQ system was used to record data triggered by a combination of plastic scintillators, a Bucharest RPC_{2013} [3] prototype and a diamond CVD detector mounted in front of the target.

Tracking performance

In order to asses position reconstruction performance of the TRD prototypes a selection on the data was implemented such that cluster quality was defined based on their total charge and shape and events with one such cluster/detector were selected. Due to various reasons pertaining to the triggered setup and read-out an acceptance of less than 0.1 % off all triggered events was accomplished.

In the left panel of Fig. 2 the residual distribution between clusters position across pads and a track fit is shown.

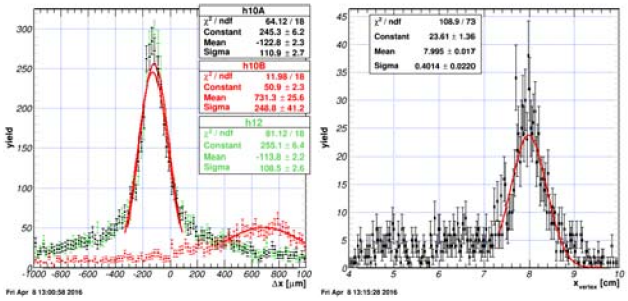

Figure 2: Tracking performances of the TRD prototypes; Left : The residual distribution between clusters position across pads and a linear track model crossing all 3 detectors; Right: Intersection of the track with the target plane. The enhance is clearly visible and it is related to the interaction region on the target.

An alignment procedure was applied based on normalizing[1] simultaneously the three distinct linear position correlations of type $\Delta x_{i-j} : \Delta x_{k-i}$ between the position across pads of each of the 3 cluster/detector. The alignment procedure produced biased results as can be seen by scanning the mean values of the residuals in the figure due to the lack of a reference detector and secondary particle contamination. A further consequence is the under/over estimation of detector resolution reported as the $Sigma$ parameter of the gaussian fit of the residual distribution. Qualitatively, a position resolution across pads better than 200 μm seem to be supported by the data.

A further exercise was to extrapolate the track fit in the prompt plane. A further selection was applied at this stage such that tracks having outliers above the $\pm$ σ level according to Fig. 2 left results were rejected resulting in a 40 % drop in tracked data statistics. The results for vertex definition are shown in Fig. 2 right where a clear enhancement around a position, shifted with 8 cm wrt. projected vertex defined by the TRD setup, and a resolution of few mm, can be seen. Qualitatively the observed shift is a nice confirmation of the trigger bias used in data acquisition in which only one quadrant of the CVD detector was used in the trigger logic.

References

[1] A. Bercuci et al., CBM Progress Report (2015)81.
[2] V. Cătănescu et al., CBM Progress Report (2009) 47.
[3] M. Petriş et al., CBM Progress Report (2012)68.

* Work supported by Romanian NUCLEU Project Contract PN 09370103.
† Special thanks to CERN-SPS operating crew and to our technicians V.Aprodu, L.Prodan and A.Radu for their highly professional contribution without which all these things would'n have been operational in due time.

[1]Correlation distribution is centered at 0 and has slope 1.

DOI:10.15120/GR-2017-1

Bucharest RPC and TRD prototypes at CERN-SPS 2016 Testbeam *

A. Bercuci[1], *V. Aprodu*[1], *D. Bartoş*[1], *G. Caragheorgheopol*[1], *V. Cătănescu*[1], *F. Constantin*[1], *M. Petriş*[1], *M. Petrovici*[1], *L. Prodan*[1], *A. Radu*[1], *and C. Şchiaua*[1]

[1]National Institute for Physics and Nuclear Engineering (IFIN-HH), Bucharest, Romania

The RPC [1],[2] and TRD [3]-[5] prototypes developed in Bucharest for low polar angles region of CBM experiment were tested at CERN-SPS at the end of 2016. The reaction products produced by colliding the Pb beam of 13 GeV/c ($run1$), 30 GeV/c ($run2$) and 150 GeV/c ($run3$) on a Pb target were used. The RPC signals were processed by fast amplifiers/discriminators NINO chip [6] of which differential outputs were covered by CAEN V1290A TDCs. The information was read-out using the MBS-DAQ system [7]. The frontend electronics used for the three TRD prototypes was based on FASP-01 and FASP-02 [8] ASICs. FASP-01 signals were processed using MADCs and MBS-DAQ operated in a trigger mode. In parallel, other regions of the TRDs were operated using FASP-02 and 2 free running systems, one already presented in previous CBM reports [9],[10] and a new one coined FASPRO [11].

Experimental setup

In Fig. 1 a downstream towards target view of the Bucharest experimental setup is presented. It consists of 2 RPC prototypes and three layers of TRDs. The TRD setup is zoomed in the right panel of Fig. 2 where, from left to right, 2 TRD_{2010} prototypes read-out on a $\sim 94cm^2$ area completed by a TRD_{2012} detector of $60 \times 60cm^2$ partially equipped with electronics. The experimental arm was completed with 2 plastic scintillators for triggering and timing purpose one mounted at $\sim 1m$ from target and a second one in front of the RPC setup.

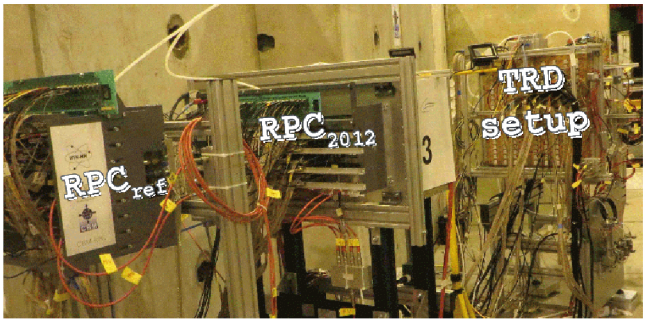

Figure 1: The Bucharest setup, from downstream to the target position RPC_{ref}, RPC_{2012} and the three TRD layers zoomed out in Fig. 2.

For each beam energy/run a different configuration of the TRD read-out was used as follows: tracking optimized in $run1$ with MBS and FASPRO on all 3 TRD detectors on parallel directions, $2D$ position information for the TRD_{2010} prototypes fully equipped with FASPRO and the TRD_{2012} alone operated with MBS on $run2$ and tracking in two divergent directions wrt. beam plane by using TRD_{2010}-TRD_{2012} in the horizontal plane with MBS and the second TRD_{2010} with a different area of TRD_{2012} operated with FASPRO at a small inclination angle wrt. horizontal plane.

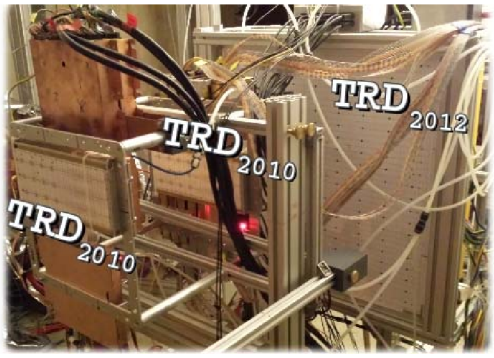

Figure 2: The TRD setup, from left to right, 2 TRD_{2010} and the 60×60 cm^2 TRD_{2012}.

For calibration purposes a pulser signal was injected on all TRDs with 0.1 Hz and varying amplitudes during the data taking.

MBS DAQ for the RPCs and TRDs detectors

The information from MBS DAQ is aimed to be used for tracking and $dE/dx - time$ studies. The acquisition of all TRD self trigger signals together with the particle arrival time from plastics were also collected up to 14 channels. Two classes of triggers were used based on the TRDs self trigger topology and plastic correlation.

Using the self trigger TRD signal the interaction rate was monitored as shown in Fig. 3 left. The hit rate per second on a $\sim$ 15.5 cm^2 area operated on the central part of the TRD_{2012} with 2 FASP-02 ASICs was recorded during $run3$. The time of flight of particles between the front plastic and the RPC can be estimated from the information shown in Fig. 3 right. The arrival time at both ends of 16 RPC strips is presented for one of the TDCs, channel wise, in units of 25 ps. In TDC channel 8 the arrival time at the front plastic is registered. Data are un-calibrated and the colour code represent the yield.

* Work supported by Romanian ANCSI/CAPACITATI Modul III Contract F04 and NUCLEU Project Contract PN 16420104.

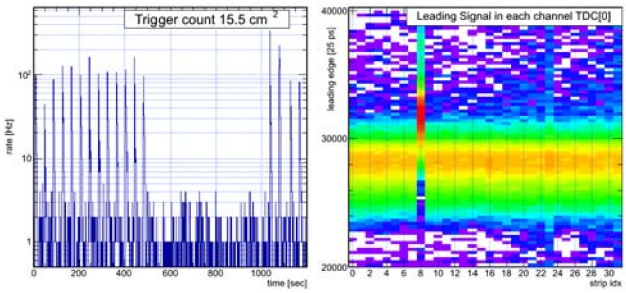

Figure 3: Left: Trigger rate variation on an area of 15.5 cm^2 of the TRD_{2012} during and off spill for 20 min acquisition time. Right: The distribution of particle arrival time on RPC_{2012} for 16 strips read-out at both ends and the plastic synchronisation signal on TDC channel 8.

Free Running DAQ based on FASP-02 ASIC for the TRD setup

The capabilities of the FASP-02 were fully exploited for the first time by the FASPRO mother-board. Together with a system of timing and data processing the DAQ is completely driven by the channel wise self triggering option of the ASIC.

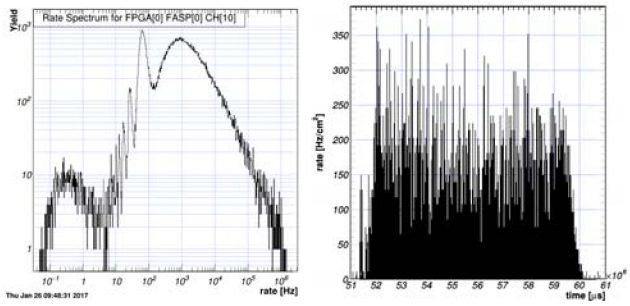

Figure 4: *FASPRO* free-running DAQ results : Left: Disribution of the inverse of time difference between two consecutive events per FASP channel with the pulser ripples up to 100 Hz, bunch distribution up to 1 kHz and the intra-bunch interactions up to 1 MHz. Right: The frequency profile of a spill of $\approx$ 9 s averaged on 1 ms intervals as seen on 94 cm^2 of the forward TRD_{2010} detector.

An example of the inverse of time difference between consecutive events distribution seen by each channel reading-out 2 paired triangular pads spanning $\sim$ 2 cm^2 of detector area is shown in Fig. 4 left. The spectrum contains 3 regions as follows pulser ripples on next interaction event up to 100 Hz, rates of consecutive events from different bunches up to 1 kHz and consecutive events from the same bunches above this limit. It is worth observing that using a channel wise read-out mode, consecutive hits compatible with rates of up to almost the theoretical limit of 1 MHz of the FASP can be recorded. The proper response time of TRDs, dictated by the drift time, is on the level of 100 ns but secondary effects produced in the detector volume and systematic effects of FEE response to signal can increase it. For the current analysis an event is defined on an interval of 150 ns. After building up events based on matching the channel-wise time labels within the predefined time window the event frequency spectrum can be reconstructed. In Fig. 4 right an SPS spill is presented cooresponding to one spike in the left panel of Fig. 3. The average rates are calculated on 1 ms intervals and are integrated on the total area operated of the forward TRD_{2010} detector in $run3$.

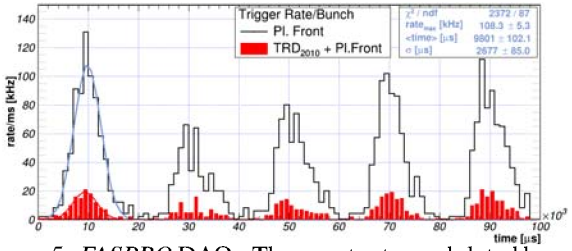

Figure 5: *FASPRO* DAQ : The event rate modulated by machine bunches, during 100 ms acquisition time, as function of time for the forward plastic scintillator w/o condition on the whole TRD_{2010} surface (black) and with (red).

A further zooming of the spill structure can be followed in Fig. 5 as measured with the free-running DAQ based on *FASPRO* [11]. Here the machine bunches interacting with the target are visible simultaneously in two detectors: the forward plastic scintillator and, after calibrating out the delay between the two, in the correlation with the forward TRD_{2010} detector. More details of this operation mode are presented in a separate report [11].

Conclusions

The detector prototypes developed in Bucharest were used in a unique setup during the 2016 CERN-SPS testbeam to scan 3 beam energies with 3 different DAQ systems used in each of the three runs in a different configuration. Such redundant information is of mandatory importance to study systematic effects in the new conditions for which these prototypes were developed.

References

[1] M. Petriş et al., CBM Progress Report (2011)55
[2] M. Petriş et al., CBM Progress Report (2012)68
[3] M. Petriş et al., CBM Progress Report (2011)47
[4] M. Petriş et al., CBM Progress Report (2012)60
[5] A. Bercuci et al., CBM Progress Report (2015)81
[6] F.Anghinolfio et al., Nucl.Instr.Meth. A533(2004)183
[7] H.G.Essel and N.Kurz, GSI Ann. Rep. (1988)188
[8] V. Cătănescu et al., CBM Progress Report (2014) 82
[9] F. Constantin et al., CBM Progress Report (2012)56
[10] F. Constantin et al., CBM Progress Report (2014)83
[11] A. Bercuci et al., this report.

DOI:10.15120/GR-2017-1

Tests of the *FASPRO* free-running DAQ for the Bucharest TRD prototypes at the CERN-SPS 2016 testbeam*

A. Bercuci[1], *G. Caragheorgheopol*[1], *V. Cătănescu*[1], *M. Petriş*[1], *M. Petrovici*[1], *and C. Şchiaua*[1]

[1]National Institute for Physics and Nuclear Engineering (IFIN-HH), Bucharest, Romania

Processing the large amounts of data expected in the central region of the TRD subsystem of the CBM experiment, based on the results obtained with the very first TRD prototypes developed by us [1], an optimal ASIC, Fast Analog Signal Processing (FASP) [2] was developed. The 2^{nd} version of the chip[3] has 16 independent channels, each providing the total charge and its arrival time information collected on the read-out unit - the pad. In order to cope with limitations in the S/N ratio along the TRD triangular pad read-out geometry [4] an analog summing is performed before charge integration. Thus each FASP channel reads-out a detector area of $\approx$ 2 cm^2 of two paired pads, alternating rectangular and tilted coupling, for robust estimation of position and PID related measurements.

The FASPRO board and Detector setup

To fully exploit the capabilities of the FASP, a new mother board, FASP-Read-Out (FASPRO), was developed to house the chip, 16 ADCs and the drivers for connection to the outside world. The board is driven by a 40 MHz clock which can also be fed from outside. On each differential output channel the digitized values of the signal amplitude and the corresponding channel-wise self-trigger time signal - the Chip Select (CS) - are delivered. The output is ready for GBTx [5] integration - the solution foreseen for the CBM experiment to ship data from the hot zone to the online/offline processing units.

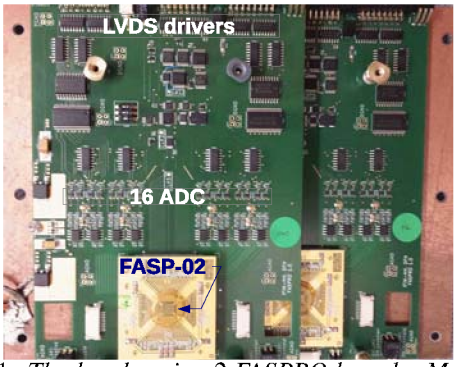

Figure 1: *The box housing 2 FASPRO boards. Major elements of the FASPRO board are emphasized on the picture.*

The free running DAQ based on FASPRO boards was tested during the CERN-SPS 2016 testbeam [6]. The detector setup used for 150 GeV/c Pb beam is shown in Fig. 2. Within this setup an inclined direction, wrt to horizontal beam plane, was used to test the tracking performance of the TRD prototype in free-running operation.

* Work supported by Romanian ANCSI/CAPACITATI Modul III Contract F04 and NUCLEU Project Contract PN 16420104.

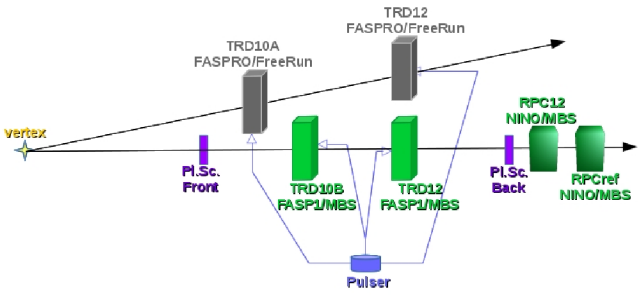

Figure 2: *Schematic view of the experimental setup used for* 150 GeV/c *Pb testbeam; the horizontal direction was operated with MBS (green) and the tilted one (gray) run with FASPRO in free-running mode for two TRDs and two plastic scintillators.*

The forward $TRD10A$ was operated with 6 FASPRO boards $i.e.$ 96 read-out channels on an area of 8.16×11.52 cm^2 organized in 3 pad rows (see Fig. 3 right). A similar read-out geometry was used on the back $TRD12$ situated at a $\approx$ 60 cm larger distance. A plastic scintillator was installed, in the beam plane, at $\approx$ 1 m from the target and a second scintillator, aligned with the first, at $\approx$ 3 m from the target, shadowed by the TRD setup. For calibration purposes a pulser signal was injected synchronously on the anode plane of all TRD detectors during the measuring time at a main frequency of 0.1 Hz and varying amplitudes. The HV U/I characteristics of all TRDs were read-out and stored with the data as described in the next section.

Overview of the Free-running DAQ

A simple DAQ, schematically shown in Fig. 3, was build to synchronize all FASPRO boards used in acquisition and to ship data to a permanent storage. A FASPRO-box (see Fig. 1) with 2 FASPs can operate 32 read-out channels $i.e.$ one pad-row in our setup. The digitized signals and their CS status are send to the Local Data Concentrators (LDC) phased with a unique 40 MHz clock. The LDCs are implemented on Xilinx Zynq 7000 cores [7] and run an event buffer for each FASP channel. For each valid data (CS status *on*) the time label is attached to data.

A further extension of the system consists of 16 dual NIM-LVDS / LVDS-NIM translators used to read external signals (see "Ext. Signals" label in Fig. 2) with the proper clock of the DAQ. We have used during the testbeam the following signals: 2 logic $ANDs$ each coming from the two PMs reading one plastic scintillator (see Fig. 2 $Pl.Sc.\ Front/Back$) and the beam start/stop signals provided by the machine. For monitoring the detector itself

DOI:10.15120/GR-2017-1

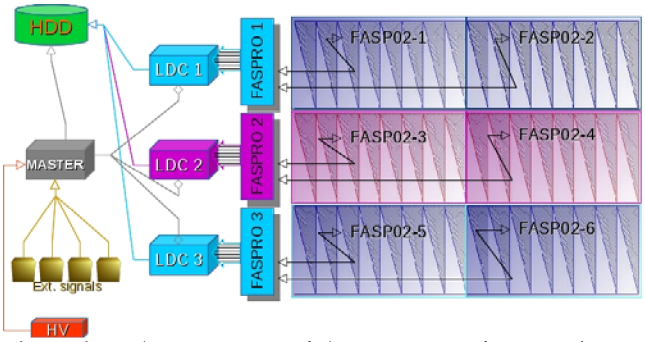

Figure 3: *Schematic view of the TRD DAQ from read-out units (triangular pads) to storage (HDD).*

during irradiation the HV parameters (U, I)[1] were included in the data flow at continuous reading interval of 1.33 ms.

Event types and characteristics

The output of the DAQ is defined by the 3-tuple (GEO, $TLAB$, VAL) with GEO the identifier of the "geographical" position of the channel, $TLAB$ the time in 25 ns clocks as registered by the FPGA counters and VAL the data measured per channel (ADC channels for FASPRO, XADC values for HV and the on/off status of the external detectors signals respectively). The channel wise data are packed offline to $EVENT$s based on their $TLAB$. For each signal source the delays are constant such that for $e.g.$ the TRDs, the $EVENT$ is directly reconstructed based only on the $TLAB$ information[2].

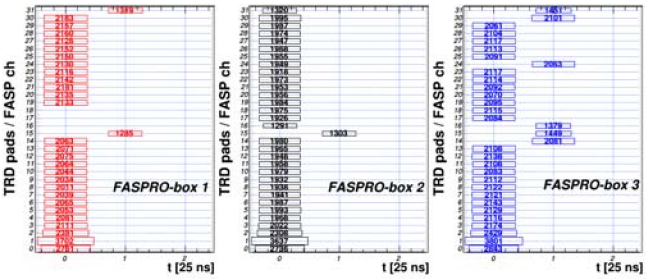

Figure 4: *Pulser event seen on $TRD10A$ (3×32 pads) by 6 FASP-02 ASICs (see Fig. 3). Each channel signal is characterized by its delay in 25 ns clocks wrt. prompt signal and value expressed in ADC channels.*

There were three types of signals which were measured quasi-synchronously during the testbeam: pulser events of constant frequency and amplitude used for FEE calibration, ^{55}Fe X-rays for assessing detector performance during irradiation and the proper beam-target events respectively. In Fig. 4 a detailed view of a pulser event is presented based only on the channel wise information from DAQ. The event is seen in 3 pad-rows/LDCs (each represented as a panel in Fig. 4) of 32 pads/channels (shown on the vertical axis) corresponding the operated area of $TRD10A$. The arrival time of each signal wrt. to prompt is represented on the horizontal axis in DAQ clocks. The response of each FEE channel to the unique signal induced by the pulser can be read in the figure. The result demonstrates the correctness of the principles implemented in our FEE-DAQ approach.

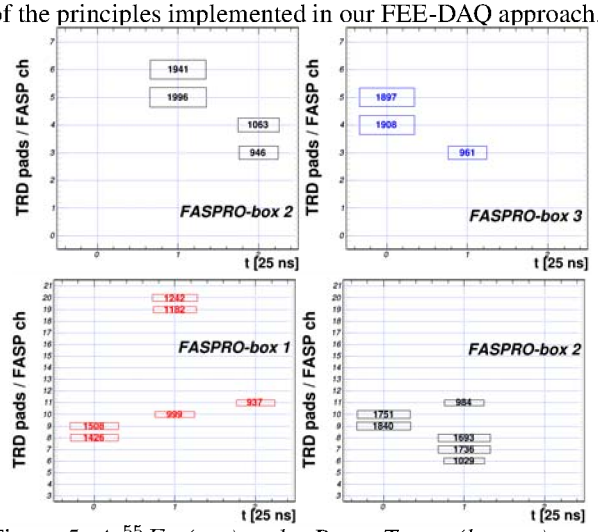

Figure 5: *A ^{55}Fe (top) and a Beam-Target (bottom) event seen on the $TRD10A$ detector in 2 adjacent rows. Data representation and matching with DAQ according Fig. 4.*

Pulser events are used for equalizing the effective gain and delay of each FASP channel but for detector efficiency/gain calibration in high counting rate conditions a $standard\ candle$ is used as $e.g.$ ^{55}Fe. Another application of such events is to provide a basis for understanding more complicated events as those produced by charged particles. A typical event of such type is shown in the top 2 panels of Fig. 5 where the interaction happens close the pad-row boundary and therefore the response is seen in 2 rows/panels. The relative delay pattern of the signals of a cluster carry detailed 2D position information but such correlations will not be discussed here. In the bottom 2 panels of Fig. 5 an event obtained in a beam-target interaction is shown. The event contains 2 distinctive interaction spots: a topological-simple type around pad/channel 20 and one with a complicated topology, spanning 2 pad-rows of TRD and a large time window front around 9. Such examples show that using the correlations induced by the triangular-pad read-out and the time/signal cluster topology accessible with FASP, the TRD can provide information with unprecedented precision both for position and PID.

References

[1] M. Petrovici et al., Nucl.Instr. and Meth. A579(2007)961.

[2] V. Catanescu et al., CBM Progress Report (2009)47

[3] V. Cătănescu et al., CBM Progress Report (2014) 82.

[4] A. Bercuci et al., CBM Progress Report (2014) 81.

[5] P.Moreira, J.Christiansen and K.Wyllie, The GBTx Link Interface Asic, Draft v1.7, October 2011.

[6] A. Bercuci et al., this report.

[7] https://www.xilinx.com/products/silicon-devices/soc/zynq-7000.html.

[1] We used two CAEN NDT 1471H HV units each having 4 channels which provide analogic, channel wise monitoring capabilities for U and I. The monitoring outputs were converted to LVDS signals by a custom made converter and digitized via the build-in XADC of the Zynq platform.

[2] The matching of different sources within an $EVENT$ needs calibration of physical delays and is not covered here

DOI:10.15120/GR-2017-1

Towards the Common Readout Interface boards for STS*

W. Zabolotny[†1], *G. Kasprowicz*[1], *A. Byszuk*[1], *M. Guminski*[1], *K. Pozniak*[1], *and R. Romaniuk*[1]
[1]Institute of Electronic Systems, Warsaw University of Technology, Warszawa, Poland

Version control friendly project management

Development of the firmware for CBM readout requires maintaining of complex HDL designs. To allow efficient management of projects incorporating multiple independently maintained IP blocks, the Tcl scripts proposed in 2015 have been further developed into the VEXTPROJ environment [1]. This environment allows rebuilding Vivado projects from the textual description stored in the version control systems. It supports importing IP blocks from remote repositories (Git, SVN, and others), and allows utilization of the "Out of Context Compilation" (OOC) to speed up rebuilding of the whole design. Figure 1 shows an example of a project consisting of locally and remotely managed sources.

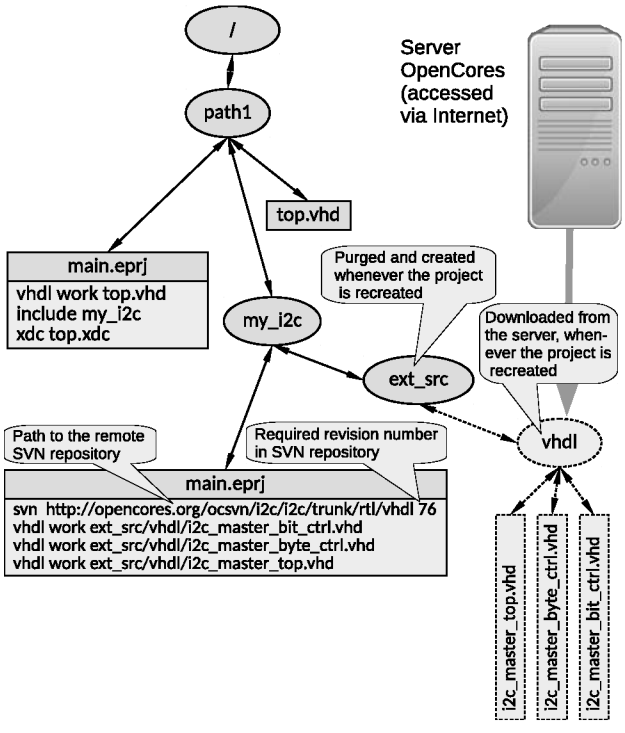

Figure 1: Example of the VEXTPROJ project, that uses the particular version of IP block stored in a remote SVN directory [1].

STS/MUCH-XYTER2 tester

The VEXTPROJ approach has been used in further development of the STS/MUCH-XYTER2 (SMX2) tester [2]. The design has been split between two repositories: "SMX2 tester" and "SMX2 model". The tester design imports the model as an OOC compiled block, which results in faster compilations. In 2016, the exhaustive tests of the SMX2 model have been performed in cooperation with the AGH and GSI teams. The tests covered the operation of the SMX2 model with varying number of uplink connections, recovery from induced and random error conditions and transmission of generated test hit data. The tests resulted in disclosing and fixing of a few subtle bugs, and improvements to the protocol [3] and the design of the SMX2 digital backend [4]. After the STS/MUCH-XYTER2 has been manufactured, the SMX2 tester has been also successfully used for communication and testing of the real ASICs.

Assessment of the new FPGA platform for STS Common Readout Interface

The work on the prototype of the Common Readout Interface (CRI) predecessor - the DPB boards, and the SMX2 tester was started when "Family 7" was the newest FPGA series available from Xilinx. Therefore the AFCK board designed for that purpose was based on Kintex 7 XC7K325T chip [5]. In the meantime, two new families - the "Ultrascale" and the next "Ultrascale+" were offered by Xilinx. As the initial step for selection of the final hardware platform for the CRI boards, the preliminary analysis of the feasibility of CRI implementation in the Ultrascale+ chips was performed. The prices of comparable "Kintex Ultrascale+" and "Zynq Ultrascale+" are similar. Therefore the Zynq Ultrascale+ ZU11EG chip was selected for the analysis. Obtained preliminary results show that it should be possible to use a single ZU11EG FPGA to concentrate data from up to 8 Common ReadOut Boards (CROB) [6] into up to 8 FLES links. The analysis included different architectures for the STS data concentration. The approach based on the heap sorter [7], offers better memory blocks utilization but requires too high clock frequency (896 MHz) to handle the incoming data stream. The approach based on the simple stream merger allows to parallelize data processing in the input stage, and group concentrated data in the longer words at the output to lower the required clock frequency. Of course, those preliminary results may be significantly changed by further progress in technology.

* Work partially supported by GSI
† wzab@ise.pw.edu.pl

Forth based AFCK board controller

The AFCK board used as a prototyping platform for STS readout requires initial configuration of various components (clock generators, clock crossbar, connected FMC boards). It is equipped with the separate ARM processor, but it is used as an MTCA MMC controller, and modification of its firmware is inconvenient. Therefore, another approach was proposed. The solution [8] is based on a very simple J1B Forth CPU developed by James Bowman [9]. The Forth language offers very good code density and supports an interactive development of control/diagnostic procedures, without a necessity to use an external compiler. Simultaneously, the developed and tested procedures (Forth "words") may be added to the initial Forth CPU program included in the FPGA configuration bitstream. It is also possible to define a procedure to be executed automatically, after the FPGA is configured or after the reset. Afterward, the interactive operation is possible. The controller may be used for configuration and diagnostics even before the Ethernet-based IPbus control connection is established, or in setups where the IPbus is not available at all. Communication with the controller is provided by the USB connector and the on-board USB/UART bridge. Defined Forth words support control of typical programmable clock generators (Si57x, IDT ICS8N4Q001), control of the internal I2C busses in the AFCK and communication with the user logic in FPGA.

Preparations for the GBT-based readout

The SMX2 tester used the "Black Box" models of the GBT e-Links. It allows direct connection to the SMX2 ASIC. However, the final setup, based on the CROB boards [6] must use the real e-Links implemented by the GBT-FPGA IP core in the tester (future CRI) and by the GBTX ASIC in CROB. Implementation of the GBT-compatible SMX2 tester and CRI required a few introductory steps. The GBT-FPGA IP core is still under development. Therefore to facilitate its replacement with the new version, the VEXTPROJ compatible version of the GBT-FPGA sources has been prepared. To test the communication with the GBTX ASIC, the dedicated test setup has been created consisting of the AFCK board and the Versatile Link Demonstrator Board (VLDB). The AFCK firmware includes the Forth controller, the GBT-FPGA core, and dedicated test cores. First tests have been performed, and the current work is focused on the verification (with the CERN GBTX-SUPPORT team) that the GBTX operation modes required by the SMX2 communication protocol are working correctly.

Controlling of the e-Link data and clock delays in the GBTX requires the GBT IC controller core, which should be delivered by the CERN team. Before it is available, it is necessary to emulate it using the I2C control of the GBTX chip. To make it possible, the original Windows-compatible Python scripts provided by CERN have been modified to ensure Linux compatibility.

The current work is aimed at implementation of the GBT-compatible SMX2 tester. First attempts, based on the 3.1.1 version of the GBT-FPGA core required the special clock-domain-crossing (CDC) blocks in the uplink channel. Fortunately, the new release of the GBT-FPGA (4.1.0 in July 2016) provides the portable CDC blocks in the GBT-FPGA core itself[1]. Further research is desired to check if using the Xilinx-specific blocks for CDC may result in even smaller resources consumption.

References

[1] W.M. Zabolotny, "Version control friendly project management system for FPGA designs", Proc. SPIE 10031 (2016) 1003146, doi:10.1117/12.2247944

[2] W.M. Zabolotny and A.P. Byszuk and D. Emschermann and M. Guminski and B. Juszczyk and K. Kasinski and G. Kasprowicz and J. Lehnert and W.F.J. Müller and K. Pozniak and R. Romaniuk and R. Szczygiel, "Design of Versatile ASIC and Protocol Tester for CBM Readout System", February 2017, JINST, vol. 12, C02060, doi:10.1088/1748-0221/12/02/C02060

[3] K. Kasinski and R. Szczygiel and W. Zabolotny and J. Lehnert and C.J. Schmidt and W.F.J. Müller, "A protocol for hit and control synchronous transfer for the front-end electronics at the CBM experiment", November 2016, NIMA, pp. 66-73, doi:10.1016/j.nima.2016.08.005

[4] K. Kasinski and R. Szczygiel and W. Zabolotny, "Back-end and interface implementation of the STS-XYTER2 prototype ASIC for the CBM experiment", November 2016, JINST, vol.11, C11018, doi:10.1088/1748-0221/11/11/C11018

[5] W.M. Zabołotny and G. Kasprowicz, "Data processing boards design for CBM experiment", Proc. SPIE 9290 (2014) 929023, doi:10.1117/12.2073377

[6] J. Lehnert and A.P. Byszuk and D. Emschermann nad K. Kasinski and W.F.J. Müller and C.J. Schmidt, and R. Szczygiel and W.M. Zabolotny, "GBT based readout in the CBM experiment", 2017, JINST, in press

[7] W.M. Zabolotny, "Dual port memory based Heapsort implementation for FPGA", Proc. SPIE 8008 (2011) 80080E, doi:10.1117/12.905281

[8] W.M. Zabolotny, "AFCK_J1B_FORTH - Forth based system for AFCK board initialization and diagnostics", https://github.com/wzab/AFCK_J1B_FORTH

[9] J. Bowman, "Swapforth is a cross-platform ANS Forth", https://github.com/jamesbowman/swapforth

[1] The newest 5.1.0 version released in January 2017 also offers that functionality.

DOI:10.15120/GR-2017-1

Σ^0 Hyperon Production in p + Nb at E_{kin} = 3.5 GeV*

L. Fabbietti[1,2], J. Friese[1] and T. Kunz[†1,2] for the HADES collaboration
[1]Physik Department E62, Technische Universität München, D-85748 Garching; [2]Excellence Cluster 'Origin and Structure of the Universe', D-85748 Garching

The production of Λ^0 – baryons (M = 1115.7 GeV/c^2) has been investigated by the HADES collaboration in various collision systems ranging from p + p to Au + Au at SIS energies. In this context it is of interest, to which amount feeding from Σ^0 (M = 1192.6 GeV/c^2) decays via the processes $\Sigma^0 \rightarrow \Lambda^0\gamma$ (BR = 100 %) and $\Sigma^0 \rightarrow \Lambda^0 e^+e^-$ (BR = 0.005 %) contributes to the observed Λ yields [1]. While at low collision energies close to the NN threshold the production cross sections $\sigma_\Lambda/\sigma_\Sigma \approx 10$ [2] suggest a feeding of ~ 10% it is expected that at energies around 1 GeV above threshold this contribution increases to ~30% [3]. For even higher energies it may reach up to 50%.

We have therefore started an attempt to identify Σ^0 – decays in the reaction p + Nb at E_{kin} = 3.5 GeV ($\epsilon \approx$ 0.67 GeV). In the collected data sample of 4.21· 10^9 events Λ particles have been reconstructed through their weak decay $\Lambda \rightarrow p\pi^-$ utilizing momentum, dE/dx and track vertex information [4]. Coincident γ detection is achieved through conversion pair $\gamma \rightarrow e^+e^-$ identification in HADES, although the design of the detector is rather optimized for low conversion probability. Furthermore, the momentum measurement for electrons is limited to $p_e \geq 50$ MeV/c because of the strong magnetic field between the two tracking stations MDCI/II and MDCIII/IV. GEANT simulations show that the conversion probability (mostly in the Nb target) for γs (E_γ ~ 80 MeV) from Σ^0 decays is only ~3.0%.

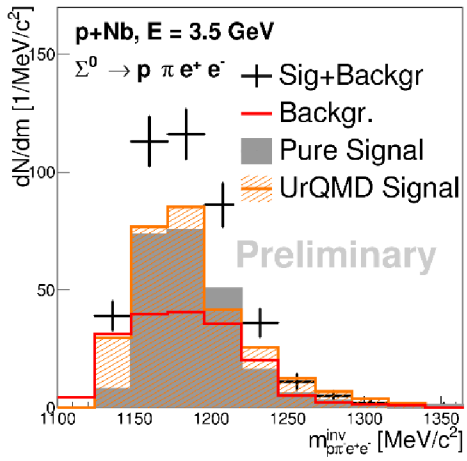

Figure 1: Invariant mass of the proton, pion and one dielectron pair for the selected Σ^0 candidates. The reconstructed events (black) are plotted together with background (red), extracted signal (grey) and UrQMD simulations (orange).

In the present analysis we require for each event with Λ content at least the momentum vector of one fully reconstructed electron or positron with a good quality RICH ring. For the identification of the converted photon we search for a second electron/positron candidate characterized by at least a RICH signal with hits in the inner tracking detectors only. The momentum of the latter is then determined by an event hypothesis method.

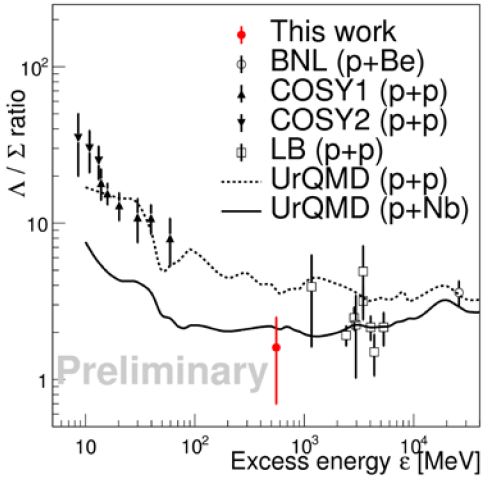

Figure 2: Λ/Σ^0 ratio as a function of the excess energy ε. For the calculation of ε the Fermi motion has not been taken into account. The statistical and systematic errors have been summed up quadratically.

The reconstructed four particle invariant mass spectrum is presented in fig. 1. The background has been determined via a sideband analysis technique. Around 220 Σ^0 candidates are visible and are reasonably reproduced by a full scale simulation using UrQMD events as an input. After acceptance and efficiency correction the signal has been extrapolated to the uncovered p_t region using Boltzmann functions. The differential cross section is extracted to be $\frac{d\sigma}{d\Omega}(\Sigma^0) = 2.3 \pm (0.2)^{stat} \pm (^{+0.6}_{-0.6})^{sys} \pm (0.2)^{norm}$ within the rapidity region of $0.5 < y < 1.1$. An extrapolation based on UrQMD predictions and measured Λ^0 rapidity distributions yields a total cross section of $\sigma^{tot}_{p+Nb}(\Sigma^0) = 5.8 \pm (0.5)^{stat} \pm (^{+1.4}_{-1.4})^{sys} \pm (0.6)^{norm} \pm (1.7)^{expol}$. The ratio $\frac{\Lambda}{\Sigma^0} = 1.6 \pm (0.1)^{stat} \pm (^{+0.5}_{-0.5})^{sys} \pm (0.4)^{expol}$ compares to the world data as shown in fig. 2.

[1] K.A. Olive et al., Chin. Phys. C, 38, 0900001 (2014)
[2] P.Kowina et. al, Eur. Phys. J. A 22, 293-299 (2004)
[3] H.Landolt, R.Börnstein, Landolt-B.12, (1988)
[4] G.Agakishiev et. al, Eur. Phys. J. A 50 (2014) 81

* Work supported by BMBF 05P15WOFCA, GSI TMLFRG 1316
† tobias.kunz@tum.de

Charged kaon and ϕ reconstruction in Au+Au collisions at 1.23A GeV*

H. Schuldes[1†] *for the HADES collaboration*
[1]Goethe-University Frankfurt

The High Acceptance DiElektron Spectrometer HADES took data of Au+Au collisions at a kinetic beam energy of 1.23A GeV. At this energy all hadrons carrying strangeness are produced well below their respective elementary production threshold ($NN \rightarrow N\Lambda K^+$: $\sqrt{s}_{thr}$ = 2.55 GeV, $NN \rightarrow NNK^+K^-$: $\sqrt{s}_{thr}$ = 2.86 GeV, $NN \rightarrow NN\phi$: $\sqrt{s}_{thr}$ = 2.89 GeV). Therefore, the study of these rarely produced particles can reveal information about the high-density phase created and about the production and propagation of strangeness in heavy-ion collisions.

In total 2.1×10^9 Au+Au events were used in the analysis, corresponding to the 40% most central events. Kaons were identified via their momentum, time-of-flight and energy loss information measured with the magnet spectrometer, consisting of Mini-Drift Chambers MDC and a superconducting magnet, and a scintillator hodoscope TOF at high polar angles (44 - 85°) or a Resisitve Plate Chamber RPC at low polar angles (18 - 45°). A detailed description of HADES can be found in [1]. The residual background of proton and pion tracks was subtracted in an iterative fitting procedure using a polynomial function. The neutral ϕ meson was reconstructed via its decay into charged kaons (BR($\phi \rightarrow K^+K^-$) = 49.8%). The uncorrelated background, mainly from mis-identification of the kaon candidates, is described using the mixed-event technique.

For the first time in the SIS18 energy regime, it is possible to perform a multi-differential analysis as a function of transverse mass and rapidity, as well as for different centrality classes, of charged kaons and ϕ mesons in the same data sample. HADES has a large phase space coverage at mid-rapidity down to the lowest m_t. The raw count rates are corrected for acceptance and efficiency losses using a Monte-Carlo simulation. The spectra are extrapolated assuming thermal production according to Boltzmann distributions. For more details see [2,3].

The resulting ratios of the 4π multiplicities K^-/K^+, as well as ϕ/K^- are found to be independent of the centrality of the collision. The multiplicity ratio ϕ/K^- is shown in Fig. 1 in comparison to measurements at similar energies in lighter systems [4–6], as well as from higher $\sqrt{s_{NN}}$ [7–9]. Whereas this ratio stabilizes at higher energies at a value of about $\sim$ 0.15, it substantially increases towards lower energies. As a consequence, ϕ feed-down decays become a sizeable source ($\sim$ 25%) for K^- production below the NN threshold energy.

This fact is not taken into account in the microscopic transport models which are commonly used to describe the particle production and dynamics of a heavy-ion collision. In these models the sub-threshold K^- production is realized almost exclusively via the so-called strangeness exchange reaction $\Lambda\pi \rightarrow NK^-$ [10]. Therefore our new measurement will help to stimulate progress in transport theoretical descriptions of strangeness production in heavy-ion collisions.

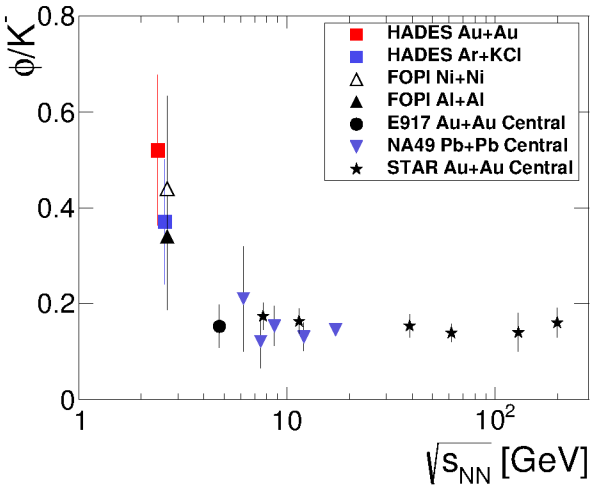

Figure 1: ϕ/K^- multiplicity ratio as a function of $\sqrt{s_{NN}}$ [2,4–9].

References

[1] G. Agakishiev *et al.* (HADES), Eur. Phys. J. A **41** (2009) 243.

[2] J. Adamczewski-Musch *et al.* (HADES), arXiv 1703.08418 (2017).

[3] H. Schuldes, PhD Thesis Goethe-University Frankfurt (2016).

[4] G. Agakishiev *et al.* (HADES), Phys. Rev. C **80** (2009) 025209.

[5] K. Piasecki *et al.* (FOPI), Phys. Rev. C **91**, (2015) 054904.

[6] P. Gasik *et al.* (FOPI), Eur. Phys. J. A **52** (2016) 177.

[7] B. Holzman *et al.* (E917), Nucl. Phys. A 698 (2002) 643.

[8] S. V. Afanasiev *et al.* (NA49), Phys. Lett. B 491 (2000) 59.

[9] J. Adams *et al.* (STAR), Phys. Lett. B 612 (2005) 181.

[10] C. Hartnack, H. Oeschler, Y. Leifels, E. L. Bratkovskaya, J. Aichelin, Phys. Rept. **510** (2012) 119.

* Work supported by BMBF (05P15RFFCA), GSI, HGS-HIRe and HICforFAIR

† h.schuldes@gsi.de

DOI:10.15120/GR-2017-1

System-size dependence of the integrated dilepton excess yield in heavy-ion collisions*

S. Harabasz[1,2†] *for the HADES collaboration*[1]

[1]Technische Universität Darmstadt, Germany; [2]Jagiellonian University, Kraków, Poland

Electromagnetic probes provide valuable information on the properties of the hot and dense medium produced in heavy-ion collisions. In particular, the yield of dilepton radiation in the invariant-mass region above the π^0 mass and below the vector meson region (around 0.7 GeV/c^2) can be related to the lifetime of the fireball [1].

An important ingredient of understanding this relation is the dependence of the integrated dilepton yield on the size of the collision system. This is possible with the data sets collected and analyzed by HADES. Fig. 1 shows the yield as a function of mean number of participating nucleons for the collisions C+C at $E_{\mathrm{beam}} = 2A$ GeV ([2], triangles), Ar+KCl at $E_{\mathrm{beam}} = 1.76A$ GeV ([3], stars) and four 10%-wide classes [4] of Au+Au at $E_{\mathrm{beam}} = 1.23A$ GeV ([5], points with systematic error rectangles). Points in blue are integrals in the range $0.15 < M_{ee} < 0.5$ GeV/c^2, studied previously in light systems in [3], red points correspond to an integration range $0.3 < M_{ee} < 0.7$ GeV/c^2, which is expected to be sensitive to medium effects also at high beam energies [6].

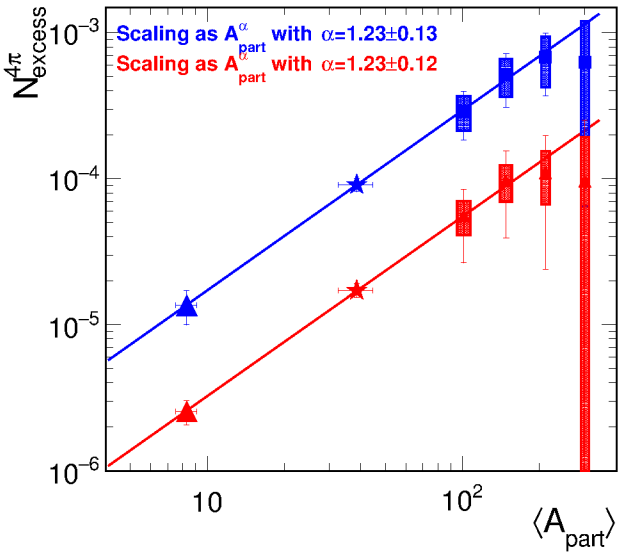

Figure 1: Dilepton excess as function of number of participants integrated in two different invariant mass ranges. Details are given in the text.

The medium radiation was distilled by subtracting contributions before the fireball formation and after its freeze-out. The latter was done by subtracting the η radiation, based on an independent analysis [7]. The former – by subtracting the appropriately normalized yield in p+p and n+p collisions at the same beam energy [8].

In order to take into account different collision energies, an ansatz was made, that for a given system, the dilepton yield scales with energy like π^0 production in the case of the lower integration range and like η in the higher integration range. The E_{beam} dependence, obtained from various measurements [2, 3, 7, 9, 10, 11, 12, 13], is in this low-energy regime stronger for η than for π^0, reflecting the higher mass of the former.

Only after proper energy scaling of the C+C and Ar+KCl points in Fig. 1 down to the values corresponding to $E_{\mathrm{beam}} = 1.23A$ GeV, it was possible to fit power law to the $\langle A_{\mathrm{part}} \rangle$ dependence of the dilepton yield in the two lighter systems and two peripheral classes of Au+Au collisions. The two most central classes are not included in the fit, since they have large systematic and statistical uncertainties. However, within these uncertainties they are compatible with the fitted line. The power law exponent turns out to be the same for both integration ranges. It is larger than unity, which means that scaling with the number of participants is stronger than linear. This points to regeneration of baryonic resonances as the source of the enhanced dilepton radiation, which in turn happens more often, if the fireball lives longer.

References

[1] T. Galatyuk *et al.*, EPJA **52** (2015) 131
[2] HADES Collaboration, PLB **663** (2008) 43
[3] HADES Collaboration, PRC **84** (2011) 014902
[4] B. Kardan, Diploma thesis 2015
[5] S. Harabasz, PhD thesis 2017
[6] P. Huck, NPA **931** (2014) 659
[7] C. Behnke, J. Phys. Conf. Ser. **599** (2015) 012029
[8] HADES Collaboration, PLB **690** (2010) 118
[9] HADES Collaboration, PRL **98** (2007) 052302
[10] DLS Collaboration, PRL **79** (1997) 1229
[11] TAPS Collaboration, Z. Phys. A **359** (1997) 65
[12] TAPS Collaboration, PRC **56** (1997) R2920
[13] E895 Collaboration, PRC **68** (2003) 054905

* Work supported by VH-NG-823, EMMI, GSI, HGS-HIRe and H-QM.

† s.harabasz@gsi.de

Dielectron helicity in Au+Au collisions at 1.23A GeV with HADES *

P. Sellheim[1,2] *and the HADES collaboration*[1]
[1]Goethe-Universität, Frankfurt am Main, Germany

HADES measured Au+Au collisions at 1.23A GeV to extend the studies of QCD matter at high temperatures and densities. This measurement complements the previous measurement of Ar+KCl collisions at 1.76A GeV [1]. The matter produced in heavy-ion collisions can be probed by dielectrons, i.e. virtual photons decaying into an electron positron pair. Electrons and positrons are identified via observables reconstructed with HADES in various detector subsystems (e.g. time-of-flight, energy loss) and used within a neural network. The identified electrons and positrons are then paired with each oppositely charged particle in the same event. After subtraction of the combinatorial background of uncorrelated pairs, the pair distributions are corrected for detector inefficiencies, acceptance effects and extrapolated to the full phase space. Finally, systematic errors are estimated to consider the uncertainties due to the spectra corrections and normalizations and background subtraction. The signal mass spectra are in agreement with the results obtained by two different methods [3, 2]. f The reconstructed invariant mass distribution revealed an excess above a mass of 0.15 GeV/c^2 due to medium radiation. In order to characterize this excess, the helicity of the dielectron signal, probing the polarization of the virtual photon, is reconstructed (see [1] for details of the helicity reconstruction). The latter describes the angle of the virtual photon to the electron (positron) in the rest frame of the virtual photon. The helicity distribution is assumed to be flat in case of thermal emission but differs from a flat distribution for non thermal dielectrons.

The resulting helicity distributions are presented in Fig. 1 for a mass range dominated by π^0-Dalitz decays (upper) and the dielectrons in the excess region (lower). The data is compared to the assumption of a flat helicity distribution. A filtering of the cocktail with the HADES acceptance shows that the helicity distribution shape is strongly modified due to the limited detector acceptance. In order to compare the data to the assumption of a flat helicity, a ratio of data over cocktail filtered by acceptance is evaluated and presented (see Fig. 1 (small boxes)). Since the ratio is closer to one in the lower ratio, the yield in the excess mass range fits better to the cocktail. In conclusion, this observation fits to the assumption that the excess seems of a thermal origin while the yield in the π^0-Dalitz mass range shows the expected anisotropy.

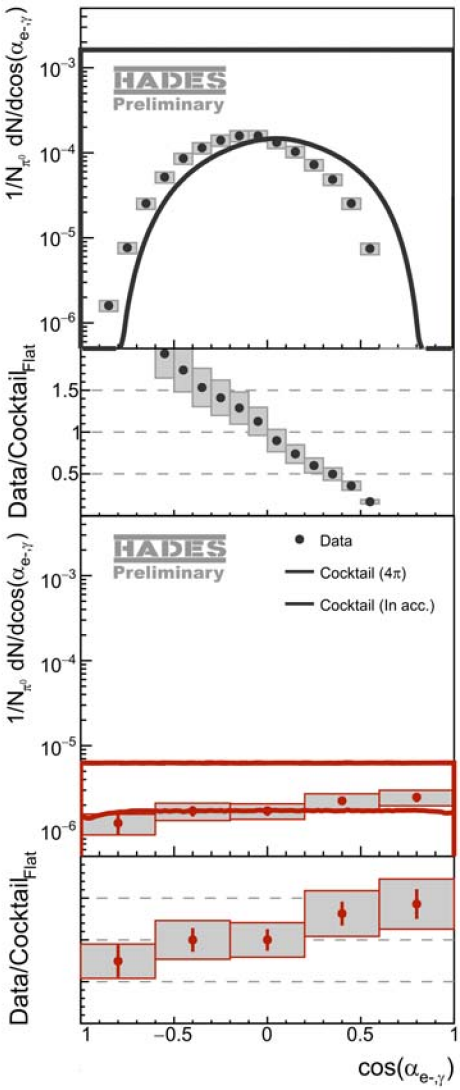

Figure 1: Reconstructed helicity distribution compared to cocktail (large boxes) and ratio of data to cocktail (small boxes). Both are shown for the mass range $0 < M_{ee} < 0.15$ GeV/c^2 (upper) and $0.3 < M_{ee} < 0.7$ GeV/c^2 (lower).

References

[1] G. Agakishiev et al., Dielectron production in Ar+KCl collisions at 1.76A GeV, Phys. Rev., vol. C84, p. 014902, 2011

[2] S.Harabasz, Reconstruction of virtual photons from Au+Au collisions at 1.23 GeV/u, PhD thesis, 2017

[3] P.Sellheim, Reconstruction of the low-mass dielectron signal in 1.23A GeV Au+Au collisions, PhD thesis, 2017

* This work has been supported by BMBF (05P15RFFCA), GSI, HIC for FAIR, HGS-HIRe and H-QM.

DOI:10.15120/GR-2017-1

Multi-differential proton flow measurements with HADES in Au+Au collisions at 1.23A GeV*

Behruz Kardan[1†] *(for the HADES Collaboration)*

[1]Goethe-Universität Frankfurt, Max-von-Laue-Str. 1, 60438 Frankfurt am Main, Germany

Collective flow phenomena are a sensitive probe for the general properties of extreme QCD matter [1], such as its shear viscosity [2]. To achieve a good understanding of these phenomena, flow observables are deduced and compared with model calculations to constrain the nuclear Equation-of-State (EoS) [3, 4]. The understanding of the EoS of dense matter is of great importance for the investigation of supernovae and compact stars [5].

HADES [6] has a large acceptance combined with a good mass-resolution and therefore allows the study of dielectron and hadron production in heavy-ion collisions with unprecedented precision. At the BEVALAC and SIS18 directed and elliptic flow have been measured for pions, charged kaons, protons, neutrons and fragments, but higher-order harmonics have not yet been studied. With the statistics of seven billion Au-Au collisions at 1.23A GeV recorded in 2012, the investigation of higher-order flow harmonics will be possible. Within the 5 weeks of the Au+Au run the SIS18 synchrotron delivered 684 hours of Au^{69+} ion beam to the HADES cave [7] with an intensity of $(1.2-2.2)\times10^6$ ions per sec. A 15-fold segmented gold target with an interaction probability of 1.51% was used. A fraction of around 80% of the total recorded events was triggered by selecting mostly central events with a charged hit multiplicity in the TOF detector $N_{ch} > 20$. According to detailed comparison of the charged track and hit multiplicity distribution with a Glauber Model simulation, this central trigger selects about 47% of the total hadronic cross section of 6.83 ± 0.43 barn, corresponding to a maximum impact parameter of $b_{max} = 10$ fm [8]. In this analysis 4.32×10^7 events were used after event selection.

In high-energy collisions of nuclei a highly excited nuclear medium is created and its collective expansion causes a correlated emission of particles. In perfectly central collisions the expansion should be isotropic, leading to radial flow, observable in the transverse-mass spectra of the produced particles. Less central collisions are characterized by an overlap region which is more anisotropically shaped. This event-shape characteristics is usually studied via the azimuthal anisotropy of the momentum space of identified particles w.r.t a corresponding symmetry plane and it is common to analyze this by a Fourier decomposition yielding the flow coefficients v_1, v_2, v_3 and higher. Due to their correlation to the collision geometry, the directed v_1 and elliptic v_2 are linked to the reaction plane, which itself is also observable via the spectators.

* Work supported by BMBF (05P15RFFCA), GSI, HGS-HIRe, H-QM and HICforFAIR

† bkardan@ikf.uni-frankdurt.de

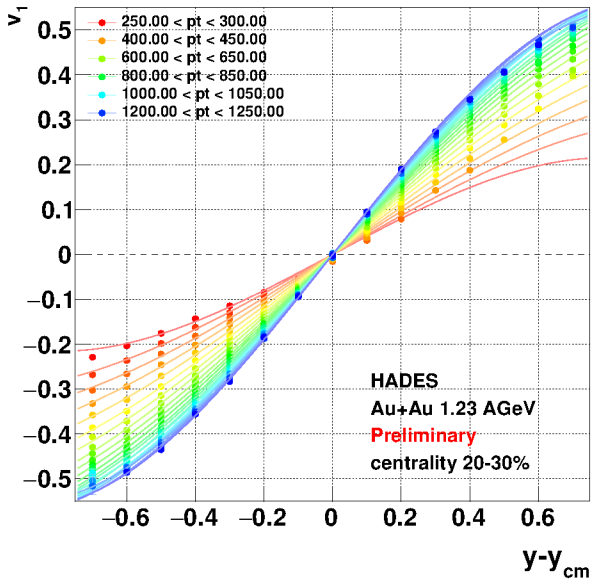

Figure 1: Preliminary data on directed flow (v_1) of protons as measured by HADES in semi-central ($20-30\%$) Au+Au collisions at 1.23A GeV, shown as a function of the center-of-mass rapidity in transverse momentum intervals of 50 MeV/c. The lines are to guide the eye.

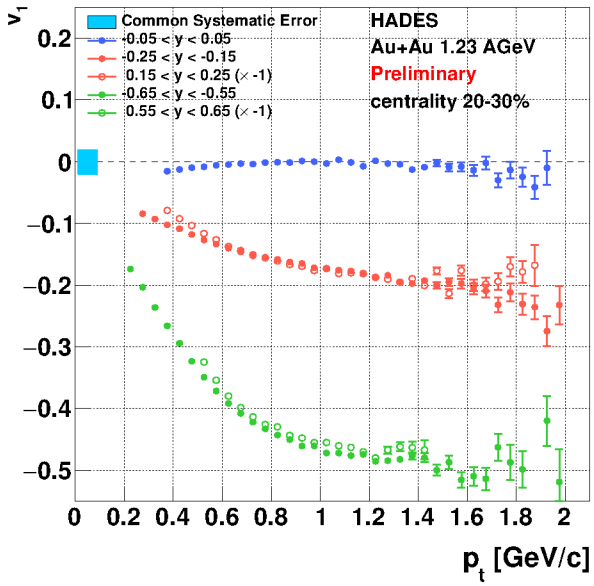

Figure 2: Comparison of the p_t dependence of proton v_1 in five rapidity intervals, symmetric around mid-rapidity.

DOI:10.15120/GR-2017-1

We present here a high-statistics, multi-differential measurement of v_1 and v_2 for protons in Au+Au collisions at 1.23A GeV, extracted over a large region of phase space using the standard event plane method. The data have been corrected for the event plane resolution [9, 10]. In addition, an efficiency correction due to the differential detector load has been applied track-by-track, as a function of the polar angle, the relative angle to the event plane and the track multiplicity in a given sector. Figure 1 shows the results on v_1. A good forward-backward symmetry with respect to mid-rapidity is seen, as expected due to the symmetry of the collision system. Remaining discrepancies are well within the systematic error, which has been estimated by embedding simulated protons into real or UrQMD background events. A similar symmetry is seen for v_2, see Fig. 3. A sizeable negative v_2 is measured around mid-rapidity. Its value clearly depends on the centrality of the collision, as illustrated in Fig. 4. The preliminary results indicate a good consistency of the first two flow coefficients of protons with FOPI data [4, 11, 12] and are in the process of being finalized. Due to the large collected events statistics and the large acceptance HADES will also be able to address the measurement of higher-order flow harmonics in the low energy regime. This will allow to extend the existing data into so far unexplored regions and will provide new insights into the properties of strongly interacting matter at extreme densities, as e.g. its viscosity. The employment of multi-particle methods will also enable the disentanglement of the contributions of collective and non-flow processes.

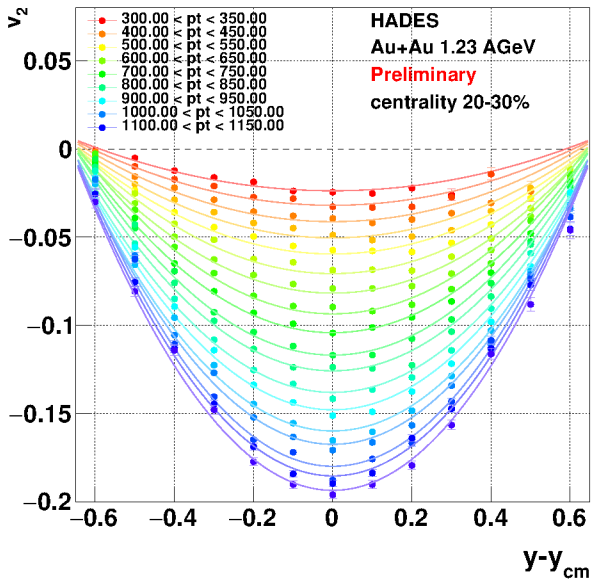

Figure 3: Preliminary data on elliptic flow (v_2) of protons measured with HADES in semi-central ($20-30\%$) Au+Au collisions at 1.23A GeV. Shown is v_2 as a function of the center-of-mass rapidity in transverse momentum intervals of 50 MeV/c (lines are to guide the eye).

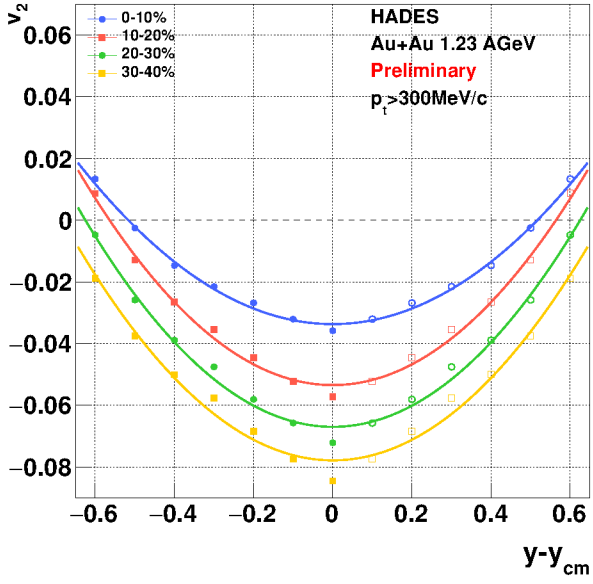

Figure 4: Preliminary data on elliptic flow (v_2) of protons measured with HADES in different centrality intervals of Au+Au collisions at 1.23A GeV. Shown is the p_t integrated v_2 as a function of the center-of-mass rapidity.

References

[1] H. G. Ritter and R. Stock, J. Phys. G **41** (2014) 124002 arXiv:1408.4296.

[2] B. Barker and P. Danielewicz, arXiv:1612.04874.

[3] P. Danielewicz, R. Lacey and W. G. Lynch, Science **298** (2002) 1592 arXiv:nucl-th/0208016.

[4] A. Le Fèvre *et al.* Nucl. Phys. A **945** (2016) 112 arXiv:1501.05246.

[5] M. Oertel, M. Hempel, T. Klähn and S. Typel, Rev. Mod. Phys. **89** (2017) no.1, 015007 arXiv:1610.03361.

[6] G. Agakishiev *et al.* [HADES Collaboration], Eur. Phys. J. A **41** (2009) 243 arXiv:0902.3478.

[7] W. Bayer et al., Accelerator Operation Report, GSI Report 2013-1, pages 255-p.

[8] B. Kardan, Diploma thesis 2015, G. Agakishiev *et al.* [HADES Collaboration], paper in preparation.

[9] A. M. Poskanzer and S. A. Voloshin, Phys. Rev. C **58** (1998) 1671 arXiv:nucl-ex/9805001.

[10] J. Y. Ollitrault, Nucl. Phys. A **638** (1998) 195. arXiv:nucl-ex/9802005.

[11] T. Galatyuk, HADES overview, Nuclear Physics A, Vol 931, November 2014, Pages 41-51.

[12] W. Reisdorf *et al.* [FOPI Collaboration], Nucl. Phys. A **876** (2012) 1 arXiv:1112.3180.

DOI:10.15120/GR-2017-1

Charged pion flow in Au+Au collisions at 1.23AGeV with HADES *

M. Gumberidze[1], *P. Tlusty*[2] *for the HADES Collaboration*
[1]Technische Universität Darmstadt, Germany; [2]Nuclear Physics Institute, (CAS), 25068 Rez, Czech Republic

The properties of a compressed system formed in a heavy-ion collision can be studied looking at the azimuthal momentum distribution of the emitted particles. If the system was in thermal equilibrium, the resulting pressure generates a common velocity in the outgoing particles: *collective flow*. The term *collective flow* includes a common radial expansion, modifying the momentum distribution of outgoing particles, and an anisotropic expansion, affecting the spatial orientation of particle momenta. The first component is called *radial flow*, the second *anisotropic flow*.

The yield of various hadrons with respect to the reaction plane can be characterized by a Fourier expansion where the different coefficients measure different anisotropies present in the system:

$$\frac{dN}{d(\phi-\phi_R)} = [1+2v_1cos(\phi-\phi_R)+2v_2cos(\phi-\phi_R)+...] \quad (1)$$

where ϕ denotes the azimuthal angle of the outgoing particles and ϕ_R is the orientation of the event plane which is determined event-by-event. The first harmonic (v_1) represents an overall shift of the distribution in the transverse plane and is called directed flow. The second harmonic (v_2) represents an elliptical volume and is called elliptic flow.

The study of collective flow in heavy-ion collisions has potential to offer insight into the equation of state of the produced matter. In particular, the shape of v_1 as a function of rapidity in the mid-rapidity region is of interest because it is sensitive to crucial details of the expansion of the participant matter during the early stage of collision. It is generally believed that the directed flow is generated early in the heavy-ion collision. The models indicate that the evolving shape and orientation of the participant zone and its surface play a role in determining anisotropy measured among these particles in the final state.

In this contribution, we focus on the results of the directed flow of positevely charged pions in Au+Au collisions. The charged pions identification in HADES [1] is done via the velocity of particles detected in the time-of-flight detectors as a function of momentum. Directed flow is measured with respect to the reaction plane determined from the spectator flow using the Forward Wall (FW) of HADES. The FW, a plastic scintillator hodoscope array, is placed at a distance of 7m behind the target at small forward angles between 0.3° and 7.3° to detect charged projectile spectators by time-of-flight. The distribution of the FW hits is used to reconstruct the event plane.

The directed flow of charged pions in Au+Au@1.23AGeV has been measured over a large region of phase space. The data have been corrected for the event plane resolution using the so-called Ollitrault method [2]. In addition, efficiency losses due to high particle multiplicities have been taken into account on track-by-track basis. Those corrections were determined from experimental data as a function of the polar θ and azimuthal $\phi-\phi_R$ angles and the local track multiplicity. In Fig. 1, the results on v_1 as a function of center-of-mass rapidity (y) is presented for four 10% centrality bins. All data points in Fig. 1 are antisymmetric around mid-rapidity, as expected due to the symmetric collision system. The most central bin 0-10% shows nearly no directed flow, where for other bins the slope of $v_1(y)$ (dv_1/dy) has negative sign showing so-called anti-flow, on contrary to the proton flow pattern. A systematic study of this effect and its comparison with transport model predictions can disentagle the influence of the reaction geometry, like shadowing of emitted pions by the spectator matter, from the effects coming from the compressed matter produced in an early stage of the collision.

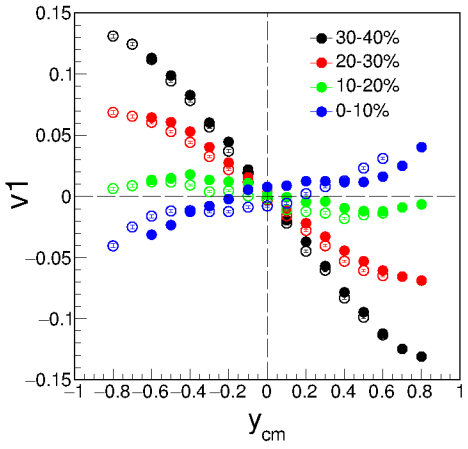

Figure 1: Rapidity dependence of the directed flow, v_1 of positively charged pions (π^+) for Au+Au collision at 1.23 AGeV for four 10% centrality bins. Closed points correspond to measured data, open are mirrored.

References

[1] G. Agakishiev *et al.* (HADES Collaboration), Eur. Phys. J. A 41 (2009) 243

[2] Y. Ollitrault arXiv:nucl-ex/9711003

* Work supported by TU Darmstadt: VH-NG-823, GSI, NPI AS CR, Rez (Czech Republic): MSMT LM2015049, GACR 13-06759S

Efficiency and volume corrections to particle number fluctuations *

M. Szala[1], *R. Holzmann*[2], *and the HADES collaboration*
[1]Goethe Universität, Frankfurt am Main, Germany; [2]GSI, Darmstadt, Germany

By varying the collision system and the beam energy of heavy-ion collisions one can access broad areas of the phase diagram of strongly interacting matter. Higher order moments of conserved quantities (e.g. baryon number, charge, strangeness) are predicted to be sensitive to a first order phase transition and especially to a critical point of the QCD phase diagram. Strong critical fluctuations would indeed modify these moments, resulting in deviations from the baseline Poisson distribution. The HADES experiment can address these signals in heavy-ion collisions at beam energies of a few GeV/u.

In the analysis of Au+Au collisions at $\sqrt{s_{NN}}$ = 2.41 GeV measured with HADES in 2012 the efficiency correction is an important step in obtaining the higher order moments of the proton number distribution.

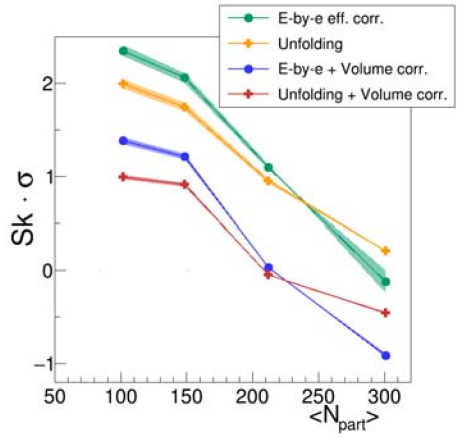

Figure 1: Measured Sk · σ of protons as function of mean number of participants. Two different methods of efficiency correction were tested, correcting the moments (green) and unfolding (yellow). The results are modified further by volume fluctuation corrections (see text).

For this purpose, detailed investigations of efficiency correction methods to the ratios of cumulants $\frac{c_3}{c_2} = Sk \cdot \sigma$ and $\frac{c_4}{c_2} = \kappa \cdot \sigma^2$ were performed with Au + Au UrQMD events and GEANT simulations. Two different approaches were tested: correction of the moments (as proposed in [1, 2]) and unfolding of the distributions [3]. After their successful assessment in the simulation, the two methods were applied to the HADES experimental data and the higher moments of the proton distributions were extracted. We find that the two methods provide plausible and consistent results in the Au + Au data (see Figs. 1, 2).

* Supported by GSI and EMMI.

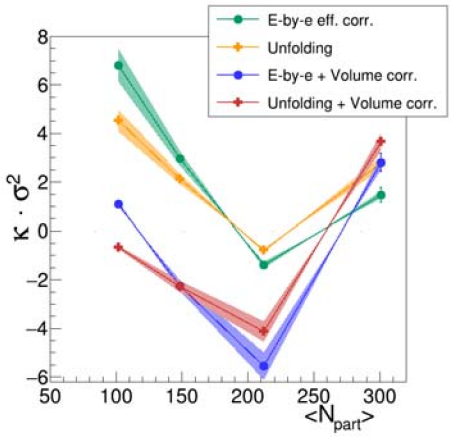

Figure 2: Measured $\kappa \cdot \sigma^2$ of protons. For most central collisions the volume corrected results show contrary behavior.

Experimentally measured dynamical event-by-event fluctuation signals such as cumulants of (net-)particle distributions can also be modified by the fluctuations of the number of participants in a given centrality selection [4, 5]. To correct the data for this effect, we have applied the procedure of Skokov et al. [4] on the higher order moments (see Figs. 1, 2). For the volume correction we assume that the volume scales like the number of participants and the corresponding N_{part} distributions are modeled with a Glauber model [6]. The necessary corrections need to be carefully studied before comparison with other experiments and theory.

As the fully conserved quantity investigated here is the baryon number, further investigations will focus on including protons bound in the fragments produced in Au+Au collisions to the efficiency and volume corrections.

References

[1] A. Bzdak, V. Koch, Phys.Rev. C91 (2015) 027901.

[2] A. Bzdak, V. Koch, Phys.Rev. C86 (2012) 044904.

[3] S. Schmitt, JINST 7 (2012) T10003.

[4] V. Skokov, B. Friman, K. Redlich, Phys. Rev. C 88 (2013) 034911

[5] P. Braun-Munzinger, A. Rustamov, J. Stachel, Nucl.Phys. A960 (2017) 114-130

[6] B. Kardan, Diploma thesis, Goethe University Frankfurt (2015)

DOI:10.15120/GR-2017-1

Collision time reconstruction and particle identification in AuAu collisions at 1.23A GeV with HADES *

G. Kornakov[†1] *for the HADES Collaboration*
[1]Technische Universität Darmstadt, Germany

The time-of-flight technique plays a central role in particle identification in HADES [1]. The time measurement is performed by a diamond START detector [2], placed in front of the target, and two STOP detectors, placed behind the magnet and the tracking detectors. Low polar angles are covered by a Resistive Plate Chamber detector [3], for the rest, a wall of fast timing scintillator bars [4] are used.

The velocity of a detected particle is calculated from the time difference between the STOP and START signals divided by the track length, measured from the collision vertex to the time of flight walls. Although the resolution of the diamond detector is of 60 ps, the collision time can be improved further if enriched with information from tracking. For each reconstructed and identified track is possible to calculate the residual between the measured and the theoretical expected time of flight. The weighted average of all residuals is called T_0. In order to avoid the statistical correlations between the estimated time and the measured time in the STOP detectors, for each individual track the T_0 time is evaluated individually by combining all the other reconstructed traces. Effects like multiple scattering and energy loss are properly incorporated in a dedicated Monte-Carlo simulation with detailed detector response functions. The result of applying such a technique is shown in the Figure 1. Since all the times can be considered to be independent, the characterisation of the difference between the START time and the T_0 as a function of number of used particles x, can be parametrized as follows: $\sigma(T_0 - T_{START}) = \sqrt{a^2 \times x^{2b} + c^2}$, where the constant a is the mean uncertainty of a single track, b is the coefficient that scales the improvement to the T_0 by adding n tracks and c is the constant resolution of the diamond detector. If instead of making the difference between both times, they are combined with weights, the collision time resolution function is obtained, as accurate as 54 ps for peripheral collisions and 31.4 ps for the most central.

Once the velocity is corrected by the new START time, each track is identified with the best mass hypothesis. For that, also the specific energy loss in the tracking detectors is used in order to be sensitive to the intrinsic charge of the produced particles in the collisions and providing separation for example for deuterons and Helium. In the Figure 2 it is shown the reconstructed mass spectrum and the identified particles by shaded areas. More than 90 % of all reconstructed tracks are identified. The rest are random combinations of traces matched to STOP detectors.

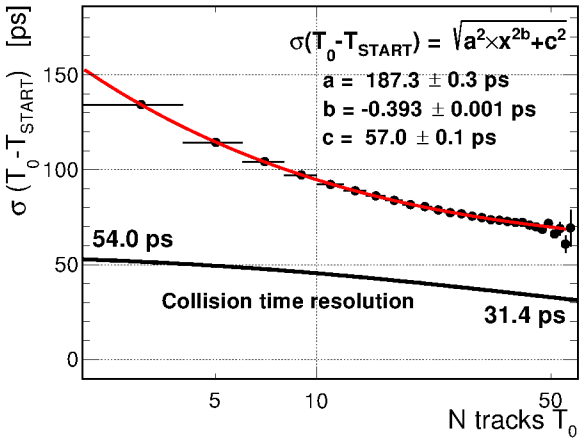

Figure 1: Collision time reconstruction using the T_0 method. The lower line is the combined resolution as a function of the number of tracks that is used in the analysis.

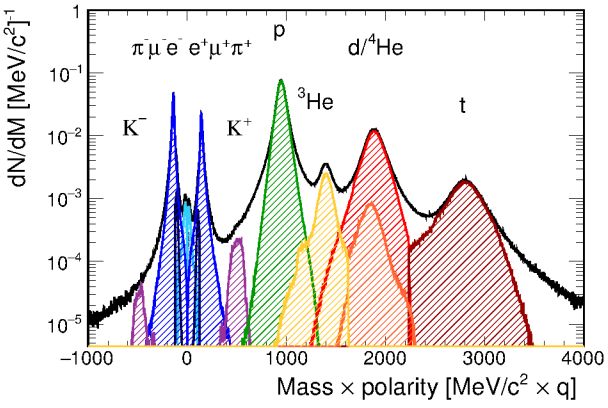

Figure 2: Mass times polarity histogram measured in HADES after applying the T_0 method.

References

[1] G. Agakishiev et al., Eur. Phys. J. A41 February 2009, p. 243-277

[2] J. Pietraszko et al., Nucl. Instrum. Meth. A763, November 2014, p. 1-5

[3] G. Kornakov at al., JINST 9, C11015, November 2014

[4] C. Agodi et al., Nucl. Instrum. Meth. A492, October 2002, p. 14-25

* Work supported by VH-NG-823 and GSI.
† g.kornakov@gsi.de

Azimuthal anisotropy of virtual photons in Au+Au collisions at $\sqrt{s_{NN}} = 2.4\,\mathrm{GeV}$ *

D. Dittert† [1] *and for the HADES collaboration* [1]

[1]Technische Universität Darmstadt, Germany

Virtual photons, that decay into dileptons, are penetrating probes which directly access the entire space-time-evolution of the fireball produced in HIC and they escape from the collision zone without further interactions. Thus they provide unique information about the various stages of the collision. Studying the azimuthal anisotropy of dileptons can accordingly give an insight into the time evolution of collectivity in the system [1].

The collective flow consists of radial flow, which affects the thermal spectra of the outgoing particles, and anisotropic flow, which affects the spatial orientation of the particle momenta. The former one is especially useful to disentangle early and late emission sources, because the effective temperature $T_{eff} \propto T + M \langle\beta_T\rangle^2$ results from the superposition of all fireball stages with decreasing temperature T but increasing flow β_T over time. The azimuthal anisotropies are small as well in the early phases of the fireball evolution, where the flow is not yet fully developed and grow larger for the later phases [2].

The flow coefficients v_1 (directed flow), v_2 (elliptic flow), v_3 (triangular flow), etc., are defined as the Fourier coefficients of the azimuthal angle expansion [3]:

$$\frac{dN}{d\Delta\Phi} \propto 1 + 2\sum_{n=1}^{\infty} v_n cos\,(n\Delta\Phi) \qquad (1)$$

In Figure 1 such a Fourier expansion is fitted to the dilepton $\Delta\Phi$-distribution below 120 MeV/c^2 and additionally the first two Fourier coefficients v_1 and v_2 are plotted separately.

To extract the $\Delta\Phi$ of dileptons, the reaction plane has to be determined, using the spectator hits in the forward wall, placed 7 m behind the detector. Then the azimuthal angle of the dilepton pair is substracted from the angle of the event plane, due to the correlation between the directed and elliptic flow components and the collision geometry. For background determination a like-sign geometric mean is used in the pion region, where correlated background pairs do not allow the use of event mixing. For the higher invariant masses the use of the event mixing method is possible and leads to a slight decrease of statistical fluctuations in the signal to background ratio. The physics background at SIS18 energies is low, with the largest contribution from η Dalitz decays on the 10 % level. Hence for a first analysis the physics background is not taken into account.

The analysis of the azimuthal anisotropy is performed in four bins of invariant mass altogether, to provide information of v_1 and v_2 vs. M_{ee}. The dileptons in the first mass bin up to 120 MeV/c^2 origin mainly from π^0 Dalitz decays, thus it is useful to compare the flow of dileptons of this mass to the one obtained from the pions. This comparison shows a good agreement between the dilepton elliptic flow and the elliptic flow of charged pions. For the higher masses a comparison to the flow of the η or the kaon could be realized. In the pion region, where statistics is high, it is also possible, to perform a multi-differential analysis and analyze the flow in different bins of centrality, rapidity and transverse momentum.

In conclusion the analysis of azimuthal anisotropies of dileptons gives a good insight into the collective behaviour of the fireball and provides additional information to complement the effective temperature, which can be used to validate different theories describing the fireball evolution.

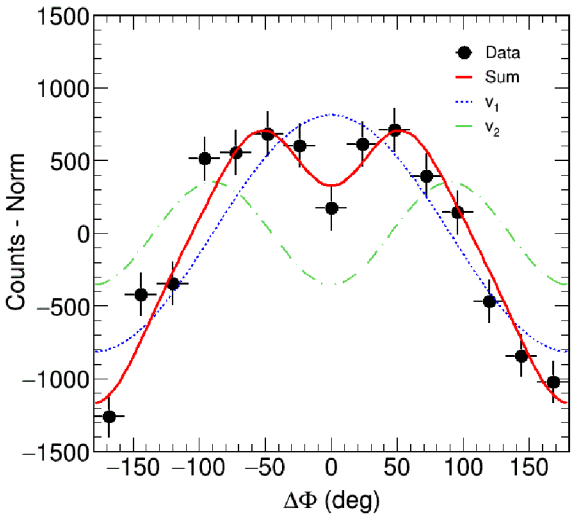

Figure 1: Azimulthal anisotropies of dileptons with $M_{ee} \leq 120\,\mathrm{MeV/c^2}$ measured with HADES in Au+Au.The data are shifted down by the norm of the Fourier expansion. The solid red line shows the sum of this expansion, fitting the data well. The blue dotted line displays the directed flow component v_1 and the green dashed line represents the elliptic flow component v_2.

References

[1] P. Mohanty et al, Phys. Rev. C 85 031903 (R) (2012)

[2] R. Rapp, arXiv:1304.2309 [hep-ph] (2013)

[3] G. Vujanovic, Phys. Rev. C 89, 034904 (2014)

* Work supported by VH-NG-823, EMMI and GSI.

† d.dittert@gsi.de

DOI:10.15120/GR-2017-1

Charge-dependent azimuthal correlations in Au+Au collisions with HADES *

F. Kornas[1], *I. Selyuzhenkov*[2], *T. Galatyuk*[1,2], *and the HADES collaboration*[2]
[1]TU, Darmstadt, Germany; [2]GSI, Darmstadt, Germany

In non-central heavy-ion collisions there could be a manifestation of quantum fluctuations through the coupling of chiral fermions with the magnetic field and the vorticity [1]. This could lead to an electric current among the magnetic field or the total angular momentum, which is measurable by using charge-dependent azimuthal correlations.
The magnetic field (or total angular momentum) is perpendicular to the reaction plane (RP) which is spanned by the beam axis and impact parameter of the collision. A separation of charge would be in this direction perpendicular to the reaction plane, the so called "out-of-plane" direction.
To disentangle the charged particle motion relative to each other, the two-particle correlator γ has been proposed [2]:

$$\gamma_{\alpha\beta} = \langle \cos\left(\phi_\alpha + \phi_\beta - 2\Psi_{\mathrm{RP}}\right)\rangle \,. \qquad (1)$$

ϕ is the azimuthal angle of the charged particle, Ψ_{RP} is the reaction plane angle, α, β account for the different particle charges and the brackets $\langle ... \rangle$ denote the average over particles and events.
The correlator γ is very useful, since all background not related to the reaction plane orientation is removed by construction. It is only sensitive to the difference of "in-plane" and "out-of-plane" background. First investigations of all known background sources indeed show that this difference is much smaller than the observed signal [3].
Yet the correlator γ cannot distinguish for same-charged particles whether they fly together in the out-of-plane or opposite in the in-plane direction. Hence a second correlator is needed to distinguish these two scenarios:

$$\delta_{\alpha\beta} = \langle \cos\left(\phi_\alpha - \phi_\beta\right)\rangle \,. \qquad (2)$$

This correlator has the disadvantage that it has large contribution also from backgrounds unrelated to the reaction plane. Therefore, a proper knowledge of all background sources is required.
Of special interest is the centrality dependence of both correlators, since any effect related to the magnetic field or the total angular momentum should decrease towards more central collisions and even vanish in case of a head-on collision. First measurements of the correlator γ by STAR [4] and ALICE [5] prove the expected centrality dependence. For the correlator δ the situation is more involved which can be attributed to unknown background contributions.

In April 2012, seven billion Au+Au collisions at $\sqrt{s_{NN}} = 2.42\,\mathrm{GeV}$ have been measured with HADES.

* Work supported by VH-NG-823, Helmholtz Alliance HA216/EMMI and GSI.

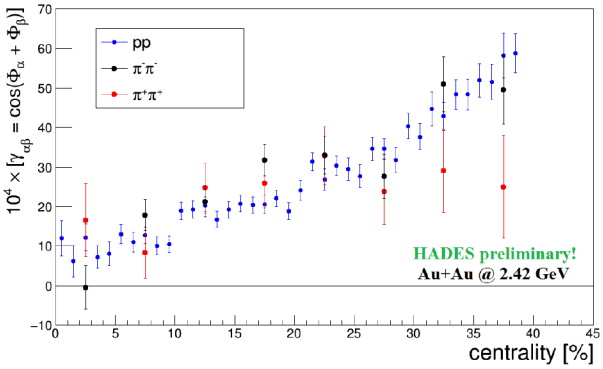

Figure 1: Preliminary results by HADES for the two-particle correlator γ as a function of the collision centrality for Au+Au collisions at $\sqrt{s_{NN}} = 2.42\,\mathrm{GeV}$. The results are shown for same-charged pairs: pp, $\pi^+\pi^+$ and $\pi^-\pi^-$. Only statistical errors are shown.

For the present analysis only $\sim 1/30$ of the total statistics is used. The analysed particles are protons and charged pions which are identified using their measured velocity as a function of momentum. The reaction plane is reconstructed in each event by a Q-vector analysis [6].
The current results for the correlator γ in case of same-charged pairs are shown in figure 1. The results are corrected for efficiency and event plane resolution. To avoid strong flow contributions a transverse momentum cut of $150 < p_t < 600\,\mathrm{MeV/c}$ for pions and $p_t > 600\,\mathrm{MeV/c}$ for protons is applied. For all three particles the correlator γ shows a strong enhancement towards more peripheral collisions. Within statistical errors the magnitudes are comparable.
HADES data provides new information about charge-dependence of correlations with respect to the reaction plane in a few GeV region of $\sqrt{s_{NN}}$ and together with the existing data from STAR and ALICE at much higher energies helps to shed light about a possible chiral magnetic effect (CME) in heavy-ion collisions.

References

[1] D.E.Kharzeev et al., Prog. Part. Nucl. Phys. 88 (2016) 1-28.
[2] S.A.Voloshin, Phys. Rev. C70 (2004) 057901.
[3] A.Bzdak, V.Koch and J.Liao, Phys. Rev. C81 (2010) 031901.
[4] B.Abelev *et al.*, Phys. Rev. Lett. 103 (2009) 251601.
[5] B.Abelev *et al.*, Phys. Rev. Lett. 110 (2013) 1.
[6] J.Barrette et al., Phys. Rev. C55 (1997) 1420.

Kaon and phi production in pion-nucleus reactions at 1.7 GeV/c*

J. Wirth[1,2], *L. Fabbietti*[1,2], *A. Scordo*[3], *and the HADES collaboration*

[1]Excellence Cluster Universe, Technische Universität München, 85746 Garching, Germany; [2]Physik Department, TU München, 85746 Garching, Germany; [3]INFN Laboratori Nazionali di Frascati, 00044 Frascati (Roma), Italy

The production and properties of open and hidden strange mesons (K^+, K^-, ϕ) in cold nuclear matter generated in pion-nucleus reactions ($\pi^- + A, A = C, W$) at $p_{\pi^-} = 1.7$ GeV/c have been studied with the HADES setup.

Of particular interest is the modification of the (anti-)kaon spectral function in nuclear matter which should be already apparent at saturation density [1]. While, for the kaon (K^+, K^0) the repulsive KN-potential has been investigated to some extent and was found to have a moderate strength ($20 - 40$ MeV) [2, 3], the existing data on in-medium effects of the antikaon produced off nuclear targets are very scare [4]. Moreover, the situation of the antikaon is more involved, since the K^- can be absorbed in nuclear matter via strangeness exchange processes on one ($K^-N \rightarrow Y\pi$) or more nucleons ($K^-NN \rightarrow YN\pi$). On the contrary, K^+ does not undergo strong absorption processes and can be treated as a quasi particle within nuclear matter, providing stringent constraints on the production mechanism of strange hadrons. In this context, also the ϕ production and absorption ($\phi \rightarrow K^+K^-$, $BR \sim 48.9\%$) off light and heavy nuclear targets is studied.

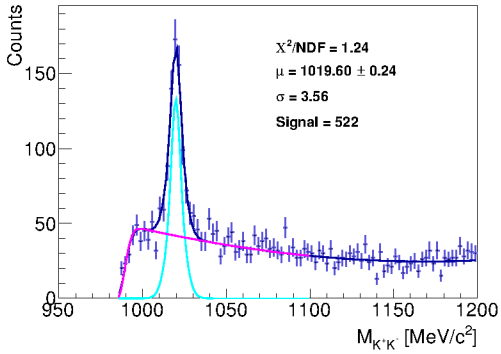

Figure 1: Invariant-mass distribution of K^+K^- pairs in $\pi^- + C$ reactions. The fit consists of two Gaussian for the ϕ signal together with the background described by a polynomial and Gaussian functions

Both charged kaons are identified by means of time-of-flight (START/RPC/TOF) and momentum measurements as well as by the specific energy loss information in the drift chambers to enhance the signal to background ratio. The neutral ϕ is reconstructed employing the invariant mass of charged kaons ($M_{K^+K^-}$) (Fig. 1), which have been selected within a distinct velocity β range. In total about 4×10^5 K^+, 2×10^4 K^- and 500 ϕ ($\pi^- + C$) and 2×10^5 K^+, 1×10^4 K^- and 300 ϕ ($\pi^- + W$) were reconstructed, respectively.

Evidence on the K^- absorption is obtained on the basis of K^-/K^+ ratios in both nuclear environments (C, W) as a function of four different kinematic observables (p, θ, p_T, y). Figure 2 shows the ratios as a function of momentum. Furthermore they are compared the expected ratios without absorption based on existing and extrapolated cross-sections (Fig. 2 gray line). A clear K^- disappearance for a higher nucleon density is observed, which is even more evident for low momenta. Moreover the ratios give a hint for K^- absorption in all four kinetic observables (p, θ, p_T, y).

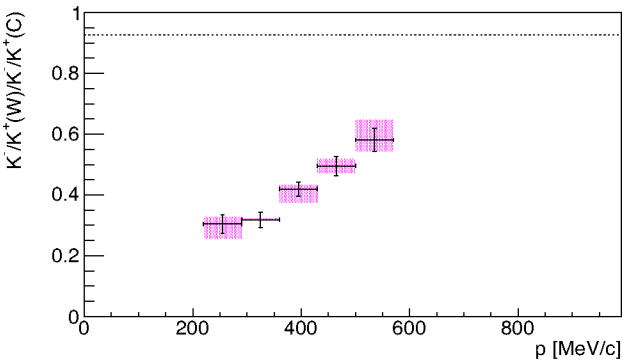

Figure 2: K^-/K^+ double ratio in $\pi^- + W$ collisions compared to $\pi^- + C$ as a function of momentum. The gray line reflects the expected double ratio without absorption.

References

[1] J. Schaffner et al., "In-medium production of kaons at the mean field level", Nucl. Phys. A625: p. 325 – 346 (1997)

[2] M. L. Benabderrahmane et al., "Measurement of the in-medium K0 inclusive cross section in π^--induced reactions at 1.15 GeV/c", Phys. Rev. Lett. 102, 182501 (2009)

[3] G. Agakishiev et al.: "Medium effects in proton-induced K0 production at 3.5 GeV", Phys. Rev. C90: p. 054906 (2014)

[4] W. Scheinast et al., "First observation of in-medium effects on phase space distributions of antikaons measured in proton-nucleus collisions," Phys. Rev. Lett. 96, 072301 (2006)

* Supported by the DFG cluster of excellence "Origin and Structure of the Universe and SFB 1258"

DOI:10.15120/GR-2017-1

$\Lambda - p$ correlation in π^--induced reactions at 1.7 GeV/c *

S. Maurus[1,2], *L. Fabbietti*[1,2], *and the HADES collaboration*[1]

[1]Physik Department, TUM, Garching, Germany; [2]Excellence Cluster "Universe", Garching, Germany

World data for elastic $\Lambda - p$ scattering over a wide range of relative momenta are quite scarce and only available for small beam momenta with a integrated statistic in the order of 200 events [1]. For π^--induced reactions the available data is even more limited [2,3]. In order to improve the theoretical description of $\Lambda - p$ scattering, new constraints are necessary to parametrize the cross sections. In this context a dedicated π^- + A (A = C, W) experimental campaign was performed at $p_\pi = 1.7$ GeV/c with the HADES detector. The recorded data is analyzed in terms of the inclusive Λ yield and Λ-p correlation. For the reconstruction of the Λ in the inclusive spectra the charged decay channel ($\Lambda \rightarrow p\pi^-$, BR = 63.9%) has been examined. Applying topological cuts, an integrated yield of ~11k Λ has been extracted with a purity of 93% ($\pi^- + W$) (Fig. 1). These extracted yields are further corrected for the limited efficiency and acceptance by means of simulations. A Boltzmann distribution has been employed to extrapolated the yield to the full momentum phase space.

After the Λ has been produced it can interact with the nuclear environment and eventually scatter elastically with a nucleon. To isolate this process, events with a matching charge pattern ($\Lambda \rightarrow \pi^- p, K^0 \rightarrow \pi^+\pi^-, p$) are selected. Based on a likelihood-method the particle species has been determined considering the specific energy-loss in the MDCs and velocity β. Since the selected pattern contains two π^- and p in the final state, an event hypothesis has to be applied to assign their corresponding mother particle (Fig. 2, $m_{\pi^+\pi^-} - m_{K^0}$ and $m_{p\pi^-} - m_\Lambda$). The best combination is selected by a simultaneous matching of the invariant mass to the nominal value within the detector resolution. This procedure leads to an extraction of ~6k events in the $\pi^- + W$ system. For a full description of all kinematic properties of the system the Λ before the scattering is reconstructed by applying energy and momentum conservation to the incoming π^- beam and the reconstructed outgoing K^0 from the $\pi^- p \rightarrow \Lambda K^0$ reaction. All of these observables will in principle allow to reconstruct the $\Lambda - p$ scattering process and extract its cross section.

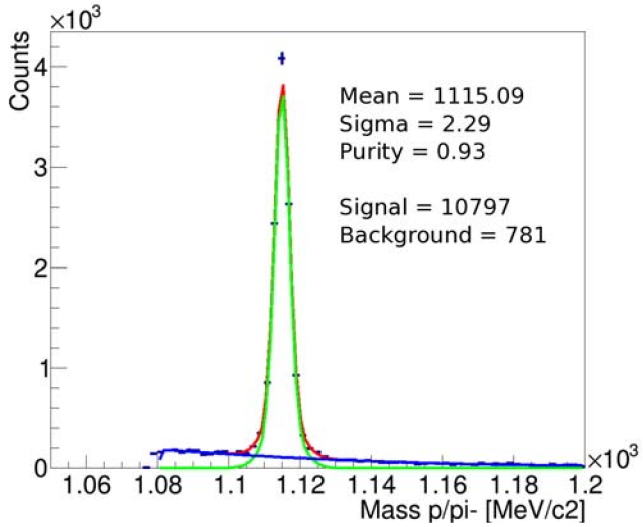

Figure 1: Invariant mass spectra of $\pi^- p$ pairs in $\pi^- W$ reactions after the topological cuts have been applied. The signal is fitted with a double Gaussian and the background is described by a polynomial together with a Gaussian.

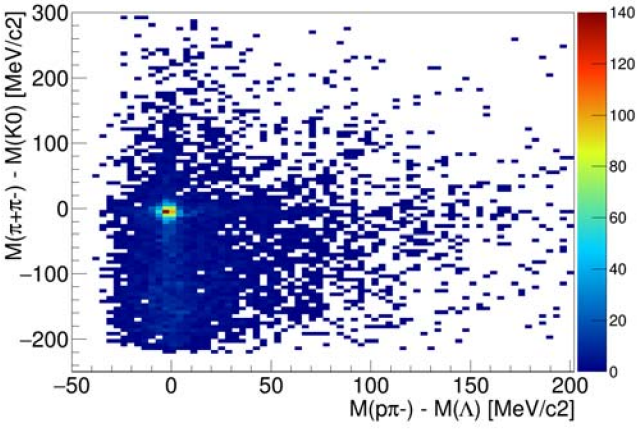

Figure 2: Correlation of the invariant mass spectra of $\pi^+\pi^-$ and $\pi^- p$ for the event pattern $pp\pi^-\pi^-\pi^+$ in $\pi^- W$. The pole mass of Λ and K^0 is subtracted, respectively.

References

[1] Engelmann et al., Phys. Lett. B19, 715 (1966)

[2] Alexander et al., Phys. Rev. Lett. 7, 348 (1961)

[3] Crawford et al., Phys. Rev. Lett. 2, 174 (1959)

* Work supported by BMBF 05P15WOFCA

Status of data acquisition software DABC *

J. Adamczewski-Musch[1], *N. Kurz*[1], *S. Linev*[1]

[1]GSI, Darmstadt, Germany.

The software framework DABC (Data Acquisition Backbone Core) [1] provides a flexible environment for distributed data acquisition with online monitoring and control capabilities. It is used for event building at the HADES experiment since 2014 [2]. Moreover, DABC has been deployed for data taking with detector and readout electronics tests [3]. This article reports the most recent applications and developments for the DABC framework.

DABC framework

Improvements

Version 2.9 of DABC was released in November 2015. A number of improvements have been introduced to the base framework since this time. These were driven by requirements showing up during the developments for the *hadaq* and *saft* plug-ins. The changes concern some internal functionality of data transport and socket classes, with the goal to improve performance, stability, and error handling. Additionally, it is now possible to configure event handler priorities for any active DABC entity, like processing modules and sockets. Moreover, the configuration syntax has also been extended, e.g. to allow more easy treatment of array values in the DABC XML files.

HTTP server

Since 2013 DABC offers monitoring and control features by means of the public *civetweb* HTTP server in combination with a proprietary JavaScript GUI [1].

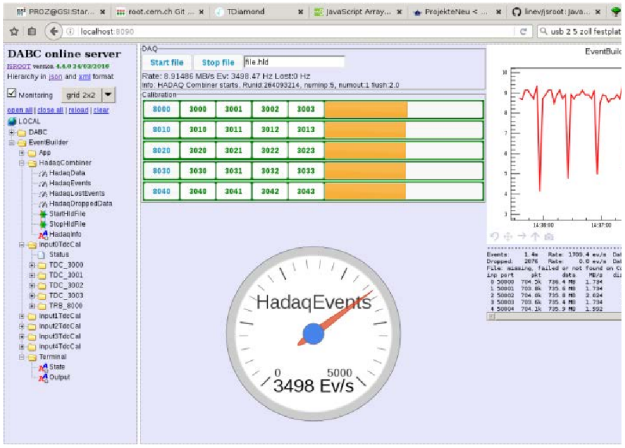

Figure 1: Example of DABC web GUI application for monitoring and control of a trb3 calibration test.

A screenshot of a web browser controlling a DABC application is shown in Fig.1.

These web control features have been implemented in close connection with the JavaScript ROOT project [4]. So the DABC web GUI benefits also from the further developments of JavaScript ROOT in 2016. Currently DABC v 2.9.1 is distributed with JSROOT version 4.4

Linux Device Drivers

PEXOR asynchronous readout

The PCIe optical receiver boards PEXOR and KINPEX are widely used for data acquisition of various front-end boards developed for FAIR. The Linux device driver *pexor* [5] is used for DABC and FESA based read out of such systems. Most recently this kernel module and the user library software have been further improved. One goal was to provide an asynchronous readout of different SFP chains without the need of the common trigger module hardware TRIXOR. This can be useful for large beam position monitoring applications, or for detector set-ups with readout chains that are to be triggered independently.

In such use case the data read out of each SFP chain is synchronized independently by means of the *gosip* protocol [5]: The host software sends a data request for a readout chain to the front-end FPGAs and polls for the data to arrive. If a chain has delivered data, it is further processed by the DAQ software and the next data request is send. If a chain has not yet sent anything, the corresponding subevent is just omitted in the collected data event. So it is possible to handle the readout of systems with different local trigger frequencies into one combined data stream. This technique has been implemented and tested with two different approaches: An explicit polling for each chain data in the DABC readout application, and an implicit polling in the kernel module software. The latter approach will have the advantage that a concurrent access to the front-end by a control system is possible, since the *gosip* operations can be locked in the kernel module. Furthermore, this implementation in the driver software is independent from DABC and may also be applied for future FESA readout.

First tests with independently triggered front-ends look promising. The developments are continued and will be ready for application in 2017.

PEXORNET

The *pexornet* Linux device driver [6] has been developed as novel approach to read out a commonly triggered PEXOR/KINPEX system. Here the kernel module registers the GSI proprietary optical receiver hardware as a

* PSP codes: HADES 1.1.2.4, SD -SEM 2.3.6.5.1.6.30

DOI:10.15120/GR-2017-1

regular Ethernet network device to the operating system. Each hardware trigger at the TRIXOR module will invoke an automatic read out in the interrupt handler of the driver. The collected data will be sent as an UDP packet via any socket that is connected to this pseudo network. So any user application may receive such data from a regular network socket and may process it at will. By means of a special DABC plug-in, however, it is possible to read from such socket and produce the same data format as the alternative DAQ system MBS [7], and apply the same Go4 [8] analysis for checking data integrity.

The *pexornet* readout has been tested in comparison to MBS with POLAND and FEBEX front-end hardware [6]. For two FEBEX devices at one SFP chain, *pexornet* achieved about the same performance as the conventional MBS readout, i.e. 150 MB/s at 7.6 kHz event rate if triggered by 20 kHz pulser [6].

Plug-in developments

HADES event builder

The *hadaq* plug-in is used for production event building at the HADES experiment since 2014 [2]. In the scope of the trb3 TDC developments [3] it has been further tested and improved. A special time sorter module in the event builder has been developed to cope with parallel high speed data streams from a single trb3 via separate UDP connections. Furthermore, the possibility to calibrate the TDC fine time values "on the fly" in the event builder before writing the raw subevents to disk has been optimized for different calibration methods (statistical approach, temperature calibration function, simple linear calibration). Advanced analysis and monitoring techniques in such a DABC code have been helpful to further understand functionalities and limitations of the FPGA TDC

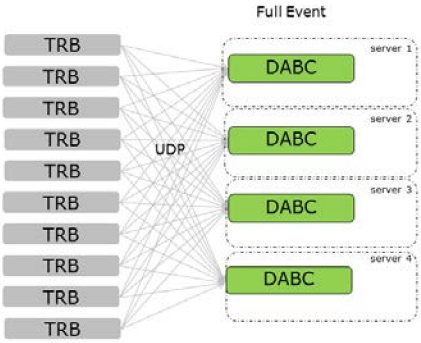

.

Figure 2: Previous HADES event building network topology: Each trb front-end hub sends to all event builders via UDP in an "n x m barrel shifter" scheme

The HADES detector is going to be equipped with numerous additional trb3 readout boards for the expected FAIR-0 beam time. To fully benefit from such an online trb3 TDC calibration, the topology of the event building network is going to be changed (see Fig.2). In the previous set up, each front-end hub was sending data via Gb Ethernet UDP connections to all receiving event builder nodes in a barrel shift mode (Fig.2). Instead, each front-end will send to a dedicated entry server only and the full event combination is done by a second TCP/IP "builder network" BNET (Fig.3) [1].

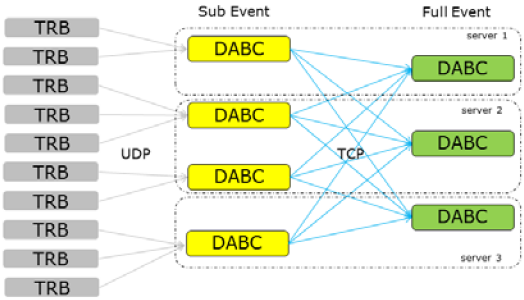

Figure 3: New HADES event building network topology as tested: The trb front-end hubs send via UDP to dedicated "subevent input" processes. Full events are built via TCP in a second stage builder network (BNET).

This allows to configure the TDC calibration modules of each entry server according to the connected front-ends. A first test of such an alternative builder topology has been carried out in December 2016. The *trbnet* hub configuration has been modified and DABC has been started with separate input and builder processes on each server (1 input and 2 builder processes at 4 server machines). Using a pulser trigger, the data taking of full events from 17 active front-end hubs could be verified. Switching between the old and new topologies is handled simply by changing a flag parameter in the HADES DAQ startup scripts.

White Rabbit SAFT library

The FAIR timing and messaging system will be based on the White Rabbit technology [9]. Therefore it can be interesting to read out timestamps and machine events from timing receiver hardware (PEXARIA or EXPLODER5) with DABC. The timing messages may then be processed together with regular event data from the experiment detectors.

A DABC plug-in has been developed based on the official FAIR SAFT library (Simple API for Timing) [10]. Here the timing events to be recorded can be configured in the DABC XML setup file. Whenever an event of the requested type arrives at the timing receiver hardware, the appropriate SAFT "Event Condition Action" (ECA) callback will be caught and evaluated by DABC. The detected timing events are queued, packed into dedicated *lmd*- or *hld*-formatted events, may be stored to a file, or may be send to an online monitoring Go4 [8] application. In future DABC applications such timing events may be simply combined as subevents with other detector data.

Performance tests of such read out have been done at a commodity PC (DELL T3500, 2 cores, Linux kernel 4.1.20) with EXPLODER5 timing receiver hardware at the PCIe slot. Version 1.0.8 of the SAFTlib was used. A

TTL pulser of different frequencies was connected to input IO1 of the EXPLODER5 to deliver an input timing event (signal rising edge) to be detected. In this test DABC was configured to produce *hld* data format as it is in use for the HADES experiment. The sequence of timing events was checked and monitored with a Go4 analysis.

Figure 4 shows the relative loss of timing events versus the event pulser frequency (plot above), and the corresponding CPU load for several relevant processes (plot below). The loss of timing events could be detected both by the overflow counter of the SAFTlib FIFO, and by histograming the time difference of subsequently collected messages in the Go4 analysis. The relative loss in Fig.4 is the ratio of detected FIFO overflows by the total number of received timing events. Note that the data points for the lowest frequency 1.2 kHz give just a worst case estimation from the total measurement time without any loss. It turned out that the event rate limit for lossless readout with this setup was at about 2 kHz. For higher frequencies, the dual-CPU host load reached 200% in total, split into the participating processes of DABC, the SAFTlib demons (*saftd* and *dbus*), and the Linux kernel interrupts (*kworker*), see plot below in Fig.3.

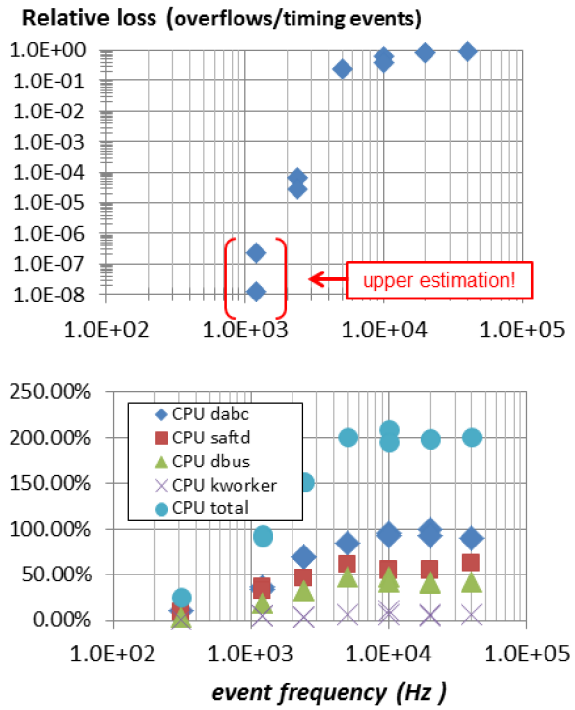

Figure 4: Relative loss of timing events (above) and host CPU consumption (below) versus event frequency for DABC *saft* plug-in tests. See text for details

This limit can probably be extended by using more powerful PC hardware, and by further optimizing of the SAFTlib. However, for the slow control use case a maximum event rate of 1 kHz may already be sufficient. For DAQ applications with trigger rates up to 100 kHz, a trigger time-latch readout with every event seems to be not possible by such SAFTlib approach. But for a downscaled trigger time latch, or to embed occasional accelerator messages into the experiment data stream, the DABC *saft* plug-in could be useful though.

New mass storage interface

Since the old tape storage tool *gstore* has almost reached the end of its life, the new software *ltsm* [11] is proposed as generic storage interface at FAIR. Therefore in November 2016 the project has started to develop a DABC plug-in that utilizes the *ltsm* libraries from the event builder process. The aim is that data acquisition software like DABC and MBS can open new files at a dedicated IBM tape storage server and can write directly data buffers to such file. This will preserve the previous use case [2] that experiment data can be written to the mass storage immediately during data taking, without requiring an intermediate file on a local disk.

First tests of the *ltsm* software looked promising. The DABC plug-in for *ltsm* is currently being developed in close collaboration with the GSI IT storage group. It is expected to be ready for application during 2017.

Outlook

The DABC software for data acquisition and monitoring on Linux X86 PC is mature and has been constantly maintained. Special improvements for the HADES experiment and various trb3 readout systems have been implemented in 2016. GSI proprietary read out hardware, like the PEXOR system, are supported up to the device driver level. Several new software interfaces, such as the FAIR machine timing *saft* plug-in, and the *ltsm* mass storage plug-in, are currently under development.

The DABC framework and the most important user plug-ins are available under GPLv2 via the DABC web site [12].

References

[1] J.Adamczewski-Musch, N.Kurz, S.Linev: “Developments and applications of DAQ framework DABC v2”, J.Phys.Conf.Series 2015, vol.664, http://iopscience.iop.org/article/10.1088/1742-6596/664/8/082027

[2] J. Adamczewski-Musch, S.Linev: “DABC as event builder at HADES experiment”, GSI scientific report 2014, doi:10.15120/GR-2015-1-MU-NQM-HADES-26

[3] http://trb.gsi.de/

[4] B.Bellenot, S.Linev “JavaScript ROOT”, J.Phys.Conf.Series, 2015, vol. 664, http://iopscience.iop.org/article/10.1088/1742-6596/664/6/062033

[5] J. Adamczewski-Musch, H.G.Essel, S. Linev : “The DABC Framework Interface to Readout Hardware”, IEEE TNS Vol.58, No.4, August 2011, pp. 1728-1732

[6] J. Adamczewski-Musch, N. Kurz, S. Linev, “MBSPEX and PEXORNET - Linux device drivers for

DOI:10.15120/GR-2017-1

PCIe Optical Receiver DAQ and control", presented at IEEE RT2016, submitted for publication at IEEE TNS
[7] http://www.gsi.de/mbs
[8] http://go4.gsi.de
[9] D. Beck et al., "Paving the Way for the FAIR General Machine Timing System", GSI scientific report 2013, doi:0.15120/GR-2014-1-FG-CS-08
[10] https://www-acc.gsi.de/wiki/Timing/TimingSystemDocumentsSaftlib
[11] T. Stibor et al., "LTSM - Lightweight TSM API", https:/github.com/tstibor/ltsm
[12] http://dabc.gsi.de

Stabilizing aged Drift Chambers under high rates

C. Wendisch [*1], *O. Fateev* [4], *L. Lopes*[2], *C. Müntz*[3], *and J. Stroth*[1,3] *for the HADES Collaboration*[†]

[1]GSI, Darmstadt, Germany; [2]LIP, Coimbra, Portugal; [3]Goethe-Universität, Frankfurt, Germany; [4]Joint Institute of Nuclear Research, Dubna, Russia

The future physics program of HADES at FAIR demands high detection standards, meanig in precision and also stability of the tracking system comprising four layers of planar drift chambers (MDC-I - IV). Compared to the exposure of 18 beam-times within 15 years, stable operation of the wire chambers has to be ensured now for factors 2-3 higher particle load than the maximum so far.

Progression of drift chambers during 15 years

Built in the end of the 1990s the drift chambers operation started with a gas mixture of helium/isobutane (60/40) to achieve the lowest material budget for the HADES detector. Later the gas was changed to argon/isobutane (84/16) to increase the primary ionization. During the beam-time in 2012 (Au+Au reactions at E_{kin} = 1.23 AGeV) massive wire aging occurred, revealed in the Malter effect, causing self sustained currents [1]. Therefore isobutane, which tends to polymerize, was substituted and now Ar/CO_2 (70/30) is used to prevent further aging in high load experiments. Since 2013, MDC II operates at a high voltage of -1770 V (drift cell size 6 x 5 mm^2) with H_2O additive to recover stability [2]. An overall stable operation was observed with the admixture of 1000-3000 ppm water vapor to the counting gas, tested in beam and in equivalent X-ray irradiation.

During X-ray tests with an intensity corresponding to the highest particle beam load reached, a sense wire broke inside sector 4 of MDCII. The consequent repair offered the opportunity to microscopically investigate the reasons for stability breakdown, expected to be aging of wires since an observed persistent Malter-effect points to wire deposits.

Wire inspection

The visual inspection of the drift chamber interior 13 wire planes, depicted in figure 1, revealed abundant black deposits randomly distributed on all cathode and field wires (aluminum, diameter 80 μm) providing the high voltage.

Investigating the material compounds of the deposits by energy dispersive X-ray spectroscopy (EDX), carbon and oxide in several μm thick layers covering the wire surface were found, shown by the inlay of figure 2. Further, no sign for aging of anode wires (tungsten, diameter 20 μm) was observed.

Cleaning all wires to remove deposits manually and via solvents in an ultrasonic bath was tested to be not successful. But operating with water vapor as gas additive turned out to be the stable solution and should also prevent further polymerization.

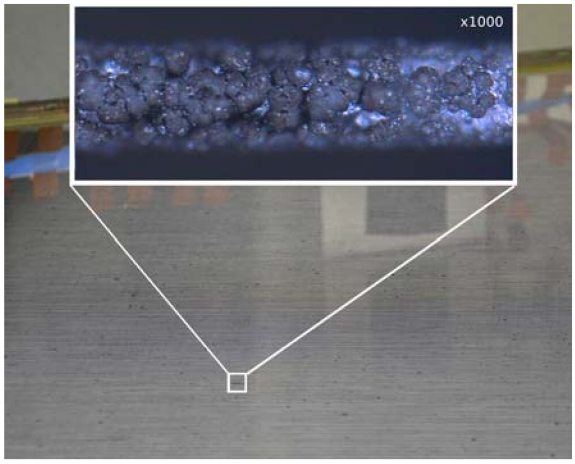

Figure 1: Single wire plane, showing dark deposits on field wires (diameter 80μm, Al) magnification 1000x, optical microscope.

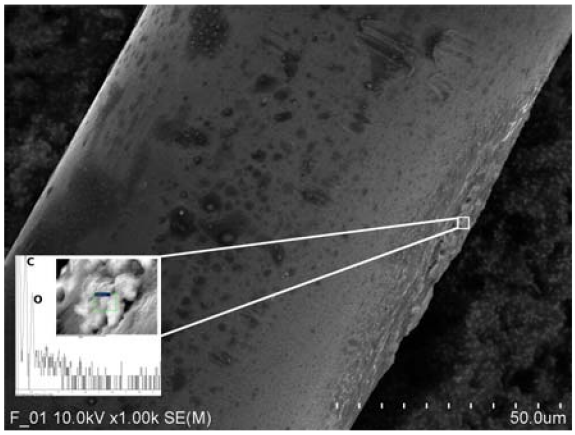

Figure 2: Scanning electron microscope view of field wire surface (diameter 80 μm, Al) magnification 1000x. Inlay shows EDX spectroscopy results: atomic compounds of deposits are carbon 73.2 %, oxygen 26.8 %.

We acknowlage Helmholtz-Zentrum Dresden-Rossendorf for the support with the EDX analysis.

References

[1] L. Malter, Phys. Rev., vol. 50 (1936) 48-58.

[2] A. Boyarski, Nucl.Instrum.Meth.A515 (2003) 190-195.

* c.wendisch@gsi.de

† Work supported by BMBF, HIC for FAIR and GSI.

DOI:10.15120/GR-2017-1

Towards new front-end electronics for the HADES drift chambers*

M. Wiebusch[1], *J. Michel*[1], *C. Müntz*[1], *M. Traxler*[2], *C. Wendisch*[2], *J. Stroth*[1,2], *and the HADES Collaboration*

[1]Goethe-Universität Frankfurt, Germany; [2]GSI, Darmstadt, Germany

Track reconstruction in HADES is realized with 24 planar, low-mass drift chambers (MDC). About 27000 drift cells provide both precise spatial information of track hit points and energy loss information. In order to handle high rates and track densities required at the future SIS100 accellerator at FAIR, an upgrade of the MDC system is necessary. This involves new front-end electronics, as the original analog read-out ASIC (ASD8) is no longer procurable.

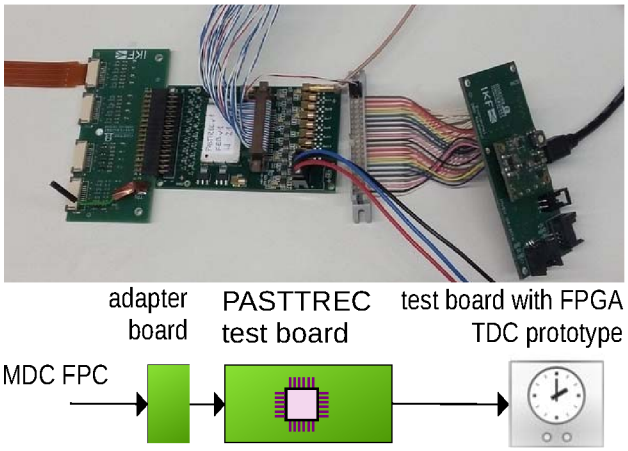

Figure 1: PASTTREC read-out line, here equipped with a stand-alone FPGA-based prototype TDC.

A promising replacement read-out chip candidate is the PASTTREC ASIC [1], developed at Jagiellonian University, Krakow, for reading-out straw tubes e.g. of the PANDA experiment and the future HADES forward tracker. It is supplemented by a high precision FPGA-based TDC [2], implemented on a TRB3 board. In parallel, a cost-efficient and lightweight but coarse binned (500 ps) FPGA-based prototype TDC was successfully tested. It is foreseen to replace the currently used dedicated TDC ASICs.

To arrive at conclusive performance results, the tests are being conducted under realistic conditions in direct comparison to the present ASIC. To do so, a spare drift chamber is employed and both signal-to-noise and dE/dx as well as time measurement precision is systematically characterized with radioactive sources and cosmic rays.

Figure 1 depicts the PASTTREC read-out line, which is attached by means of a dedicated flex cable (MDC FPC) to the detector. One key issue is the compatibility of the PASTTREC ASIC with the present flex-based signal routing which significantly affects the noise immunity together with determining the optimum amplifier and shaper settings for the chip. Due to the unique arrangement of the two innermost sense wire layers (see figure 2) it is possible to assess the time (and spatial) precision by correlating adjacent drift cells. Plotting the difference against the sum of both drift time signals for perpendicular tracks of cosmic muons (triggered by an external scintillator) allows to access the drift time precision. This is done by projecting a selected data sample (small drift time difference) on the axis representing the drift time sum. The width of the resulting peak is closely related to the time precision. This study, together with future beam tests, will help to answer the other key question on the possibility of assigning an ASIC optimized for straw tube signals to read out the mini (cell) drift chambers of HADES. Compared to MDC, the straws (operated at 2 atm gas pressure, avg. 50% longer track path) provide longer drift times and more primary ionization. The decision on the replacement of the existing electronics is foreseen to be taken in the second half of 2017.

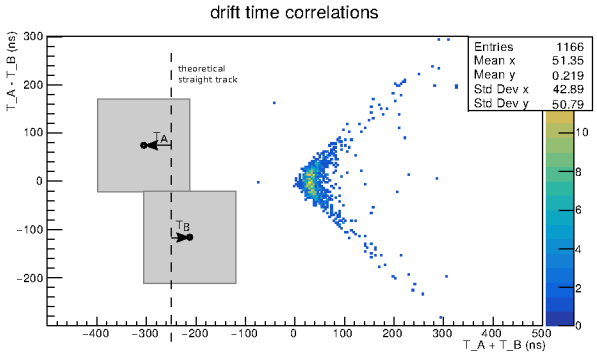

Figure 2: Drift time correlations from two adjacent, shifted cells (see schematic inlay) as function of drift time sum and difference.

References

[1] M. Idzik, G. Korcyl, D. Przyborowski, P. Salabura, J. Smyrski and P. Strzempek, doi:10.1109/RTC.2016.7543165

[2] C. Ugur, et al., 264 Channel TDC Platform applying 65 channel high precision (7.2 ps RMS) FPGA based TDCs, in: IEEE Mediterranean Workshop on Time to Digital Converters, 2013.

* supported by BMBF, HGS-Hire and GSI

Tracking resolution studies of the HADES Forward Detector

A. Blanco[1], *L. Fabbietti*[2,3], *R. Lalik*[2,3], *K. Nowakowski*[4], *P. Salabura*[4], *L. Silva*[1], *and A. Zinchenko*[5]

[1]LIP-Laboratório de Instrumentação e Física Experimental de Partículas , 3004-516 Coimbra, Portugal; [2]Excellence Cluster 'Origin and Structure of the Universe', 85748 Garching, Germany; [3]Physik Department E62, Technische Universität München, 85748 Garching, Germany; [4]Smoluchowski Institute of Physics, Jagiellonian University of Cracow, 30-059 Kraków, Poland; [5]Joint Institute for Nuclear Research, 141980 Dubna, Russia

The forthcoming upgrade of the HADES detector (see Fig. 1) with the newly developed Forward Detector will allow for measurements in the until now inaccessible angular region of the very forward direction ($\theta < 7°$). The new Forward Detector will essentially extend the HADES acceptance in the kinematic region specially important for hyperon spectroscopy in the elementary and light-ion target reactions. The Forward Detector consists of two tracking stations based on straw tubes developed for the PANDA Forward Spectrometer [1] and a time-of-flight wall using RPC detector benefiting from the NeuLAND development [2]. Since the Forward Detector operates in a magnetic field free region of HADES, a precise reconstruction of displaced secondary vertices of Λ, Σ^0 and Ξ requires good spatial resolution and challenging reconstruction procedures, momentum reconstruction using time of flight information from RPC and kinematical refit analysis.

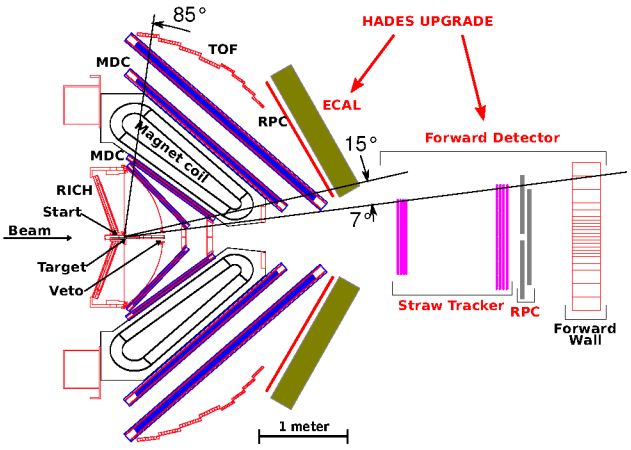

Figure 1: Upgrade of the HADES setup.

The straw tracker comprises eight double straw layers organized in two stations of four layers each, placed 3 m (the first station) and 4.6 m (the second station) downstream from the target. The layers are rotated respectively by 0, 90, 0, 90° and 0, 90, -45 and +45° around the beam axis. Each layer consists of tubular 10.1 width (diameter) straws made of 20 μm thin Mylar foil, filled with Ar:Co_2 (90:10 mixture) at over-pressure of 2 atm, and a 20 μm thick copper sense wire. The first module contains 80 straws (in each plane of a single double plane layer) and the second 112 straws. The stations have a hole for the beam opening, with a width of 8 straws in the first module and 16 in the second module.

The RPC detector is located behind the second straw module at about 5 m distance from the target. It is made of four modules organized in two front and two backward stations, rotated accordingly by 0 and 90° around the beam axis. Each module is made of twelve gas gaps spanning the whole module area with a segmented readout of 30 strips in each module.

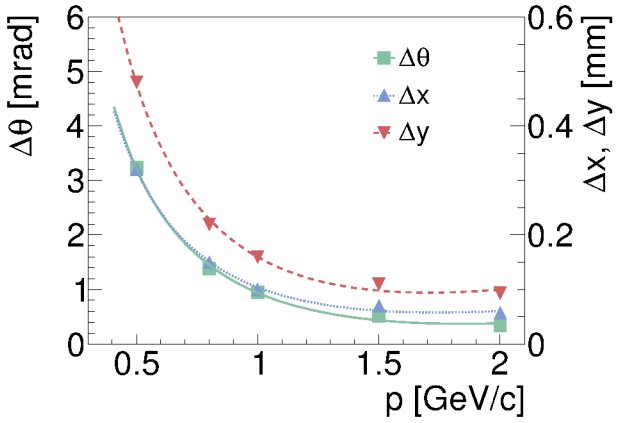

Figure 2: The θ, x and y resolutions in function of momentum. Fitted curves are only parametrizations for the simulated points and cannot be extrapolated.

The complete geometry of the Forward Detector, digitization and tracking algorithms have been implemented and integrated in the HADES simulation framework.

The tracking resolution was investigated by means of mono-energetic protons emitted from the target region into the detector acceptance. Five different proton momenta were studied: 0.5, 0.8, 1.0, 1.5 and 2 GeV/c. The resolution is defined as one standard deviation of a spectrum of differences between simulated and reconstructed values. Three main track parameters were under investigation: θ — track polar angle and x,y — coordinates of intersection between track and the first plane of the first layer. In both cases, a strong momentum dependency was observed resulting from multiple scattering. The resolution results are summarized in Fig. (2).

References

[1] W. Erni et al. *EPJA*, 49(2):25, 2013.

[2] J. Machado et al. *JINST*, 10(01):C01043, 2015.

DOI:10.15120/GR-2017-1

Temperature dependence of dark noise for H12700 MAPMTs : A quantitative approach*

V. Patel[1], *C. Pauly*[1], *J. Förtsch*[1], *and K.-H.Kampert*[1]
[1]Bergische University of Wuppertal

Motivation

The CBM RICH project will use Hamamatsu H12700 MAPMTs for detection of di-leptons. These MAPMTs are specially designed to detect single photons e.g. from Cherenkov radiation. One of the primary tasks at our laboratory in University of Wuppertal is to do QC tests for all the MAPMTs delivered by Hamamatsu. These tests are being done since fall 2015 and are still on going with every delivery. We measure various parameters and compare them with specifications which we agreed upon with Hamamatsu. During these tests we found that the dark rate of same MAPMTs differ depending on whether it was measured in summer or winter due to variation of temperature in our lab. However, without active temperature control in our setup, it was not possible to determine this effect quantitatively. Good understanding of the temperature behaviour of the PMTs is important in view of the required cooling efforts needed later in the experiment. According to the specification, the allowed level of dark rate is 6.4 kHz per MAPMT and, if during QC test this limit is exceeded, we return the MAPMT to manufacturer.

Experimental Setup

To study the temperature dependence of dark rate we used a climate chamber. It has automated temperature control for a variety of settings. The setting of the climate chamber was made such that one particular temperature settles for three hours and then increases to the next step in two minutes. The main reason to do so was to give MAPMT time to get into equillibrium with surrounding temperature. For measuring dark rate n-XYTER cards were used outside the climate chamber. This made sure that the n-XYTER does not contribute to change in noise and we measure noise contribution only from a MAPMT. The n-XYTER was connected to a water cooling system which kept its temperature at 22 °C while the PMT was subjected to varying temperature settings.. At any given temperature the n-XYTER takes data of rates at thresholds from 30 to 100 in steps of ten in every 15 minutes. Thus, we have a dataset of approximately ten observations for each temperature. The complete test required 36 to 40 hours for one MAPMT. We tested three MAPMTs and they all showed similar results. A typical temperature dependence behaviour of a PMT is shown in Figure 2. The results are discussed as follows.

Figure 1 shows that there is an exponential behaviour in increase of dark rate with change in temperature. As temperature increases beyond 30 °C this becomes a serious issue.

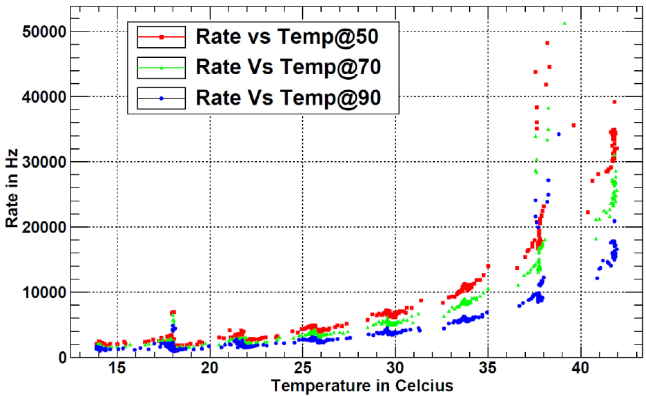

Figure 1: Relation between temperature (°C) and dark rate (Hz) for different thresholds at the ADC.

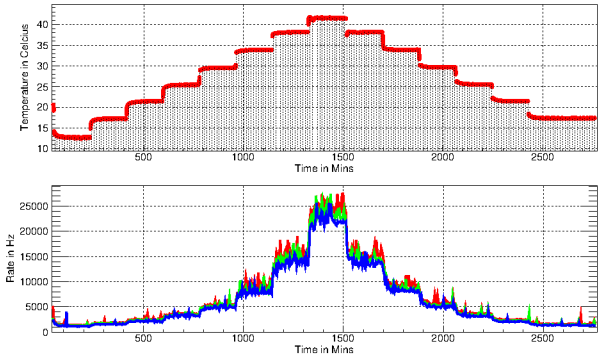

Figure 2: Time evolution of the temperature in the climate chamber and corresponding change of dark rate in the MAPMT at three different ADC thresholds.

Figure 2 shows the evolution of both temperature in the climate chamber and change in dark rate of the PMT as a function of time. We can observe a clear correlation between environmental temperature and dark rate of the MAPMT.

Analytical description of temperature dependence

An important result of this study is the deduction of an analytical description of dark rate for the MAPMTs. This can help us to estimate the dark rate at room temperature

* BMBF grant 05P15PXFCA, and GSI.

Table 1: Comparision of measured and extrapolated rates

PMT Number	Rate(Hz) @ Temp(°C)	Rate(Hz) @ Temp(°C)	Extrapolated Rate(Hz)	Difference(%) bet measured & extrapolated
HA0150	494 @ 22.96	1162 @ 29.10	1033 @ 29.10	-11%
HA0151	353 @ 22.96	637 @ 29.10	736 @ 29.10	13%
HA1089	816 @ 27.06	1213 @ 30.11	1177 @ 30.11	-3%
HA1215	855 @ 27.06	1744 @ 32.69	1680 @ 32.69	-4%
HA1469	1161 @ 20.82	3332 @ 26.05	3112 @ 26.05	-6%

(or to extrapolate to any temperature). Since we check many other parameters of these MAPMTs in an independent setup, this relation is implemented there so that we can claim about dark rate related failures of MAPMTs with proper proofs. The dark rate temperature dependence of the PMT follows an exponetial behaviour, and can be described as:

$$Darkrate(T) = Darkrate(T0) \cdot e^{(\lambda \cdot (T - T0))}$$

where T0 = 20 °C is the reference temperature and (T-T0) is the difference . The exponetial coefficient λ has been verified for three different MAPMT and it is found to be similar for all MAPMTs, while the dark rate at room temperature varies strongly between different MAPMTs.

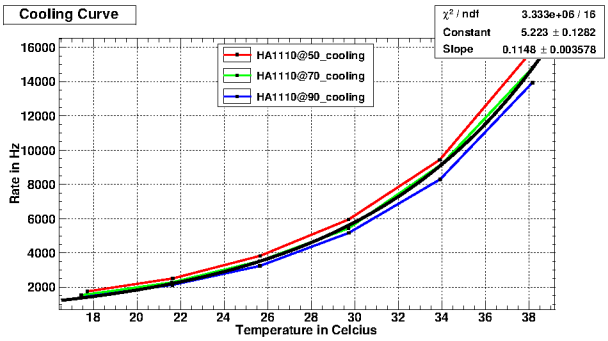

Figure 3: Fits of the rate constant

From our measurements we deduce an average value for $\lambda = 0.12$. Using this value one can extrapolate the rate values to any temperature. This exponential coefficient has been implemented to calculate the dark rate of MAPMTs in our main setup where we study different parameters of MAPMT. In our present Quality Control tests we extrapolate dark rate to 25 degrees which helps us to claim about PMT performance with Hamamatsu. The authenticity of this value has been varified in our main setup which is shown in Table 1.

The Table1 shows the measured dark rate for various PMTs at two different temperatures (column 2+3). Column 4 shows the expected dark rate, extrapolated from the first measurement (column 2) to the temperature of the second measurement (column 3) using exponential extrapolation with $\lambda = 0.12$. The difference between measurement of rate at higher temperatures and extrapolation is shown in column 5, and proves the validity of the analytical description.

Discussion

The studies presented in this article provide a good understanding of the temperature behaviour of H12700 MAPMT, which is necessary to plan the required cooling and temperature control efforts in the final detector design. The main observations can be summarized as follows:

- Strong increase of dark rate with temperature is observed which puts stringent requirements on the operating conditions in the detector. Temperature above 30 °C must be avoided in order to keep dark rate (and thus data rate of the self-triggered acquisition system) in tolerable levels.
- With Hamamatsu we agreed on an upper dark rate value of 6 kHz at room temperature. In order to qualify this criteria for all PMTs, the measured dak rates have to be extrapolated to room temperature using the found correlation law. An exponential coefficient of $\lambda = 0.12$ could be deduced, which allows for rate extrapolation to room temperature in the PMT QC setup.
- The weak threshold dependence of measured dark noise rates confirm the single photon nature of these noise signals, which can not be suppressed by simply increasing the threshold. This can be also infered from Figure [3]
- Our measurements in the climate chamber show no hysteresis effects of dark rate with temperature change. The dark rate is a direct consequence of the actual PMT temperature.

References

[1] M. Calviab *et al.* , Characterization of the Hamamatsu H12700A-03 and R12699-03 multi-anode photomultiplier tubes,LHCb-PUB-2014-043, September 2014

[2] P. Koczon *et al.*, Readout of the Hamamatsu H8500-03 MAPMT with n-XYTER chip, CBM Progress Report 2009, Darmstadt 2010,p.20

[3] J. Förtsch *et al.*, The new H12700 PMT for CBM , CBM Progress Report 2014, Darmstadt 2015 ,p.63

DOI:10.15120/GR-2017-1

Correlation analysis tool using the Schrödinger equation (CATS)*

D. Mihaylov[1] *and L. Fabbietti*[1]

[1]Physics Department E62, TU München, James-Franck-Str., 80805 Garching, Germany

Femtoscopy

The femtoscopy investigates particle correlations using the experimentally accessible two-particle correlation function $C(k)$. Theoretically $C(k)$ can be defined in terms of a source function $S(k,r)$, which describes the relative two-particle spatial distribution at thermal freeze-out, and the two-particle wave function $\Psi(k,r)$, which carries information about the interaction potential $V(r)$ between the particle species of interest (equation 1).

$$C(k) = \int S(k,\vec{r}) \cdot |\Psi(k,\vec{r})|^2 \mathrm{d}\vec{r} \qquad (1)$$

The HADES collaboration has published a femtoscopy analysis of $p\Lambda$ correlations, extracted form the experimental data collected during the 3.5 GeV pNb beam-time, which demonstrated that measuring the correlation function may be used in order to differentiate between different potentials [1]. This is a very nice proof that femtoscopy can be used, among other things, in order to expand our knowledge about hyperon-nucleon interactions. Although the currently available data does not provide enough statistics to achieve those goals, it is expected that once HADES is moved to the FAIR facility high-precision femtoscopy studies will be possible. In addition we are involved in the femtoscopy program of ALICE at LHC, which will give us the opportunity to directly compare and analyze results stemming from different collision systems.

CATS

The femtoscopic data analysis poses many difficulties. This report concentrates on one in particular, namely the theoretical modeling of $C(k)$. From eq. 1 it is evident that both the emission source and the wave-function have an influence on the profile of $C(k)$. Hence it is essential that one is capable to accurately compute $C(k)$ based on any source and potential. Solving eq. 1 analytically is feasible only for larger source-sizes and usually in the absence of Coulomb interaction (e.g. the Lednicky model [2]). Thus it is better to use numerical methods. However the currently openly available tools are either not very flexible and easy to integrate into any analysis framework or evaluate the wave-function by using certain approximations which may lead to inaccuracies when working with smaller sources.

The considerations above motivated the development of the "Correlation Analysis Tool using the Schrödinger equation" (CATS), which relies entirely on numerical methods to evaluate the correlation function. CATS is developed as a stand-alone C++ class and is designed to handle any short-range potential with or without the inclusion of the Coulomb interaction and/or quantum statistics. The wave function is computed by solving the Schrödinger equation fully numerically and thus obtaining an accurate solution event at small radii. The numerical solver has an adaptive grid which optimizes the performance. In addition CATS is capable of working with either an analytical or a data-defined source. This allows to extract the emission source from transport models. CATS is currently in test phase but will be made available to the general public in the future. So far we have confirmed that CATS is in agreement with other theoretical calculations that are optimized to work with larger sources but starts to deviate, as expected, in the case of smaller sources (fig. 1).

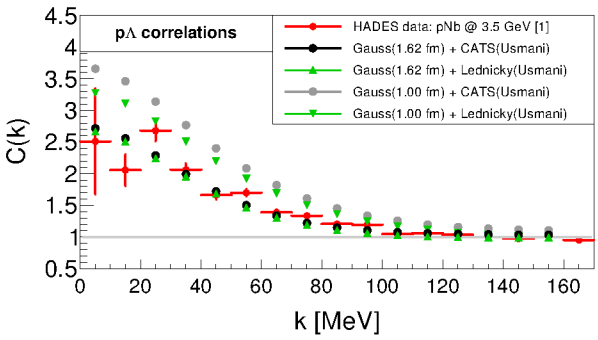

Figure 1: Comparison of the $C(k)$ predictions using different tools. The interaction is modeled by the Usmani potential. The source is assumed to have a Gaussian shape.

Summary

We have used our experience in investigating particle interactions using femtoscopy to develop a numerical tool called CATS, which allows for a fast and accurate computation of the theoretical correlation function for any source and potential. In addition this tool is very flexible which will make it a valuable asset for future femtoscopy studies.

References

[1] J. Adamczewski-Musch et al. (HADES Collaboration), Phys. Rev. C 94, 025201 (2016)

[2] R. Lednicky and V. L. Lyuboshits, Sov. J. Nucl. Phys. 35, 770 (1982)

* Work supported by SFB1258

DOI:10.15120/GR-2017-1

Report from the ALICE group at GSI

R. Averbeck, S. Masciocchi, and the GSI ALICE group*
GSI, Darmstadt, Germany

ALICE is currently engaged in the Run-2 period of the LHC operation at CERN, which started in 2015. Collisions of lead nuclei (Pb) at the highest energy ever reached in the laboratory (at the center-of-mass energy per nucleon pair of 5.02 TeV) were recorded in 2015, and a second Pb–Pb run will take place in 2018. During the heavy-ion period in Autumn 2016 proton–lead collisions were investigated which do not only provide a reference for the Pb–Pb system but are also interesting in their own right. Data were recorded at two collision energies: a first period was devoted to $\sqrt{s_{\rm NN}} = 5.02$ TeV to match the energy of the Pb–Pb run and to increase the statistics of the p–Pb data sample recorded in 2013 with a new minimum bias data sample. Collisions at the highest reachable energy of 8 TeV were recorded in a second period at high interaction rate, with triggers from the muon system, the calorimeters and the transition radiation detector (TRD). The remaining running time was dedicated to proton–proton collisions at 13 TeV.

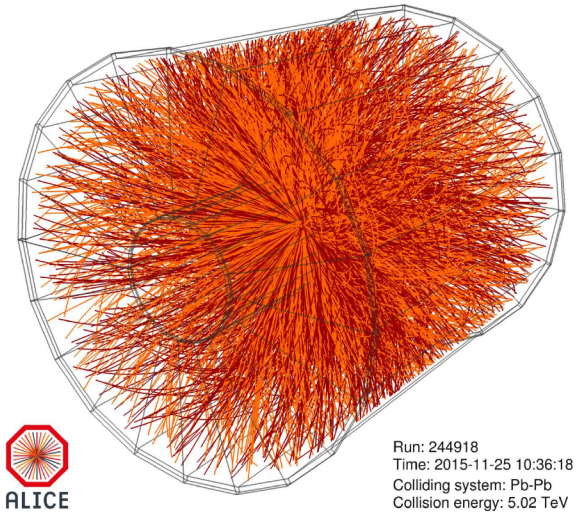

Figure 1: Event display of one of the first lead-lead collisions at the Large Hadron Collider at the top energy of 5.02 TeV per nucleon pair in the center of mass, recorded by the ALICE detector in November 2015.

The GSI ALICE group is deeply involved in Run-2, starting from the responsibility to continuously operate the Time-Projection-Chamber (TPC) and the participation in the obligatory shifts to run the experiment at CERN, up to the analysis of the recorded data and the publication of the results.

* s.masciocchi@gsi.de

Since 2015, large field distortions due to space charge effects were observed in the TPC, operated then with an Ar:CO_2 gas mixture. These distortions cause a significant displacement of the electron clusters produced by traversing particles and recorded with the readout chambers. As a consequence, the track reconstruction performance was seriously affected. Detailed investigations and extensive systematic studies (both from the software and the hardware sides) were conducted by the TPC experts to characterize the features of the distortions and to look for possible reasons for the unexpected size of the phenomenon. A full explanation is not yet available, however a strong correlation with the use of the Ar:CO_2 gas is now suspected. In early 2017, the gas in the TPC was changed back to the original Ne:CO_2:N_2 mixture, and the strong distortions in first approximation are no longer present since then. To mitigate the impact of the distortions on the 2015-16 data, a complex calibration procedure has been developed (with leading contributions from the GSI ALICE group), which is based on the computation of time-dependent corrections of the distortions in the TPC, exploiting also the tracking information from the TRD. This development anticipates to some extent the data calibration procedure for data read out in continuous mode from the upgraded TPC in 2021, where Pb nuclei will collide at a rate of 50 kHz, corresponding to an average of five pile-up events in the TPC at any moment. The correction framework allowed a successful re-processing of all high interaction proton–proton, proton–lead and lead–lead data recorded in 2015 and 2016.

In 2017, a high-statistics data sample of proton–proton collisions will be recorded at $\sqrt{s} = 13$ TeV in order to be able to measure reference spectra up to high transverse momenta. The Collaboration will further exploit a high-multiplicity trigger to study features of events with a very high multiplicity of produced particles which, surprisingly, were observed to resemble some aspects typical for heavy-ion collisions.

The GSI ALICE group is engaged in the analysis of data from all collisions systems and, recently, made public several results of high scientific impact. All relevant results are discussed individually in contributions to this GSI Annual Report. Here, a short overview is given.

The production of J/ψ mesons is measured in proton–proton collisions as a function of the charged-particle multiplicity, showing an increase of the J/ψ abundance which is faster than that of the charged-particle multiplicity. In comparison with models, the data support a scenario in which multi-parton interactions play a significant role. J/ψ production in Pb-Pb collisions at 5.02 TeV con-

DOI:10.15120/GR-2017-1

firms the enhanced yields at low transverse momenta in comparison to the expected rates, even considering the energy loss of charm quarks in the quark-gluon plasma. This confirms that J/ψ mesons are produced via statistical (re)combination of charm quarks at the LHC. This novel behaviour is further proven by the observation of non-zero elliptic flow of J/ψ mesons, measured by ALICE at forward rapidity, in the di-muon decay channel. Two charmonium measurements earned contributed talks at the Quark Matter 2017 conference by the leading analyzers, both doctoral students in the ALICE group at GSI.

Fundamental improvements in methodology are being implemented in the analysis of other observables, preparing the path to further publications in the near future, coordinated by scientists from the GSI ALICE group. The measurement of the nuclear modification factor R_{AA} of electrons from open heavy-flavor hadron decays at low transverse momentum allows to probe with unprecedented precision the role of shadowing in Pb–Pb collisions at the LHC and, possibly, will give hints about the hadronization mechanism for charm (via coalescence or via fragmentation in vacuum). A new analysis method was developed to improve the precision of the lifetime measurement of (anti-)hyper-triton. In the future, the GSI ALICE group will strengthen the analysis efforts related to (anti-)(hyper-) nuclei studies in ALICE, exploiting the excellent particle identification capabilities of the apparatus.

Until June 2017, ALICE has published 178 peer reviewed scientific papers, with an average of 85 citations each, including a report from 2017 on the observation of an 'enhanced production of strange particles in high-multiplicity proton–proton collisions'. This phenomenon, which was one of the first proposed signatures of quark-gluon plasma formation, was observed for the first time unambiguously in collisions of protons in which a large number of charged particles was produced. This result is likely to challenge existing theoretical models that do not predict such an increase of strange particles yields in these events [ALICE collaboration, Nature Physics 2017, doi:10.1038/nphys4111].

The GSI ALICE group is centrally involved in the preparation of the experiment upgrades, to be completed until the end of 2020. These upgrades will allow ALICE to fully exploit the improved performance of the LHC in Run-3, when Pb nuclei will collide with a rate of 50 kHz.

The construction of new readout chambers for the ALICE TPC, equipped with Gas Electron Multiplier (GEM) foils (see Fig. 2), is moving from the prototype stage to the final production chambers. The preparations for the building and testing of the Outer Read-Out Chambers (OROC) are completed. Two full-size chambers were completed in November 2016 and extensively tested in the laboratory with an ^{55}Fe source and x-ray tubes. For the x-ray measurements, a dedicated testing facility was set up, which will be used further by colleagues from the PANDA experiment (see Fig. 3).

The test results obtained from the GSI OROC chambers, together with those from the Inner Read-Out Chamber built at Yale University (USA), allowed the TPC upgrade team to successfully pass the Production Readiness Review, a crucial milestone required by CERN in the course of the development of a new detector, in March 2017. This achievement allows the mass production of the final chambers to start. Further tests of the chambers with a test beam and in the ALICE hall at Point-2 of the LHC are planned for May and July 2017, respectively.

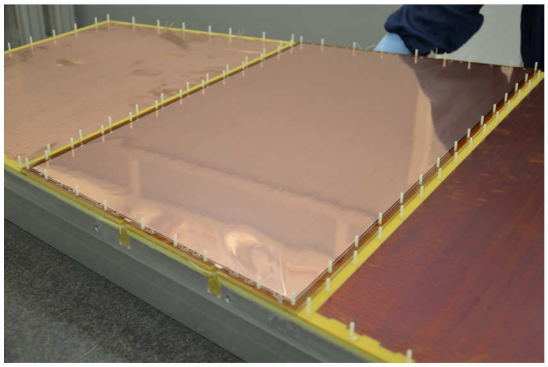

Figure 2: Inner structure of an OROC chamber during its assembly, showing the subdivision of the chamber into three regions which will house three stacks of GEMs. Two stacks on the left are already mounted, while in the third region (on the right) the chamber backplane with the readout pads is visible.

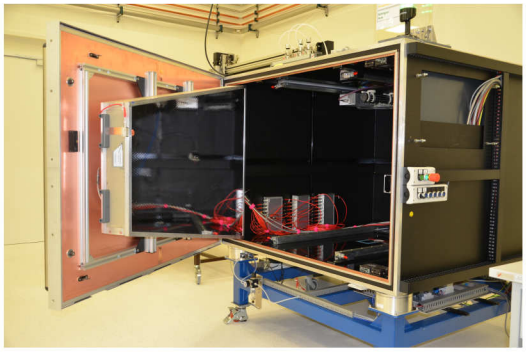

Figure 3: OROC chamber mounted on the door of the so-called Panda box. Inside the box, two high-rate x-ray tubes are mounted for testing chambers under high radiation rates. This testing facility has been prepared to be also used for the test of the PANDA GEM forward tracker.

DOI:10.15120/GR-2017-1

ALICE measurement of the J/ψ nuclear modification factor at mid-rapidity in Pb-Pb collisions at $\sqrt{s_{\rm NN}} = 5.02$ TeV*

A. Andronic[1], *I. Arsene*[2], *R.T. Jimenez Bustamante*[1,3], *S. Masciocchi*[1], *S. Weber*[1,4], *D. Weisser*[3] *for the ALICE Collaboration*

[1]GSI; [2]Oslo University; [3]Heidelberg University; [4]Darmstadt University

Introduction

The suppression of charmonium production induced by color screening of quarks was proposed more than 30 years ago as a probe of the formation of the Quark-Gluon Plasma (QGP) [1]. At LHC energies, the number of produced $c\bar{c}$ pairs per events is one order of magnitude larger than at RHIC, therefore new mechanisms like (re)generation, start playing a role in charmonium production. A charmonium enhancement was predicted for the most central A-A collisions [2, 3]. The nuclear modification factor of the J/ψ mesons ($R_{AA}^{J/\psi}$) measured by ALICE at $\sqrt{s_{\rm NN}} = 2.76$ TeV [4, 5], showed a striking enhancement compared to the one measured at lower energies [6, 7], supporting the models including (re)generation. The transport and comovers models assume the creation of charmonium states through continuous dissociation and regeneration throughout the lifetime of the medium [8, 9, 10]. On the other hand the statistical hadronization model [11] assumes creation of charmonium at the phase boundary.

With the increase of the collision energy at the LHC in Run-2, and the accompanying increase in number of initial $c\bar{c}$ pairs, all models predict a further increase of the J/ψ production by (re)generation. The measurement at $\sqrt{s_{\rm NN}} = 5.02$ TeV and the comparison to lower energies provides important information for the suppression and regeneration picture.

Analysis and results

The ALICE experiment [12] allows to measure J/ψ at mid-rapidity ($|y| < 0.8$) in the decay channel e^+e^-https://www.google.com/gmail/. Two main detectors are used for the electron reconstruction. The Inner Tracking System (ITS), consisting of six layers of silicon detectors located around the interaction point, is used for tracking, vertex determination and triggering. The Time Projection Chamber (TPC) is the main tracking detector, and is also used for particle identification via the measurement of the specific energy loss in the detector gas (dE/dx). The electrons are identified using the TPC information, and the invariant mass distribution is constructed using opposite sign pairs.

The analysis presented here is based on 75 million minimum bias events in Pb-Pb collisions at $\sqrt{s_{\rm NN}} = 5.02$ TeV. This corresponds to a similar statistics to the one collected by ALICE during the LHC Run 1 for the most central events, and more than 10 times the statistics collected for peripheral events. This sample allows to measure the J/psi production in 5 different centrality classes: 0-10%, 10-20%, 20-40%, 40-60%, and 60-90%.

The inclusive R_{AA}, containing both prompt and non-prompt contribution at $\sqrt{s_{\rm NN}} = 5.02$ TeV as a function of centrality is shown in the left panel of Fig. 1 compared to the ALICE measurement at $\sqrt{s_{\rm NN}} = 2.76$ TeV at mid-rapidity [5]. The centrality dependence, characterized by a similar suppression with centrality at the two energies, however an increase of 18% is observed in the most central collisions. Within our systematic uncertainties the results at both energies are compatible. The main systematic uncertainty is due to the reference J/ψ cross section in pp collisions and corresponds to 16%. The measurement is also compared to different models in Fig.1.

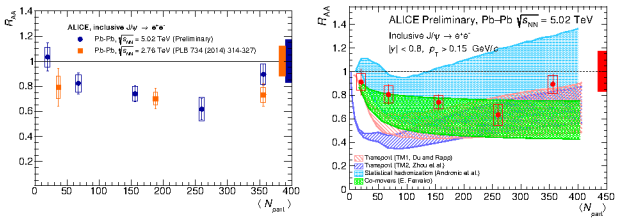

Figure 1: *Left:* R_{AA} at mid-rapidity ($|y|$ <0.8) as a function of centrality. *Right:* R_{AA} compared to different theory models.

References

[1] T.Matsui, H.Satz, Phys Lett B.178 (1986) 416.

[2] P. Braun-Munzinger, J. Stachel, Phys. Lett. B 490, (2000) 196–202 .

[3] R. L. Thews, M. Schroedter, J. Rafelski, Phys. Rev. C 63, (2001) 054905.

[4] ALICE Coll., Phys.Rev.Lett. 109 (2012) 072301.

[5] ALICE Coll., Phys. Lett. B 734 (2014) 314–327.

[6] NA 50 Coll., Eur. Phys. J. C 39, 335 (2005).

[7] PHENIX Coll.Phys. Rev. C 84, 054912 (2011).

[8] X Zhao, R. Rapp, Nucl. Phys. A 859 (2011) 114–125.

[9] K. Zhou et al, Phys. Rev. C 89 5, 459 (2014) 054.

[10] E.G. Ferreiro, Phys. Lett. B 731 (2014) 57–63.

[11] A.Andronic, P. Braun-Munzinger, J. Stachel, Phys. Lett. B 652 (2007) 259-261.

[12] Int. J. Mod. Phys. A 29 (2014) 1430044.

* Work supported by GSI, BMBF, CONACYT, H-QM ,Heidelberg University, and HGS-HIRe

Measurement of J/ψ production as a function of event multiplicity in pp collisions at $\sqrt{s} = 13$ TeV with ALICE *

S. Weber[1,2], *A. Andronic*[1,2], *I. Arsene*[3] *for the ALICE Collaboration*

[1]GSI, Darmstadt, Germany; [2]Technische Universität Darmstadt, Germany; [3]Universitetet i Oslo, Norway

The event multiplicity dependent production of charmonium gives insight on processes on the parton level and on the interplay between the hard and soft mechanisms in particle production. ALICE has performed multiplicity dependent measurements in pp collisions at $\sqrt{s} = 7$ TeV of inclusive J/ψ production at mid- and forward rapidity [1], reaching multiplicities of about 4 times the mean values. The results are consistent with a linear, or stronger than linear increase. Similar observations were also made for J/ψ originating from beauty-hadron decays, and for open-charm hadrons [2].

A new measurement of J/ψ production as a function of event multiplicity in pp collisions at $\sqrt{s} = 13$ TeV was performed with the ALICE detector [7]. J/ψ particles were reconstructed at mid-rapidity ($|y| < 0.9$) in the dielectron decay channel, employing the tracking and PID capabilities of the ALICE Inner Tracking System (ITS) and the Time Projection Chamber (TPC).

In order to have access to high multiplicities the data taking was performed using a trigger on high event multiplicities, based on a large deposited charge in the ALICE V0 scintillator arrays sub-detector, which consists of two scintillator arrays at forward ($2.8 < \eta < 5.1$) and backward ($-3.7 < \eta < -1.7$) rapidity. The charged-particle multiplicity was measured at mid-rapidity ($|\eta| < 1.0$), applying corrections for detector inefficiencies, depending on the offset of the primary interaction vertex in beam direction. Multiplicities of about 7 times the mean value in minimum bias collisions. The signal was extracted in 8 bins of the charged-particle multiplicity from the invariant mass distribution by bin counting in the J/ψ signal region after subtracting the combinatorial background, estimated with the event-mixing technique.

Figure 1 shows the normalized inclusive J/ψ yield (i.e. the yield per event divided by the mean yield per event in minimum bias collisions) as a function of the normalized charged-particle multiplicity. A smooth monotonic increase in the J/ψ yield is observed, which at high multiplicities is clearly stronger than linear. The data are compared to theoretical model predictions. In the PYTHIA8 event generator [3] multiple parton interactions are a key meachanism for particle production. For open-charm hadrons at $\sqrt{s} = 7$ TeV, this mechanism was shown to explain the data [2], the current J/ψ data is slightly underestimated from this model.

The EPOS 3 event generator [4] assumes parton ladders as sources of particle production, each composed of a pQCD hard process with initial and final state radiation. This model provides a very good description of the presented measurement.

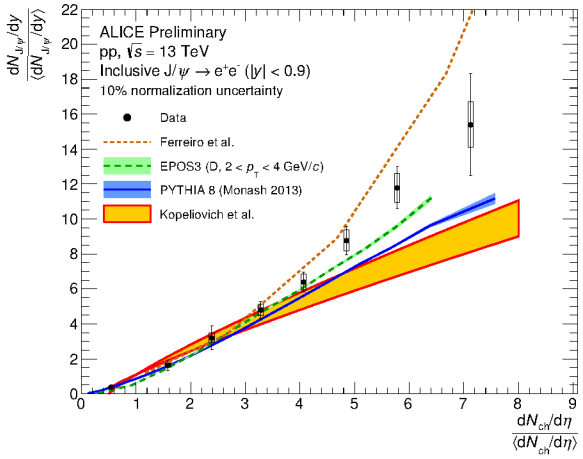

Figure 1: Multiplicity dependence of inclusive J/ψ production at mid-rapidity at $\sqrt{s} = 13$ TeV and comparison to theoretical model predictions.

In the percolation model [5], the screening of color strings leads to a stronger than linear increase at high multiplicities. At very high multiplicities it seems to slightly overestimated the observed increase.

A model by Kopeliovich et al. [6] assumes that high multiplicities are the results of contributions from higher Fock states in the incoming protons, leading to an increase of J/ψ production with the event multiplicity, with a flattening expected at high multiplicities. The current data are underestimated by this model.

References

[1] B. Abelev, et al., Phys. Lett. B712 (2012) 165–175.

[2] J. Adam, et al., JHEP 09 (2015) 148.

[3] T. Sjostrand, S. Mrenna, P. Z. Skands, Comput. Phys. Commun. 178 (2008) 852–867.

[4] K. Werner, B. Guiot, I. Karpenko, T. Pierog, Phys. Rev. C89 (6) (2014) 064903.

[5] E. G. Ferreiro, C. Pajares, Phys. Rev. C86 (2012) 034903.

[6] B. Z. Kopeliovich, H. J. Pirner, I. K. Potashnikova, K. Reygers, I. Schmidt, Phys. Rev. D88 (11) (2013) 116002.

[7] K. Aamodt, et al., JINST 3 (2008) S08002.

* Work supported by GSI, BMBF, Helmholtz Alliance HA216/EMMI, H-QM, and HGS-HIRe

DOI:10.15120/GR-2017-1

J/ψ measurements in pp collisions at $\sqrt{s}$ = 13 TeV using EMCal-triggered events with ALICE at LHC*

C. Jahnke† [1,2], *T. Dahms*[1,2], *and the ALICE Collaboration*

[1]Excellence Cluster Universe, Technische Universität München, Garching, Germany; [2]Physik Department, Technische Universität München, Garching, Germany

Introduction

Measurements of J/ψ production in proton-proton (pp) collisions provide important information on perturbative and non-perturbative quantum chromodynamics. The production of the heavy-quark pairs can be described perturbatively while their hadronisation into quarkonium state is a non-perturbative process [1, 2]. These processes are not fully understood yet and additional experimental data are necessary to further constrain the theoretical model calculations. Additionally, pp measurements provide a baseline for proton-nucleus and nucleus-nucleus collisions allowing studies of the quark-gluon plasma properties.

In this work we study the J/ψ production in pp collisions at a centre-of-mass energy of $\sqrt{s}$ = 13 TeV at mid-rapidity with ALICE [3].

Analysis strategy

The data set used in this analysis were recorded using the Electromagnetic Calorimeter (EMCal) trigger [4], which is used to measure high-p_{T} electrons and photons. The availability of a high-p_{T} electron trigger enhances significantly the sampled luminosity relative to the available sample of minimum bias (MB) triggered data, extending the reached p_{T} for the J/ψ measurement. Fig. 1 shows the cluster energy distribution for two different trigger thresholds (at 5 GeV (EGA2) and at 7 GeV (EGA1)) compared to a MB triggered data.

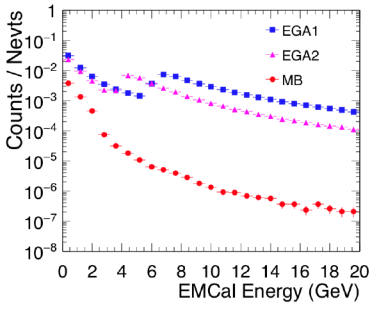

Figure 1: Cluster energy distribution for EMCal-triggered data (EGA1 at 7 GeV and EGA2 at 5 GeV) and for MB-triggered data.

The J/ψ are reconstructed via their dielectron decay channel in events where at least one of the decay electrons triggered the EMCal. The electrons/positrons are identified using the Time Projection Chamber (TPC) [3] and we require at least one of the legs of J/ψ in the EMCal, with a cluster energy above the trigger threshold and a ratio of energy over momentum (E/p) around unity. The J/ψ measurement is performed in the transverse momentum interval $5 < p_{\mathrm{T}} < 20$ GeV/c. In Fig. 2, the invariant mass spectrum is shown for two different trigger threshold: $E > 5$ GeV (left) and $E > 7$ GeV (right). For both thresholds a clear peak is observed around the expected mass for J/ψ.

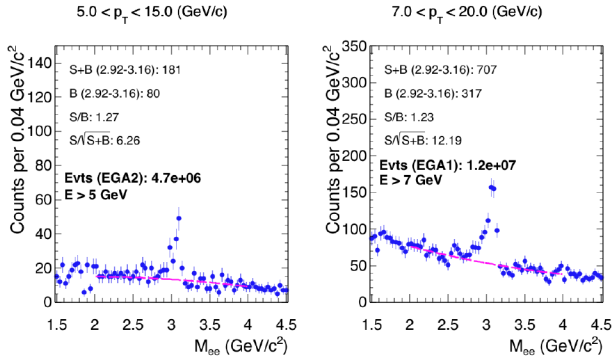

Figure 2: Invariant mass spectrum for trigger data with threshold at 5 GeV (left) and 7 GeV (right).

The J/ψ yield is obtained after subtracting the combinatorial background, which is described by a second-order polynomial.

We are currently working on the efficiency corrections and the evaluation of the systematic uncertainties of the results. Our goal is the measurement of the inclusive J/ψ cross-section as well as the separation of prompt and non-prompt J/ψ. Using this data, it should also be possible to study the dependence of high p_{T} J/ψ production on the charged particle multiplicity, which is an interesting observable to assess possible multi partonic interactions and the interplay between the hard and soft mechanisms in charmonia production.

References

[1] H. Fritzch, Phys. Lett. **B67** (1977) 217.

[2] R. Baier and R. Ruckl Phys. Lett. **B102** (1981) 364.

[3] ALICE Collaboration, JINST **3** (2008) 08002.

[4] ALICE EMCal Group, ArXiv:1008.0413 (2010).

* Work supported by GSI, BMBF, and the DFG cluster of excellence "Origin and Structure of the Universe".

† cristiane.jahnke@cern.ch

Measurements of low-mass dielectrons in pp collisions at $\sqrt{s} = 13$ TeV with ALICE *

I. Vorobyev[†1,2], *A. Chauvin*[1,2], *T. Dahms*[1,2], *A. Dashi*[1,2], *O. Vazquez Doce*[1,2], *and the ALICE Collaboration*

[1]Excellence Cluster Universe, Technische Universität München, Garching, Germany; [2]Physik Department, Technische Universität München, Garching, Germany

The hot and dense system created in ultra-relativistic heavy ion collisions is believed to be a deconfined state of quarks and gluons. Electromagnetic probes such as electron-positron pairs are a unique tool to investigate the whole space-time evolution of such a system. In proton-proton collisions, measurements of dielectron production serve as important vacuum reference to quantify modifications observed in heavy ion collisions. Measurements of low-mass dielectrons could also shed light on the underlying physics processes in those proton-proton collisions with high charged-particle multiplicities.

The current analysis focuses on a comparison of raw dielectron mass spectra in minimum bias events and in events collected with a trigger on high charged-particle multiplicities. To this purpose, the ratio of properly normalised dielectron spectra in high multiplicity (HM) and minimum bias (MB) events is calculated:

$$\frac{\langle N_{\rm ch}({\rm MB})\rangle}{\langle N_{\rm ch}({\rm HM})\rangle} \times \frac{1/N_{\rm HM}\,{\rm d}N_{\rm ee}/{\rm d}m_{\rm ee}|_{\rm HM}}{1/N_{\rm MB}\,{\rm d}N_{\rm ee}/{\rm d}m_{\rm ee}|_{\rm MB}}, \qquad (1)$$

where $\langle N_{\rm ch}\rangle$ is the average charged particle multiplicity and $N_{\rm HM}$ ($N_{\rm MB}$) is the number of recorded high-multiplicity (minimum bias) events.

The dielectron analysis is performed in the central barrel spectrometer of ALICE [1]. Event selection for both multiplicity classes is based on the information from the V0 detectors. Charged particle tracks are reconstructed with the help of the central barrel tracking detectors ($|\eta| < 0.8$) : the Inner Tracking System and the Time Projection Chamber (TPC). Specific energy loss in the TPC and time-of-flight information from the TOF detector are used for electron identification.

Electron and positron candidates from the same event are combined to pairs forming the unlike-sign spectrum. The combinatorial background is estimated via the geometric mean of like-sign pairs within the same event. Conversions of real photons in the detector material (e.g. beam pipe and support structures) are removed from the raw signal by their orientation relative to the magnetic filed.

A cocktail of several dielectron sources is used to estimate the expected ratio (1) as a function of the invariant mass. For the light flavour part, the different hadronic sources of dielectrons via Dalitz or two-body decays are taken into account using a fast Monte-Carlo simulation. Simulations of high-multiplicity events are based on measurements of ratios of charged-particle $p_{\rm T}$ distributions as a function of multiplicity [2].

The contribution of correlated semileptonic decays of open charm and bottom mesons is estimated with PYTHIA simulation. For the multiplicity dependence, the results on D-meson production as a function of multiplicity [3] bracket the expectation for the ratio (1) between 1 and 2.5.

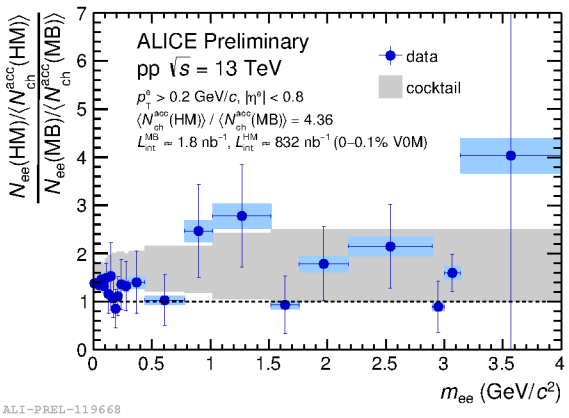

Figure 1: Ratio of dielectron spectra scaled with charged particle multiplicity.

In Fig. 1 the results for the ratio of the dielectron spectra in high multiplicity over minimum bias events scaled by multiplicity factor $\langle N_{\rm ch}\rangle|_{\rm HM}/\langle N_{\rm ch}\rangle|_{\rm MB}$ = 4.36 are shown. The data are in agreement with the expected deviation from a perfect multiplicity scaling over almost the full investigated mass range of 0–4 GeV/c^2. Beyond ≈0.2 GeV/c^2 the data are also consistent with unity, i.e. multiplicity scaling. Higher precision data are necessary to investigate possible modifications of the dielectron spectrum in more details. For this purpose, approximately 5 times more proton-proton data from 2016 will be analysed, and the reduction of systematic uncertainties as well as improvements in cocktail calculations are expected.

References

[1] ALICE Collaboration, JINST **3** (2008) 08002.

[2] ALICE Collaboration, Phys. Lett. B **753**, 319 (2016)

[3] ALICE Collaboration, JHEP **09**, 148 (2015)

* Work supported by GSI, BMBF, HGS-HIRe, Technische Universität München and the DFG cluster of excellence "Origin and Structure of the Universe".

† ivan.vorobyev@tum.de

DOI:10.15120/GR-2017-1

Hadronic cocktail of dielectron sources in pp collisions at $\sqrt{s} = 13$ TeV *

O. Vázquez Doce[†1,2], *A. Chauvin*[1,2], *T. Dahms*[1,2], *A. Dashi*[1,2], *I. Vorobyev*[1,2], *and the ALICE Collaboration*

[1]Excellence Cluster Universe, Technische Universität München, Garching, Germany; [2]Physik Department, Technische Universität München, Garching, Germany

In the study of low mass dielectrons produced in heavy ion collisions, experimental data are usually compared to a hadronic cocktail, that is the sum of all known hadron sources contributing to the dielectron spectrum.

We have obtained for the first time the dielectron mass spectrum from high multiplicity triggered pp collisions at $\sqrt{s} = 13$ TeV, The ratio between this spectrum and the one from minimum bias (MB) events, after normalization by the average charged particle multiplicity, has been compared to a hadronic cocktail expectation. The goal is to search for possible deviations in the mass spectrum when the charged particle multiplicity rises. It is expected an enhancement in the low mass region that is acceptance related, caused by modifications of the p_{T} spectra of hadrons [1]. The region dominated by heavy flavour sources should be enhanced as well, due to higher production yields of charm and bottom mesons in the high multiplicity events [3]. Any other effect like modifications in the relative contributions of different mesons, suppression of short lived vector mesons due to final state interaction with comovers or enhancement due to resonance production in π-π annihilation can be studied.

For the light flavour part of the hadronic cocktail, the different hadronic sources of dielectrons are taken into account using a fast MC simulation. Acceptance, resolution and relative efficiency effects of the ALICE spectrometer are taken into account. The cocktail inputs are based on ALICE measurements in pp collisions at $\sqrt{s} = 13$ TeV. For π^0 the used input parametrization is a Tsallis fit of the p_{T} measured spectra of charged pions by ALICE [2]. Other light hadron spectra are generated via m_{T} scaling.

For the simulation of the high multiplicity events, we apply to the minimum bias cocktail two different weights based on measurements of ratios of p_{T} distributions of charged particles as a function of multiplicity [1], in order to obtain a lower and upper limit for the high multiplicity cocktail. The lower limit is based in the p_{T} spectra of multiplicities $N_{\mathrm{ch}}^{\mathrm{acc}} \geq 2\langle N_{\mathrm{ch}}^{\mathrm{acc}}\rangle$, corresponding to an increase in the average multiplicity by a factor 3. For obtaining the weight of the upper limit case, we use the previous p_{T} spectra divided by the one from low multiplicities $1 \leq N_{\mathrm{ch}}^{\mathrm{acc}} < \langle N_{\mathrm{ch}}^{\mathrm{acc}}\rangle$, in order to account for an increase in the average multiplicity by a factor 6.

With these ingredients, the expected ratio of high multiplicity over minimum bias events from light flavour sources after acceptance cuts can be seen in Fig. 1, represented as a band between the lower and upper multiplicity increases considered for the High multiplicity (HM) cocktail. The effect of the efficiency is shown as well. Both minimum bias and high multiplicity cocktails are normalised using as normalization parameter the number of dielectrons from π^0 Dalitz decays before acceptance cuts.

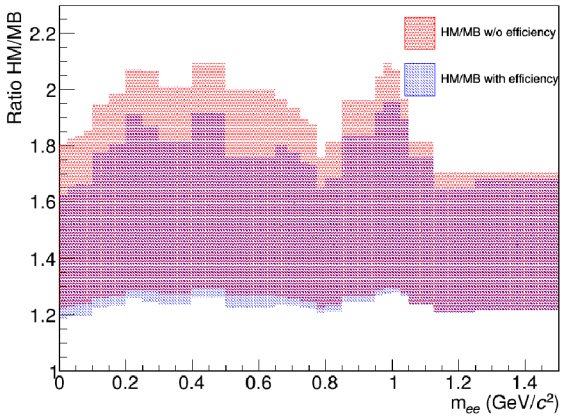

Figure 1: Ratio of the dielectron mass spectrum after acceptance cuts from HM and MB cocktail for the light flavour sources. The blue band represents the ratio HM/MB varying from the lower to the higher multiplicity increases considered for the HM cocktail. The red band represents this ratio when the efficiency weight is not applied.

For the heavy flavour part of the cocktail, we estimate the contribution of correlated semileptonic decays of open charm and bottom mesons making use of a PYTHIA simulation based on the official MC production with enhanced open heavy-flavour contributions of ALICE. We have used this simulation to check the average D meson p_{T} as a function of dielectron invariant mass, and measured values of the enhancement factor of D mesons as a function of its mean p_{T} [3] are used for simulating the high multiplicity dependence.

References

[1] J. Adam et al. (The ALICE Collaboration), Phys. Lett. B **753** (2016) 319.

[2] A. Ortiz Velasquez, ALICE Analysis Note, ALICE-ANA-3034.

[3] J. Adam et al. (The ALICE Collaboration), J. High Energ. Phys. **09** (2015) 148.

* Work supported by GSI, BMBF, HGS-HIRe, Technische Universität München and the DFG cluster of excellence "Origin and Structure of the Universe".

† oton.vazquez.doce@cern.ch

Machine learning for the analysis of low-mass dielectrons in Run II data with ALICE

A. Chauvin[*†1,2], *T. Dahms*[1,2], *A. Dashi*[1,2], *O. Vasquez Doce*[1,2], *I. Vorobyev*[1,2], *and the ALICE Collaboration*

[1]Excellence Cluster Universe, Technische Universität München, Garching, Germany; [2]Physik Department, Technische Universität München, Garching, Germany

Dielectron pairs are an experimental tool to investigate the Quark Gluon Plasma (QGP), which is expected to be created during ultra-relativistic heavy-ion collision. The measured electron-positron pairs are created at different stages of the evolution of the hot and dense medium and do not interact strongly with the latter. Hence, dielectron pairs can probe the full space-time evolution of the system, thereby allowing us to investigate the predicted restoration of chiral symmetry as well as the initial temperature of the QGP.

Machine Learning is a statistical tool that allows combining a large number of variables to perform classification and regression analysis known as Multi-Variate Analysis(MVA) [1]. Combined with complementary analyses, such as overtraining studies and reweighting, a Multi-Variate Analysis can be performed in our analysis e.g. for background rejection and electron identification.

Photon conversions contribute to the background of the dielectron signal. Besides contributing to the combinatorial background, electron pairs from photon conversions contaminate our signal in the very lowmass region ($<$100 MeV/c^2). So far a cut on φ_V (the pair orientation relative to the magnetic field direction) [2] is applied. A cut of φ_V $<$2 rad leads to a signal efficiency of 61% and a background rejection of 99%. The Multi-Variate Analysis

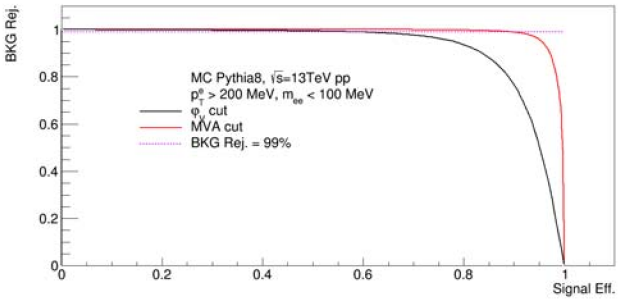

Figure 1: Receiver Operating Characteristic curve for cuts on φ_V and on the MVA output, the background rejection is plotted as a function of the signal efficiency

allows us to consider a total of 16 track and pair variables which are then combined using Boosted Decision Trees. The optimal cut to apply is found when performing overtraing. This consists of looping over the hyperparameter phase-space to look for the first local maximum of the Receiver Operating Characteristic curve of the test sample as shown in Figure 1. This way, one can ensure the selected parametrisation does not depend on the training sample. Thus, for the same background rejection of 99%, a signal efficiency of 89% is achieved by a cut on the newly computed variable.

On top of conversion pairs, MVA can also be used to reject combinatorial background and to perform electron identification. In order to tune Monte-Carlo simulation to match data, reweighting methods [3] can be applied on different types of pairs to be classified. This way, an estimation of the different contributions from the different classes to the spectrum can be evaluated [4]. A MVA relying on Monte-Carlo simulation can be performed for electron identification. In ALICE [5] particle identification is performed using three main detectors: the Inner Tracking System, the Time Projection Chamber and the Time Of Flight detector. So far, cuts are applied separately on the signals in these different detectors. A MVA can combine these signals on top of the other track variables. To do so, Monte-Carlo simulation need to be reweighted in order to correct the different detectors responses [6]. In this case one can expect an increase of the efficiency and the purity, which would reduce the statistical and systematic errors.

References

[1] A. Hocker *et al.*, PoS ACAT (2007) 040 [physics/0703039 [PHYSICS]].

[2] T. Dahms, arXiv:0810.3040 [nucl-ex].

[3] A. Rogozhnikov, J. Phys. Conf. Ser. **762** (2016) no.1, 012036 doi:10.1088/1742-6596/762/1/012036 [arXiv:1608.05806 [physics.data-an]].

[4] S. Lehner, ALICE-ANA-3478.

[5] K. Aamodt *et al.* [ALICE Collaboration], JINST **3** (2008) S08002. doi:10.1088/1748-0221/3/08/S08002

[6] A. Capon, ALICE-ANA-3486.

* Work supported by the DFG cluster of excellence "Origin and Structure of the Universe"

† alex.chauvin@cern.ch

DOI:10.15120/GR-2017-1

Measurement of low-p_{T} electrons from heavy-flavour hadron decays at mid-rapidity in Pb–Pb collisions at $\sqrt{s_{\mathrm{NN}}}$ = 2.76 TeV with ALICE *

S. Hornung †[1,2], *R. Averbeck*[1], *A. Dubla*[1,2], *S. Masciocchi*[1], *and the ALICE collaboration*

[1]GSI, Darmstadt, Germany; [2]Heidelberg University, Germany

Transverse momentum (p_{T}) spectra and the nuclear modification factor (R_{AA}) of electrons from heavy-flavour hadron decays are measured in the most central (0–10%) and in semi-central (20–40%) Pb–Pb collisions at $\sqrt{s_{\mathrm{NN}}}$ = 2.76 TeV. The modification of the p_{T} spectra is studied at mid-rapidity ($|y| < 0.8$) in the p_{T} interval 0.5–3 GeV/c. The R_{AA} is calculated using a new proton-proton (pp) reference cross section.

In ultra-relativistic Pb–Pb collisions at the Large Hadron Collider (LHC) strongly-interacting matter, characterised by high energy density and temperature, is produced. Under these conditions, the formation of a deconfined state of quarks and gluons, the Quark-Gluon Plasma (QGP), is predicted by Quantum ChromoDynamic (QCD) calculations on the lattice. Heavy quarks, i.e. charm and beauty, are produced on a timescale which is smaller than the QGP thermalization time. Heavy quarks interact with the QGP and suffer energy loss while propagating through it.

The modification of the p_{T}-spectra in Pb–Pb collisions with respect to those in pp collisions at the same energy is quantified by the nuclear modification factor R_{AA}:

$$R_{\mathrm{AA}} = (\mathrm{d}N_{\mathrm{AA}}/\mathrm{d}p_{\mathrm{T}})/(\mathrm{d}\sigma_{\mathrm{pp}}/\mathrm{d}p_{\mathrm{T}}) \cdot (1/\langle T_{\mathrm{AA}}\rangle), \quad (1)$$

where $\mathrm{d}N_{\mathrm{AA}}/\mathrm{d}p_{\mathrm{T}}$ is the measured yield in Pb–Pb collisions and $\mathrm{d}\sigma_{\mathrm{pp}}/\mathrm{d}p_{\mathrm{T}}$ is the corresponding cross section in pp collisions. The average nuclear overlap function, $\langle T_{\mathrm{AA}}\rangle$, is estimated via Glauber model calculations and is proportional to the average number of binary nucleon–nucleon collisions in a given Pb–Pb centrality class.

Low-p_{T} heavy-flavour measurements are crucial to test the binary scaling of heavy-quark yields in heavy-ion collisions. In addition, they allow to extract information about potential initial state effects, such as the modification of the parton distribution functions in nuclei with respect to nucleons. They also give information about different hadronisation mechanisms, namely fragmentation in the vacuum and coalescence in the medium. At high p_{T}, heavy quark are sensitive to the medium density, through the mechanism of parton energy loss.

For this analysis, a data sample recorded with ALICE at $\sqrt{s_{\mathrm{NN}}}$ = 2.76 TeV is used. Fig. 1 shows the R_{AA} of electrons from heavy-flavour hadron decays at mid-rapidity ($|y| < 0.8$) as a function of p_{T} in the 10% most central Pb–Pb collisions at $\sqrt{s_{\mathrm{NN}}}$ = 2.76 TeV. The new low-p_{T} measurement (open markers) is shown together with the high p_{T} results obtained using the TPC+EMCal detectors of ALICE to identify the electrons (closed marker) [1]. The statistical and systematic uncertainties are shown as error bars and boxes, respectively. The normalisation uncertainties of the low (high) p_{T} measurements are indicated by empty (filled) box at R_{AA} = 1.

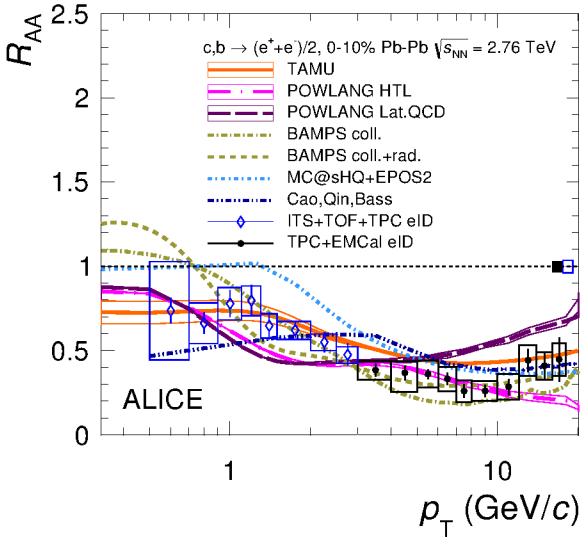

Figure 1: Heavy-flavour decay electron R_{AA} at mid-rapidity as a function of p_{T} in the 10% most central Pb–Pb collisions at $\sqrt{s_{\mathrm{NN}}}$ = 2.76 TeV compared to model calculations [1].

At hight p_{T}, R_{AA} is less than one, showing a suppression of the yield of electrons from heavy-flavour hadron decays in Pb–Pb collisions due to the energy loss of heavy quarks in the QCD medium. For $p_{\mathrm{T}} < 1.5$ GeV/c, R_{AA} is compatible with unity within systematic uncertainties, consistent with binary collision scaling. Models which include shadowing, such as TAMU and POWLANG, predict an R_{AA} smaller than one even at low p_{T}, and are in better agreement with the data compared to other models not including shadowing.

References

[1] ALICE Collaboration, J. Adam et al., arXiv:1609.07104 [nucl-ex].

* Work supported by GSI, Heidelberg University, BMBF and HGS-HIRe

† S.Hornung@gsi.de

The nuclear modification of charged particles in Pb-Pb at $\sqrt{s_{NN}}$ = 5.02 TeV measured with ALICE *

J. Gronefeld[1], *A. Andronic*[1], *P. Huhn*[4], *M.L. Knichel*[2], *J. Otwinowski*[3], *E. Pérez-Lezama*[1,4], *F. Sozzi*[1,2], *A. Toia*[1,4] *for the ALICE Collaboration*

[1]GSI Darmstadt; [2]Universität Heidelberg; [3]The Henryk Niewodniczanski Institute of Nuclear Physics, Polish Academy of Sciences, Cracow, Poland ; [4]Universität Frankfurt

Introduction

Transverse momentum spectra measurements at RHIC at $\sqrt{s_{NN}}$ = 200 GeV [1, 2] have shown that charged-particle yields in heavy-ion collisions are suppressed compared to a superposition of independent nucleon-nucleon collisions (binary collision scaling). This observation is related to parton energy loss in the hot and dense QCD matter created in the collision of heavy ions, leading to a modification of transverse-momentum (p_T) distributions of the resulting particles, as initially suggested by Bjorken in 1982 [3].
Results from ALICE [4] show that hadron yields at high p_T in central Pb–Pb collisions at $\sqrt{s_{NN}}$ = 2.76 TeV are suppressed even stronger than at RHIC, indicating a hotter and denser medium. This suppression is present up to very high p_T and can also be seen in jets [5].
The suppression is quantified in terms of the nuclear modification factor:

$$R_{AA}(p_T) = \frac{1}{\langle T_{AA} \rangle} \frac{dN_{AA}/dp_T}{d\sigma_{pp}/dp_T}.$$

Here, dN_{AA}/dp_T represents the p_T-differential charged-particle yield in nucleus-nucleus (AA) collisions, while $d\sigma_{pp}/dp_T$ stands for the p_T-differential cross section in proton-proton (pp) collisions. The average nuclear overlap function $\langle T_{AA} \rangle$ is determined by Glauber Monte-Carlo calculations for each class of centrality. It relates to the number of binary collisions $\langle N_{coll} \rangle$ ($\langle T_{AA} \rangle = \langle N_{coll} \rangle / \sigma_{inel}^{NN}$) and is strongly dependent on the collision centrality. In absence of medium effects, the nuclear modification factor will be equal to unity, while $R_{AA} < 1$ indicates a suppression of charged-particle yields compared to binary collision scaling.

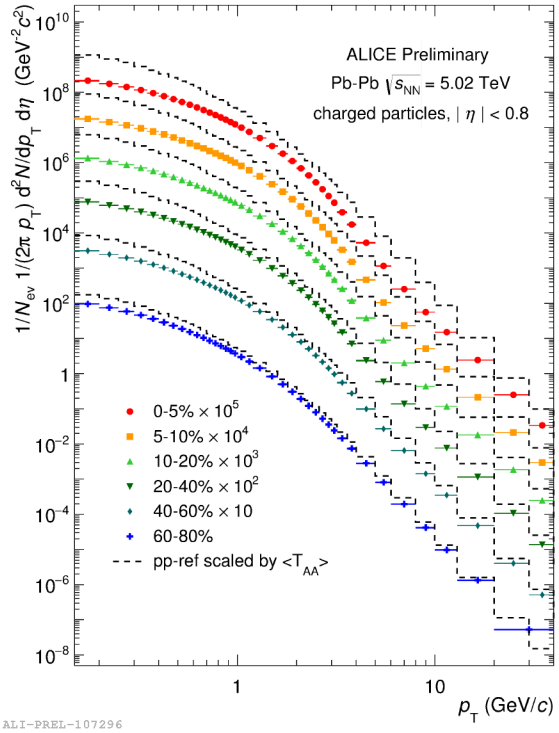

Figure 1: Transverse- momentum distribution of charged particles measured in Pb–Pb collisions for different classes of centrality. The dotted curves represent the measured p_T distribution in pp collisions scaled by the nuclear overlap functions (T_{AA}).

Analysis

Primary charged particles are defined as all prompt charged particles produced in the collision including all decay products, except for products from weak decays of strange hadrons such as K_S^0 and Λ.
To obtain the charged-particle yield as a function of p_T, corrections are made for tracking efficiency and acceptance ($\sim$ 70%), for contamination by secondary particles from weak decays or secondary interactions ($\sim$ 10%, important at low p_T) and for p_T resolution ($\sim$ 2%, important at $p_T > 20$ GeV/c). To account for differences in the particle composition of event generators and the data, the charged-particle reconstruction efficiency was calculated from the particle-dependent efficiencies weighted by the relative abundances of each particle measured in pp at 7 TeV and Pb–Pb at 2.76 TeV. The correction for contamination with secondary particles is taken from Monte-Carlo simulations. The abundances of secondary particles in data and MC is estimated by analyzing the distance of closest approach of tracks to the event vertex (DCA). It is found that the contamination correction from Monte Carlo has to be scaled up by about 30% to match the data.

The total relative systematic uncertainties are in the range range 3.3-7% for pp and 2-6% for central Pb–Pb col-

* Work supported by GSI, BMBF, EMMI, H-QM, and HGS-HIRe

DOI:10.15120/GR-2017-1

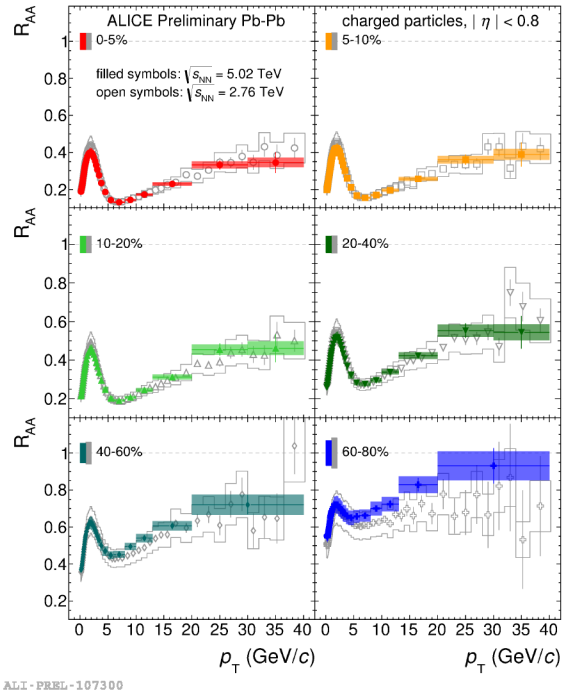

Figure 2: The nuclear modification factor R_{AA} as a function of transverse momentum, p_T, for different centrality classes in Pb–Pb collisions. The filled symbols represent the measurement at $\sqrt{s_{NN}} = 5.02$ TeV while the open symbols stand for the measurement at $\sqrt{s_{NN}} = 2.76$ TeV [4]. The normalisation uncertainty is shown for both energies as a box around unity.

lisions (0-5%) and 4-5.5% in peripheral Pb–Pb collisions (60-80%). Overall, the systematic uncertainties in the current analysis were reduced by about 50% compared to previous analyses, owing to an improved reconstruction and calibration procedure in Run2, as well as to improved track selection methods.

Results

The transverse momentum distribution of charged particles from Pb–Pb collisions is shown in Fig. 1 for six classes of centrality. The spectra are compared with the pp measurement scaled by the nuclear overlap function. Comparing the spectra one observes that the p_T distribution in peripheral collisions is similar to the scaled spectrum in pp collisions while the difference increases towards more central collisions.

The nuclear modification factors as a function of p_T for six centrality intervals are shown in Fig. 2. The filled symbols represent the measurement at $\sqrt{s_{NN}} = 5.02$ TeV, while the open symbols represent the published measurement at $\sqrt{s_{NN}} = 2.76$ TeV [4]. Both measurements exhibit similar features, showing only moderate suppression ($R_{AA} \sim 0.6 - 0.7$) for peripheral collisions (60-80%). In more central collisions, a pronounced minimum at about $p_T \sim 6 - 7$ GeV/c develops, while for $p_T > 7$ GeV/c there is a significant rise of the nuclear modification factor. Within their systematic and statistical uncertainties the measurements at 2.76 TeV and 5.02 TeV agree. Having in mind that the spectra tend to harden for higher center-of-mass energies, this agreement could hint at a stronger energy loss in a hotter and denser medium.

Summary

The strong suppression of charged-particle yields observed in Pb–Pb collisions at $\sqrt{s_{NN}} = 5.02$ TeV exhibits the same characteristics as at $\sqrt{s_{NN}} = 2.76$ TeV. A strong suppression is observed in central collisions, with the maximum suppression around $6 - 7$ GeV/c becoming smaller towards higher p_T. Compared to the previous measurement it was possible to significantly reduce the systematic uncertainties. ALICE is currently analyzing the full 5.02 TeV dataset. In addition, the improved analysis method is being extended to the $\sqrt{s_{NN}} = 2.76$ TeV dataset, in order to further improve the precision in the comparison of the results at the two collision energies.

References

[1] PHENIX Collaboration, *Suppression of hadrons with large transverse momentum in central Au+Au collisions at* $\sqrt{s_{NN}} = 130$ *GeV*, *Phys. Rev. Lett.* **88** (2002) 022301, *arXiv:* 0109003.

[2] STAR Collaboration, *Centrality dependence of high /pt hadron suppression in Au+Au collisions at* $\sqrt{s_{NN}} = 130$ *GeV*, *Phys. Rev. Lett.* **89** (2002) 202301, *arXiv:* 0206011.

[3] J. Bjorken, *Energy loss of energetic partons in quark - gluon plasma: Possible extinction of high* p_T*jets in hadron–hadron collisions*, Preprint **FERMILAB-PUB-82-059-THY** (1982) .

[4] ALICE Collaboration, *Centrality dependence of charged particle production at large transverse momentum in Pb-Pb collisions at* $\sqrt{s_{NN}} = 2.76$ TeV, *Phys.Lett.* **B720** (2013) 52-62, *arXiv:* 1208.2711.

[5] ALICE Collaboration, *Measurement of jet suppression in central Pb-Pb collisions at* $\sqrt{s_{NN}} = 2.76$ *TeV*, Phys. Lett. B **746** (2015) 1,*arXiv:* 1502.01689.

[6] P. Skands, S. Carrazza and J. Rojo,*Tuning PYTHIA 8.1: the Monash 2013 Tune*, Eur. Phys. J. C **74** (2014) no.8, 3024, *arXiv*:1404.5630.

[7] T. Pierog, I. Karpenko, J. M. Katzy, E. Yatsenko and K. Werner, *EPOS LHC: Test of collective hadronization with data measured at the CERN Large Hadron Collider*,Phys. Rev. C **92** (2015) no.3, 034906, *arXiv:*1306.0121.

Hypertriton measurements with ALICE at the LHC

L. Kreis[1,2], *A. Andronic*[1], *B. Dönigus*[3] *for the ALICE Collaboration*

[1]GSI Helmholtzzentrum für Schwerionenforschung, Darmstadt, Germany; [2]Institut für Kernphysik, Technische Universität Darmstadt, Darmstadt, Germany; [3]Institut für Kernphysik, Goethe-Universität Frankfurt, Frankfurt, Germany

Hypernuclei are unstable bound systems of hyperons and nucleons. The hypertriton consists of a proton, a neutron and a Λ baryon. It is the lightest known hypernucleus with a mass of $m = 2.992\,\mathrm{GeV}$.

The lifetime is expected by theory to be close to the lifetime of the free Λ baryon [1]. Recent measurements in heavy-ion collision experiments give a hint of a shorter lifetime. However clarification of this effect needs new measurements with higher precision.

Antihypertriton and hypertriton are rarely-produced particles. Benefiting from the large particle multiplicities in Pb–Pb collisions at the LHC (anti-)hypertriton can be reconstructed in the two particle decay channel using the excellent particle identification capabilities.

$$^{3}_{\Lambda}\mathrm{H} \rightarrow {}^{3}\mathrm{He} + \pi^{-}$$
$$^{3}_{\Lambda}\overline{\mathrm{H}} \rightarrow {}^{3}\overline{\mathrm{He}} + \pi^{+}$$

The hypertriton candidates are reconstructed from their decay products, which are identified by their specific energy-loss in the Time Projection Chamber. Figure 1 shows the invariant mass distribution of the hypertriton candidates in the rapidity interval $|\eta| < 0.9$. It was reconstructed in 43×10^6 Pb–Pb collisions at a center-of-mass energy per nucleon-nucleon pair of $\sqrt{s_{\mathrm{NN}}} = 5.02\,\mathrm{TeV}$ for the $0-80\%$ most central collisions. This is the first measurement of hypertriton in data from LHC Run 2, recorded in 2015. The maximum likelihood fit consists of a Gaussian signal and a polynomial background. An uncorrected (anti-)hypertriton signal of 132 ± 23 counts with a significance of 7.1σ is observed.

Results on the hypertriton in Pb-Pb collisions at $\sqrt{s_{\mathrm{NN}}} = 2.76\,\mathrm{TeV}$ have been published by the ALICE Collaboration in 2016 [2]. A binned method was used for the lifetime extraction. The present feasibility study represents an ongoing effort to improve the precision by using an improved lifetime extraction method based on an unbinned maximum likelihood estimation procedure.

The decay vertex can be reconstructed with the Inner Tracking System. Its six layers of silicon detectors allow to precisely determine the primary vertex of the collision and the position of the displaced vertices.

The invariant mass fit is used to determine the signal- and sideband-ranges. The lifetime τ is calculated from the distance L between the displaced decay vertex and the primary vertex of the collision. It can be extracted with the exponential decay $N(t) \approx \exp(t/\tau)$. The proper decay length can be expressed as $ct = L \cdot cm/p$, where m is the mass and p is the momentum. It can be inserted into the exponential decay

$$N(ct) = \exp\left(-L\frac{m}{\tau \cdot p}\right).$$

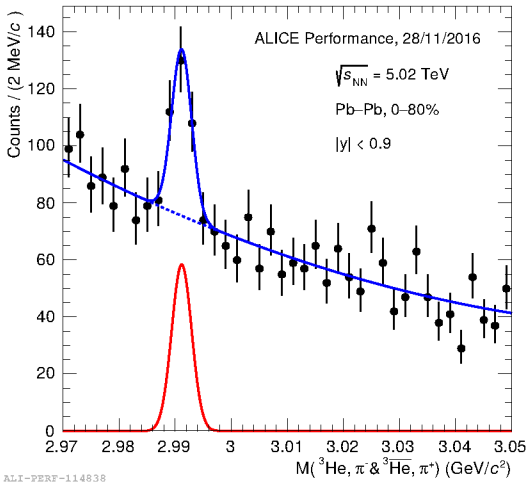

Figure 1: Fit to the invariant mass of hypertriton candidates. The continuous line shows the total fit to the data, the dashed line shows the background fit

The number of counts for the signal and the background in the signal region is determined in the fit to the invariant mass. The shape of the background is evaluated in the sidebands by a fit of the sum of two exponential decay functions. The maximum likelihood fit is performed simultaneously in the signal and sideband regions for the signal and background, and background-only fit functions, respectively. The reconstruction efficiency of hypertriton depends on the decay vertex position. A ct-dependent correction is introduced to correct for this effect. The signal fit function is weighted with this correction, which is calculated in a dedicated Monte-Carlo simulation. This newly-developed method will allow improved measurements of the hypertriton lifetime by the ALICE Collaboration. This may allow to resolve the current ambiguity of the hypertriton lifetime.

References

[1] H. Kamada et. al., "π mesonic decay of hypertriton", Phys. Rev C 57, 1998

[2] ALICE Collaboration, "$^{3}_{\Lambda}\mathrm{H}$ and $^{3}_{\Lambda}\overline{\mathrm{H}}$ production in Pb-Pb collisions at $\sqrt{s_{\mathrm{NN}}} = 2.76$ TeV", Phys. Lett. B 754, 2016

DOI:10.15120/GR-2017-1

Study of the strong interaction with baryon femtoscopy in pp collisions at 7 TeV with ALICE*

O. Arnold[1,2], *L. Fabbietti*[1,2], *and the ALICE collaboration*

[1]Physik Department E62, Technische Universität München, James-Franck-Str. 1, D-85748 Garching, Germany;
[2]Excellence Cluster Universe, Technische Universität München, Boltzmannstr. 2, D-85748, Garching, Germany

Motivation

The understanding of the hyperon-nucleon interaction is an important ingredient for the description of various physical systems. On the one hand side, it helps to better understand the mechanism of the binding of Λ hyperons inside of nuclei. On the other side, the information about the strength of the interaction is of importance to describe heavy astronomical objects like neutron stars. It is expected that in the interior of heavy neutron stars hyperons are produced, since this leads to an energetically more favored configuration. This appearance leads in various model calculations often to a strong softening of the equation of state, usually that strong that the models have a hard time to describe such heavy objects. Since the scattering data on the Λ-p interaction is rather scarce it would be beneficial to study it in more details.

With help of the femtoscopy technique one can access such pair interactions. Femtoscopy is based on the measurement of a two-particle correlation function at low relative momenta. Experimentally, the latter is constructed by a ratio of pairs from the same $A(k^*)$ and from mixed event $B(k^*)$. The mixed event sample does not contain correlations from femtoscopic origin and is thus just an uncorrelated yield of pairs [1]:

$$C(k^*) = \frac{A(k^*)}{B(k^*)}\,, \qquad (1)$$

where $k^* = \frac{1}{2}|\mathbf{p}_1^* - \mathbf{p}_2^*|$ is the momentum of the particles in the rest frame of the pair $\mathbf{p}_1^* + \mathbf{p}_2^* = 0$. At small relative momenta $k^* < 150$ MeV/c the correlation function deviates from unity if the pairs are correlated due to e.g. strong final state interactions. The size of the emission region can be reconstructed with this method.

Analysis strategy

For the femtoscopy study, the pp 7 TeV ALICE data sample was analyzed, which was recorded in 2010. The events were selected with the minimum bias trigger condition. The z-position of the primary vertex was required to lie within 10 cm of the center of the ALICE detector. The goal was to obtain the correlation function among proton pairs as well as p-Λ pairs, where the p-p correlation function serves as benchmark to extract the source size of the pp collision system. Protons are identified with the TPC for momenta below p<0.75 GeV/c. Above this threshold also the TOF information is required to reject contaminations from other species. The hyperons were identified by their decays involving charged particles $\Lambda \rightarrow p\pi^-$ using the invariant mass technique. To reject contributions from combinatorial background, several topological cuts were applied to reduce the source of particles not stemming from the hyperon decay. Around 6M Λ hyperons ($S/B \sim 20$) were reconstructed.

The goal was to investigate the sensitivity of the measured p-Λ correlation function when it is compared to model calculations [2] with different scattering parameters. As an example we tested parameters predicted by chiral effective field theory calculations at leading order (LO) and next-to-leading-order (NLO) expansion [3]. The p-p and p-Λ correlation functions were fitted simultaneously using the NLO parameters for p-Λ. After the fit converged the LO parameters were plugged in to investigate the difference. This is displayed in Fig. 1. One can see that the p-Λ correlation function develops a sensitivity on the scattering parameters. However, the current statistics is not enough to perform a clear separation of the two parameter sets.

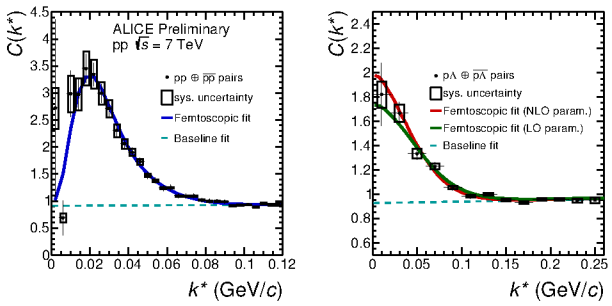

Figure 1: Simultaneous fit of the p-p and p-Λ pair. The p-Λ pair was fitted using the NLO parametrization. Afterwards the LO parametrization was plugged in.

References

[1] M. Lisa *et al.*, "Femtoscopy in relativistic heavy ion collisions", Ann. Rev. Nucl. Part. Sci. (2005) 357-402

[2] R. Lednicky, V.L. Lyuboshits, "Final State Interaction Effect on Pairing Correlations Between Particles with Small Relative Momenta", Sov. J. Nucl. Phys. 35 (1982) 770

[3] J. Haidenbauer *et al.*, "Hyperon-nucleon interaction at next-to-leading order in chiral effective field theory", Nucl. Phys. A 915 (2013) 24-58

* Work supported by GSI, FIAS, HIC4FAIR, HGS-HIRe, BMBF

New flow observables: Symmetric Cumulants*

L. Fabbietti[1,2], *A. Bilandzic*[1,2], *and the ALICE Collaboration*

[1]Physik Department E62, Technische Universität München, 85748 Garching, Germany; [2]Excellence Cluster 'Origin and Structure of the Universe', 85748 Garching, Germany

A measurement of new flow observables, so-called Symmetric Cumulants, which quantify the correlations between event-by-event fluctuations of two different flow harmonics, provide stronger constraints for the medium properties of Quark-Gluon Plasma (QGP), a new state of matter produced in heavy-ion collisions.

Introduction

The key measurement in the exploration of QGP properties is the measurement of anisotropic flow phenomenon. In non-central heavy-ion collisions the initial volume containing the deconfined nuclear matter is anisotropic in the coordinate space. Interactions within this anisotropic volume cause the anisotropy to be transferred from the coordinate space into the momentum space. The resulting anisotropy in momentum space will cause an anisotropic distribution of particles recorded in the detector after each heavy-ion collision, and is therefore an observable quantity. Anisotropic flow is quantified via so-called flow harmonics v_n, which are coefficients in the Fourier series expansion of particle yields in the momentum space.

Anisotropic flow harmonics v_n directly reflect the properties of produced QGP. Their measurements have demonstrated that the QGP produced at the LHC is one of the best examples of a perfect fluid, i.e. the ratio of its shear viscosity to entropy density (η/s) is very close to a universal lower bound of $1/4\pi$ which is obtained from theoretical arguments based on the AdS/CFT conjecture, the fundamental duality between general relativity and conformal field theory.

Symmetric Cumulants

What remains completely unknown is how the η/s of QGP depends on temperature, and this study has been just initiated by the theorists [1]. This question triggered among the experimentalists the development of new flow observables, since the effect of the η/s temperature dependence in individual flow harmonics v_n is masked by other contributions. One recent example are Symmetric Cumulants, which quantify the relationship between event-by-event fluctuations of two different flow harmonics, v_m and v_n [2].

In Fig. 1 a first measurement is shown of these new observables by the ALICE Collaboration [3] and comparison to the theoretical HIJING model. The HIJING model was used to estimate the strength of non-flow correlations. For the data, the positive results of SC(4,2) (red markers) suggest a positive correlation between the fluctuations of v_2 and v_4. The negative results of SC(3,2) (blue markers) predict that finding v_2 larger than average $\langle v_2 \rangle$ enhances the probability of finding v_3 smaller than average $\langle v_3 \rangle$, i.e. a negative correlation between fluctuations of v_2 and v_3. Taking everything into account, SC observables are the least biased measure of the correlation between event-by-event fluctuations of two different harmonics v_m and v_n.

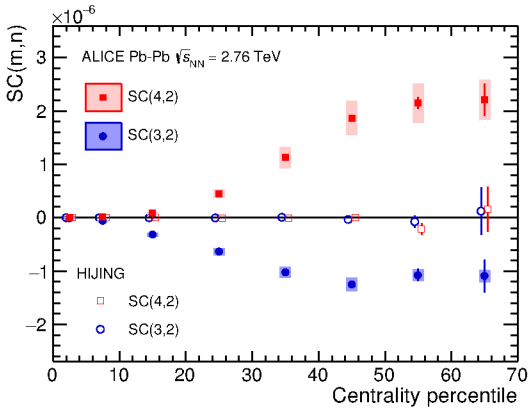

Figure 1: Centrality dependence of observables SC(4,2) (red filled squares) and SC(3,2) (blue filled circles) in Pb–Pb collisions at lower energy of 2.76 TeV. Systematic errors are represented with boxes. Results for theoretical HIJING model are shown with hollow markers.

Remarkably, it was shown [3] that these new correlation observables are sensitive both to the fluctuations of the initial conditions and to the transport properties of QGP, with the potential to discriminate between the two respective contributions. Together with individual flow harmonics v_n, they will allow for verification of theoretical predictions for each individual stage of heavy-ion evolution.

References

[1] H. Niemi, K. J. Eskola, R. Paatelainen and K. Tuominen, Phys. Rev. C **93** (2016) no.1, 014912 doi:10.1103/PhysRevC.93.014912

[2] A. Bilandzic, C. H. Christensen, K. Gulbrandsen, A. Hansen and Y. Zhou, Phys. Rev. C **89** (2014) no.6, 064904 doi:10.1103/PhysRevC.89.064904

[3] J. Adam *et al.* [ALICE Collaboration], Phys. Rev. Lett. **117** (2016) 182301 doi:10.1103/PhysRevLett.117.182301

*Work supported by BMBF Verbundsprojekt ALICE at HIG rate 05P15WOCA1.

DOI:10.15120/GR-2017-1

Using event-shape-engineering in the search for the Chiral Magnetic Effect *

J. Onderwaater[1,2], A. Dobrin[3], J. Margutti[4], I. Selyuzhenkov[1], S. Voloshin[5] for the ALICE Collaboration

[1]GSI; [2]Heidelberg University; [3]CERN; [4]Utrecht University; [5]Wayne State University

The event-shape-engineering technique (ESE) is used to study charge-dependent correlations in classes of events with different flow magnitude. Results for Pb-Pb collisions at $\sqrt{s_{\rm NN}} = 2.76$ TeV recorded with ALICE at the LHC are used to constrain the contribution from the Chiral Magnetic Effect.

The postulated chiral magnetic effect (CME) in heavy ion collisions is a result of parity violation in strong interactions that create a chiral imbalance for fermions in the produced medium, which in combination with an extremely strong magnetic field (B) leads to a charge separation [1]. An observable that is commonly used to measure the charge separation is the two-particle correlation with respect to the reaction plane, $\gamma_{\alpha\beta} = \langle\cos(\varphi_\alpha+\varphi_\beta-2\Psi_{\rm RP})\rangle$, where φ is the azimuthal angle of particles with electric charge α, β, and $\Psi_{\rm RP}$ is the reaction plane angle [2]. In this correlation the contribution from reaction-plane independent background correlations cancels, while other sources of background as well as the CME signal are still present. The ALICE Collaboration has previously observed a significant charge dependence [3]. In order to better understand the origin of the observed correlations, now $\gamma_{\alpha\beta}$ has been measured in event classes with different magnitude of elliptic flow v_2 for fixed centrality ranges using the ESE technique [4,5]. The varying magnitude originates from fluctuations in the initial state of the colliding nuclei. The contribution from CME is assumed to scale with the square of the magnitude of the direction of the magnetic field projected on the event plane. The variation of the magnetic field for different initial states is calculated for different initial conditions. The contribution from background is assumed to scale linearly with v_2. Within the range of v_2 observed for each centrality class, the dependence of the CME contribution on v_2 is approximated to be linear with a different slope. Using this information about the signal and background dependence on v_2, the following function is constructed for a fit to the data and the model calculations with B:

$$F_1(v_2) = p_0(1 + p_1(v_2 - \langle v_2\rangle)/\langle v_2\rangle).$$

The function is constructed such that for data normalized to unity at $\langle v_2\rangle$, p_0 is fixed at 1. If only background is present, $p_1 = 1$ and $F(0) = 0$. The fits and the data are shown in Figure 1. In combination with a fit to the models to estimate $p_{1,\rm CME}$, we can extract an estimate for the CME fraction $f_{\rm CME}$:

$$f_{\rm CME}\, p_{1,\rm CME} + (1 - f_{\rm CME}) = p_{1,\rm data}.$$

Figure 2 shows the extracted values for $f_{\rm CME}$. The statistical errors in 0-10% centrality and 50-60% are too large to reveal any information about the possible presence or absence of a CME signal. For 40-50% the fraction is negative . In the 10-40% range, the indication is that the CME, if present, represents a small fraction of the observed charge dependence of $\gamma_{\alpha\beta}$.

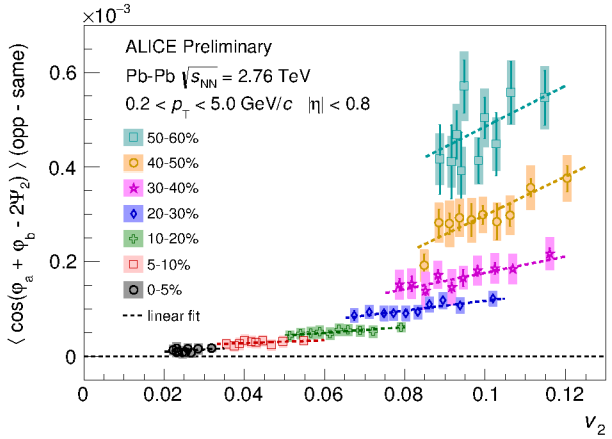

Figure 1: $\gamma_{+-} - \gamma_{++/--}$ as a function of v_2 for various centrality classes.

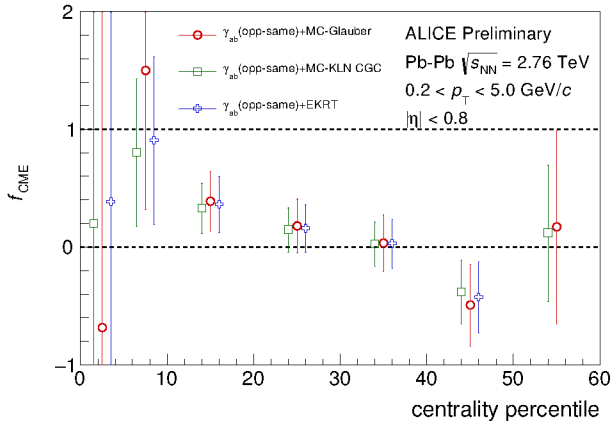

Figure 2: The observed fraction $f_{\rm CME}$ as a function of centrality assuming different initial state models.

References

[1] D. Kharzeev, Phys. Lett. B633 (2006) 260-264

[2] S. Voloshin, Phys. Rev. C70 (2004) 052901

[3] J. Schukraft, Phys. Lett. B719 (2013) 394-398

[4] ALICE Collaboration, Phys. Rev. Lett 110 (2013) 012301

[5] Quark Matter 2017, presentation by A. Dobrin for the ALICE Collaboration, https://indico.cern.ch/event/433345/

* Work supported by GSI, BMBF and TU Darmstadt.

Experience with the upgraded ALICE TPC readout system (RCU2)

C. Lippmann and the ALICE collaboration*
GSI, Darmstadt, Germany

The readout of the ALICE TPC comprises 557 568 electronics channels on 4 356 Front-End Cards (FECs). The FECs are grouped in 216 readout partitions, distributed in 18 sectors each on the two sides of the TPC. Within each partition, a Readout Control Unit (RCU) interfaces the FECs to the trigger processor, to the Data Aquisition System (DAQ) and to the Detector Control System. The readout bus to the FECs is implemented as a 40 bit wide parallel bus.

Figure 1: The RCU2 board.

The new version of the Readout Control Unit, the RCU2 (see Fig. 1) was installed in 2016. It increases the segmentation of the readout bus from two to four separate branches, each reading between 4 and 7 FECs. All functionality is incorporated into a single FPGA. The Microsemi SmartFusion2 was chosen, even though it had only just been released. It integrates an inherently reliable and radiation tolerant FLASH-based FPGA fabric, a 166 MHz ARM Cortex processor and high-performance communication interfaces all on a single chip. As bandwidth of the optical readout link to the DAQ system 300 MByte/s was chosen (was 160 MByte/s). A secondary FPGA (Microsemi ProAsic 3) is responsible solely for radiation monitoring. It counts Single Event and Multi Bit Upsets in dedicated memories and is not required for the basic operation of the RCU2.

The upgrade to the new RCU2 system was performed during the extended winter technical stop of the CERN Large Hadron Collider (LHC) in January and February 2016. Replacing the 216 RCUs and 1080 backplane and adapter cards took about 3 weeks. The newly installed boards were tested immediately for the basic functionality. More time was spent correcting errors and commissioning the system. With the new system, the first physics collisions were recorded in April 2016.

During the course of the year 2016 the performance of the RCU2 was optimized by implementing new features into the RCU2 firmware. The firmware on the 216 installed cards can be updated remotely using ethernet.

- Data ordering following the pad row structure of the readout chambers was implemented to allow optimal speed of the online cluster-finding algorithm in the High Level Trigger system.
- A double buffer structure was implemented for each of the four readout branches. This allows to write the raw data from a channel on a FEC into one buffer while at the same time reading and clearing (reformatting) the other buffer. The buffers are switched once both processes are done.
- In sparse readout mode only channels on the FEC that actually contain some data are adressed. This feature reduces the time needed to read out data from low occupancy events.
- Usage of a Multi Event Buffering scheme allows to accept a new trigger even though not all data from the previous event has been read out.
- Improvements in the protocol on the readout bus were applied, significantly reducing the time needed for a single bus transaction.

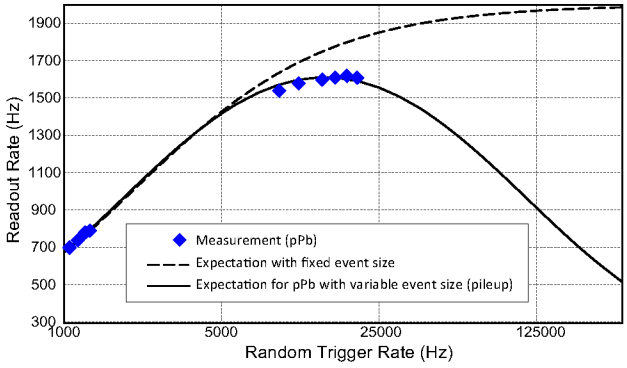

Figure 2: Expected and measured readout rates. Note that the data size and thus the readout time increases at high interaction rates due to event pileup in the TPC drift volume.

During the p–Pb campaign at the LHC in autumn 2016 minimum bias collision events have been recorded at an unprecedented rate (for a TPC) of 1.6 kHz (see Fig. 2). Moreover, a very stable operation without interruptions due to e.g. radiation effects is observed.

* C.Lippmann@gsi.de

DOI:10.15120/GR-2017-1

Space-charge distortion corrections in the ALICE TPC*

H. Appelshäuser[1], *M. Arslandok*[2], *C. Garabatos*[3], *E. Hellbär*[1], *M. Ivanov*[3], *C. Lippmann*[3], *R. Münzer*[1], *K. Schweda*[3], *R. Shahoyan*[4], *J. Wiechula*[1]
for the ALICE Collaboration
[1]IKF, Frankfurt, Germany; [2]PI, Heidelberg, Germany; [3]GSI, Darmstadt, Germany; [4]CERN, Geneva, Switzerland

The ALICE TPC [1] was operated during the first period of data taking at LHC, commonly denoted as Run 1, from 2009–2013 with two different gas mixtures: Ne-CO_2-N_2 (90-10-5) until 2010 and Ne-CO_2 (90-10) from 2011 on. For reasons of operational stability, the gas mixture was changed to Ar-CO_2 (88-12) during the LHC first long shutdown, before the start of Run 2 in 2015. The operational stability turned out to be excellent, even at high luminosities.

At high collisions rates and large charged-particle multiplicities, the TPC drift volume contains a large number of positive ions that pile up due to the slow ion drift velocity. The resulting field distortions modify the electron drift lines, introducing drift field distortions that have to be corrected. In most of the TPC drift volume, the observed distortions in neon and argon, i.e. the *bulk* distortions, are as expected from the known gas properties of the Ar- and Ne-based mixtures, such as primary ionization and ion mobility. In Run 1, small *local* space-charge distortions of up to a few mm were observed in neon. However, in Run 2, these local distortions exceed the simple extrapolation from neon to argon by a factor of up to 10–20 and reach up to several centimeters, see Fig. 1. This is of similar magnitude as the distortions expected for Run 3 after the ALICE TPC upgrade with GEM-based readout [2] at lead-lead collision rates of 50 kHz. However, in Run 3 the distortions are expected to be continuous, with relatively small gradients, as they are resulting from space charge distributed over a large volume. The distortions encountered in Run 2, on the other hand, have large gradients.

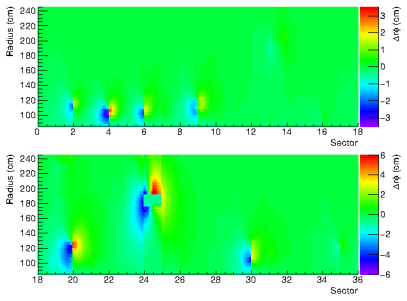

Figure 1: Measured space-charge distortions near the central electrode $\Delta r\phi$ in Pb-Pb collisions at 4.5 kHz interaction rate as a function of the TPC sector and the radius for the A (top) and C side (bottom).

These dynamic distortions were measured as 3 dimensional maps by interpolating tracking information from external detectors, i.e. the silicon-based inner tracking system (ITS) at inner radii as well as the transition radiation detector (TRD) and the time of flight detector (TOF) which are located at outer radii when compared to the TPC. Reconstructed TPC clusters are compared with their expected position obtained from the interpolated reference tracks.

In order to collect sufficient statistics, a distortion map is created as the average of the measured distortions over a time interval of typically 20 minutes. Changes in the interaction rate and thus the amplitude of the distortions are accordingly scaled by the instantaneous luminosity. This procedure does not take into account local fluctuations of space charges which amount to up to 20 - 30 %. During track reconstruction, the coordinate of each TPC cluster is corrected according to these parameterized maps. The quality of the *average* distortion correction can be appreciated from the bias of the mean signed distance of the closest approach (DCA) of TPC tracks to the primary vertex before and after correction shown in Figure 2.

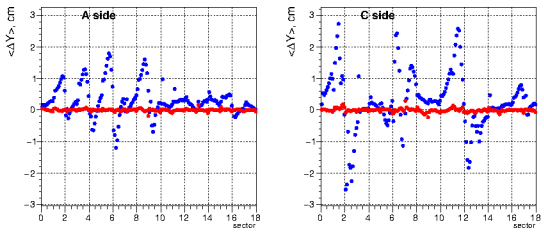

Figure 2: Bias of the mean distance of closest approach of TPC tracks ($p_T > 2$ GeV/c) to the primary vertex in Pb-Pb collisions at 4.5 kHz interaction rate before (blue) and after (red) distortion correction.

For the next data taking period, starting in May 2017, the same gas mixture as used in Run 1 (Ne-CO_2-N_2 (90-10-5)), for which the observed distortions were small, will again be injected into the TPC. The higher ion mobility should lead to a reduction of the space-charge distortions by a factor of two. Possibly a larger reduction will be observed. Already with a factor 2 reduction of the distortions, the challenges related to event-by-event fluctuations in the space-charge distortions, which are not taken into account, will become negligible and the tracking and PID performance will be further improved.

References

[1] ALICE TPC Collab., Nucl. Instr. Meth. A 622 (2010) 316.
[2] ALICE Collab., CERN-LHCC-2013-020 (2013).

* Work supported by GSI, BMBF, EMMI, H-QM, and HGS-HIRe.

Upgrade of the ALICE Time Projection Chamber*

T. Rudzki[†1,2], *U. Frankenfeld*[1], *J. Hehner*[1], *M. Jahn*[1], *L. Karayan*[1], *S. Masciocchi*[1,2], *D. Miśkowiec*[1], *T. Morhardt*[1], *R. Patra*[3], *and B. Voss*[1]

[1]GSI, Darmstadt, Germany; [2]Physikalisches Institut, Heidelberg, Germany; [3]Variable Energy Cyclotron Centre, Kolkata, India

Introduction

ALICE (A Large Ion Collider Experiment) is one of the four large experiments at the CERN LHC. It was designed and built with the aim of studying collisions between lead ions and learning about the properties of the extreme matter created therein. The experiment successfully took data from pp, Pb–Pb, and p–Pb collisions during the LHC Run 1 at half of the nominal LHC beam energy, and continues its studies at (nearly) full energy in the Run 2. A significant increase of luminosity is planned for Run 3.

The Time Projection Chamber (TPC) is the main tracking and particle-identification detector of the ALICE Central Barrel which covers midrapidity $-0.9 \leq \eta \leq 0.9$ and the full azimuth $0 < \varphi < 2\pi$ (Fig. 1). The TPC volume is divided in two halves by a central cathode kept on a potential of -100 kV. The charged particles traversing the gas volume (Ne-CO_2) ionise the gas. The released electrons drift towards the TPC endplates which are equipped with 18 inner and outer readout chambers (IROCs and OROCs). There, the signal is amplified and information about position, timing and charge is digitised and provided to the data acquisition system.

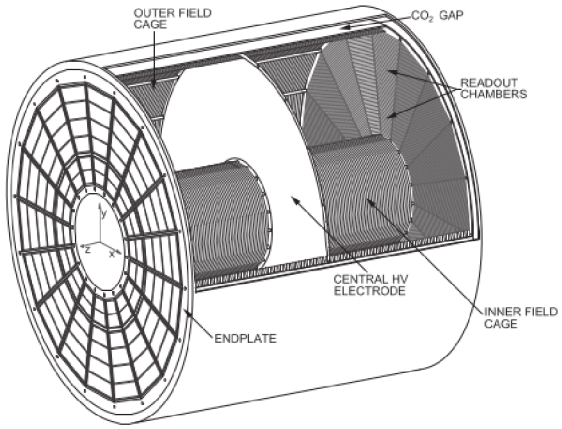

Figure 1: The ALICE TPC at the Large Hadron Collider. Each endplate is equipped with 36 readout chambers.

In 2019-2020, the ALICE experiment will be upgraded to cope with high rates (50 kHz) of Pb-Pb collisions expected in the LHC Run 3. Therefore, the current readout chambers of the TPC – multi-wire proportional chambers (MWPCs) with a gating grid which are capable for rates below 3 kHz – will be replaced by ones equipped with GEMs [1, 2].

GEMs, Gas Electron Multipliers, are 50 μm thick kapton foils, covered on both sides with a copper layer, with small holes. A potential difference of 200–400 V between the two sides of the foil is applied resulting in a strong electric field inside the holes. In this field, the incoming electrons are accelerated and ionise the gas. In an ALICE TPC OROC, the foils are arranged in three stacks of four GEMs (Fig. 2) which are operated at a gain of 2,000 and an ion backflow below 1 % [1].

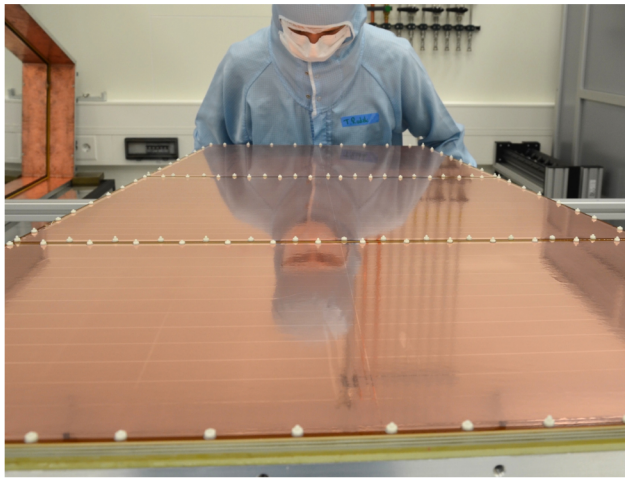

Figure 2: OROC equipped with three stacks of 4 GEMs.

First fully operational GEM OROC

The TPC Upgrade is an international project with many participating institutions. In this collaborative work, GSI fulfills two tasks: framing GEMs for the largest, outermost stack (OROC3) and assembly of OROCs. For this purpose, the test stand for gain uniformity measurements, formerly used to test the Transition Radiation Detector chambers of ALICE, was moved to the clean room and a second test setup, originally designed for the planar GEM-tracker of PANDA, was adapted to perform high-irradiation tests.

In 2016, the QA and framing of GEM foils started. The foils are already tested once and optically scanned at HIP, Helsinki. Arriving at GSI, a basic QA is repeated to make sure that the foils did not get damaged during transport.

* Work supported by GSI, BMBF, EMMI, H-QM and HGS-HIRe
† t.rudzki@gsi.de

DOI:10.15120/GR-2017-1

The leakage current of each foil segment, normalised to its area, is recorded to rate their quality [3].

At the end of 2016, the first fully functioning GEM-based OROC was assembled and commissioned in the lab at GSI. The supplied voltages were tuned such that all stacks have the nominal gain of 2,000. This was reached with minor deviations of 50, 100 and 0 V (for the three GEM stacks, respectively) from the nominal voltage of 4.2 kV (Fig. 3).

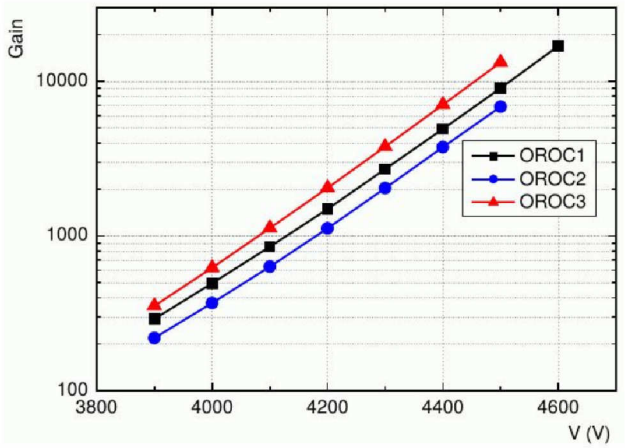

Figure 3: Gain curve of the three GEM stacks of the first OROC, obtained with an ^{55}Fe source.

The upgrade should preserve the performance of the current TPC. This results in the following requirements:

- Gain uniformity with an RMS below 20 %.
- $\frac{\sigma_E}{E}$ of ^{55}Fe photopeak below 12 %.
- Ion backflow below 1 %.
- Operation stability at high radiation rates (ALICE conditions).

In Fig. 4 the gain uniformity map of the OROC is shown. The blue bars are either transition regions between the stacks or in the lowest stack floating segments in two different foils leading locally to a significant reduction in gain. The RMS of the remaining part of the scan is 20 % of the mean and fully satisfying. The ion backflow was found to be at around 0.6 % which is comparable to the values of small prototypes (Fig. 5).

The energy resolution was measured for each stack using an ^{55}Fe source. All three results of $\frac{\sigma_E}{E}$ were around 14 % which will be a subject of further optimisation.

Finally, the chamber was mounted inside the PANDA box and was exposed to x-ray irradiation leading to a pad current of 10 nA/cm^2 which is expected for Run 3 in the TPC. The chamber behaved well and the resolution did not deteriorate.

Conclusion and outlook

The first OROC, described in this note, successfully passed the required tests. In addition, another chamber has been assembled at GSI in 2017. This chamber represents the final design and has an even better performance.

The TPC Upgrade group at GSI is ready for the mass production of OROCs. This is scheduled to begin in summer 2017 and to continue until autumn 2018.

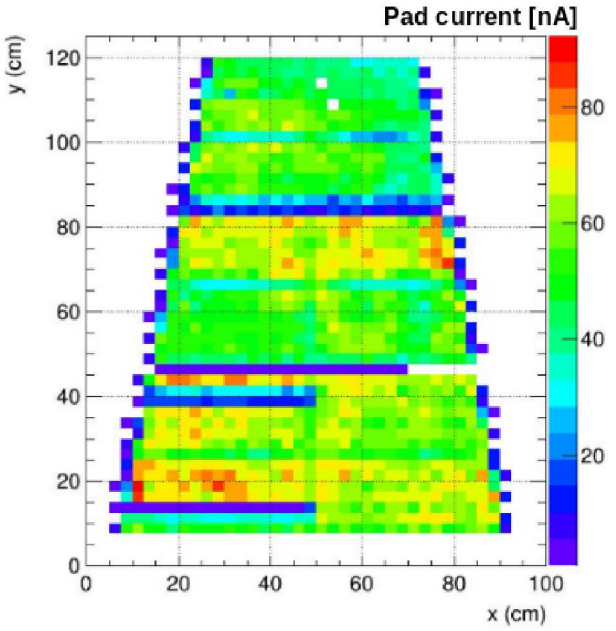

Figure 4: Gain uniformity scan of the OROC. The 3 GEM stacks are clearly visible.

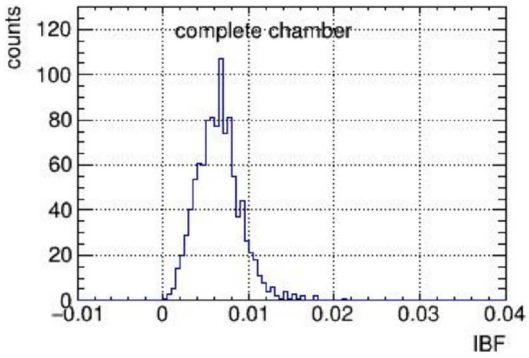

Figure 5: Ion backflow of the OROC - the required value of 1 % is achieved.

References

[1] ALICE Collaboration, Technical Design Report for the Upgrade of the ALICE TPC, CERN-LHCC-2013-020, https://cds.cern.ch/record/1622286

[2] ALICE Collaboration, Addendum to the Technical Design Report for the Upgrade of the ALICE TPC, ALICE-TDR-016-ADD-1, https://cds.cern.ch/record/1984329

[3] Jahn, M. "Quality assurance for gas electron multipliers with the leakage current test", Bachelor thesis, University of Heidelberg, 2017.

DOI:10.15120/GR-2017-1

Study of secondary discharges in Ar-CO_2 (90-10) and Ne-CO_2-N_2 (90-10-5)*

A. Deisting[†1,2], *C. Garabatos*[1], *and S. Masciocchi*[1,2]

[1]GSI Helmholtzzentrum für Schwerionenforschung GmbH, Darmstadt, Germany; [2]Physikalisches Institut, Ruprecht-Karls-Universität Heidelberg, Heidelberg, Germany

Introduction

The Large Hadron Collider (LHC) will provide lead-lead collisions at an interaction rate of 50 kHz from 2021 onwards. To exploit the full rate, the ALICE Time Projection Chamber (TPC) [1] will be upgraded with new ReadOut Chambers (ROCs). These ROCs will utilise stacks of four Gas Electron Multipliers (GEMs) [2] and hence allow for continuous read-out, while preserving the energy and momentum resolution of the current Multi-Wire Proportional Chambers [3]. The discharge mechanism of GEM foils was studied to ensure stable operation of the ROCs at LHC.

Study of secondary discharges

This study has been conducted with a set-up of two 10×10 cm^2 GEM foils mounted with an inter GEM distance of 2 mm. The distance of the last GEM (GEM2) to the anode plane is as well 2 mm. While the electric field between GEM1 and GEM2 is referred to as transfer field (E_{T}), the field between GEM2 and the anode plane is called induction field (E_{Ind}). During a discharge in one of the two GEMs a signal is induced on the anode plane and, after some attenuation, read out with an oscilloscope. The active volume of the detector is flushed with Ar-CO_2 (90-10) or Ne-CO_2-N_2 (90-10-5), enriched with ^{222}Rn. While a high voltage difference (ΔU_{GEM2}) was applied across GEM2, ΔU_{GEM1} was kept at a moderate value. Hence the ionisations produced by the α-decays of Rn trigger discharges in GEM2. A more detailed description of the set-up used here can be found in [4, 5].

In previous studies the phenomenon of *secondary discharges* ("secondaries") was discovered [6]. Two parameters have been found to characterise these discharges: First, they occur always after an initial discharge and the corresponding measured signal is higher than the signal of the original discharge. Second, these discharges are only observed starting from a certain E_{Ind} value [7].

To quantify the onset of secondary discharges, the probability to observe one of them after an initial discharge is measured by: $P_2 = \frac{\#\text{ secondary discharges}}{\#\text{ initial discharges}}$. Plotting P_2 versus e.g. E_{T} (figure 1) shows a clear onset of the secondary discharges for a given electric field. In our work we showed that secondary discharges are caused by a discharge of the induction (transfer) gap if E_{Ind} (E_{T}) is high enough [4]. However the underlying mechanism is not yet understood.

Secondaries in different gas mixtures

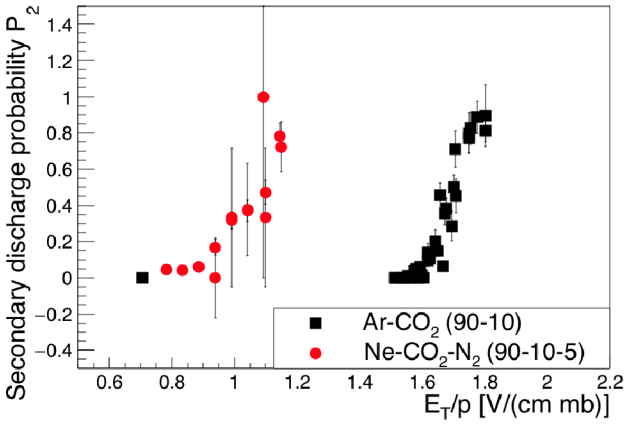

Figure 1: Both measurements were done with the same set-up. For the Ar-CO_2 (Ne-CO_2-N_2) measurement ΔU_{GEM2} was set to 423 V (455 V). ΔU_{GEM1} was varied in both cases in the range between 260 V and 290 V.

Fig. 1 shows P_2 for secondary discharges in the transfer gap between the two GEMs. For Ar-CO_2 (90-10) and Ne-CO_2-N_2 (90-10-5) a steep rise of P_2 from 0 to 1 can be seen. Defining the onset field as the field at which $P_2 = 0.5$, an onset field of 1.69 ± 0.05 V cm^{-1} mb^{-1} and of 1.05 ± 0.08 V cm^{-1} mb^{-1} is observed for the Argon- and Neon-based gas-mixture, respectively. For the ALICE TPC upgrade, Ne-CO_2-N_2 (90-10-5) is foreseen as the baseline gas mixture as well as transfer fields of 4 kV cm^{-1}. Since these foreseen transfer fields are higher than the observed onset of the secondary discharges, measures to mitigate secondaries are needed. A promising ansatz is the use of decoupling resistors as shown in [5].

References

[1] *Nucl. Instr. Meth. Phys. Res. A* **622** (2010) 316–367

[2] *Nucl. Instr. Meth. Phys. Res. A* **386** (1997) 531–534

[3] *CERN-LHCC-2013-020*

[4] A. Deisting, C. Garabatos, *JINST* **12** Nb. 05 (2017) C05017

[5] A. Datz, *Bachelor thesis Uni. Heidelberg* (2017)

[6] V. Peskov, P. Fonte, arXiv:0911.0463

[7] P. Gasik, RD51 Collaboration meeting (2016-03)

* Work supported by GSI, BMBF, H-QM, HGS-HIRe, and University of Heidelberg

† alexander.deisting@cern.ch

DOI:10.15120/GR-2017-1

Quadruple GEM PCB simulator *

P. Gasik† [1,2] *and the ALICE TPC collaboration*

[1]Physik Department E62, TU München, 85748 Garching, Germany; [2]Excellence Cluster 'Origin and Structure of the Universe', 85748 Garching, Germany

A major upgrade of the ALICE TPC is foreseen during the LHC Long Shutdown 2 (2019-20) when the existing MWPC-based readout chambers will be replaced with detectors employing the Gas Electron Multiplier (GEM) technology. The key parameter for a long-term operation of the GEM-based TPC is the stability against electrical discharges. A thorough investigation of the discharge properties of GEM-based detectors has been already reported by the Collaboration in e.g. [1].

The next important goal is the final assessment of the HV supply scheme planned to be used with the upgraded readout chambers. Behaviour of the system in case of a spark occurrence, propagated discharges or an emergency trip of a power supply is of a great importance. The possibility of an over-voltage across any GEM foil must be avoided as it may lead to the development of a destructive discharge. In order to test the reaction of the powering scheme on the violent events, as listed above, we have designed and built a GEM detector simulator based on the conventional electronic elements.

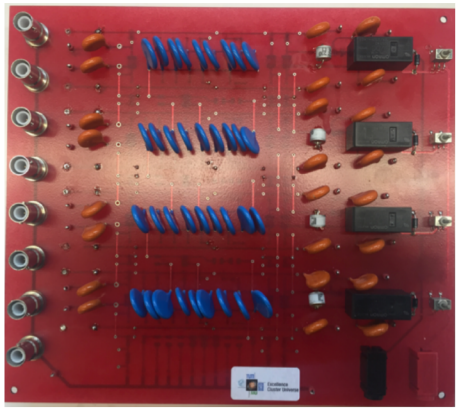

Figure 1: Quadruple GEM PCB simulator.

Figure 1 shows a picture of a double-layer PCB (top view) equipped with capacitors and resistors corresponding to the realistic values of a quadruple GEM Inner Read-Out Chamber for the upgraded ALICE TPC. HV is applied to 8 channels (corresponding to 8 GEM electrodes) via SHV connectors. The device allows for the simulation of a short in one of the GEM segments (in each layer) using HV relays or a spark occurrence by employing a Gas Discharge Tube (GDT) which creates a spark after a breakdown voltage is reached. GDTs can simulate a discharge across one segment of GEM (its equivalent capacitor) or between GEMs in one of the transfer or induction gaps and their breakdown voltage corresponds to the realistic settings applied to the detectors. Voltages on electrodes in question can be monitored on a scope using standard 1:10 probes via decoupling HV capacitors, included in the design.

An example of operation of the PCB simulator is presented on figure 2, where a GEM discharge signal recorded with a real detector (top panel) is compared to the one recorded with the GEM PCB simulator (bottom panel, scope screenshot). The signal waveform shows modulations which are due to the inductance of the system, resulting in periodic oscillations. The signal from the simulator nicely reproduces main features of the real detector signal, such as amplitude ($\sim$ 500 mV), oscillation frequency ($\sim$ 10 MHz) or signal damping ($\sim$ 1 μs).

The device presented in this report can serve as a testing tool for the assessment of the HV scheme without a need to use a real detector.

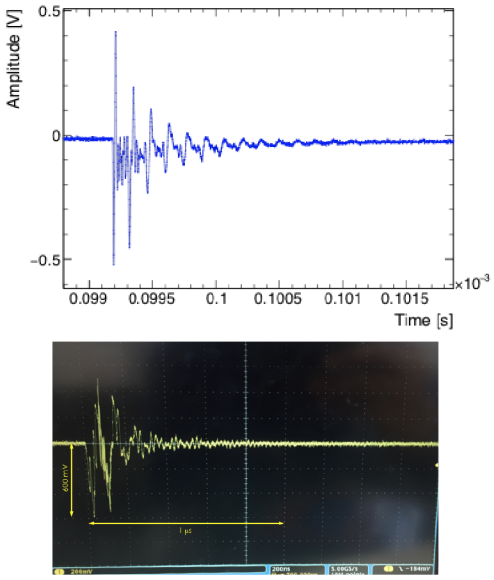

Figure 2: Discharge signal recorded on the oscilloscope with a real detector (top) and with the GEM PCB simulator (bottom).

References

[1] ALICE Collaboration, CERN-LHCC-2015-002 (ALICE-TDR-016-ADD-1) 2015.

* Work supported by BMBF 05P15WOCA1, Excellence Cluster 'Universe'

† p.gasik@tum.de

Digitization for the ALICE GEM TPC*

A. Mathis[†1,2], *J. Wiechula*[3], *L. Fabbietti*[1,2], *P. Gasik*[1,2], *and the ALICE collaboration*

[1]Physik Department E62, Technische Universität München, Garching; [2]Excellence Cluster 'Origin and Structure of the Universe', Garching; [3]Institut für Kernphysik, Goethe-Universität, Frankfurt am Main

The ALICE Collaboration is planning a major upgrade of its central barrel detectors to benefit from the significantly increased LHC luminosity beyond 2019 [1]. In order to record at an increased interaction rate of up to 50 kHz in Pb-Pb collisions, the TPC, the main device for charged-particle tracking and particle identification (PID) in ALICE, will be upgraded with GEM-based (Gas Electron Multiplier [2]) readout chambers [3] allowing for continuous operation in an ungated mode. The increase in interaction rate and the requirements of a trigger-less, continuous readout demand for significant upgrades of the front-end cards, the computing system and the corresponding calibration, reconstruction and simulation framework.

Event generators, such as HIJING [4], are powerful tools to obtain a deeper insight into the particle production mechanisms at the highest energies, and the corresponding final state interactions. A meaningful comparison of such models to experimental data is, however, only possible when the full process of signal formation in the detector is properly modelled in the simulation. Consequently, the upgraded readout scheme of the ALICE TPC demands for a complete re-design of the *digitization*, in which these processes are handled.

The first step after the simulation of the incident particle traversing the detector and the conversion of the corresponding energy deposit into number of electron-ion pairs, is the electron transport in the active volume of the detector. The electrons drift up to 250 cm from the point of their creation until the readout chambers on both ends of the TPC, during which diffusion and attachment occurs. Having reached the readout chambers, the electrons are amplified in the stack of four GEM foils. Fluctuations of the amplification process are modelled according to the findings reported in [5]. The electrons extracted from the last GEM in the stack induce a signal on the pad plane during their drift. Due to the charge spread in the GEM stack and the Coulomb field exerted by the resulting electron cloud, a signal may as well be induced on adjacent pads. These effects are incorporated in the *pad response function*, as displayed in Fig. 1. The latter is computed using a Garfield [6, 7] / COMSOL [8] simulation of the movement of the electrons in the field between the pad plane and the last GEM. The induced current for different starting positions of the electron cloud is calulated and normalized to that expected in the centre of the pad.

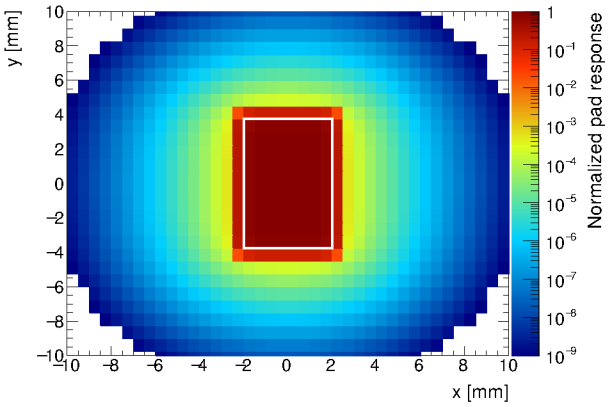

Figure 1: Pad response function of an Inner Readout Chamber of the ALICE GEM TPC for different starting points of the electron avalanche. The white shape indicates the outline of the pad.

The bottom side of the last GEM couples capacitively to the readout anode and thus upon extraction of electrons from the GEM, a signal of opposite polarity is induced on all pads of the readout chamber. This *common mode effect* leads to an effective baseline shift and hence to additional noise in the system. Furthermore, the signal processing in the front-end cards is modelled, during which the avalanche is convoluted with the Gamma4 shaping function and the resulting signal sampled with 5 MHz. The final entity, a *Digit*, which is defined as an ADC value on a given pad and time bin, is then written to disk for further processing.

The simulation framework allows to run in triggered and continuous mode. A first validation will be possible with data measured in a beam test at CERN in May 2017 with a final readout chamber and final front-end cards. Long term tests of the stability and the powering scheme of the readout chambers will be continued in the ALICE cavern.

References

[1] B. Abelev *et al.*, CERN-LHCC-2012-012 (2012).

[2] F. Sauli, NIM A **386** (1997) 531.

[3] B. Abelev *et al.*, CERN-LHCC-2013-020 (2013).

[4] X.-N. Wang and M. Gyulassy, Phys. Rev. D44 (1991) 3501.

[5] A. László *et al.*, JINST 11 (2016) P10017.

[6] R. Veenhof, http://garfield.web.cern.ch.

[7] T. Gunji, private communication.

[8] COMSOL Multiphysics® v. 5.2.

* This research was supported by the DFG cluster of excellence 'Origin and Structure of the Universe' and the BMBF Verbundprojekt 'ALICE at high rate' 05P15WOCA1.

† andreas.mathis@ph.tum.de

DOI:10.15120/GR-2017-1